

---

# **Corrosion in crystalline silicon photovoltaic modules and the influence on performance**

---

By Nikoleta Kyranaki

## **Doctoral Thesis**

Submitted in partial fulfilment of the requirements for the  
award of

Doctor of Philosophy of Loughborough University

August 2020

© Nikoleta Kyranaki 2020

# Abstract

The work presented in this thesis comprises research into degradation paths that cause corrosion of different components of solar photovoltaic (PV) cells and quantifies the impact of corrosion on the energy yield of PV modules.

PV modules are exposed to different climatic conditions when they are installed in the field. This exposure causes various degradation modes which affect their reliability to produce electricity and their overall durability. Harsh environments can decrease the lifetime of a PV module below 25 years, which is the threshold lifetime suggested for all climates by most PV manufacturers. Crucially, this is also the expected period over which the cost of generated electricity is most often based yet has not been validated given the relative youth of the PV market. Reduction of the PV module lifetime through degradation and failures can significantly affect the financial and technical viability of solar PV as a source of clean electricity and more robust predictions of module lifetime are urgently required.

One very significant cause of failure is corrosion. Environmental moisture penetrates the PV laminates and reacts with the different polymers and metallic parts of the construction, accelerated by higher levels of temperature. From hydrolysis of the most commonly used encapsulant (Ethylene Vinyl Acetate, EVA), acetic acid is produced and attacks further the cell electrical contact metallisation, cell interconnection ribbons and back contact of the PV cells. Corrosion affects mainly the series resistance ( $R_s$ ) of a PV module, causing severe decrease of the PV electrical power output, and is currently understood to be the second highest cause of energy yield loss of systems installed in the last 10 years.

The main areas requiring research have been identified as: determination of the temporal evolution of the distribution of moisture content within a PV module subjected to a given environment; full understanding of the chemical reactions taking place and separation of the impact of the different component degradation on the PV performance of a PV module; investigation of the corrosion impact on the performance of PV modules exposed to outdoor conditions, for a non-tropical climate.

The paths that the moisture follows within a PV module have been already investigated through theoretical simulations. However, these simulations currently lack rigorous experimental validation, that includes accurate values of moisture concentration accumulated within a PV module. To this end, a method that measures the equilibrium moisture content absorbed by the polymers contained in a PV module is applied, accompanied by a non-destructive method for the quantification of the moisture presence within a PV module. The values that result from the moisture measurements are used for verification of theoretical simulations implemented with COMSOL Multiphysics. Values of moisture concentration at different positions within a PV module are needed for understanding of the corrosion of the different metallic components contained in a PV module.

Published studies of the various mechanisms of corrosion of different components of a PV cell exist but stop short of relating this to power output. This is addressed here, in which a method that separates the impact of each mechanism on the degradation of the electrical power output is presented, thus allowing prediction of specific failure modes for a given bill of materials and operating environment. Half encapsulated PV cells (with either front or rear side exposed) are immersed in acetic acid baths or stored in an environment of high level of relative humidity and temperature (damp heat conditions). The results are compared to the findings of fully encapsulated PV modules aged under the same damp heat (DH) conditions. Both electrical and material characterisation are involved for identification of the different mechanisms. Results show that the most severe degradation is caused by accumulation of acetic acid on the front side of the solar cells. Although aluminium reacts severely with moisture, the aluminium back contact corrosion was found to be a negligible failure mode for fully encapsulated PV modules. Additionally, the impact of different back sheets on corrosion is studied, which again seems to be negligible, as the moisture accumulated at the front side of a PV cell is mainly affected by the diffusion coefficient of the encapsulant.

Finally, the impact of corrosion on PV modules installed in the field is poorly addressed in current literature, especially for PV modules exposed to non-tropical climates. The simulations available are not based on the physics of the degradation mode, but are empirical relationships whose parameters are extracted by fitting to indoor performance data. This approach makes these methods unreliable for

outdoor predictions. Moreover, they are not validated against real outdoor data. The research in this work has achieved a method to partially understand this effect, as it is very difficult to separate the electrical signatures of different failure modes that occur simultaneously. The method involves the estimation of the series resistance evolution of PV modules operating at Loughborough University for 7 years, combined with visual inspection. The results show that seven years is a short period to observe significant corrosion in a temperate climate, but the method applied is adequate for its detection.



# Acknowledgements

First, I would like to express my deep appreciation to my current supervisors Tom Betts, David Whalley and David Hutt for their significant contribution and their valuable advice on the research presented in this thesis. Especially, I would like to thank Tom Betts for his support during the years needed for the completion of this PhD.

In addition, I would like to say a big thank you to Ralph Gottschalg and Jiang Zhu for recruiting me and giving me the opportunity to get a Marie Curie fellowship, within the Solar-Train project. Moreover, their initial supervision for the first year of my PhD was very important to start and continue my work.

I am grateful to Kevin Bass, Alex Smith, Martin Bliss, Keith Yendall and Fabiana Lisco for their important guidance and useful tips regarding the use of the equipment located at CREST and the materials department. Moreover, I am thankful to Daniel Montiel Chicharro, as he initially taught me how to manufacture mini-modules. Furthermore, my deep thanks go to Francesco Mariottini and Ashenafi Weldemariam Gebregiorgis for a valuable collaboration on coding and experimental set up.

Furthermore, I want to deeply thank Ralph Gottschalg, Florian Herbst, Michael Wendt and Johannes Nagel for the exceptional collaboration at Fraunhofer Center for Silicon Photovoltaics (CSP), Marko Topič, Marko Jankovec, Stefan Mitterhofer, Jan Slapšak and the rest colleagues at University of Ljubljana for their remarkable help, and Mike Van Iseghem, Nikola Hrelja, Eric Lajoie-Mazenc, Julien Dupuis and the rest team at Electricité de France (EDF) for the experience gained while working with them. Moreover, I am grateful to Ana Rosa Lagunas and Aziz Nairi for providing some of the backsheets and solar cells, which were tested for the needs of this thesis.

I would also like to thank Elena Koumpli and George Koutsourakis for their great support, as without them, moving first time abroad and starting a PhD would be a much more difficult situation. A big thank you goes to all previous and current

CREST fellows for being very nice colleagues and friends and supporting me through the PhD experience.

I am very grateful to all the Solar-Train supervisors for the collaboration and the very useful skills that they taught me during the Solar-Train meetings and summer schools. I am even more thankful to the Solar-Train ESRs for being great colleagues and for all the funny moments that made the PhD experience much more enjoyable.

I owe a big thank you to my Master's supervisor Yiannis Tripanagnostopoulos, as he found out about the Marie Curie fellowships and convinced me to apply, even if I was not believing in myself.

I am very thankful to my parents Eirini Vigkliari and Georgios Kyranakis because without them I would not be the person that I am, and not have reached so far.

Last but not least, I want to thank Lazaros Karavasilis for being a great partner and for all the emotional support that he provided whenever I felt discouraged and not strong enough to deal with the difficulties of doing a PhD.

**This study has received funding from the European Union's H2020 programme SOLAR- TRAIN under grant agreement No 721452.**

# Contents

Chapter 1	Introduction.....	1
Chapter 2	Failure modes of PV modules.....	11
2.1.	Introduction .....	11
2.2.	Operation of PV cells.....	11
2.3.	Failure modes of PV modules .....	16
2.4.	Summary of degradation causes and effects .....	31
2.5.	Implications for the following research .....	36
Chapter 3	Moisture Ingress into PV Modules .....	37
3.1.	Introduction .....	37
3.2.	Background literature review .....	38
3.3.	Methodology.....	42
3.4.	Investigation of moisture ingress and egress in polymer – glass laminates for PV encapsulation.....	43
3.5.	Identification of the absorption isotherm that PV module polymers follow.....	51
3.6.	Direct quantification of moisture ingress into PV laminates with the use of humidity indicator cards .....	60
3.7.	Acetic acid generation shortly after moisture saturation of polymer laminates .....	75
3.8.	Comparison of measured and simulated moisture profiles within a PV module.....	79
3.9.	Conclusions.....	86
Chapter 4	Corrosion behaviour of different components in a PV module.....	88
4.1.	Introduction .....	88
4.2.	Background review of corrosion reactions.....	89
4.3.	Experimental Investigation of Corrosion in PV modules.....	93
4.4.	Conclusions.....	129

Chapter 5	The impact of corrosion on PV modules aged in the field.....	131
5.1.	Previous studies and models of corrosion in the field.....	131
5.2.	Site information and data collection method.....	134
5.3.	I-V curve fitting .....	136
5.4.	Results .....	145
5.5.	Conclusions.....	155
Chapter 6	Thesis Conclusions.....	157
6.1.	Conclusions arising from this work .....	157
6.2.	Future avenues for research identified in this work .....	161

# Chapter 1 Introduction

The solar photovoltaic (PV) market is growing rapidly, with the cumulative global PV capacity growing from 100.5 GW in 2012 to 480 GW in 2018 [1], [2]. According to predictions by DNV GL [3], presented in Figure 1-1, the world installed power station PV capacity will reach 11.6 TW by 2050, showing a big growth. Moreover, at that time, the predicted power station PV capacity will be almost equal to the capacity of all the other power sources combined.

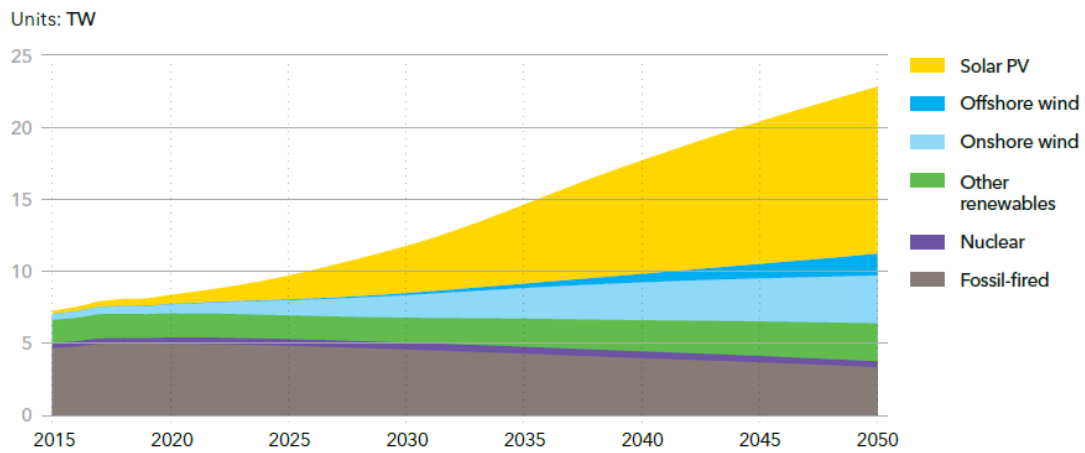


Figure 1-1 The upward trend of the global installed power station capacity [3].

One of the main factors making the PV market increasingly attractive is the continuing decrease in the cost of electricity produced by PV systems. The price of their main component, the PV module, is continuously falling, with a decrease of 0.09 €/Wp<sup>1</sup> or 25% (for mainstream PV modules), during 2018 – 2019 [4]. The capital cost of the PV modules (or panels) and systems is the most significant factor that affects the levelized cost of electricity (LCOE) and is part of the total life cycle costs (LCC) (Figure 1-2). The LCOE is estimated by:

$$LCOE = \frac{\text{Life Cycle Cost (LCC)}}{\text{Life Cycle Energy produced(LCE)}}, \quad (1-1)$$

<sup>1</sup> Euros per watt at peak performance

where LCC is made up of several costs, C:

$$LCC = C_{Dev} + C_{Panel} + C_{Elec.} + C_{Civil} + C_{O\&M}, \quad (1-2)$$

with  $C_{Dev}$  representing the development and planning,  $C_{Panel}$  the PV panels,  $C_{Elec.}$  the electrical apparatus,  $C_{Civil}$  the mounting structure and civil work, and  $C_{O\&M}$  the operation and maintenance [5]. To further decrease the LCOE, the energy produced by a PV system needs to be increased and remain optimal throughout the years of operation. For this reason, the degradation rate of PV systems must be minimal [6]. In case of high degradation rate, except the increase of the LCOE due to the decrease of the energy produced, further costs are required for repair or even replacement of parts that may fail. Relevant costs should be minimised, for the achievement of further investments on installation of PV systems, to meet and exceed the expectations of the projections presented in Figure 1-1. Figure 1-3 shows the relationship between the LCOE and the degradation rates of residential and commercial PV systems installed during the year 2010 [7]. The LCOE value for residential PV systems installed during 2019 in Europe was between 6.19 EUR cents / kWh (southern countries) and 32.15 EUR cents / kWh (northern countries), while the average LCOE for utility scale PV systems installed during 2018 worldwide was 4.21 EUR cents / kWh [8].

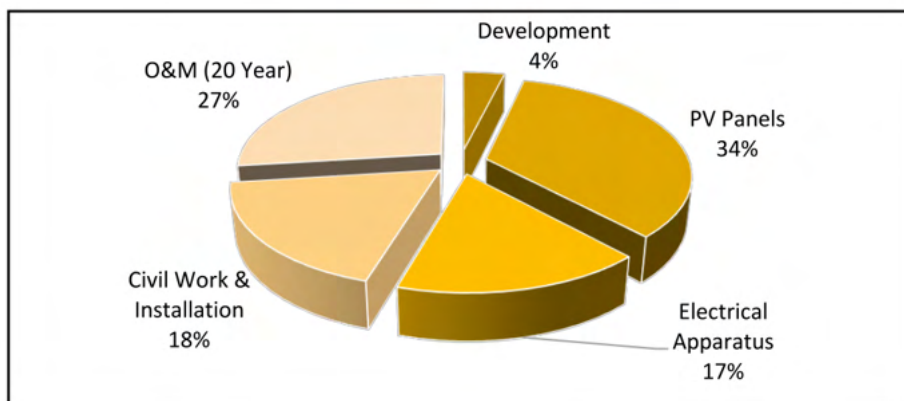


Figure 1-2 Proportion of costs included in the LCC [5].

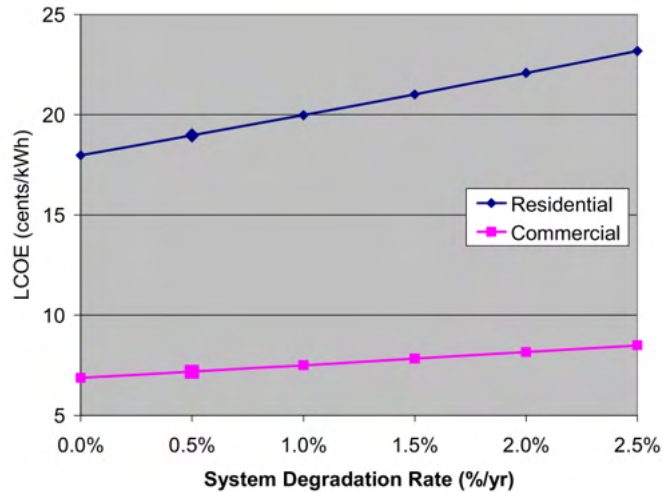


Figure 1-3 Relationship between the system degradation rate (% / year) and the LCOE (USD cents / kWh) for the year 2010 [7].

The most significant part of a PV system, responsible for the energy production, is the PV module. As the technologies most widely used in the field are monocrystalline (c-Si) and multicrystalline (mc-Si) silicon [9], the research presented in this thesis focuses on these specific technologies. A c-Si or mc-Si PV module consists of several components:

- The cells
- The metallisation
- The interconnections
- The encapsulant
- The top cover
- The rear cover
- The bypass diodes
- The junction-box

In Figure 1-4, the structure of a typical c-Si or mc-Si PV module is presented. For these specific types of cells, the PV module structure includes an antireflective (AR) coating (combination of silicon dioxide with silicon nitride or titanium dioxide [10], [11]) that is added to the surface of the cell to minimise the reflected light. The material of the AR coating commonly acts also as a passivation layer, which inhibits

carrier recombination at the surface of the cell [12]. In addition for most common cells, metallisation is required on the front and the rear side of a cell for the collection of the generated current. The front side metallisation has the form of a grid for which the most commonly used material is silver. The rear side metallisation, in the case of aluminium Back Surface Field (Al-BSF) technology, completely covers the surface of the cell and is usually aluminium [13]. In the case of Passivated Emitter and Rear Contact (PERC) cells, a passivation layer ( $\text{AlO}_x$ ,  $\text{SiN}_x$ ,  $\text{SiO}_x$ , or a combination of them) is applied also between the rear side of the silicon wafer and the aluminium back contact [14]. The impact of the passivation layer on the degradation rate is discussed thoroughly later in the thesis. Interdigitated back contacts (IBC) constitute a different metallisation structure, where both positive and negative contacts are placed on the rear side of a solar cell [15]. Further research is required to conclude if the IBC concept is more robust than the Al-BSF, regarding the degradation rate. The PV cells are connected by copper (Cu) ribbons which are coated with solder (with composition Sn-Pb, Sn-Pb-Ag or Sn-Ag-Cu [16]) which collect and transfer the generated current.

Two layers of polymer material (e.g. Ethylene Vinyl Acetate or EVA, ionomer, etc.) [17] are used as an encapsulant, one on the top and one on the back side of the cells. For the final encapsulation, a piece of glass is placed on the top of the module for the protection of the PV cells from the various environmental factors and mechanical support. A sheet of polymer (e.g. Polyethylene Terephthalate (PET), Tedlar Polyvinyl Fluoride, etc.) [18], mono- or multi- layer, or another piece of glass is placed on the back of the module to form the backsheet, for the same reasons. Finally, an aluminium frame is usually built around the edges of a PV module for mechanical support and further protection of the PV module from moisture penetration [19]. To complete the module, a junction box (that can be seen in Figure 1-4b) is attached to the rear side of the module, that contains the bypass diodes and the cables which connect the cell strings (sequences of PV cells) to the external terminals. Bypass diodes are used to protect the modules from local overheating when some of the cells become disconnected or shaded.

Figure 1-4c and d shows two configurations of PV module, one containing Al-BSF PV cells and another including Passivated Emitter and Rear Contact (PERC) PV cells.



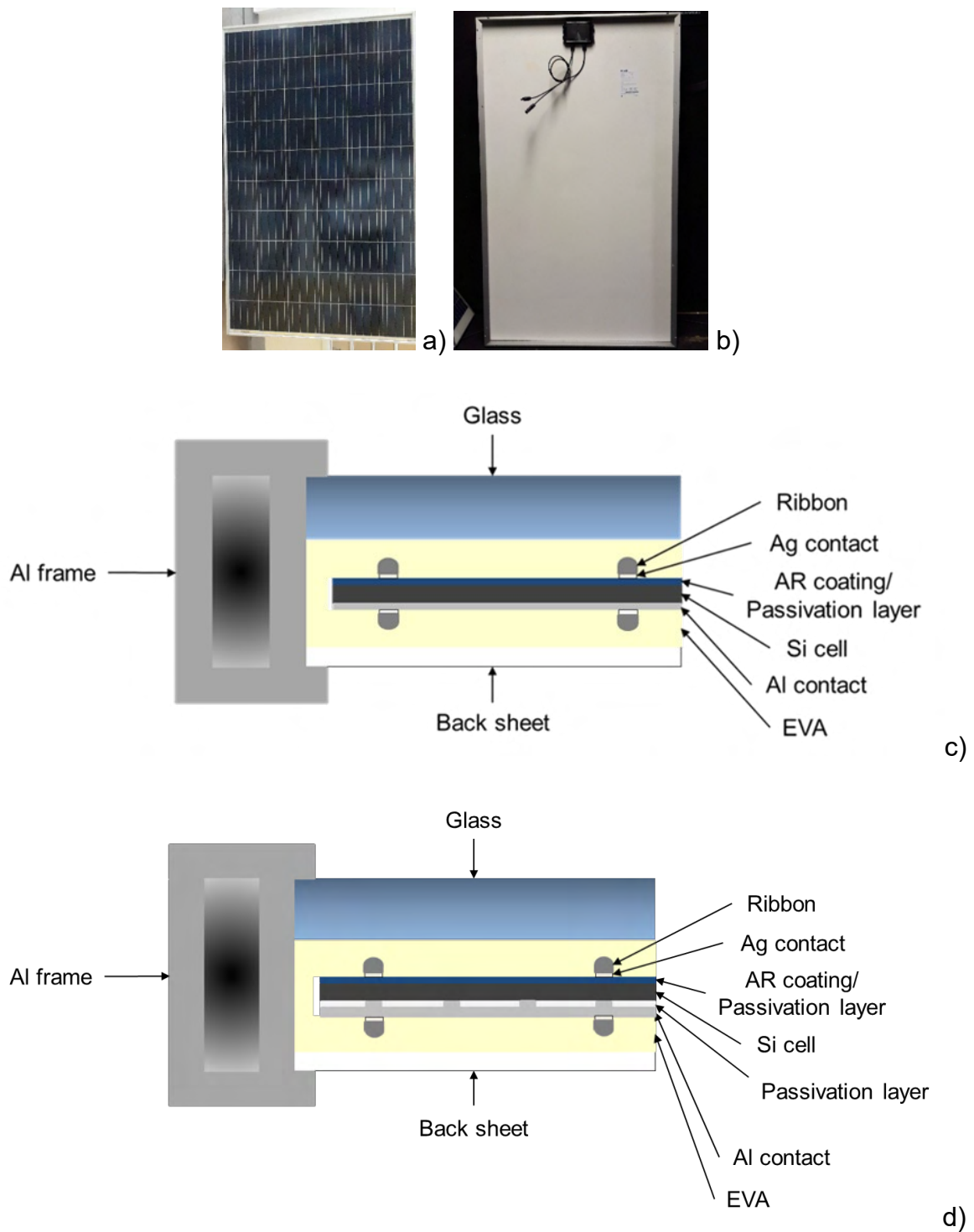


Figure 1-4 a) The front side, b) the rear side, c) the cross – section of a typical Al-BSF c-Si / mc-Si PV module and d) the cross – section of a typical PERC c-Si / mc-Si PV module.

The different components of the PV modules mentioned above have been observed to degrade when exposed to the environment under real operating conditions and can lead to the reduction in performance discussed above. For example, the

backsheet and the encapsulant can react with ultraviolet (UV) light and moisture. In combination with high temperatures they may produce an environment that can corrode the different metallic components (e.g. ribbons, front- and rear-side metallisation). Moreover, the metallic components mentioned above and the antireflective coating, are likely to degrade because of chemical/electrochemical reactions in the presence of moisture and high voltage, or it is possible for them to undergo mechanical or thermomechanical fatigue due to thermal cycling or external loads such as wind or snow. The literature review presented in Chapter 2 will describe in more detail these interactions, which can result in different degradation patterns and, subsequently, failure modes. The impact of the degradation mechanisms on the electrical performance will also be analysed.

The research reported in this thesis formed a part of the Solar-Train project under grant agreement No 721452, funded by European commission under the Marie Skłodowska-Curie Actions. The overall aim of that project was the forecasting of the PV module lifetime by the study of the different degradation mechanisms, the understanding of the effect of climate on them and the prediction of the performance reduction due to them. The Solar-Train partners and the work package collaborations are presented in Figure 1-5 and Figure 1-6, respectively.

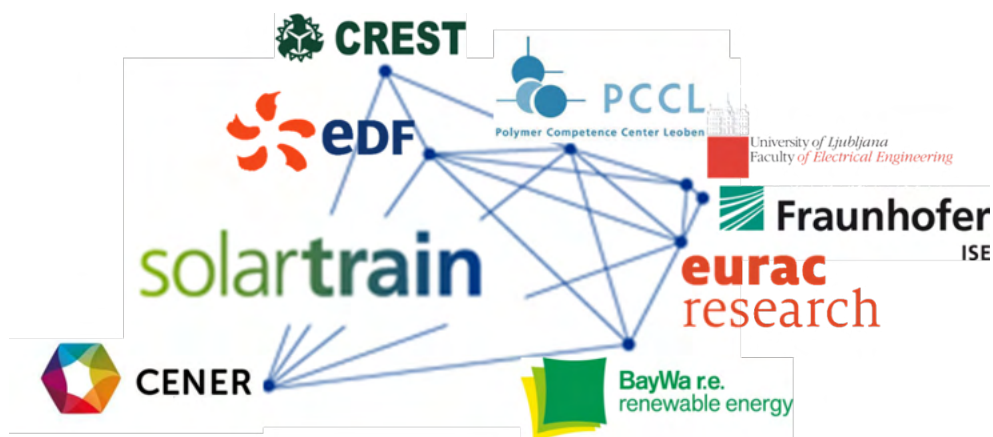


Figure 1-5 The Solar-Train partners.

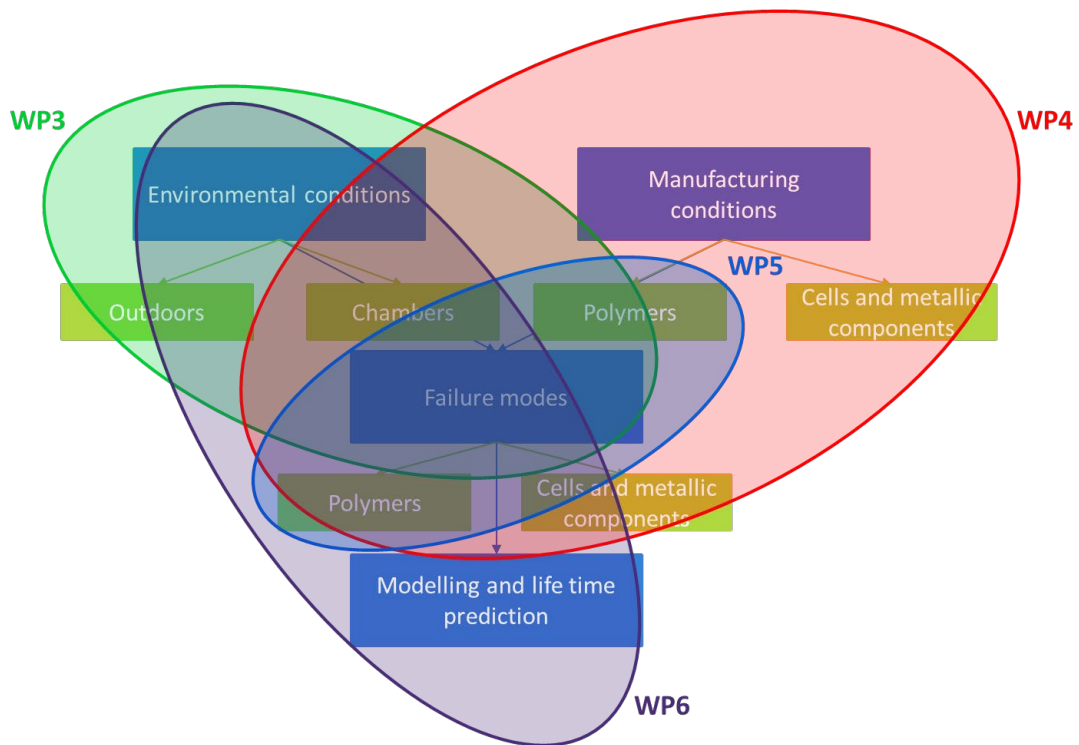


Figure 1-6 Solar-Train work packages (WPs) and collaborations.

### Aims and objectives

Due to the impact of degradation on the LCOE of a PV system, it is important to reduce its effects and investigate its causes so that it can be reduced in future designs. Corrosion is the second highest concern of systems installed in the last 10 years [20] after discolouration, and has not been thoroughly investigated. The aim of the research presented in this thesis is therefore to analyse the degradation paths that cause corrosion of the different components of the PV cells and quantify the impact of corrosion, as a degradation mode, on the energy yield of solar photovoltaic (PV) modules. To achieve this aim, a number of objectives were developed:

- Quantification of the humidity ingress through the polymers.
- Description of the reaction of the different metallic components with moisture and acetic acid produced by encapsulant degradation.
- Investigation of the impact of corrosion on the electrical performance of a PV module.

The overall work presented in this thesis is summarised in Figure 1-7. The research conducted for the investigation of these topics, indicated in red ellipses, is described in the paragraphs below.

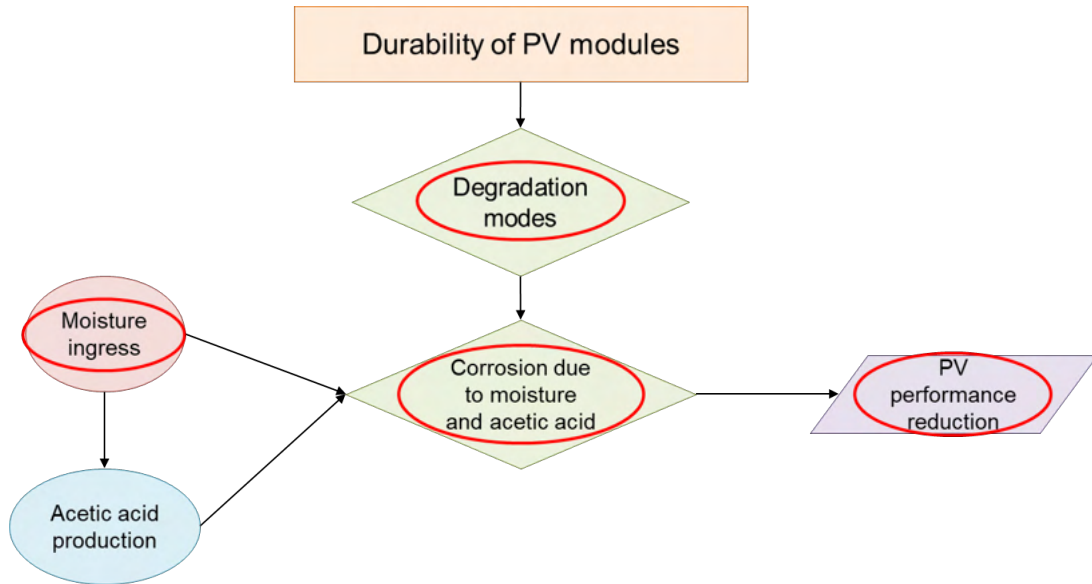


Figure 1-7 Thesis overall structure. The red ellipses indicate the topics analysed.

## Degradation mechanisms

The different failure modes observed on PV modules, their degradation mechanisms and their impact on the PV performance are thoroughly described through a literature review.

## Moisture ingress

Moisture triggers various types of failures. Humidity usually penetrates the PV structures directly through the backsheet and/or the module edges to reach the encapsulant and finally the cells. The paths that the moisture follows have been simulated and are well understood theoretically. However, the mentioned paths have not been verified experimentally, and the absorbed moisture content has not been accurately quantified. Chapter 3 verifies experimentally the moisture paths and describes a method for the correct calculation of the equilibrium moisture

content of the polymers. Moreover, an experimental method for quantification of the presence of moisture is developed and compared to simulation.

### **Corrosion due to moisture and acetic acid**

When moisture penetrates the PV module, it may react with the metallic components, causing corrosion. In addition, acetic acid produced by the hydrolysis of EVA attacks further the metallic components [21]. Corrosion is one of the main failure modes as it can cause severe degradation to PV modules exposed to hot and humid environments (e.g. 24% power output loss after 18 years of exposure) [22]. The components of the module that corrode are the ribbons, the metallisation, the antireflective coating / passivation layer (depending on the material and the stress conditions) and the aluminium back contact, and the specific chemical reactions involved are well understood [23], [24]. However, which component shows the most serious degradation in the field and causes the most severe power loss is unknown. Moreover, the severity of corrosion in case of lack of acetic acid and for different moisture diffusion coefficient of the backsheet is not yet well researched. Chapter 4 presents a combination of experimental methods that distinguish between the front and rear side corrosion and identify the different electrical signatures observed due to each. Furthermore, the impact of corrosion on PV cells is studied for the absence of acetic acid and for varied water vapour transmittance.

### **PV performance reduction**

It is well known that corrosion is more rampant for hot and humid environments. The tropical climate combines both requirements for the development of corrosion [25]. However, whether corrosion is a major failure for a PV module exposed to other types of climate is not well researched. Furthermore, although it is well known that corrosion affects mainly the series resistance of a PV module [26], the impact of corrosion on the power output degradation of a PV module installed in the field is not yet understood. Chapter 5 investigates the research topics mentioned above, by analysing the evolution of the power output and the series resistance of PV modules installed at Loughborough University.

Finally, Chapter 6 concludes all the presented work and suggests potential future research that could be conducted, regarding the investigation of different aspects of the analysed topics.

# Chapter 2 Failure modes of PV modules

## 2.1. Introduction

The recognition of the failure modes of a PV module and how these affect their reliability in the field has been a subject of investigation since the 1970s, when this topic was first researched under the Flat-Plate Solar Array project sponsored by the U.S. Department of Energy [27]. Research has since been conducted on the identification of the origin of the different failure modes and the understanding of their impact on the performance of PV modules. However, even today, knowledge about the various degradation paths, how they influence the performance of PV modules and how they are linked to different climatic conditions is insufficient. In this chapter, the published failure modes observed in PV modules are identified and analysed. Moreover, their influence on the parameters of the diode model (single or double), which is often used to represent the electrical operation of a PV cell, is described.

## 2.2. Operation of PV cells

To enable understanding of the impact of different failure modes on the performance of PV modules, the operating principles of a PV cell will be described first. The “one-diode model” (or single-diode model) is often used to represent PV cell electrical behaviour and can be scaled to represent PV modules of many interconnected cells also. The following paragraphs explain the origin of the five parameters of this model and what they represent in relation to the equivalent circuit.

A solar cell is a semiconductor (p-n junction) which produces voltage and electric current when exposed to light (photovoltaic effect). Photons with equal or higher

energy than the band gap energy of the material cause carrier excitation [28]. However, although the material produces current due to the described procedure, it also consumes, as a semiconductor which behaves as a diode. For this reason, an ideal solar cell may be represented as a current source connected with a diode in parallel (Figure 2-1). The accompanying equation that describes this representation is [29]:

$$I = I_{ph} - I_d \quad (2-1)$$

where  $I_{ph}$  is the photocurrent and  $I_d$  is given by the Shockley ideal diode equation:

$$I_d = I_0 \left[ \exp\left(\frac{qV}{k_B T}\right) - 1 \right] \quad (2-2)$$

where  $I_0$  is the saturation current of the diode, which represents the recombination current due to the recombination of the carriers within the depletion region,  $q$  is the electron charge,  $k_B$  is the Boltzmann constant,  $V$  the voltage across the cell terminals and  $T$  the temperature of the cell. The  $I_{ph}$  is mainly dependent on the photon flux incident on the cell, and the bandgap of the material.

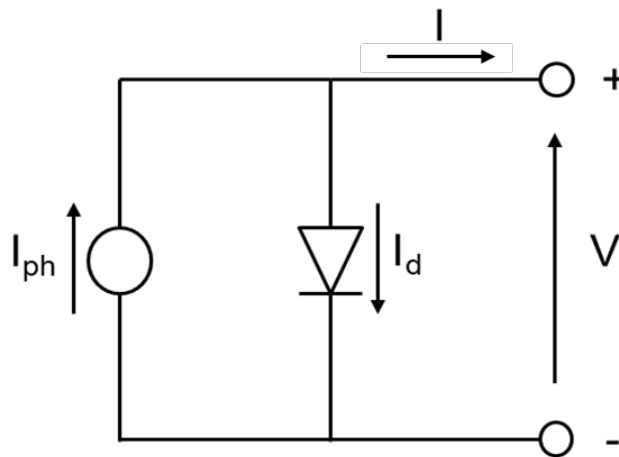


Figure 2-1 The circuit representation of an ideal PV cell.

In Figure 2-2, an I-V curve, which represents the current ( $I$ ) that flows from the terminals indicated in Figure 2-1 (circles with + and -), as a function of the voltage ( $V$ ) applied across them, is presented. Moreover, the key points: short circuit current ( $I_{sc}$ ), open circuit voltage ( $V_{oc}$ ), current at the maximum power point ( $I_{mpp}$ ) and



voltage at the maximum power point ( $V_{mpp}$ ) are indicated. The maximum power point ( $P_{max}$ ) is the point of the I-V curve where the product of the I multiplied by V is maximum. Furthermore, the Fill Factor (FF) of a PV cell is defined as:

$$FF = \frac{P_{max}}{I_{sc} \cdot V_{oc}}, \quad (2-3)$$

while the efficiency ( $\eta$ ) of a PV cell is calculated by:

$$\eta = \frac{P_{max}}{P_{in}}, \quad (2-4)$$

where  $P_{in}$  is the incident power of the light to the surface of the PV cell.

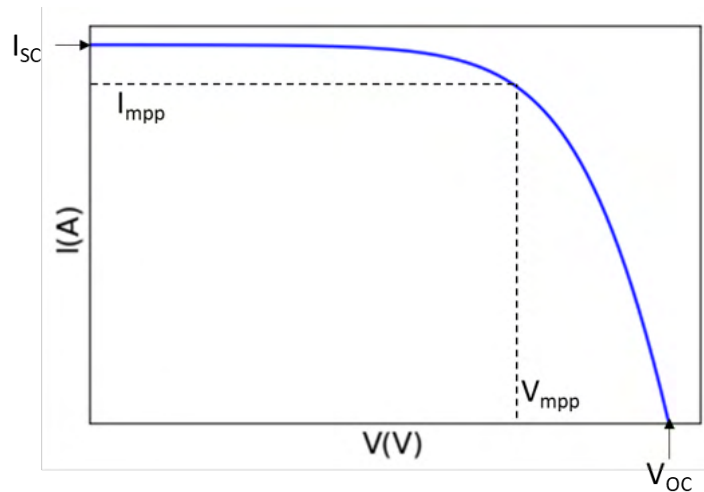


Figure 2-2 A typical I-V curve of a PV cell with the key points  $I_{sc}$ ,  $V_{oc}$ ,  $I_{mpp}$  and  $V_{mpp}$  indicated.

The ideal single-diode model presented above does not describe fully the operation of a real solar cell, as it does not include the impacts of parasitic resistances and additional carrier recombination that exist due to imperfections in the PV cell material and the additional components attached to it (e.g. contacts and interfaces) [28]. To represent these effects, the ideal model is modified as shown in Figure 2-3 [29].

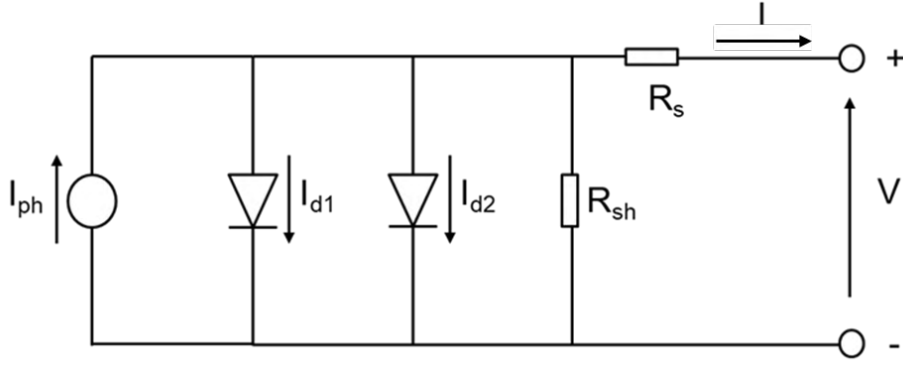


Figure 2-3 The circuit representation of a real PV cell.

The current, can then be represented by:

$$I = I_{ph} - I_{01} \left[ \exp\left(\frac{q(V+IR_s)}{k_B T}\right) - 1 \right] - I_{02} \left[ \exp\left(\frac{q(V+IR_s)}{2k_B T}\right) - 1 \right] - \frac{V+IR_s}{R_{sh}} \quad (2-5)$$

where  $I_{01}$  is the same as  $I_0$  in the equation of the one-diode model and  $I_{02}$  is the saturation current of the non-ideal diode, which represents the additional carrier recombination within a PV cell due to material defects.  $R_s$  is the series resistance and represents the aggregation of resistance in the emitter, base, front and rear contacts, finger contacts and the collecting busbars.  $R_{sh}$  is the shunt resistance and represents parallel high-conductivity leakage paths which are caused by damage of the crystal or impurities near to and within the junction [29]. The relationship above can be approximated as:

$$I = I_{ph} - I_0 \left[ \exp\left(\frac{q(V+IR_s)}{nk_B T}\right) - 1 \right] - \frac{V+IR_s}{R_{sh}} \quad (2-6)$$

where  $n$  represents the lumped ideality factor with  $1 \leq n \leq 2$ . For  $n \approx 1$  the behaviour of the cell is almost ideal and  $n \approx 2$  indicates increased influence of carrier recombination within the p-n junction of the PV cell. The ideality factor is an indicator of the quality of the semiconductor [30].

Figure 2-4 shows how the variation of each parameter of the diode model affects the I-V curve of a PV cell. For the calculation of the I-V curve of a PV module which contains  $N_s$  number of cells connected in series, Kirchhoff's law is applied. According to this, the current passing through the total of the PV cells will be the same, while the voltage of the PV module will be equal to the sum of the voltages

of the PV cells. The equation representing the I-V curve of a PV module with  $N_s$  number of cells connected in series is the following [31]:

$$I = I_{ph} - I_0 \left[ \exp \left( \frac{q(V + IN_s R_s)}{nN_s k_B T} \right) - 1 \right] - \frac{V + IN_s R_s}{N_s R_{sh}}, \quad (2-7)$$

The various degradation mechanisms and failure modes of PV modules affect these parameters differently, as will be discussed later in this chapter. Moreover, how these parameters change, due to artificial and natural aging, will be discussed in later chapters. It must be noted, that although it seems that the  $V_{OC}$  increases with increased  $n$  (Figure 2-4b), the decrease of FF is significant, and for a real PV cell, increase of  $n$  and  $I_0$  usually co-exist.

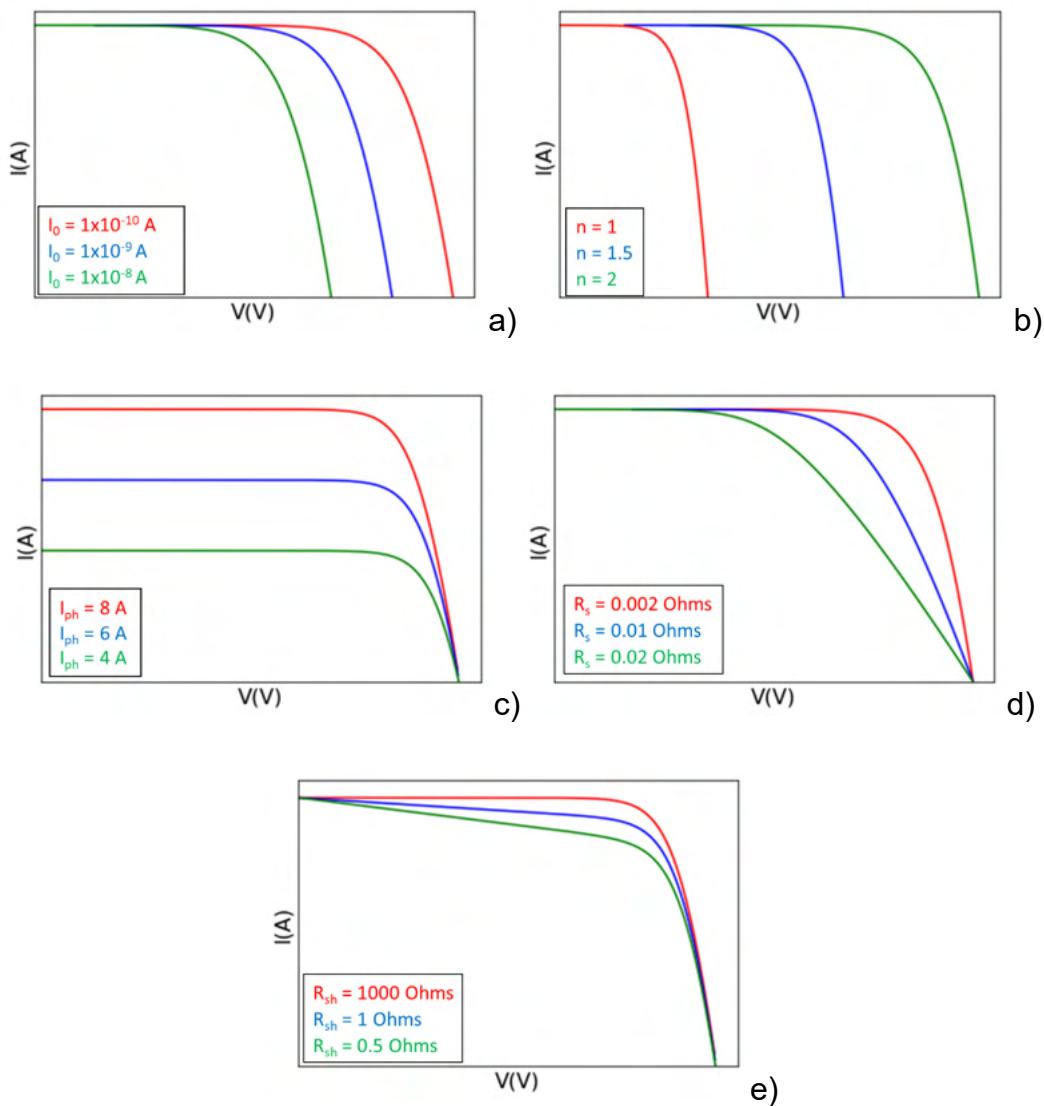


Figure 2-4 The impact on the I-V curve of a PV cell due to variance of a)  $I_0$ , b)  $n$ , c)  $I_{ph}$ , d)  $R_s$  and e)  $R_{sh}$ .

## **2.3. Failure modes of PV modules**

In this section, the key terms used in literature to describe the reliability and failure of PV modules will be defined as used in this thesis. Then follows a review of the major influences that lead to a reduction in PV module efficiency when exposed to outdoor environments and a rationale for the focus of this work.

### **2.3.1. Definition of key terms**

**Reliability:** Reliability is the probability that a device's performance will meet the manufacturer's specification for particular operating conditions and duration [32]. In the case of PV modules, reliability determines the manufacturer's warranty.

**Durability:** Durability is the ability of a device to last for a long period of time without the need of repair [33]. For PV modules, durability is linked to the lifetime, a term that is debated and not fully defined.

**Degradation:** Degradation is the gradual decrease of the performance of a device due to the conditions to which it is exposed, which may or may not result in insufficient performance according to the manufacturer's warranty [34].

**Failure:** A failure of a PV module is a condition that:

- (1) causes loss of performance below a specified level which cannot be reversed;
- (2) generates a hazard of unacceptable risk in terms of health and safety.

A cosmetic issue that does not lead to (1) or (2) is not perceived as a PV module failure. A PV failure is considered a breach of warranty only if it occurs while the PV module operates under the conditions for which it was designed [19].

### **2.3.2. Degradation mechanisms seen in operational PV systems**

The most common degradation mechanisms that have been observed in the field and will be thoroughly described in this chapter are [34], [35]:

- Corrosion
- Disconnected cells and string interconnect ribbons
- Delamination / bubbles
- Encapsulant discolouration
- Backsheet embrittlement
- Cell cracks
- "Snail trails"
- Potential Induced Degradation (PID)
- Degradation of the antireflective (AR) coating / passivation layer
- Light-Induced Degradation (LID) and Light and elevated Temperature Induced Degradation (LeTID)
- Frame detachment / breakage
- Glass breakage
- Soiling
- Burn marks / Hot spots
- Defective bypass diode
- Junction box failure

### **2.3.3. Failure mode classification based on time period**

The various failure modes are classified into infant-mortality, those that occur in the midlife of PV modules and wear out (Figure 2-5) [32].

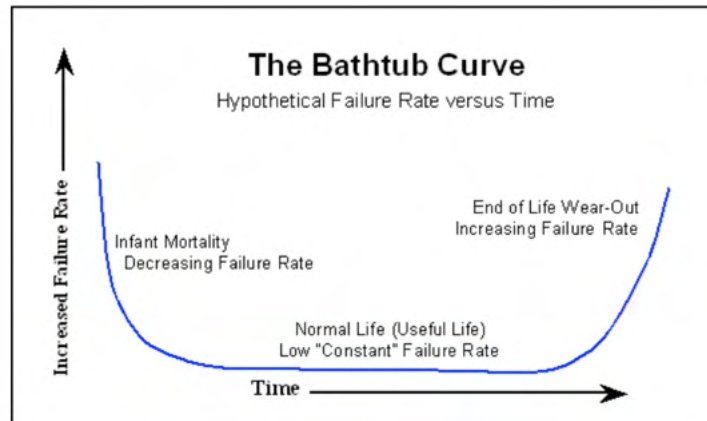


Figure 2-5 Failure rates of PV modules during their lifetime [32].

Infant-mortality failure modes occur during the early life of a PV module [19]. The failure rate is decreasing during this period: the weaker units stop operating and a more durable population remains. The most significant infant-mortality failure modes in the field are junction box failure, glass breakage, defective cell interconnect, loose frame and delamination. Another degradation mode that occurs very early, but does not cause failure, is LID (further discussion on the mechanism will follow in section 2.3.10), which appears in a significant proportion of PV modules after installation [19]. LID is considered unavoidable for the majority of currently deployed PV cell technologies and the warranty curve on the PV module datasheet is normally estimated so the power loss due to this degradation mode is already ~2% at year zero (Figure 2-6).

The failure modes that normally occur during the midlife of PV modules are defective cell interconnects, glass breakage, junction box and cable degradation, burn marks, corrosion and encapsulant failures (Figure 2-6) [19]. The order in which these failure modes occur in this period is more random. It is hard to forecast which failure mode will present as their occurrence depends on multiple drivers and some modes are linked [32]. Furthermore, although the overall failure rate may be estimated for already aged PV modules, it cannot be accurately predicted, although statistical approaches have been developed for this purpose.

Wear out failure modes occur at the end of the operational life of PV modules, or rather they largely define the maximum lifetime of a PV module. The lifetime ends when a safety-compromising problem occurs or the PV module conversion

efficiency falls below a certain level, which is usually determined between 80% and 70% of the initial rating [19]. It should be noted that this is often referred to as “power loss”, but is more precisely the power loss under specified conditions (typically IEC Standard Test Conditions). Used in this thesis, “power loss” should be taken with this second meaning, unless specified otherwise. The principal PV module degradation mechanisms are delamination, corrosion, partial cell isolation due to cell cracks, and laminate discoloration, leading altogether to 0-20% power loss, with average 10% after 15 years of operation, according to Köntges et al. [19]. However, these numbers might have changed, as the specific research was conducted on 2014 and the studied PV modules were already 15 years old. In Figure 2-5 the wear out period starts at the point where the slope starts to rise and increases exponentially as time proceeds as units age and start to fail at an increasing rate [32].

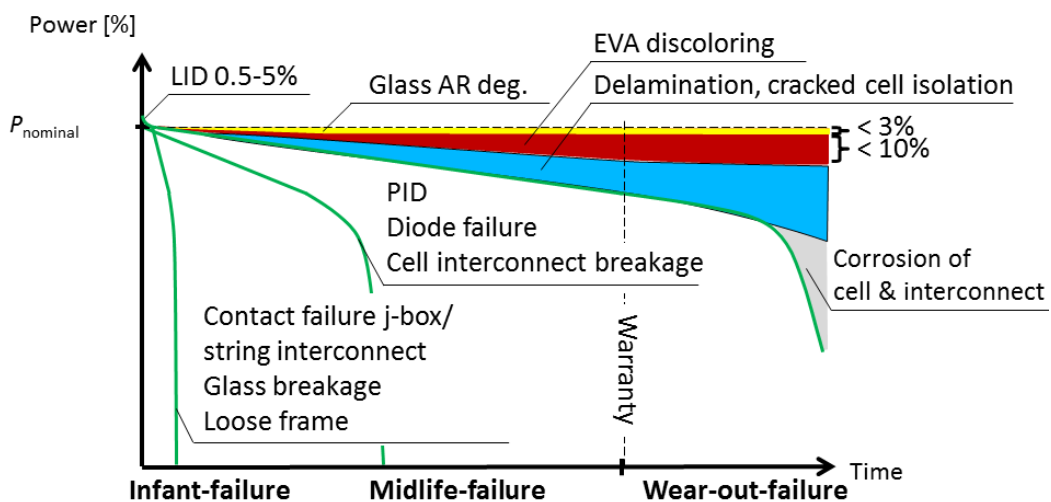


Figure 2-6 Classification of failure modes according to the time period in which they occur and their impact on the module performance [19].

Figure 2-7 shows an overview of the combination of the frequency and the severity, according to the impact on PV performance, of each degradation mechanism [20]. The reduction of encapsulant discoloration, due to the UV protection additives that are used during the last 10 years, is visible. Furthermore, the evolution on the manufacturing of the PV cells had a negative impact on their PID tolerance (see section 2.3.8), due to the increase of the power output produced by each cell and subsequently module, leading to higher difference of potential between the first and

the last module installed on a PV array. Further description of each degradation mechanism is given in the following sections.

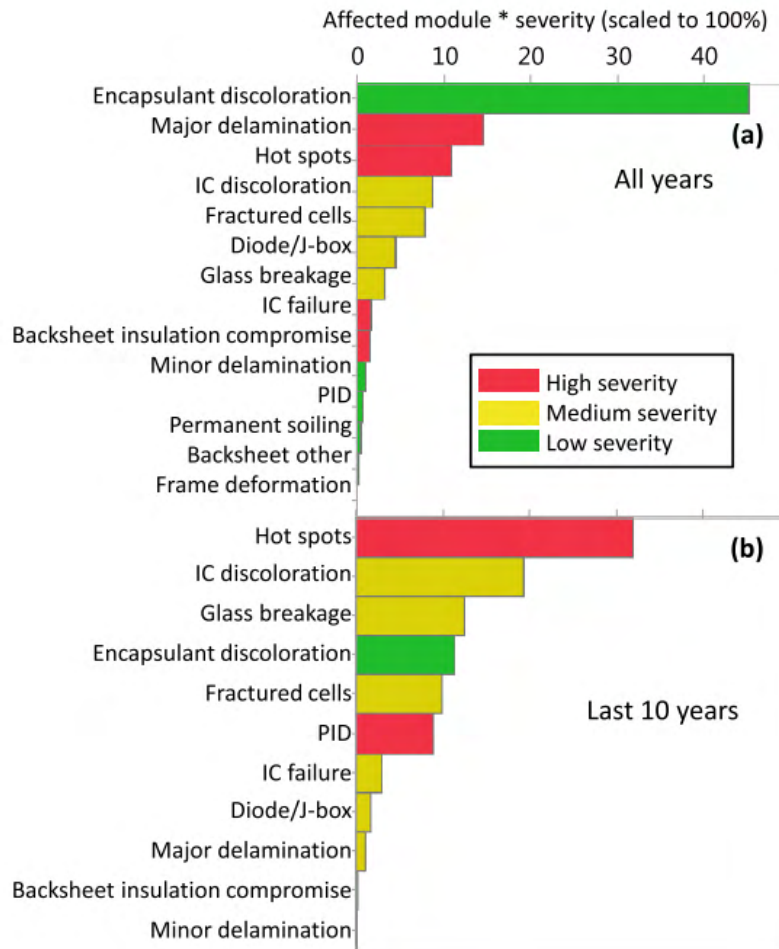


Figure 2-7 Overview of the combination of the frequency and the significance of each degradation mode for PV modules installed within the time period a) prior-2000 – 2017 and b) 2007 – 2017 [20]. Corrosion is mentioned as Internal Circuit (IC) discoloration.

### 2.3.1. Corrosion

Corrosion is a wear out (could occasionally be observed earlier in the lifetime of a PV module) degradation mode and one of the most frequently occurring in the field [36] with frequency x severity factor (the number of the modules affected were multiplied by the severity factor, which is 5, due to medium severity, and then scaled to 100%) 20% on the PV modules installed during the last 13 years [20]. Moisture penetration through the backsheets and the laminate edges of the module creates the conditions for corrosion [37], which are chemical, physical or electrochemical



reactions between this moisture and, for example, the AR coating, aluminium back contact, solder joints and silver fingers (Figure 2-8) [26]. Corrosion of most of these components can cause an increase of the series resistance [38] and resulting loss in voltage and power at the maximum power point. Moreover, severe corrosion of the metallisation and the busbars can lead to their detachment from the cell surface and subsequently to decrease in current collection [39]. Production of acetic acid due to hydrolysis of the Ethylene Vinyl Acetate encapsulant (which occurs because of exposure to moisture, high temperature and UV) can also accelerate corrosion [40]. Corrosion will be reviewed further in the following chapters, as it is the degradation mode that the work presented in this thesis investigates extensively, among the various other degradation mechanisms (Figure 2-7, where corrosion is presented as IC discolouration).

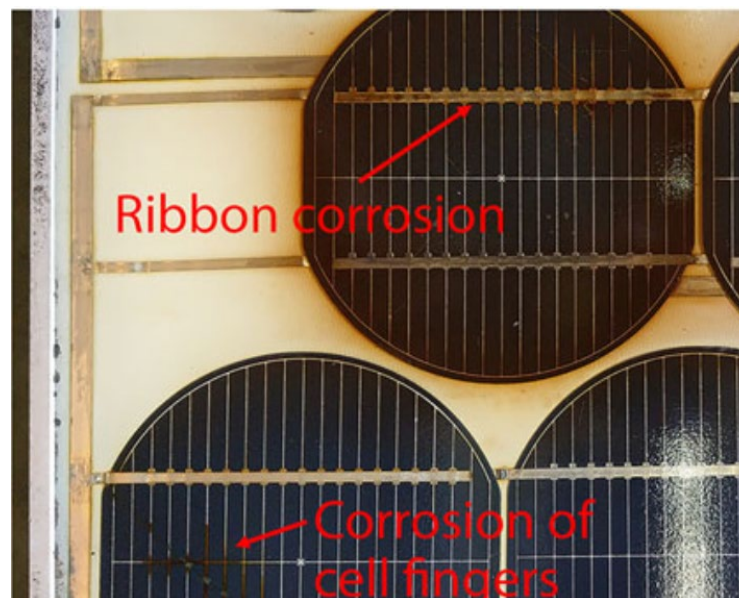


Figure 2-8 Corrosion of ribbon and silver fingers [41].

### 2.3.2. Disconnected cells and string interconnect ribbons

Thermo-mechanical fatigue is responsible for the creation of structural defects in the soldering alloy. These may be voids or cracks that are created or expand under high stress conditions, leading to thread-like (almost broken) joints, causing increased series resistance and, subsequently, decreased performance [42]. More specifically, when a PV module undergoes thermal cycling, the different coefficients

of thermal expansion of the solder (alloy of Sn and Pb), the ribbon (Cu) and the silver contact (Ag paste) are the main cause of the initiation and propagation of voids and cracks [43]. Figure 2-9 presents an electroluminescence (EL) image of a PV module affected by thermo-mechanical fatigue, after a thermal cycling test, and shows the infrared emission of the PV cells due to the current flow caused by the applied voltage at the terminals. Very bright spots show high current flow, while dark spots represent the points that the ribbons are disconnected and do not allow any current to pass from the ribbon to the cell.

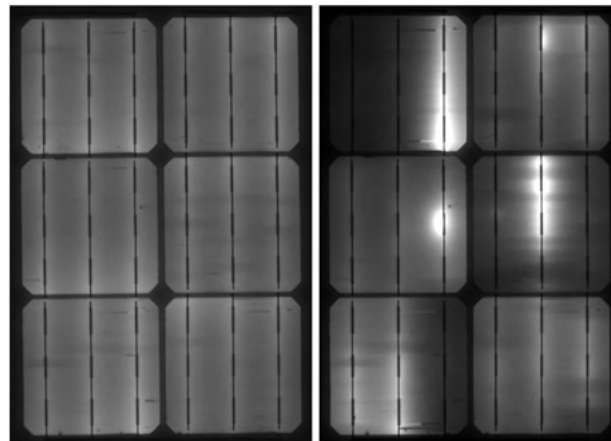


Figure 2-9 PV module before (left) and after (right) application of thermo-mechanical fatigue [18].

### 2.3.3. Delamination

Delamination is defined as the debonding of the different material layers which form the structure of a PV laminate [42]. Delamination can occur between the encapsulant and the cells, between the encapsulant and the front glass, or between the encapsulant and the backsheet [44]. Moreover, the different layers of which the backsheet is composed can also delaminate from each other [45]. Front-side delamination at the glass/encapsulant and cell/encapsulant interfaces is more frequently observed than rear-side delamination according to field experience [42]. Delamination is a major concern because it generates two consequences: an increase in the light reflection and moisture retention in the module [10]. Furthermore, when moisture penetrates, chemical reactions take place, resulting in degradation of different parts of the module (e.g. through corrosion, or encapsulant discolouration) [10], [46]. It is more likely to occur in hot and humid climates as the

reactions are accelerated due to high levels of relative humidity, temperature and UV exposure [47]. Delamination may be homogeneous (extended to a large surface) or heterogeneous (occurring on scattered regions). A type of heterogeneous delamination are bubbles, where the affected area is visibly swollen. A bubble typically is caused by a chemical reaction which results in gas release. When it happens in the PV module rear-side, a gap is formed in the encapsulant or the backsheet [10]. Examples of delamination and bubbles are presented in Figure 2-10.

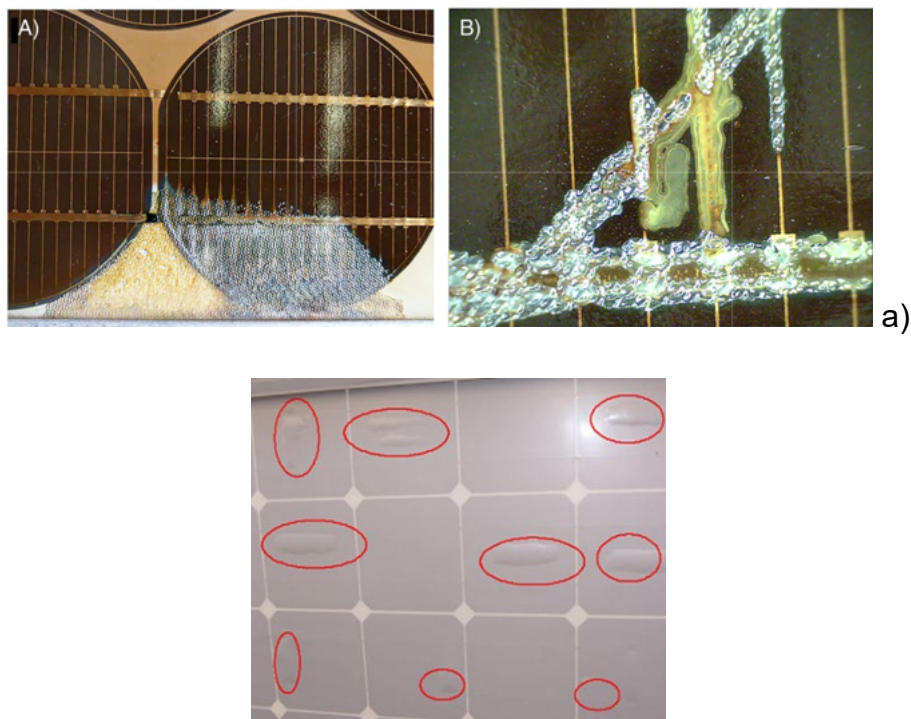


Figure 2-10 a) Delamination within a PV module [41] and b) bubbles on the backsheet of a PV module [10].

#### 2.3.4. Encapsulant discolouration

One of the most often observed degradation mechanisms in PV modules (mostly regarding older PV modules but also observed for a number of new) is discolouration of the encapsulant (Figure 2-11). Ethylene vinyl acetate (EVA) is the most frequently used encapsulant [19] because of the good mechanical properties that it shows and the low price [48]. Because of ultraviolet (UV) exposure, temperature and humidity, discolouration of EVA can appear such as yellowing or

browning. At high levels of temperature and humidity, combined with UV light, EVA reacts according to the Norrish I reaction, producing polyenes which are responsible for the yellow colour [49]. EVA lifetime can be lengthened by using UV stabilizers and anti-oxidants. However, the stabilizer and anti-oxidant concentration declines slowly at high temperatures and accumulated UV irradiation exposure. When the stabilizer concentration decreases below a certain critical threshold value, fast encapsulant degradation occurs [50]. Discolouration of EVA is one possible cause of the slow loss of short-circuit current which is observed in most crystalline silicon modules [51]. Regarding other types of encapsulants, some show similar behaviour to EVA (e.g. Polyvinyl Butyral - PVB) and for some of them very good resistance to UV irradiation is observed (e.g. silicones, ionomers) [52]. Discolouration may be homogeneous or heterogeneous.

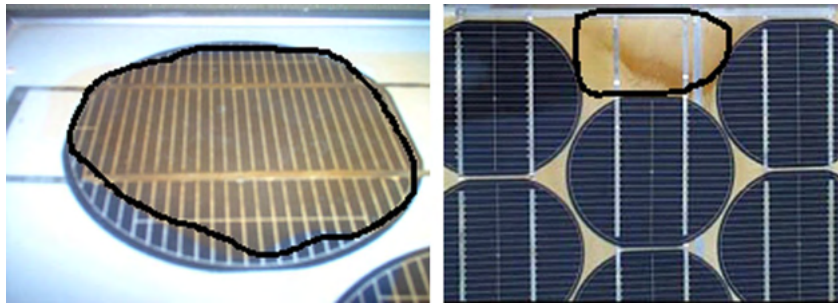


Figure 2-11 Encapsulant discolouration on a PV module [53].

### 2.3.5. Backsheet embrittlement

Backsheet embrittlement (Figure 2-12) causes the cracking of the backsheet due to the decomposition of the Polyethylene Terephthalate (PET) layer. In this PET layer photo-degradation occurs due to UV exposure (reaching at the inner side through the gaps formed between the edges of the cells, or the rear side by light reflection from the ground or other rows of PV modules) and hydrolysis associated with relative humidity and temperature that causes material incoherence [54]. Similar behaviour has been observed with Polyamide (PA) based backsheets, which seems to be enhanced on the side in contact with the EVA encapsulant due to acetic acid production in that material [55]. The backsheet embrittlement may lead to accelerated rates of corrosion, delamination and encapsulant discolouration due to

the consequent increased moisture ingress rate. Moreover, safety issues can arise because of increased polymer conductivity [56].



Figure 2-12 Cracked PET backsheet observed on PV module aged outdoors [54].

### 2.3.6. Cell Cracks

Micro cracks in solar cells are frequently observed in photovoltaic modules [57]. They cause a loss of structural integrity in the cell and can give rise to carrier recombination and current shunt paths. Sometimes, although the cracks are not observable by eye, different colour lines (brown or white) are sometimes noticeable on the cell, due to local formation of finger corrosion or snail trails (see 2.3.7) [10]. Micro cracks may have only a small influence on the power output of a new module, because the different sections of the cell are still electrically connected. However, during the module aging with associated thermal and mechanical stresses, the cracks expand (Figure 2-13), which may eventually lead to complete electrical separation, resulting in inactive cell parts [58]. Microcracks may also expand due to mechanical load (e.g. wind, snow) [59] or due to thermal cycling [60]. With the expansion of cell cracks, the  $I_{mp}/I_{sc}$  ratio decreases, due to degradation of the junction properties (increased shunt or recombination currents). In the case of isolated parts of the cells no longer functioning, according to [57],  $I_{sc}$  decreases.



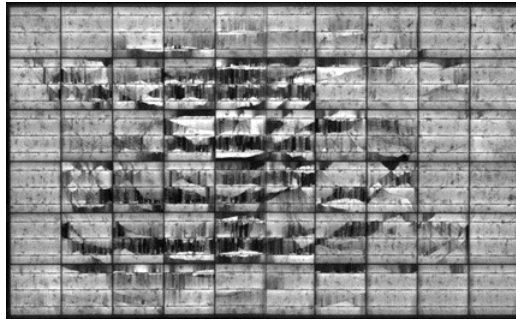


Figure 2-13 EL image of a PV module that has experienced a large number of cell cracks.

### 2.3.7. Snail trails

“Snail trails” or “snail tracks” (Figure 2-14) is a silver grid corrosion phenomenon of c-Si solar cells [61]. These tracks are visible dark lines which are caused because of discoloured contact fingers on the cell surface, appearing either at the cell edges and/or along micro cracks. Due to the location of these features, moisture ingress is thought to be the most likely cause. The environmental moisture can easily penetrate the backsheet of the module due to its water permeability. This allows water access to the cell front surface via diffusion near the edges and through micro-cracks [62]. The grid finger discolouration is thought to be caused by chemical reactions that occur between the silver contact fingers and the front-EVA layer [63]. These reactions include interaction of the silver contacts with acetic acid, carbon dioxide and anti-oxidants that contain phosphorus and are enhanced by moisture, oxygen and UV that reach the inner layers of a PV module [61]. Snail trails do not affect the power output of a PV module directly, but the cracks to which they may be related do, in the way described above in section 2.3.6 [64].

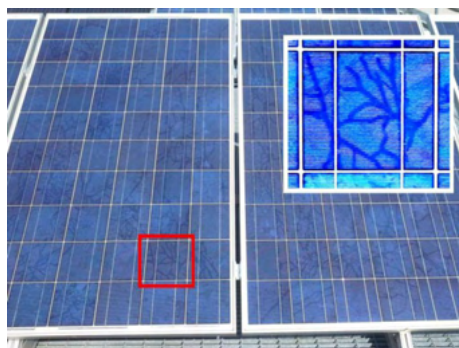


Figure 2-14 Snail trails on a PV module [21].

### 2.3.8. Potential induced degradation (PID)

There are two types of PID, one related to passivation (PID-p) and one associated with shunting (PID-s). The PID-p occurs because of accumulation of negative carriers (when the cell is p-type) on the silicon nitride (AR coating), under the influence of high voltage (positive for p-type cells). High levels of relative humidity and high temperature accelerate the procedure due to increased conductivity of the encapsulant and the AR coating. Leakage current is also observed as, due to the same conditions, the silver ions migrate from the contacts towards the polymers [65], [66]. PID-p causes temporary reduction of the short circuit current and the open circuit voltage and is fully reversible when the affected PV module is exposed to light, which seems to reverse and prevent such an accumulation, as some of the initially photo-generated holes recombine with the accumulated electrons and restore the module functionality [66], [67]. PID-s is caused by sodium ions that migrate from the glass and diffuse into the AR coating and the cell, due to high levels of voltage, causing severe shunting. Moisture and high temperature accelerate this reaction by increasing the conductivity of the encapsulant [68]. Shunting PID causes severe loss of FF, open circuit voltage reduction and lastly short circuit current decrease. This type of failure is partially reversible by applying thermal treatments or reversed voltage bias between the circuit and the grounded module frame [69]. PV modules that have experienced PID-p and PID-s are shown in Figure 2-15.

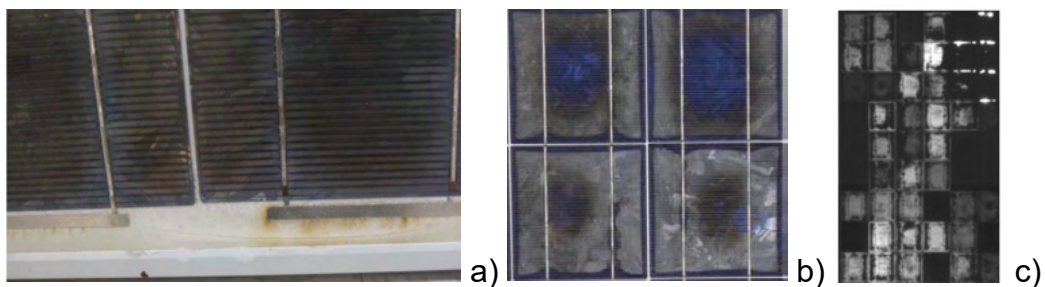


Figure 2-15 PV module affected by a) PID-p and b) PID-s [65]. The EL image of a PV module affected by PID-s is shown in c) [70].

### 2.3.9. Degradation of AR coating / passivation layer

The performance of the cells of a PV module can be optimised by adding an anti-reflective coating to maximise the light absorbed by the cell. Increased short-circuit current and open-circuit voltage can be achieved by a low reflectivity, which subsequently increases the efficiency of a PV cell [71]. The materials most often used as AR coatings are a combination of silicon dioxide and silicon nitride or titanium dioxide, and the thickness of them is chosen for the achievement of minimum light losses. During the PV module lifetime, AR coating discolouration (Figure 2-16) can occur because of UV light exposure, resulting in decreased light transmission to the cells [10]. A further mechanism for AR coating degradation after a certain period is diffusion of minority carriers (positive or negative, depending the type of cell) towards the AR coating, due to high levels of positive or negative voltage, accelerated by temperature and relative humidity [66] (see PID above). The combination of silicon nitride and silicon dioxide is observed to be more affected when compared to AR coating made of only silicon nitride [72]. Moreover, it has been proposed that high levels of temperature and humidity (that may also create an acidic environment) may cause AR coating corrosion [73], [65]. As mentioned in [74], AR coating degradation can lead to a decrease in the  $I_{sc}$  and  $V_{oc}$ . The passivation layers show similar behaviour, as they are constructed of silicon dioxide (see Figure 1-4 from Chapter 1) [75]. AR coating degradation may be homogeneous or heterogeneous.

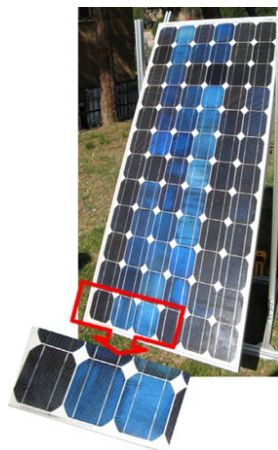


Figure 2-16 Colour lightening of cells due to AR coating degradation [10].



### **2.3.10. Light-induced degradation (LID) and light and elevated temperature induced degradation (LeTID)**

The performance of a PV cell degrades due to illumination or current injection. This type of degradation mode is called light-induced degradation (LID). The phenomenon is usually confused with light and elevated temperature induced degradation (LeTID), as the external factors that accelerate both degradation mechanisms are the same and the temperature ranges that affect each phenomenon are not fully distinguished [76]. LID was first and most commonly observed in monocrystalline silicon (c-Si) cells and secondarily in multicrystalline (mc-Si) solar cells [77] while for LeTID, the Passivated Emitter and Rear Contact (PERC) cells are mainly affected [78]. The cause of LID is a formation of bonds between the boron dopants in the semiconductor and the oxygen induced during the manufacturing process of a silicon solar cell<sup>2</sup>. The process is accelerated when a cell is illuminated [79]. On the contrary, LeTID is a combination of LID and another mechanism that occurs due to the diffusion of hydrogen towards the bulk of the cell, which is part of the layer deposited as rear-side passivation layer ( $\text{AlO}_x$ ,  $\text{SiO}_x$ , or a combination of them) [80]. The process is accelerated by exposure to light and/or high temperature [81]. For longer periods of exposure after a saturation point has been reached, the hydrogen forms a stable bond with existing defects of the cell, a reaction that causes annihilation of the LeTID effect [77]. The parameter affected mainly by LID and LeTID is the open circuit voltage, which decreases due to increased carrier recombination [76], [79]. The EL image of a PV system affected by LID (Figure 2-17), is similar to that of a module that develops PID (Figure 2-16), but the performance degradation caused by PID is much more catastrophic than that due to LID. The influence of LID or LeTID on the EL image of the PV cells, will be discussed thoroughly in Chapter 4.

---

<sup>2</sup> For the manufacturing of the c-Si or mc-Si PV cells full or partial melting of silicon is required, respectively, and oxygen existing on the walls of the silica crucible diffuses towards the silicon [205].

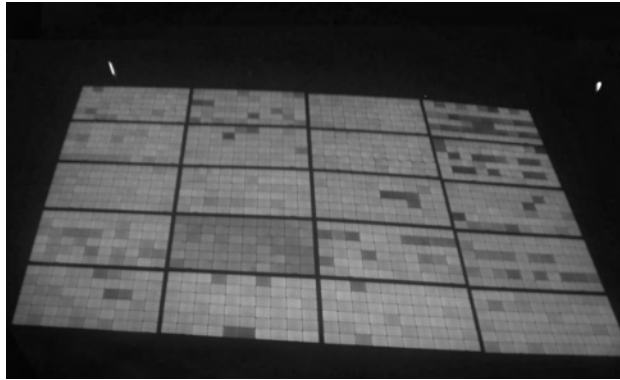


Figure 2-17 EL image of a PV system affected by LID [82].

### 2.3.11. Burn marks / hot spots

A hot spot occurs when a solar cell produces less current than the other cells of the string that are connected. This is the case for totally or partially shaded, damaged or electrically mismatched cells. When one of the mentioned incidents occurs, the affected cells operate at reverse bias and the power that would be produced by the connected cells is transformed into heat in the defective cell(s) [83]. Moreover, high temperature spots can develop because of solder bond failures, ribbon breakages and defective bypass diodes. Sometimes, hotspots may cause burn marks (Figure 2-18) [84]. The damage that a hot spot can cause is irreversible and may be catastrophic, depending the failure that it will trigger.

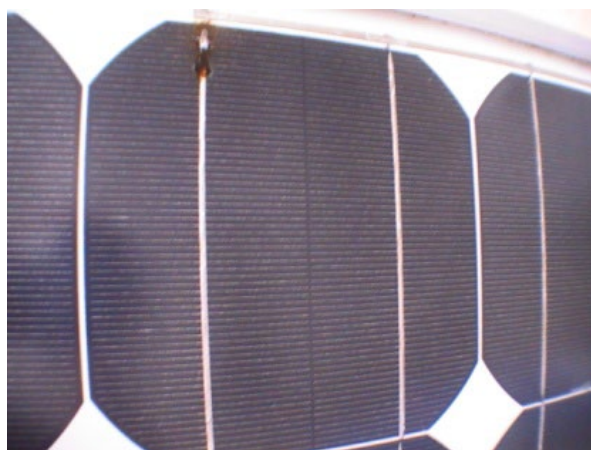


Figure 2-18 Burn marks on the ribbon of a PV module due to ribbon breakage [7].

## **2.4. Summary of degradation causes and effects**

The causes and the effects of the different degradation mechanisms of PV modules are summarised in Table 2-1, while their impact on PV electrical performance is presented in Table 2-2.

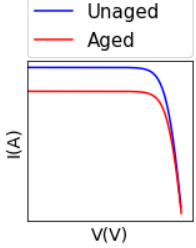
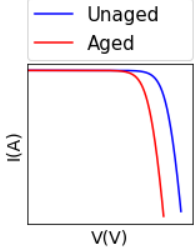
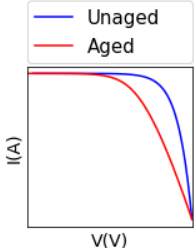
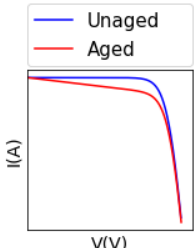
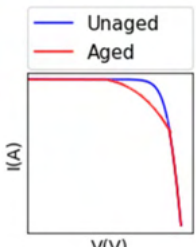
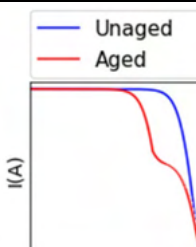
Table 2-1 The different PV degradation mechanisms linked to their causes and effects. Their impact on the electrical performance of the PV modules is described in Table 2-2.

<b>Degradation mechanisms</b>	<b>Causes</b>	<b>Effects</b>
Corrosion	High humidity, high temperature, acetic acid exposure due to hydrolysis of EVA	Damage of the metallic connections, electrical performance degradation
Disconnected cells and string interconnect ribbons	Poor soldering, mechanical load, thermal cycling, hot spots	Hot spots, burn marks, safety risk, activation of bypass diodes, performance degradation
Delamination	Faults during the encapsulation, high humidity, high temperature, hot spots, UV irradiance, high semiconductor doping, salt accumulation	Ingress of liquid water, increase of the light reflection, corrosion, exposure of electrical components to mechanical loads, hot spots, encapsulant discolouration, safety issues, performance degradation
Bubbles	UV irradiance, high humidity, high temperature, hot spots, trapped gases during the encapsulation	Hot spots, increase of light reflection, performance degradation
Encapsulant discolouration	Faults during the encapsulation, inadequate choice of additives and stabilizers, using glass with no UV filter, UV irradiance (shorter wavelengths), high temperature, high humidity, delamination	Loss of transparency, hot spots, activation of bypass diodes (heterogeneous discolouration), aesthetic issues, performance degradation
Backsheet embrittlement	High temperature, high humidity, UV irradiance	Increased moisture ingress, corrosion, delamination, encapsulant discolouration, increased polymer conductivity, safety issues
Cell cracks	Faults during manufacturing process, cell thickness, faulty transportation and installation, mechanical / thermomechanical loads (wind, snow etc.), thermal cycling	Development of longer and wider cracks from smaller cracks, “dead” or “inactive” cell parts, disconnections, hot spots, snail trails, performance degradation

Snail trails	High temperature, UV irradiance, high humidity, oxygen, carbon dioxide, electrochemical corrosion, encapsulant and backsheet chemical composition, fingers chemical composition, cell cracks	Aesthetical issue, minor electrical performance degradation
Potential induced degradation (PID)	High temperature, high humidity, solar irradiance, operating and open circuit system voltage, grounding concept, encapsulant material, back-sheet material, front cover material, anti-reflective coating (ARC) thickness and homogeneity, doping	Leakage current, severe electrical performance degradation
Degradation of antireflective (AR) coating / passivation layer	High temperature, high humidity, solar irradiance, electrochemical corrosion	Increased cell reflection, decreased cell passivation, increased carrier recombination, electrical performance degradation
Light-induced degradation (LID) and light and elevated temperature induced degradation (LeTID)	Solar irradiance, current injection, high temperature, type of cells, boron dopant of the semiconductor, oxygen induced during the manufacturing process of a cell (LID), hydrogen rich dielectrics due to rear-side passivation and firing temperature (LeTID)	Electrical performance degradation
Frame detachment	Defect in the adhesive element, faulty installation, mechanical load, snow or ice accumulation	Ingress of moisture, corrosion, delamination, encapsulant discolouration, mechanical fatigue, interconnection breakage, cell cracks, safety issue
Frame breakage	Faulty installation, mechanical load, snow or ice accumulation	Ingress of moisture, corrosion, delamination, encapsulant discolouration, mechanical fatigue, interconnection breakage, cell cracks, safety issue

Glass breakage	Faulty installation, mechanical load, snow or ice accumulation, hot spots	Ingress of moisture, corrosion, hot spots, delamination, encapsulant discolouration, safety issue
Soiling	Dirt/salt accumulation, rare cleaning	Temporary or permanent transparency loss, activation of bypass diodes (heterogeneous and severe soiling), hot spots, delamination (in case of soiling permeation), electrical performance degradation
Burn marks	High temperature (combining with solder bond failure, ribbon breakage, localised heating from application of reverse current flow etc.), cracked cells, shading	Aesthetic issue
Hot spots	High temperature, disconnected cells and string interconnect ribbons, damaged cells, shading, defective bypass diodes, delamination, bubbles, encapsulant discolouration	Burn marks, encapsulant discolouration, delamination, bubbles, semiconductor damage
Defective bypass diode	Disconnection, mechanical stresses, high temperature, thermal cycling	Hot spots, burn marks, power loss

Table 2-2 The influence of the different degradation mechanisms on the I-V curve of a PV module (the table is a combination of the information found in [19] and the literature cited in the current chapter) .

$I_{sc}$		<p>Homogeneous/heterogeneous discolouration, homogeneous/heterogeneous soiling, homogeneous/heterogeneous delamination, homogeneous/heterogeneous AR coating corrosion of the cells, cracked cells (with cell surface isolation), PID-p</p>
$V_{oc}$		<p>Short-circuit bypass diode, inverted bypass diode, passivation degradation, PID-p, PID-s, LID, short-circuited cells, e.g. by cell interconnection ribbon</p>
$R_s$		<p>Solder corrosion, homogeneous soldering disconnections, broken cell metallisation / interconnect ribbons</p>
$R_{sh}$		<p>Heterogeneous encapsulant discolouration, heterogeneous soiling, heterogeneous delamination (due to cell mismatch)</p>
<p>Change in slope</p>		<p>Heterogeneous corrosion of AR coating of the cells, PID-p</p>
<p>Inflex points</p>		<p>Activation of the bypass diodes due to heterogeneous encapsulant discolouration, heterogeneous soiling, heterogeneous delamination, broken cell interconnect ribbons, cracked cells</p>

## **2.5. Implications for the following research**

The work presented in this chapter described the possible degradation mechanisms that a PV module undergoes when it is exposed to outdoor conditions. High levels of humidity trigger the occurrence of a large number of them, including corrosion. For this reason, moisture ingress into PV laminate structures is researched in Chapter 3. Furthermore, as corrosion shows a combination of high frequency and medium severity (just two degradation mechanisms show high severity) and the reactions that occur are not fully investigated yet, it constitutes the degradation mode studied in Chapter 4. Moreover, the impact of corrosion on PV modules aged in the field, at a non-tropical climate, is analysed in Chapter 5.



# Chapter 3 Moisture Ingress into PV Modules

## 3.1. Introduction

As shown in the literature review of Chapter 2, PV modules that operate outdoors are subjected to different environmental factors. Moisture ingress is regarded as one of the main factors, which contributes to more than one type of failure. The different components that make up PV modules (encapsulant, backsheet and metallisation) can degrade in the presence of moisture combined with high levels of temperature [85]. In the case of modules using ethylene vinyl acetate encapsulants (EVA), acetic acid is generated as a product of the hydrolysis reaction, causing further corrosion of the metallic components [21].

As moisture ingress is a significant factor, this chapter investigates the moisture diffusion through the polymers and the content accumulated within the PV modules. To begin with, the common models of diffusion are introduced followed by a review of previous studies of moisture ingress in PV modules. The experimental studies undertaken in this research are then described and the results presented and discussed.

## 3.2. Background literature review

### 3.2.1. Fick's Laws

The models that best describe diffusion of moisture through polymers (the common material of the encapsulant layers and often the backsheet in a PV module) according to literature [86], [87] are based on Fick's diffusion laws. Fick's first law is given by [88]:

$$J = -D\nabla c \quad (3-1)$$

where  $J$  is the mass flux,  $D$  the diffusion coefficient and  $c$  the concentration.

By taking into consideration the continuity equation for mass [88]:

$$\frac{\partial c}{\partial t} + \nabla \cdot J = 0 \quad (3-2)$$

Fick's second law is obtained [88]:

$$\frac{\partial c}{\partial t} = D \nabla^2 c \quad (3-3)$$

For the simulation of moisture penetration in a laminate of glass – EVA – EVA – backsheets structure, moisture is assumed to penetrate the stack only through the backsheets (moisture ingress through the edges is regarded as negligible, as the backsheets surface is much larger than the edge area [89]). In this case Fick's second law can be simplified to only one dimension (1D solution). Assuming continuity between the two materials, Fick's law is solved twice, once for the diffusion coefficient of the backsheets and once for the EVA. The expression for each solution becomes [90]:

$$C(x, t) = C_S + \frac{4(C_S)}{\pi} \sum_{m=0}^{\infty} \frac{1}{2m+1} \sin\left[\frac{(2m+1)\pi x}{l}\right] e^{\left(-\frac{D(2m+1)^2 \pi^2 t}{l^2}\right)} \quad (3-4)$$

where  $C_S$  is the saturation concentration,  $D$  the diffusion coefficient and  $l$  the thickness of the polymer.

In the case of a mini-module<sup>3</sup> that includes multiple cells in the laminate, the moisture penetrates the structure through the backsheet, reaches the front side cell-EVA interface through the gaps between the cells and diffuses towards the centre of each cell, which are simulated as thin impermeable layers. To accommodate the non-uniform structure and calculate the moisture diffusion through the rear side of the PV module and towards the centre front side of the PV cells, the full 3D solution of Fick's law is taken into consideration:

$$\frac{C(x,y,z,t)-C_S}{C_0-C_S} = \frac{64}{\pi^3} \sum_{m=0}^{\infty} \frac{1}{2m+1} \sin \left[ \frac{(2m+1)\pi x}{l_x} \right] e^{-\left(\frac{(2m+1)\pi}{l_x}\right)^2 Dt} \cdot \sum_{n=0}^{\infty} \frac{1}{2n+1} \sin \left[ \frac{(2n+1)\pi y}{l_y} \right] e^{-\left(\frac{(2n+1)\pi}{l_y}\right)^2 Dt} \cdot \sum_{i=0}^{\infty} \frac{1}{2i+1} \sin \left[ \frac{(2i+1)\pi z}{l_z} \right] e^{-\left(\frac{(2i+1)\pi}{l_z}\right)^2 Dt} \quad (3-5)$$

### 3.2.2. Diffusion models applied to PV modules

A Finite Element Analysis (FEA) based model that assumes Fickian diffusion of the water, calculated with the equations described in section 3.2.1, considering a constant diffusion coefficient, has been developed previously and is widely used for estimation of moisture concentration within a PV module. The specific model seems to describe adequately the moisture ingress within a PV module, in comparison to moisture sorption measurements, although a slight overestimation or underestimation is observed for different types of polymers [91], [92]. To correct this problem, Mitterhofer et al. [92] have presented an alternate model which models transport with two different diffusion coefficients, one within the bulk material and one within channels which represent porous voids that hypothetically exist in the polymer. The simulations show good agreement with the moisture sorption measurements, for different polymers. Kempe [93] has simulated the moisture content fluctuation in PV modules hypothetically installed in various sites (Florida, Colorado and Arizona), by assuming Fickian diffusion. Hulsmann and Weiss [86] have modelled moisture ingress, following Fick's law, in PV laminates exposed to accelerated damp-heat tests specified in the IEC 61215 standard, and

---

<sup>3</sup> A mini-module is a small sized PV module, with structure similar to that described in Chapter 1. However, the indoors tested mini-modules usually do not contain frame and junction box.

unaccelerated in four different types of climate. Both studies demonstrate only simulation of the moisture ingress, based on permeation measurements of the single layers of the polymers, but not verification. According to the results, the PV modules showed saturation moisture content between 0.8 and 2.1 kg/m<sup>3</sup>, depending on the exposure conditions and the polymers used. Jankovec et al. [89], [91] have simulated and experimentally validated moisture sorption in different types of polymers and polymer stacks by application of Fick's law and Slapsak et al. [94] and Virtuani, Annigoni and Ballif [95] followed the same method for modelling moisture ingress in PV modules.

It is notable that all the published research on the topic shares a common reliance: the application of Henry's law is assumed as the absorption isotherm that the polymers follow. Henry's law states that the moisture a polymer absorbs is proportional to the environmental relative humidity, depending on the Henry-coefficient, which gives the solubility [96]. However, there is some indication that the polymers used for PV encapsulation do not follow Henry's law. According to Meitzner and Schulze [97] Poly Vinyl Butyral (PVB) encapsulant follows an alternative absorption isotherm.

According to the literature research presented above, the applicability of the combination of Fickian diffusion and Henry's law is questionable, as the moisture ingress might be overestimated or underestimated regarding the time dependence and the saturation content. Furthermore, different types of polymers might demonstrate different behaviour.

### **3.2.3. Measurement of moisture ingress in PV modules**

Characterisation of moisture ingress (spatial and temporal development) has been carried out through measurements on laminated structure samples, some including PV cells, some without. Jankovec et al. [91] and Slapsak et al. [94] have reported the use of digital humidity sensors laminated into the samples for quantification of the moisture level in PV-type laminates of different structures. However, as the sensors' design use is to measure relative humidity in air, the values measured are

referenced according to that calibration rather than to the real moisture content of the polymers. For example, the saturation content of a PV module, encapsulated with EVA and exposed to damp-heat of 85°C and 85% relative humidity, is 85% humidity, instead of the real moisture content absorbed by the EVA. The method is reliable for the representation of the diffusion law that the polymers follow when the encapsulation polymer used is EVA, as the measurements show a good correlation with Fickian diffusion, but re-calibration is needed<sup>4</sup> according to the real moisture content of the polymers and not the percentage of moisture that the sensors would measure if exposed to air. Carlsson et al. [98] have measured the moisture level in glass-polymer laminates by measuring the conductivity of titanium oxide (TiO<sub>2</sub>) films. For the formation of the sensor the TiO<sub>2</sub> films are deposited on glass substrates. Then the sensor is laminated on the polymer of interest. This method can only measure the moisture ingress at the glass-polymer interface, as glass is required for the formation of the sensor. Kempe et al. [99], [100] report the use of encapsulated calcium (Ca) films in glass-glass laminates, for the qualification and quantification of the presence or absence of moisture. The Ca film reacts with moisture producing calcium oxide, which causes a colour change (yellow to transparent). The quantity reacted may be measured electrically, by the variance of the electrical conductivity. The method is still under development and yet not applied to PV modules. Kapur et al. [101] report a method for quantification of the moisture content in EVA within glass-glass structures by application of Fourier Transform Infrared (FTIR) spectroscopy at the near infrared region. The method involves acquisition of the transmittance spectra, calculation of the ratio between the CH peak and the moisture peak and calibration by measurement of samples with known moisture content, measured by Karl-Fischer Titration. However, the measurement of the moisture content of EVA is not as accurate, as the moisture peaks overlap with the polymer's characteristic peaks. Finally, Kumar et al. [102] have applied Short-Wave Infrared (or near infrared) Reflectometry for the quantification of the moisture content accumulated within a PV module, which is a similar method to the one presented by Kapur et al. [101], but requires reflectance spectra acquisition. The error of the measurement is 0.13 mg/cm<sup>3</sup>, with the lowest limit of detection

---

<sup>4</sup> Measurement of the moisture content absorbed by a polymer when exposed at specific conditions, by humidity sensors and a different method.

estimated as  $0.066 \text{ mg/cm}^3$  and the value detected for EVA at  $85 \text{ }^\circ\text{C} / 85\% \text{ RH}$  calculated as  $\sim 3 \text{ mg/cm}^3$ . Moreover, for samples exposed to a standard DH test, the measurement is affected by optical changes of the polymer, due to aging.

By comparison of the moisture measurement methods described, the digital humidity sensors is the predominant measurement method, as it shows good agreement with the Fickian diffusion for EVA and the only step required for improvement of their accuracy is re-calibration according to the real moisture content that the polymers absorb.

### **3.3. Methodology**

As described above, although Fick's laws have been used for the description of the moisture diffusion through a PV module, they may overestimate or underestimate the time-dependent moisture content. Moreover, Henry's law was commonly applied for the estimation of the boundary conditions of the simulations, although evidence shows that may lead to misleading results. Furthermore, the methods developed for moisture content measurement need improvement regarding their applicability and accuracy. The purpose of the research in this chapter is the quantification and theoretical prediction of the moisture concentration in PV laminates of different structures. The research presented includes quantification of the moisture uptake of the polymers involved in PV encapsulation under environmental equilibrium, and maps of the moisture spatial distribution over time, when the environmental relative humidity is varied. For the achievement of this goal, different experimental approaches were combined:

- The moisture levels measured by digital humidity sensors embedded in laminates, in the form of relative moisture content, were fitted to Fick's diffusion law, to investigate its suitability for describing moisture ingress into PV modules.
- The validity of applying Henry's law to the materials commonly used in PV modules was examined, by fitting to the saturation moisture content of the polymers reached at different levels of temperature and relative humidity.

- Finally, a new moisture quantification method was investigated which includes the embedding of humidity indicator cards at the front side of PV cells, encapsulated within PV module test laminates. The method researched is low cost and compatible with different types of PV cells and module structures, and could be used for the quantification of the moisture ingress within the front side cell-EVA interfaces of a PV module.

### 3.4. Investigation of moisture ingress and egress in polymer – glass laminates for PV encapsulation

#### 3.4.1. Methods

For a deeper understanding and improved interpretation of the measurements of the moisture ingress into the polymers used in PV laminate structures, the moisture profile of stacks was theoretically modelled and experimentally verified as shown in the flowchart of Figure 3-1. In this case, the measurements of the relative humidity were performed using digital humidity sensors embedded within the structures.

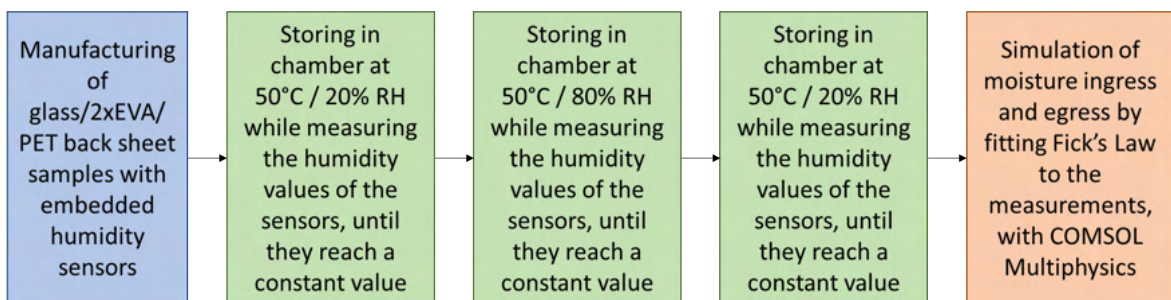


Figure 3-1 Flowchart of the procedure followed for the investigation of moisture ingress and egress in polymer – glass stacks for PV encapsulation.

The following samples (shown in Figure 3-2) were prepared for the experimental testing procedure:

- Sample type J: This sample was a laminated glass – EVA – EVA – backsheets (PET) structure with dimensions 20 x 20 cm. Three digital miniaturised humidity sensors (Sensirion model SHT25) designated HJ1, HJ2 and HJ3

were soldered onto a single strip of Printed Circuit Board (PCB) and embedded at the EVA – EVA interface (Figure 3-3a).

Sample type S: This sample had the same structure as J, but the three sensors were embedded at different interfaces: one sensor (HS1) at the backsheet-EVA interface, one (HS2) between the EVA sheets and one (HS3) between the EVA sheet and the glass (Figure 3-3b).

The humidity sensors measure the dielectric properties of a polymer, embedded in them, which absorbs moisture according to the humidity to which they are exposed. The sensors were dried before use. There is on-board digital conversion and communication externally is over an I<sup>2</sup>C interface, requiring in total two power and two data lines. The PCBs contain a thick copper plane on each side and slots where the sensors are soldered, with the sensing surface exposed to the polymer. All the PCB strips were connected to a PC with a data acquisition card for the acquisition of the measurement data. The thicknesses of the two layers of EVA is 0.46 mm [103] while the thickness of the backsheet is 0.295 mm [104].

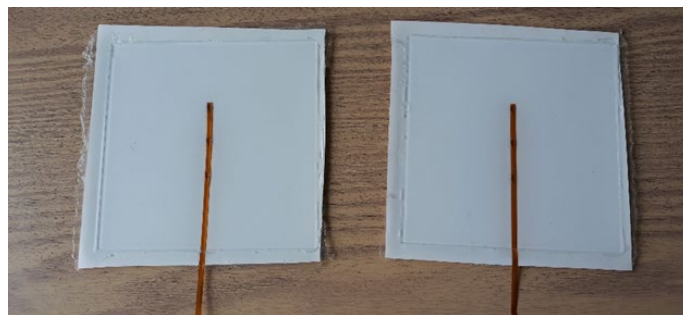


Figure 3-2 Samples with embedded digital humidity sensors.

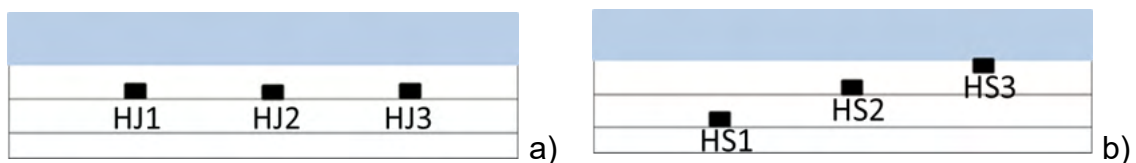


Figure 3-3 Cross sections of a) J and b) S samples. The top layer represents the glass and the bottom the backsheet.



Both samples were placed in an environmental chamber with temperature and humidity control set to the following conditions:

- 1<sup>st</sup> phase: T = 50°C and RH = 20%. This step was used for all of the sensors to reach the same level of humidity. The duration of this procedure was 237 hrs until the reading was stable.
- 2<sup>nd</sup> phase: T = 50°C and RH = 80% for observation of the humidity ingress.
- 3<sup>rd</sup> phase: T = 50°C and RH = 20% for the investigation of the humidity egress.

For the comparison of the moisture ingress curves, the measurements presented here have been normalised linearly, so they have the same starting and ending moisture value.

### 3.4.2. Conversion of the relative humidity measured by the humidity sensors to molar concentration

For the simulations in COMSOL Multiphysics, presented in 3.4.3, the relative humidity (%) measured by the digital humidity sensors must be translated into the actual moisture content (mol/m<sup>3</sup>) that is absorbed by the polymers. For this purpose, the relationship presented below, based on Henry's law (see 3.2.2), is applied to the sensor measurements [95]:

$$c_{EVA} = \frac{c_{sat,EVA} \cdot RMC}{100} \quad (3-6)$$

where:

- $c_{EVA}$  is the moisture content of the EVA in kg of water per m<sup>3</sup> of EVA.
- $c_{sat,EVA}$  is the saturation moisture content of EVA in kg/m<sup>3</sup> at the specific temperature of the experiment. For this experiment the saturation moisture content is 2.2 kg/m<sup>3</sup> (T = 50°C), measured by Mocon moisture permeation measurement, which was conducted with PERMATRAN instrument [91].
- RMC is the relative moisture content in relation to the saturation content of the EVA (note: it is *not* the volume of moisture relative to the volume of the

polymer). For the simulations in section 3.4.3, it is assumed that the digital humidity sensors measure the relative moisture content of the EVA, as their operation in air regards the measurement of relative humidity. Further research is presented in section 3.5 that elaborates on the detail of what the sensors measure in such a setup.

Finally, the moisture content in kg/m<sup>3</sup> is converted into molar concentration in mol/m<sup>3</sup>, by:

$$c_{EVA,mol} = c_{EVA} \cdot 55.5 \quad (3-7)$$

where 55.5 is the number of moles of water equivalent to 1 kg of water.

### 3.4.3. COMSOL Multiphysics simulations

For the simulation of moisture penetration through the backsheet of the samples described in paragraph 3.4.1 and the calculation of the backsheet's diffusion coefficient, Fick's law is solved in 1D and fitted to the measured data using COMSOL Multiphysics software. The diffusion coefficient of EVA does not need to be calculated, but may be received approximately from the literature, as it does not vary significantly the moisture penetration when no cell is present<sup>5</sup>, because the diffusion coefficient of PET is a hundred times lower.

According to the studied cases included in this work, for the design of a cross section of the samples, 2D spatial dimension is selected. The appropriate physics are included in the COMSOL submodule "*Transport of Diluted Species*" from the module "*Chemical Species Transport*". As the study regards the evolution of the moisture ingress and egress within the specific samples, "*Time Dependent*" solution is selected. The parameters needed for the initial and boundary conditions are set in the "*Transport Properties*" part and listed in Table 3-1. The number of "*Transport Properties*" sections needed depends on the number of materials studied. The thicknesses of the two layers of EVA is set at 0.46 mm [103] while the thickness of the backsheet is set to 0.295 mm [104] in the "*Geometry*" section. The backsheet

---

<sup>5</sup> When the PV cell is present, the diffusion coefficient of the EVA is very important regarding the moisture diffusion within the EVA layer between the front side of the PV cell and the glass.

diffusion coefficient is determined by fitting the simulated moisture concentrations over time to the measured values with the “*least square method*”. Within the COMSOL options for the optimisation study, a “*Global Least-Squares Objective*” is selected and the “*Sparse Nonlinear OPTimizer (SNOPT) Method*” is used. SNOPT is recommended for problems containing a non-linear function and is compatible with the determination of constraints. The mesh selected is chosen to provide a balance between accuracy and computation period. The time duration is set to 75600 s, with step 3600 s, at the “*Study*” part.

Table 3-1 Definition of the parameters used for the simulation of the moisture penetration through the backsheet of a PV laminate and the determination of the PET diffusion coefficient by fitting.

Name	Value	Description
<b>T<sub>amb</sub></b>	323.88 K	ambient temperature
<b>C<sub>ini</sub></b>	26.86 mol/m <sup>3</sup>	initial concentration*
<b>C<sub>0</sub></b>	102.56 mol/m <sup>3</sup>	boundary concentration**
<b>D<sub>eva</sub></b>	1.5e-10 m <sup>2</sup> /s	EVA diffusion coefficient

\*The initial concentration is the moisture concentration of the stacks after the 1<sup>st</sup> phase of the experiment.

\*\*The boundary concentration is the moisture concentration applied by the chamber during the moisture ingress (2<sup>nd</sup> phase of the experiment).

#### 3.4.4. Moisture ingress and egress – Results and discussion

Comparing the experimental and simulation results on the same graph<sup>6</sup> (Figure 3-4), although a good fit is observed ( $R^2 = 0.89$ ), the simulation curve of the backsheet / EVA interface appears to underestimate the moisture ingress (RMC) initially by a maximum of 14% and later overestimate it by a maximum of 9.7%. In addition, for the measurements of the sensors embedded at different polymer interfaces of the sample S, it is observed from the simulation that the sensors encapsulated closer to the glass (HS2 and HS3) show an ingress time lag compared to the sensor encapsulated close to the backsheet (HS1). However, this time lag cannot be identified from the measurements, as such small differences are difficult

<sup>6</sup> The concentration values resulted from the simulation were converted to RMC values following the reverse of the methodology described in section 3.4.2.

to be measured. In case of moisture egress, the same behaviour as for moisture ingress is observed. The simulation underestimates the moisture concentration (RMC) by a maximum of 7.9%, then overestimates by 10% and finally underestimates again by a maximum of 2%, for the sensor embedded within the backsheet / EVA interface.

The results of the moisture ingress and egress simulation are shown in Figure 3-5. According to the simulation, the sample needs between 86 and 114 hrs to become saturated, while according to the measurements, the saturation occurs for 139 - 167 hrs of exposure. The fitted value of the diffusion coefficient of the backsheet is  $D_B = 4.32 \times 10^{-12} \text{ m}^2/\text{s}$  and is similar to that reported by Jankovec et al. ( $3.1 \times 10^{-12} \text{ m}^2/\text{s}$ ), measured by the Mocon method using PERMATRAN [91]. The mentioned method consists of two chambers, one at high and one at low level of relative humidity, both at specific value of temperature. The polymer is placed between the two chambers and the moisture that penetrates it is measured. For the case of moisture egress, the determined value of the backsheet diffusion coefficient is  $D_B = 4.4 \times 10^{-12} \text{ m}^2/\text{s}$ . This value is similar to the value calculated for the moisture ingress (1.8% difference and within uncertainty when considering even only the humidity sensor measurement contribution).

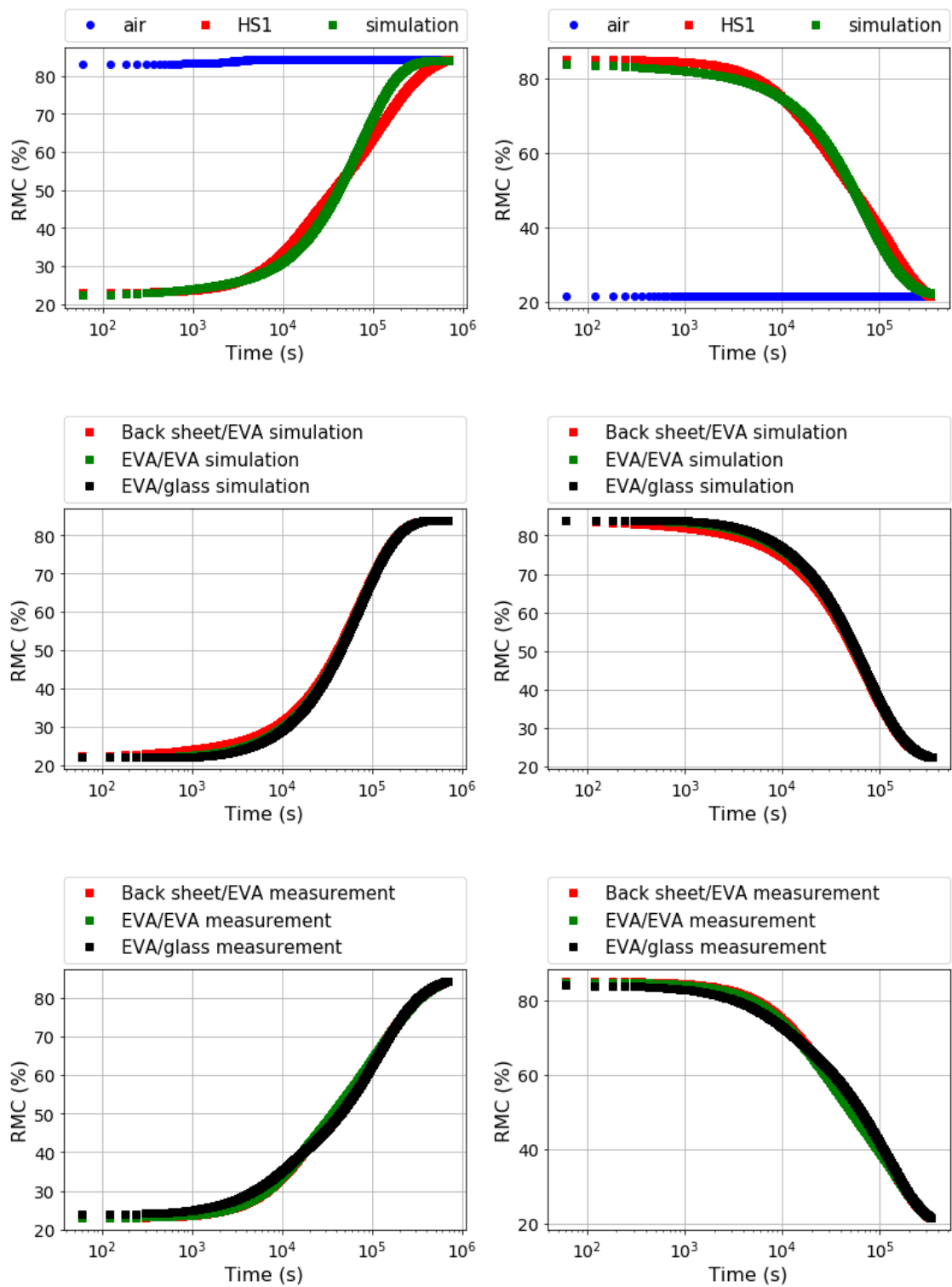


Figure 3-4 Plots of the experimental and simulation results of the RMC evolution over time, during moisture ingress (left) and egress (right), within the different interfaces of the sample.

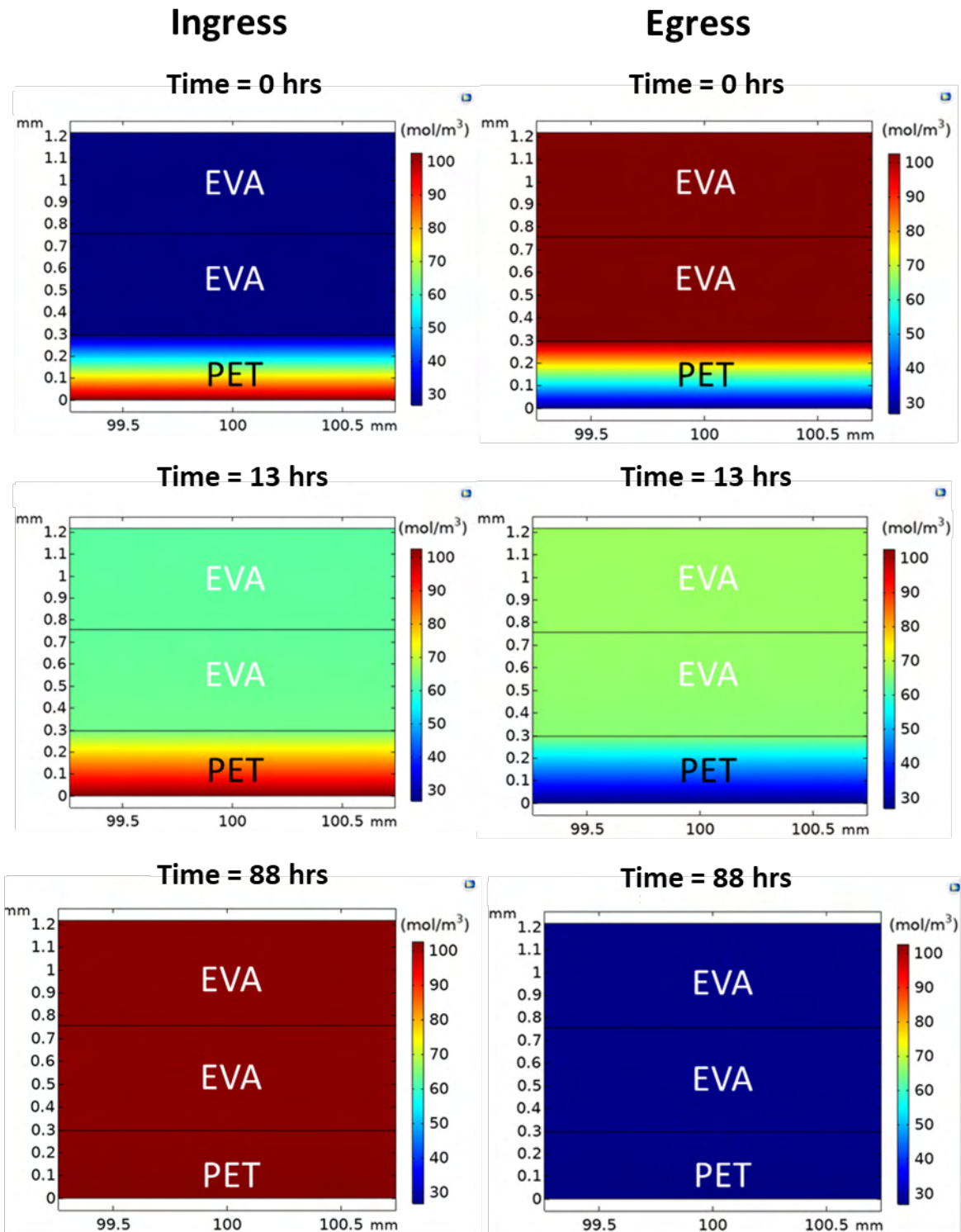


Figure 3-5 The moisture profile for moisture ingress (left) and egress (right) of the sample simulated with the PET diffusion coefficient calculated by fitting the 1D Fick's law solution to the experimental data with the least mean square method. The upper boundary of the profiles represents the glass position.

A possible reason for the differences between measured and simulated curve shapes is that the digital humidity sensors are designed to measure the relative humidity in air and not the moisture content of a polymer (encapsulation of sensors). According to the datasheet information, the polymer embedded in the sensor absorbs moisture proportionally to the relative humidity of the environment. However, there are indications from the literature [97] that the relationship between the moisture content of the EVA and ambient relative humidity is not directly proportional, something that is not taken into consideration in the above use of the sensors. This topic is analysed further in section 3.5 in which the relationship between EVA moisture content and ambient relative humidity is identified.

Moreover, the nature of the physics that the diffusion follows is under question, as there are a number of publications that suggest that diffusion coefficients of the polymers may vary with the moisture content [105], [90], [106], or that the moisture ingress follows a dual sorption process [92]. However, more detailed material analysis on the polymers is demanded, to investigate their behaviour and suggest the most appropriate model.

### **3.5. Identification of the absorption isotherm that PV module polymers follow**

As mentioned already in section 3.2.2, a volume of work has been published on theoretical simulations of moisture ingress into PV modules. However, all the research conducted to date assumes that the absorption isotherm (a curve that describes the change of the quantity of gas or liquid, absorbed by a solid-phase environment, with pressure at constant temperature [107]) which the polymers in the PV module follow is Henry's law. The law is expressed as:

$$c_{\text{polymer}} = S \cdot p_{\text{H}_2\text{O}} \quad (3-8)$$

where,  $c_{\text{polymer}}$  ( $\text{m}^3/\text{m}^3$ ) is the moisture concentration in the polymer,  $S$  ( $\text{m}^3/(\text{m}^3 \cdot \text{Pa})$ ) is the solubility of the moisture in the polymer and  $p_{\text{H}_2\text{O}}$  (Pa) is the partial pressure of the water in the atmosphere in contact with the polymer surface [96], or as:

$$c_{\text{polymer,eq}} = K_H \cdot C_{\text{environment,eq}} \quad (3-9)$$

where,  $c_{\text{polymer,eq}}$  ( $\text{m}^3/\text{m}^3$ ) is the equilibrium moisture concentration of the polymer,  $K_H$  is the Henry coefficient (dimensionless) and  $C_{\text{environment,eq}}$  ( $\text{m}^3/\text{m}^3$ ) is the equilibrium coefficient of the environment. Henry's law is valid for hydrophobic, non-porous materials above the glass transition temperature [97]. However, EVA with VA content around 33wt%, which is the most commonly used for encapsulation of PV cells [108], is somewhere in between hydrophobic and hydrophilic [109]. Moreover, EVA cannot be regarded as non-porous for the entire range of relative humidity values as, for greater quantities of moisture absorbed, more plasticisation occurs and larger gaps are generated within the polymer chain. Accordingly, water disrupts more hydrogen bonds, more free volume is generated and increased mobility of the chains is observed [110], something that should cause increased solubility of the moisture in the polymer. In addition, PET can be either hydrophilic or hydrophobic, depending on the additives used during its manufacture [111], [112], while the porosity of the material may also vary [113].

Within the research available in the literature, an alternative absorption isotherm is identified by Meitzner and Schulze [97], that is applicable to microporous or non-porous and less hydrophilic polymers: the Type III isotherm from the Brunauer, Emmett and Teller (BET) classification [114]. In this, the relationship between the moisture concentration ( $v/v$ ) of the absorbed penetrant and the relative pressure (which is equal to the air RH) has the form presented in Figure 3-6 [115].

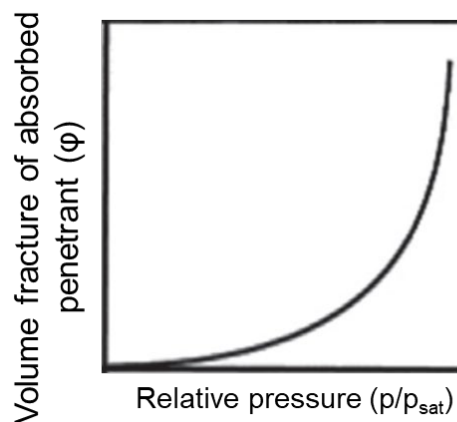


Figure 3-6 The absorption isotherm Type III according to the Brunauer, Emmett and Teller (BET) classification [115].



The most exact representation of the relationship expressed above is given by the equation of Perrin and Favre [116]:

$$\varphi = \frac{e^{(k_s - k_p)\alpha - 1}}{(k_s - k_p)/k_p} \quad (3-10)$$

where  $\varphi$  is the moisture concentration (v/v) of the absorbed penetrant ( $m^3/m^3$ ),  $\alpha$  is the activity (or the RH normalised to unity),  $k_s$  (dimensionless) is a parameter that represents the interactions between the penetrant molecules and  $k_p$  (dimensionless) is a parameter that describes the interactions between the penetrant and the polymer. The equation developed by Perrin and Favre is preferred to that of Flory-Huggins [117], [118], as it takes into consideration additionally the interactions between the penetrant molecules and not only those between the penetrant and polymer molecules. For the correct application of the Perrin and Favre model it is assumed that the vapour pressure in the polymer is increased negligibly when more molecules accumulate within the gaps of the polymer matrix, as the polymer matrix is large enough that change of the polymer volume is not observed (Figure 3-7) [116].

To examine if a better fit between the simulation and experimental results of moisture absorption into the PV modules could be obtained, in this research, a modified version of the Perrin and Favre model was fitted to the results described in section 3.3.1, for its validation. In this case, the reason for using a modified version of the model was that the results obtained by the experimental setup were not volume fractions, as in the model, but w/w concentrations, which were converted to w/v concentrations by multiplication by the polymer's density. In case of multilayer laminate, an effective density was calculated by dividing the sum of the masses of the polymers by their overall volume. Eq. (3-10) was modified as below, to match the modified measurements:

$$\varphi = \frac{e^{(k_s - k_p)\alpha - 1}}{(k_s - k_p)/k_p}, \quad (3-11)$$

$$d_w \cdot \frac{V_w}{V_p} = d_w \cdot \frac{e^{(k_s - k_p)\alpha - 1}}{(k_s - k_p)/k_p}, \quad (3-12)$$

$$\frac{m_w}{V_p} = k_1 \cdot (e^{k_2 \cdot \alpha} - 1), \quad (3-13)$$

where,  $\frac{V_w}{V_p}$  is the v/v concentration,  $\frac{m_w}{V_p}$  is the w/v concentration and  $d_w$  is the fraction of the moisture mass per volume of moisture. The quantity represented by  $d_w$  cannot be defined as density, because the volume of the moisture vapor is much smaller than the volume of the polymer. Moreover, although the density of the moisture vapor varies according to the partial pressure,  $d_w$  is assumed to be constant, as any change of partial pressure in the polymer is regarded as negligible due to the large difference between the volumes of water and polymer. Furthermore, to reduce the number of fitted parameters from three to two,  $k_1 = \frac{d_w}{(k_s - k_p)/k_p}$  and  $k_2 = k_s - k_p$ .

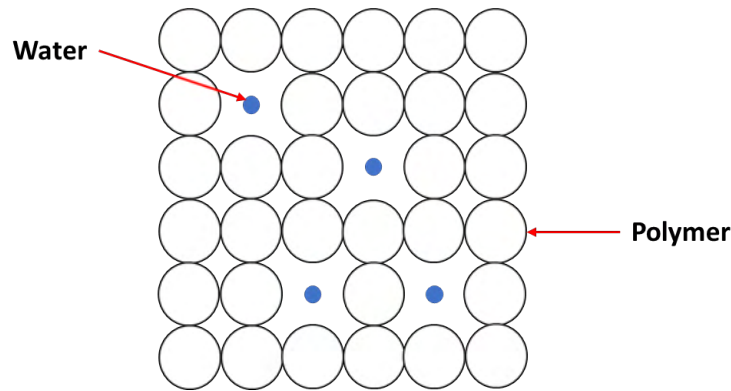
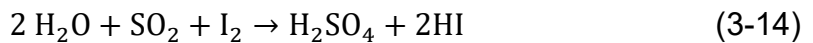


Figure 3-7 The polymer matrix and the absorbed moisture.

### 3.5.1. Experimental procedure

To determine the form of the relationship between the polymer equilibrium moisture content and the air relative humidity to which it is exposed, single polymer samples of one type of EVA and two different backsheet types (multilayer PET and multilayer PET containing Al foil) were tested. In addition, a laminate of PET+Al foil - 2xEVA was prepared for investigation of the moisture absorption occurring within a multilayer structure resembling a PV module. The samples were loaded, with both sides exposed, into an environmental chamber set to different temperature and relative humidity combinations according to Table 3-2, for 24 hrs, sufficient for the samples to reach saturation. Three samples were tested for each type of polymer

for each condition. After reaching saturation, the samples were removed from the chamber and their moisture content measured by Karl-Fischer Titration. In this method, a sample of mass 1 gr is placed in a dry bottle and heated at 180°C for 15 minutes. The moisture released is driven into a bottle containing a pyridine/methanol solution, including chemically bound iodine and sulphur dioxide. Simultaneously, I<sub>2</sub> is generated by the electrolysis of the solution, due to an external current. For measurement of the moisture mass, the moisture reacts according to the following reaction:



An electrode is used, to detect variance of the electrical properties of the solution, due to the presence or absence of moisture. The mass of the moisture is proportional to the integrated current, which causes the I<sub>2</sub> generation, up to detection of change of the electrical properties of the solution, due to absence of moisture. The system is calibrated by measurement of an empty dry bottle and of a bottle that contains a substance of known moisture content. The whole experimental procedure is summarised in Figure 3-8.

Table 3-2 Combination of exposure conditions.

Temp. \ RH	20%	40%	60%	85%	95%
50 °C		X		X	X
85 °C	X	X	X	X	X

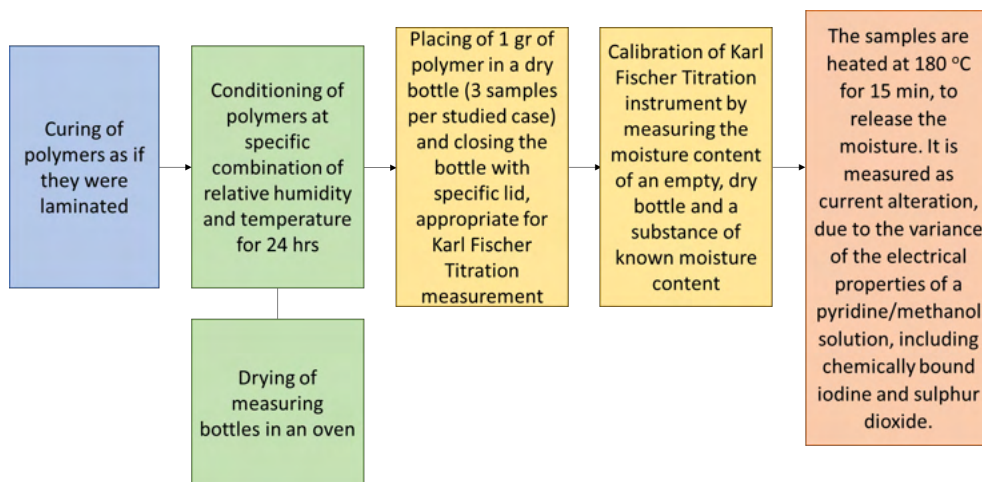


Figure 3-8 Experimental procedure.

### 3.5.2. Relation between moisture content of the polymer layers and the relative humidity levels to which they are exposed

To test the applicability of the Perrin and Favre relationship to these materials, eq. (3-13) was fitted to measurements obtained as described in section 3.5.1, modified as per section 3.5. A point at 0% RH is needed for fitting the absorption isotherm, but due to the limitations of the chamber, it was extrapolated. All values were normalised to that baseline, so for 0% RH the moisture vapor mass was 0 kg. This step is required as real polymers do not reach 0 kg at 0% RH, due to moisture incorporated within the polymer matrix. The fitting was performed with the Broyden–Fletcher–Goldfarb–Shanno algorithm with bound constraints [119], as implemented in the Python function `scipy.optimize.minimize()` [120].

Figure 3-9 presents comparisons of curves obtained with the Perrin and Favre model, with the respective curve using Henry's law and the values measured, for the different polymers. The fitting parameters are listed in Table 3-3. Comparing the saturation contents of all samples, the EVA is seen to absorb the least moisture (1.17 kg/m<sup>3</sup> saturation value at 85°C, compared to 5.79 kg/m<sup>3</sup>, 5.86 kg/m<sup>3</sup> and 2.96 kg/m<sup>3</sup>, for the PET, PET+Al foil and PET+Al foil - 2xEVA, respectively). Furthermore, for all cases the R<sup>2</sup> values show the Perrin and Favre relationship describes the absorption isotherm of the polymer significantly better than Henry's law. This observation is validated by the plot of the residuals between the measurement points and those estimated by the Perrin and Favre model and Henry's law against the activity, for all samples at 85°C (Figure 3-11). This specific condition was chosen due to the higher number of measurements per material, for more robust identification of any pattern. According to Figure 3-11 a pattern is not recognised for the residuals estimated for the Perrin and Favre model, which shows that the fitting is not biased by a systematic error. On the contrary, for the residuals calculated for Henry's law, a "U-like" pattern is observed (with non-progressive value at high activities for samples containing EVA), confirming the bias of the model to overestimate the moisture content for the middle activity values and underestimate it in the case of high environmental relative humidity. The smaller range of the

aforementioned “U-like” behaviour for samples including EVA, shows that Henry’s law describes better the absorption isotherm of the EVA than the PET.

According to Figure 3-9, the moisture content of EVA is observed to saturate at high relative humidity and temperature values. Moreover, the error of the measurement is much higher than the other cases ( $\pm 0.48 \text{ kg/m}^3$  at  $85 \text{ }^\circ\text{C}$  /  $85\% \text{ RH}$  compared to  $\pm 0.05 \text{ kg/m}^3$ , at the same conditions for multilayer PET with Al foil). A possible reason is that the EVA degrades at high temperature and relative humidity values, producing acetic acid due to hydrolysis, so the real moisture uptake is difficult to obtain, a hypothesis that needs further investigation. Figure 3-10 demonstrates the comparison between the moisture uptake measured for free standing EVA layers and the one calculated for the EVA encapsulated into the PET+Al foil - 2xEVA stacks. The calculation was performed by the application of the relationship presented below:

$$\left(\frac{m_w}{V_p}\right)_{\text{EVA enc.}} = \left(\left(\frac{m_w}{V_p}\right)_{\text{stack}} \cdot l_{\text{stack}} - \left(\frac{m_w}{V_p}\right)_{\text{PET+Al foil free}} \cdot l_{\text{PET+Al foil free}}\right) / (2 \cdot l_{\text{EVA}}), \quad (3-15)$$

where  $\left(\frac{m_w}{V_p}\right)_{\text{EVA enc.}}$  is the w/v moisture concentration in the encapsulated EVA,  $\left(\frac{m_w}{V_p}\right)_{\text{stack}}$  and  $l_{\text{stack}}$  are the w/v moisture concentration and the thickness of the PET+Al foil - 2xEVA stack,  $\left(\frac{m_w}{V_p}\right)_{\text{PET+Al foil free}}$  and  $l_{\text{PET+Al foil free}}$  are the w/v moisture concentration and the thickness of the free standing PET+Al foil and  $l_{\text{EVA}}$  is the thickness of the EVA layer. When the EVA is encapsulated with a backsheet, there is an indication that EVA absorbs a different moisture content (in this case higher, but more exposure conditions should be considered for a valid conclusion) than when it is free standing, probably because of interactions occurring between the different polymer layers, or different degree of cross-linking when the EVA is cured stand-alone, compared to when it is laminated. In this case, a higher amount of moisture was absorbed, but this may not be universally true.

According to these findings, it is concluded that the moisture content absorbed by a PV module is mainly affected by the moisture content that the EVA absorbs, which is the largest part of the polymer stack and the polymer that the cells are in direct contact, and secondarily by the interaction with the backsheet (equilibrium between the two polymers, or impact of backsheet on the cross-linking degree of the EVA).

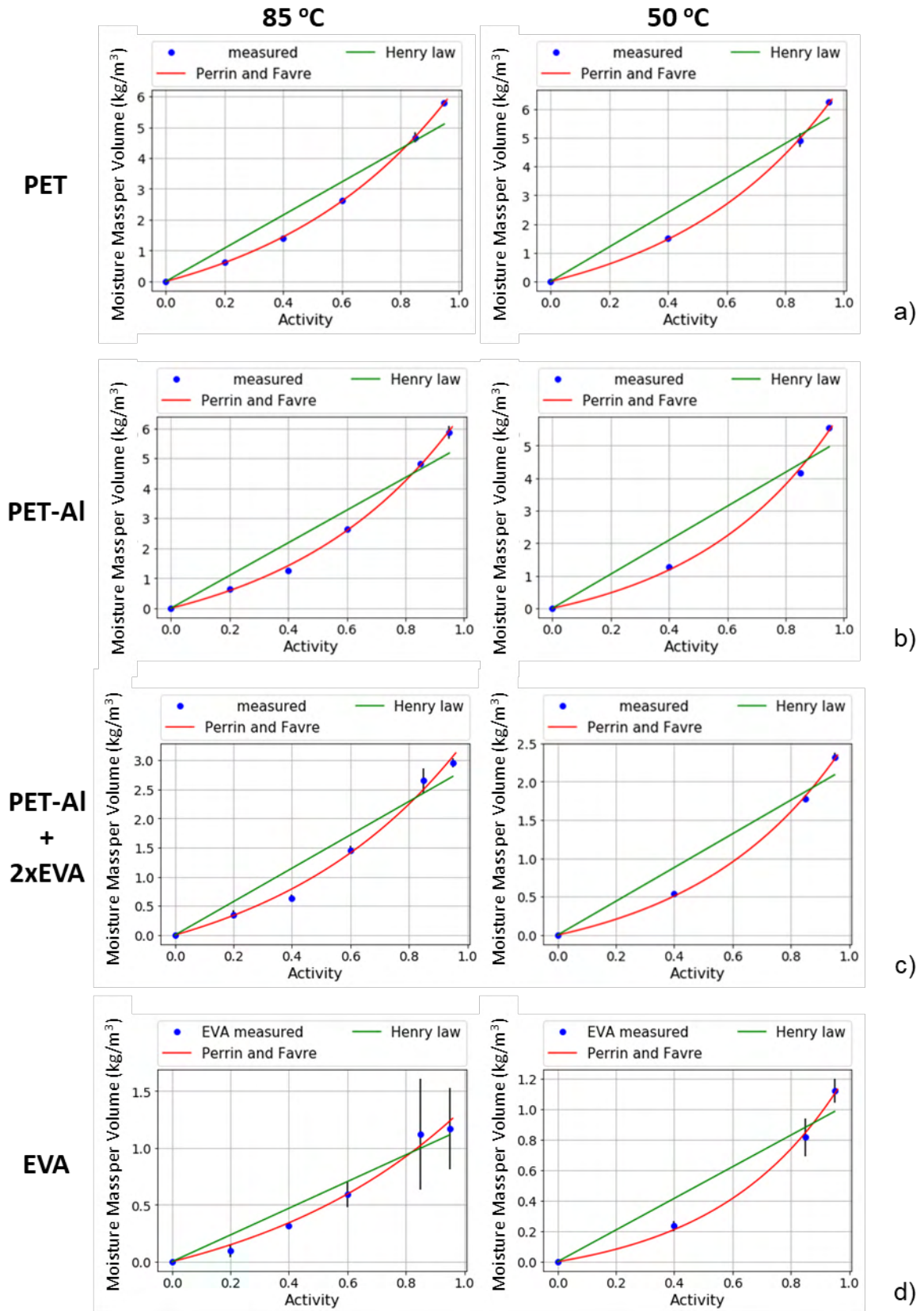


Figure 3-9 Measured and fitted absorption isotherm for the a) multilayer PET, b) PET with Al foil, c) PET+Al foil - 2xEVA stack and d) EVA, at 85°C and 50°C from left to right. Activity is the RH normalised to unity.

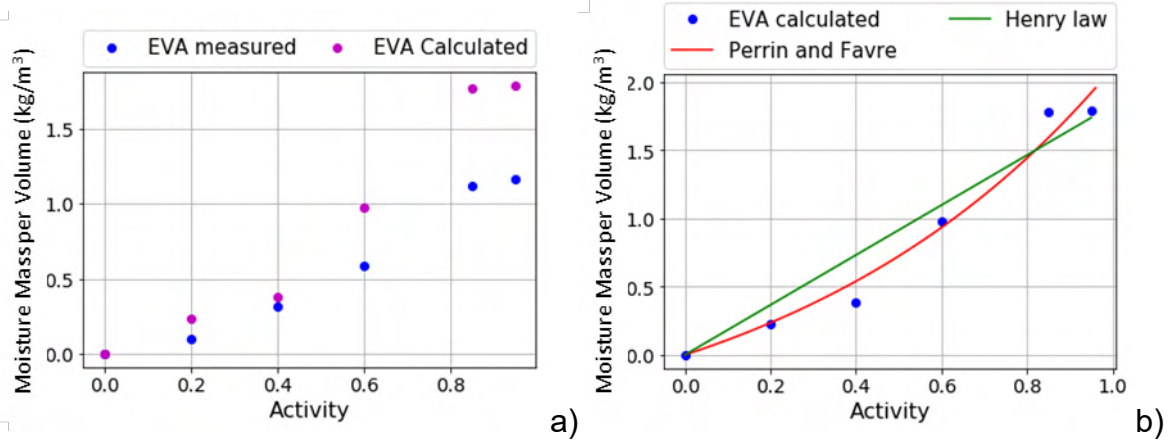


Figure 3-10 a) Comparison between the moisture uptake of free standing EVA (measured) and EVA, part of the PET+Al foil - 2xEVA sample (calculated). b) Moisture uptake of the EVA, calculated from the PET+Al foil - 2xEVA sample, and fitted absorption isotherm at 85°C. Activity is the RH normalised to unity.

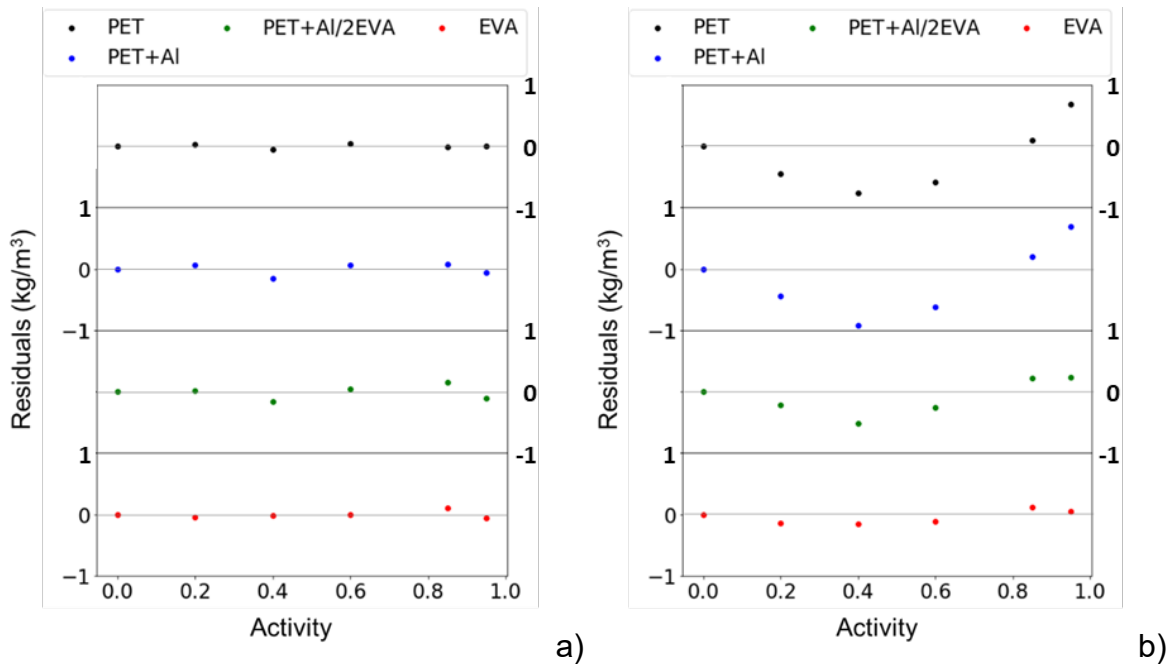


Figure 3-11 Residuals between measurement points and values estimated by a) Perrin and Favre model and b) Henry's law plotted against the activity, for all samples at 85°C. Activity is the RH normalised to unity.

Table 3-3 Fitted parameters of the Perrin and Favre model and Henry's law for all samples.

		$k_1^*$ (kg/m <sup>3</sup> )	$k_2$	$R^2$ Perrin- Favre	$R^2$ Henry	Max Overrate (kg/m <sup>3</sup> )	Max Underrate (kg/m <sup>3</sup> )
Multilayer @ 85 °C	PET	1.58	1.62	1.00	0.94	0.72	0.75
Multilayer @ 50 °C	PET	1.43	1.77	1.00	0.96	0.98	0.58
Multilayer @ 85 °C	PET+Al	1.42	1.73	1.00	0.93	0.78	0.82
Multilayer @ 50 °C	PET+Al	0.96	2.01	1.00	0.94	0.96	0.58
PET+Al 2xEVA @ 85 °C	foil –	0.95	1.52	0.99	0.94	0.36	0.37
PET+Al 2xEVA @ 50 °C	foil –	0.44	1.93	1.00	0.95	0.39	0.24
EVA @ 85 °C		0.49	1.33	0.99	0.94	0.13	0.13
EVA @ 50 °C		0.14	2.30	1.00	0.93	0.22	0.13
EVA @ 85 °C Calculated from PET+Al foil – 2xEVA @ 85 °C		0.80	1.29	0.97	0.93	0.19	0.20

\* $k_1$  parameter is within the range expected, as it is comparable to the concentrations measured for the polymers

### 3.6. Direct quantification of moisture ingress into PV laminates with the use of humidity indicator cards

For the practical quantification of the moisture content that accumulates at the front side of a PV cell encapsulated within a PV module, a different measurement method is needed. The developed measurement method described in this section involves encapsulation of humidity indicator cards. This method has been used before, but without any attempt at calibration [121], [122]. The cards are chosen as they are chemically compatible with the encapsulation of the cells and they do not introduce additional moisture transport paths, as the measurement is optical without requiring



any wiring to protrude from the laminate. Furthermore, the method is potentially low cost, something that could make it easily adopted by measurement laboratories.

### 3.6.1. Embedding of Humidity Indicator Cards and their Calibration

#### 3.6.1.1. Humidity indicator cards

The humidity indicator cards supplied by RS (Figure 3-12) include dots approximately 11 mm in diameter that consist of blotting paper impregnated with cobaltous chloride, which is sensitive to contact with moisture. When cobaltous chloride becomes hydrated, it transforms from a blue colour to pink. Each dot contains a different concentration of cobaltous chloride, allowing them to respond to different levels of humidity [123]. The principle of the operation of the cards is that a specific amount of moisture is absorbed by the paper, which comes to equilibrium with the environment. The absorbed moisture hydrates the cobaltous chloride, while maintaining the moisture equilibrium with the environment as the amount of paper is much more than the cobaltous chloride. As will be shown below, it was found that by choosing the appropriate dot, measurement of more moisture levels could be achieved, as the colour of the dots changes gradually over a range of humidity levels. For this work, dots designed to indicate levels of 40, 50 and 60% relative humidity were used to examine the range of moisture levels that could be recorded.

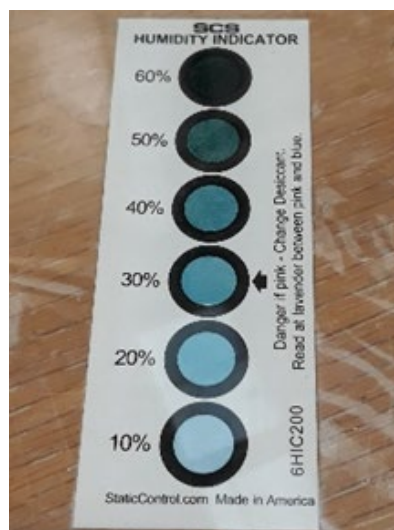


Figure 3-12 Humidity indicator card.

### 3.6.1.2. Calibration procedure

Calibration of the measurement method was required for the representation of Relative Moisture Content (RMC) by the different colour shades of the dots. For the calibration, three samples were measured, and the procedure below was followed:

Encapsulation of the humidity indicator cards in a laminate structure of EVA-humidity indicator card-EVA-glass (Figure 3-13). This structure (with no moisture barrier on one side) was chosen to allow fast saturation of the inner layer for a rapid calibration. Furthermore, with the EVA and glass placed on the top of the humidity indicator card, the calibration method is representative of the humidity (RMC) measurements in a PV module, as the properties of the glass and the EVA layer, through which the observations are made, are exactly the same as in a PV module.

Loading the laminates in an environmental chamber (Thermatron SM-32) at 85 °C and at increasing levels of relative humidity in steps from 40% to 85%. A 48-hour dwell time was used at each humidity level (Figure 3-13) to ensure saturation (According to Jankovec et al. [124] a single layer of EVA needs 1 hour to saturate, so 48 hours should be more than enough for the saturation of the whole stack).

RGB colour coordinates of the three dots to be monitored were acquired by processing photographs of the samples. The images were acquired for each humidity level at the end of the dwell times, and the RGB coordinates were plotted on a colour space, after transformation from the R, G, and B dimensions to the two dimensional x-y colour space (Appendix 1), to obtain the calibration curve [125].

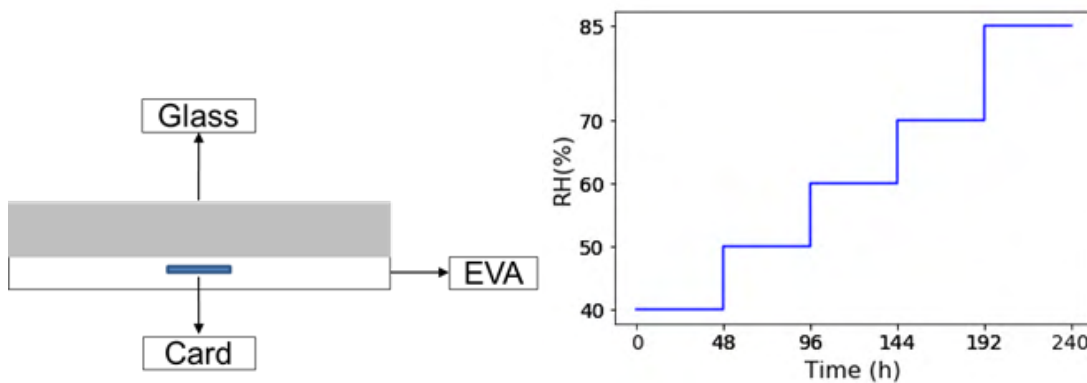


Figure 3-13 Left: EVA-humidity indicator card-EVA-glass structure. The card faces towards the glass. Right: RH conditions for calibration of the measurement method (all at 85 °C).

### 3.6.1.3. Camera configuration and calibration

The camera used for imaging the calibration samples and the PV devices was a Canon EOS 450D. The lens aperture was set at f/8, for more repeatable colour measurement, as less light, from the artificial light source, enters the lens, which may vary over the full duration of the experiment. In addition, the ISO of the camera was set at 100, to further reduce the sensitivity to light. The reduction of the sensitivity was important, so that the measurements would be comparable for the entire duration of the calibration, as they were not affected by slight variation of the artificial light source. For these reasons, the shutter speed was very low (set at 0.8 seconds). The white balance was set to 4000-5000K, as the photos were shot under artificial light. Figure 3-14 shows the measurement set up.

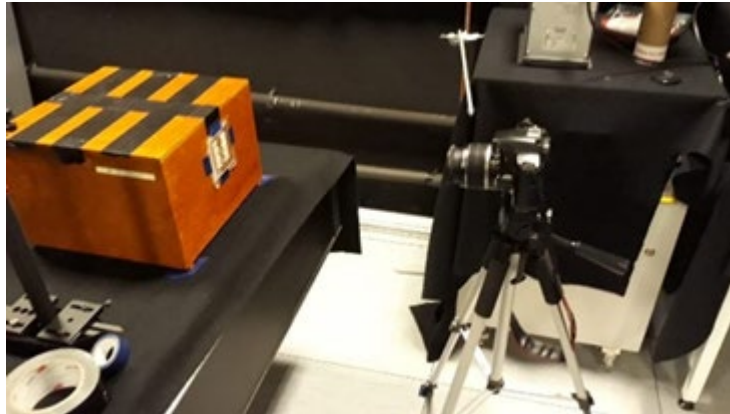


Figure 3-14 Humidity indicator card measurement set up.

For the verification of the repeatability of the measurements due to the stability of the room artificial lighting, before every set of sample measurements, images of blue, red and green reference cards were taken (Figure 3-15). The colour measurements of the reference cards were the same for all the sets of sample measurements and verified the repeatability.

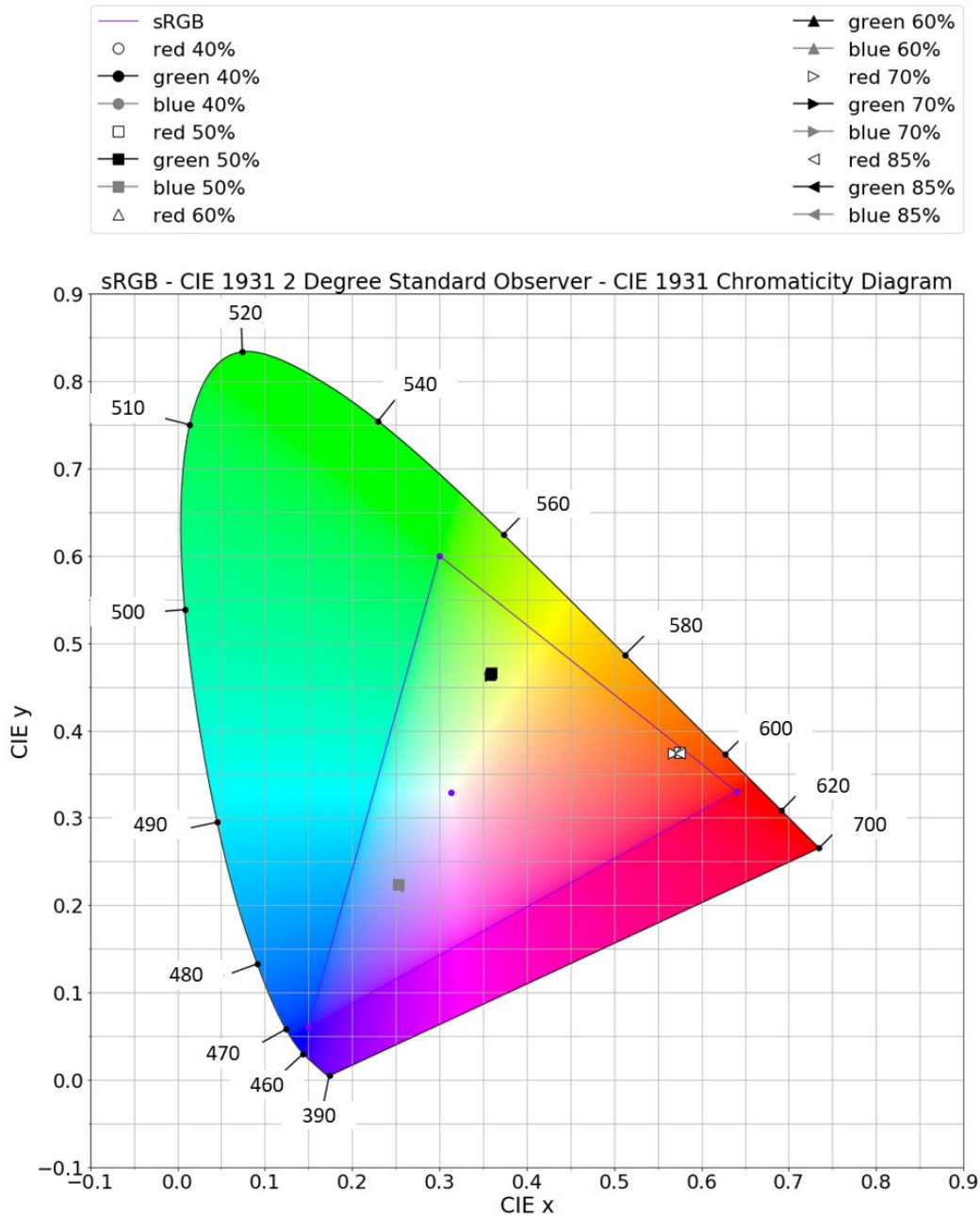


Figure 3-15 Repeatability of colour measurements using images of three reference cards, representing the three RGB coordinates. These measurements were received before the humidity indicator card images at each moisture level. The % values in the legend represent the humidity test before which these measurements were made.

### 3.6.2. Calibration – Results

Images of the encapsulated humidity indicator cards (viewed through the EVA and glass layers) for each RMC level of the calibration (40%, 50%, 60%, 70% and 85%) are presented in Figure 3-16. Colour change between exposure levels are obvious

for all the dots. It is observed that the dots continue to change colour, even if they are in a chamber with higher relative humidity than the one that they could theoretically measure. Moreover, the colour of the dots is supposed to change from blue to purple and then to pink. Instead, the colour varied to green and finally to brown. The reason is that the cobalt (II) chloride of the dots reacts with free radicals of the peroxides contained in the EVA during lamination [126]. When the new compound is hydrated, the cobalt (II) is transformed to cobalt (III) and the colour of the dot changes to green. Finally, when all the quantity of the peroxides and most of the cobaltous chloride has reacted with moisture, the remaining cobalt (III) is transformed back to cobalt (II) and the colour of the dot changes to brown [127]. Even if the dots do not measure according to the manufacturer's standards, they are still suitable for moisture measurement, as the peroxides act as a catalyst, but dedicated calibration is required.

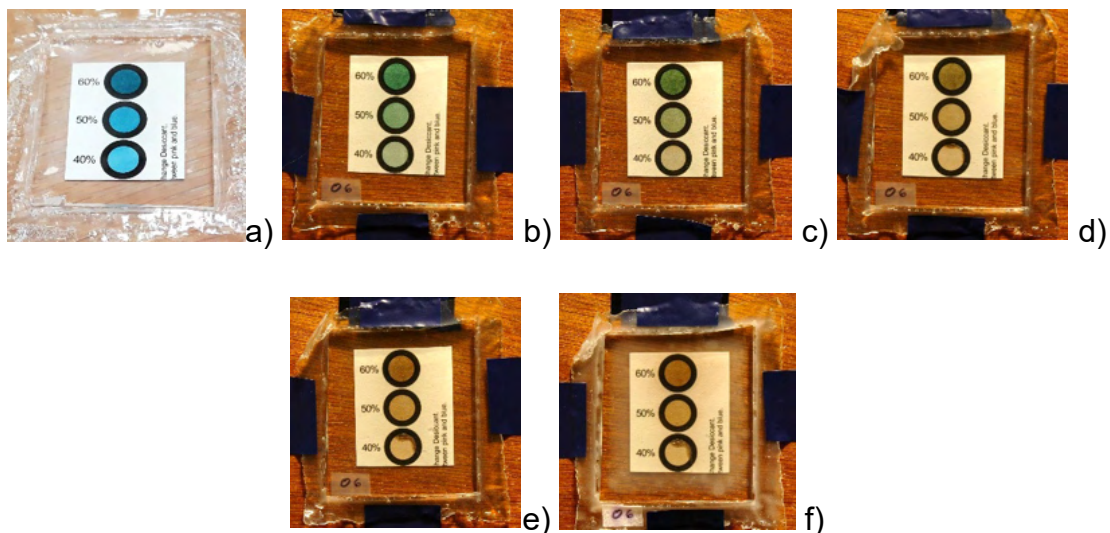
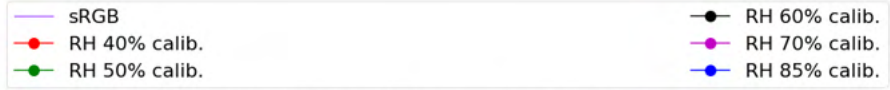


Figure 3-16 Appearance of the humidity indicator cards after a) lamination, and exposure to b) 40%, c) 50%, d) 60%, e) 70% and f) 85% RH.

Figure 3-17 shows the calibration steps for each dot. The RGB 3D colour coordinates were extracted from 10,000 pixels from each dot, for the different calibration steps. The procedure was repeated for three images of the same sample and then for three different samples. Each point is the x and y colour co-ordinate, after transformation of the average RGB 3D coordinates to a 2D axis. The error bars indicate the plus-minus standard deviation in the measurements from the 10,000 pixels. The average standard deviation of the colour measurement is in the range

$\pm 0.003$  (x-value) and  $\pm 0.005$  (y-value) for the dot that is designed to indicate 40% humidity (based on the 40% RH and 50% RH colour measurements only),  $\pm 0.006$  (x-value) and  $\pm 0.007$  (y-value) for the 50% dot and  $\pm 0.01$  (x-value) and  $\pm 0.011$  (y-value) for the 60% dot. As mentioned, the average error of the 40% dots was calculated by taking into consideration only the first two moisture/colour measurements (at 40% RH and 50% RH), as for the rest, some bubbles of different colour appeared on the sample that increased the error. The different colour of these bubbles (brown) is possibly caused by the interaction of the card with gases generated within the encapsulant during its exposure to high levels of moisture and temperature (see section 3.7). Moreover, the bubbles may be initiated due to faulty lamination on this specific card. Furthermore, smaller errors are observed for the level of 85% RMC for most of the dots, which is to be expected, as the remaining concentration of cobaltous chloride, which has not reacted yet with moisture, is much smaller. This is also the reason why the RGB coordinates for all the dots at 85% RH have similar values to those observed for 70% RH. According to the calibration points, the smallest errors are observed for the dot that can indicate 40% humidity (when the errors due to the bubbles are not considered), but also the smallest range of measurements (x axis between 0.342 and 0.384). This is reasonable, as the concentration of cobaltous chloride is smaller. To the contrary, the dot that can indicate 60% humidity shows the biggest errors and the largest range (x axis between 0.319 and 0.444). A larger range of values is preferred to aid differentiation between measurements when the colour space values are used to estimate the moisture in a PV laminate measured by the humidity indicator cards. Therefore, the 50% humidity dot is preferred to be used for moisture measurements, as it balances smaller error but sufficient range.



sRGB - CIE 1931 2 Degree Standard Observer - CIE 1931 Chromaticity Diagram

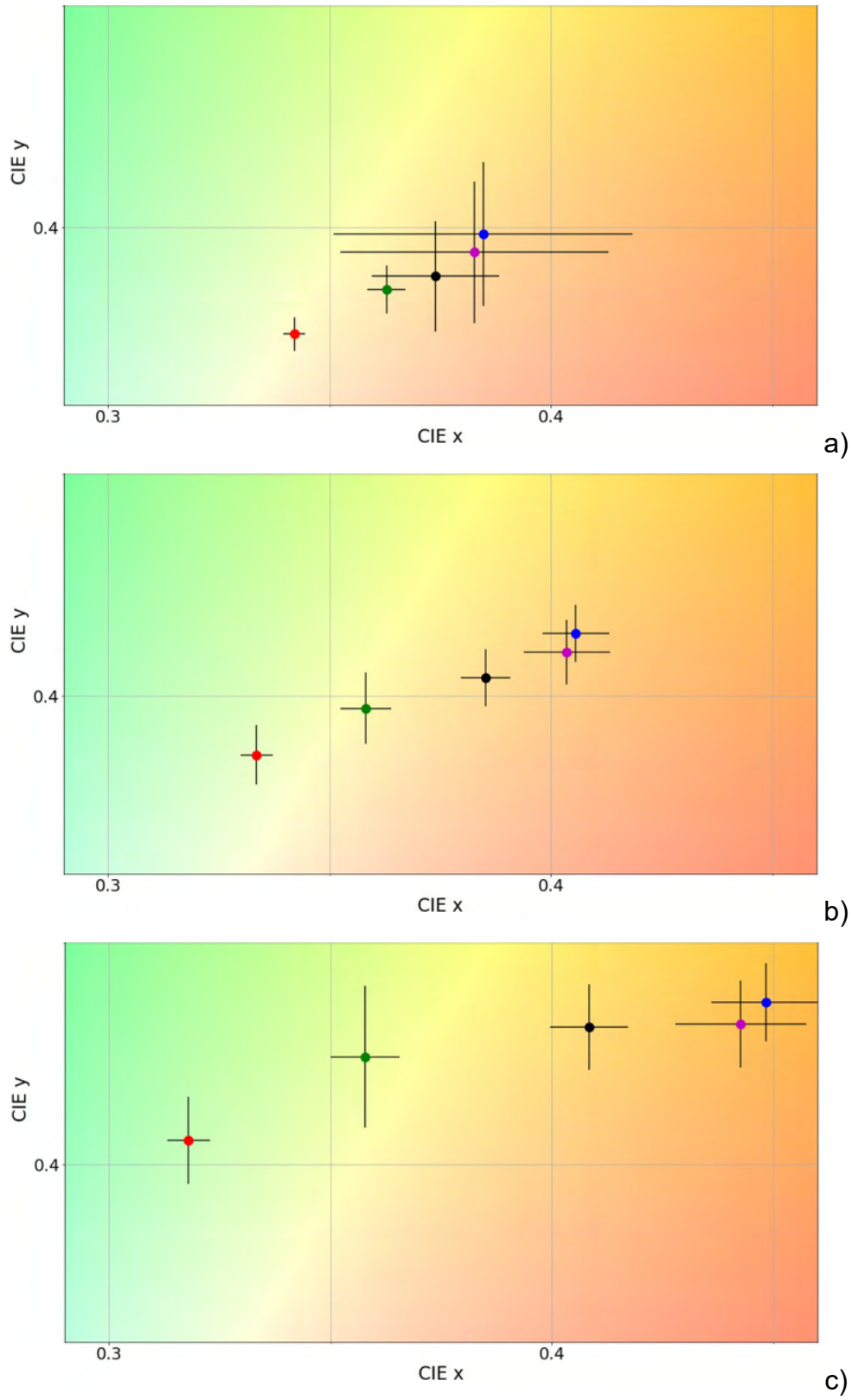


Figure 3-17 Calibration points for the humidity indicator dots of a) 40%, b) 50% and c) 60%.



To obtain the calibration curve for the 50% humidity dot, a different linear interpolation was assumed between two sequential RMC levels (Figure 3-18), with each line segment separated into 100 intervals (except the line segment defined by 70% and 85% RMC, which was separated into 150 intervals), to achieve 0.1% measurement resolution. Different straight-line equations are necessary, as the change of the colour is not linear in relation to the RMC. The RMC intervals were matched to their specific colour coordinates, accordingly.

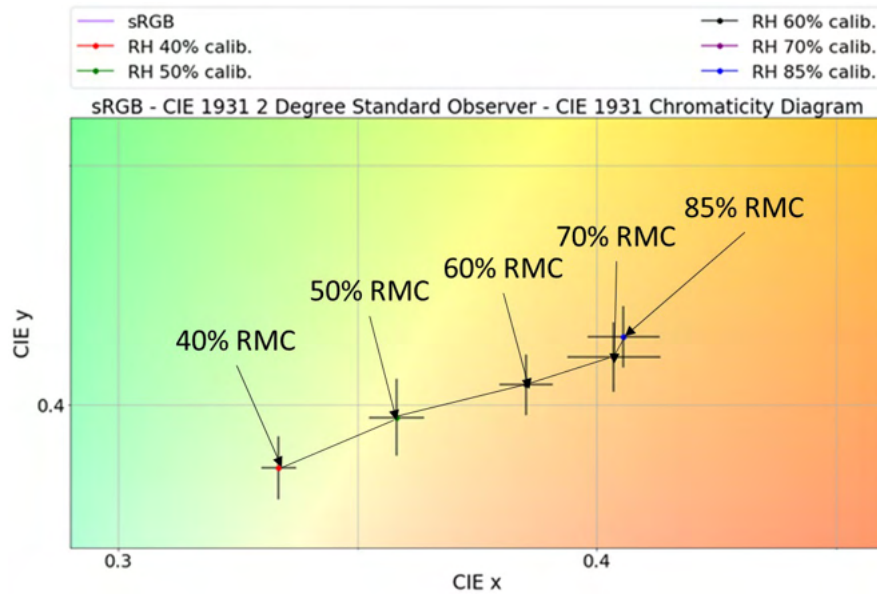


Figure 3-18 Calibration curve for the dot designed to indicate humidity of 50%. Each point on the CIE xy diagram represents a level of RMC. The RMC levels, respective to the region between two measured RMC levels (e.g. between 40% and 50% RMC), are calculated by linear interpolation.

### 3.6.3. Application to single cell PV modules

For the application of the method to single cell PV modules, dots designed to indicate 50% (preferred according to the calibration) and 60% (tested as an alternative) humidity were embedded at the front side of the cell during lamination. Three samples were prepared, two with EVA constituting the encapsulant and two types of PET (multilayer with aluminium foil and single layer transparent) backsheet, and one half-encapsulated, with the rear side exposed to the environment (Figure 3-19). c-Si PV cells were used, soldered with standard Pb-Sn-Cu ribbons. Figure 3-20 shows a cross-section of the structure. The samples are summarised in Table 3-6.



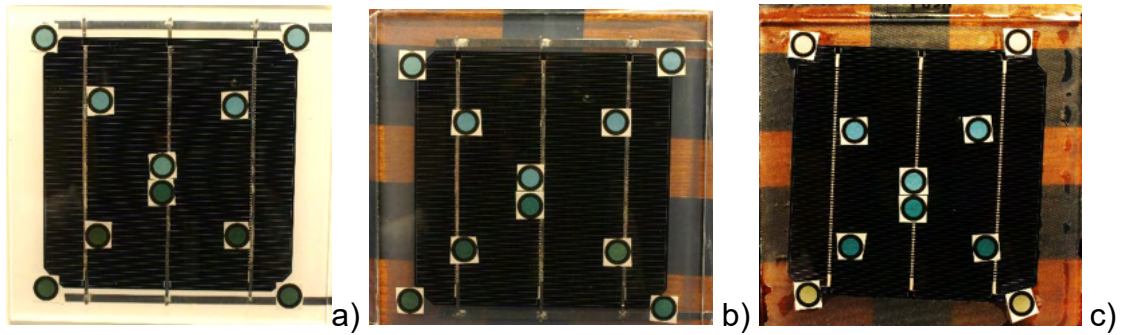


Figure 3-19 PV modules containing humidity indicator cards with a) multilayer PET with aluminium foil, b) single layer transparent PET backsheet and c) half-encapsulated with the rear side exposed. For all the samples, the five upper cards are 50% dots and the five lower cards are 60% dots.

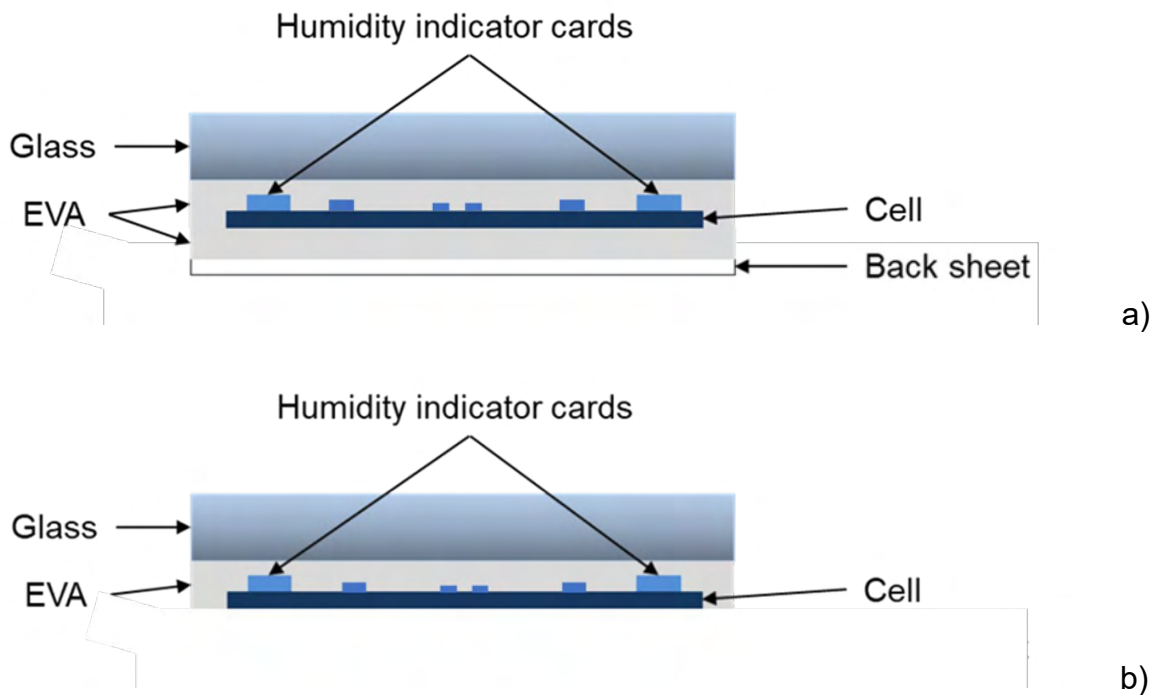


Figure 3-20 Cross-section of the PV module with embedded humidity indicator cards at the front side of the PV cell when a) a backsheet is included and b) no rear side encapsulation is included.

Table 3-4 The names and types of the samples tested.

Name	Type
<b>BHC3</b>	PV module containing multilayer PET with aluminium foil
<b>THC3</b>	PV module containing transparent PET
<b>HEB4</b>	half-encapsulated PV cell with the rear side exposed

The mini modules were loaded into a chamber<sup>7</sup> at DH conditions (85% RH / 85 °C). The dot colour measurements were made in the same way as in the calibration section. Humidity at different positions across the PV cells was extracted from the colour change of the dots, as compared to the calibration curve (Figure 3-18).

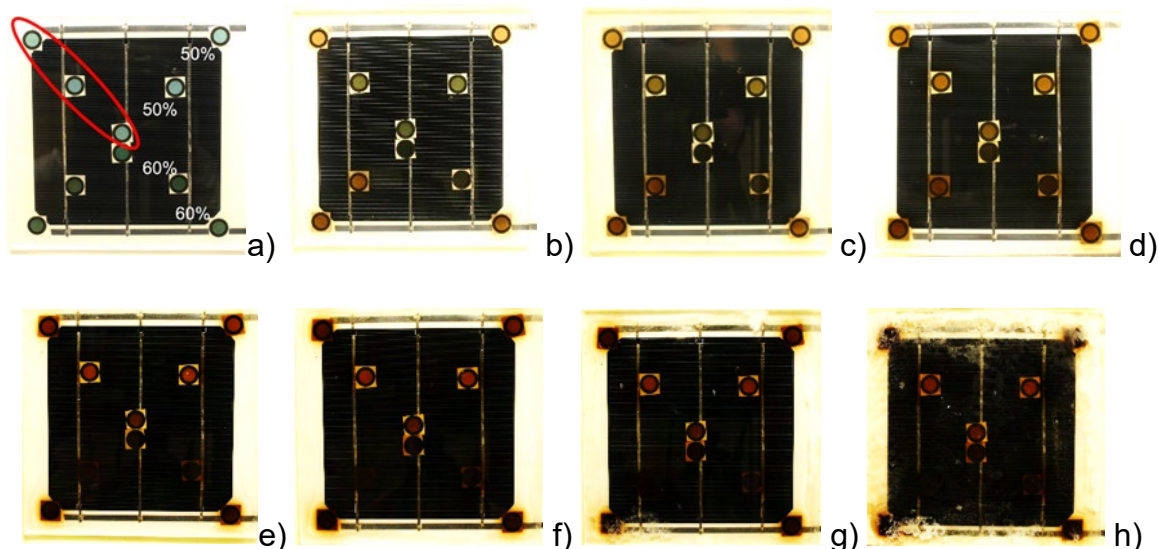


Figure 3-21 PV modules with embedded humidity indicator cards, encapsulated with multilayer PET backsheets with Al foil and exposed to 85% RH / 85 °C for a) 0 hrs, b) 503 hrs, c) 974 hrs, d) 1763 hrs, e) 2402 hrs, f) 3023 hrs, g) 3383 hrs and h) 5350 hrs.

Figure 3-21 shows the variance of the dot colour for the sample encapsulated with the multilayer PET backsheet with aluminium foil (for the measurements of the reference cards, see Appendix 2). Colour analysis was carried out for the three dots (described as corner, inner and centre) indicated in Figure 3-21a for each sample, with the colour evolution plotted over the calibration curve in Figure 3-22. For the translation of each colour measurement to RMC content, the closest point of the calibration curve to the measured coordinates is calculated. The RMC evolution over time<sup>8</sup> of the three studied points is presented in Figure 3-23a. The same procedure was repeated for the dots located at the same positions within the PV module laminated with the single layer transparent PET backsheet (Figure 3-23b) and the PV laminate that does not include rear side encapsulation (Figure 3-23c).

<sup>7</sup> The samples were aged in a Thermoatron SM-32 chamber for up to 974 hours of exposure and then moved to a Sanyo Gallenkamp HCC065.PF4 chamber for the rest of the experiment duration.  
<sup>8</sup> The RMC evolution stops at 85% as it is assumed that the sample is saturated at this value.

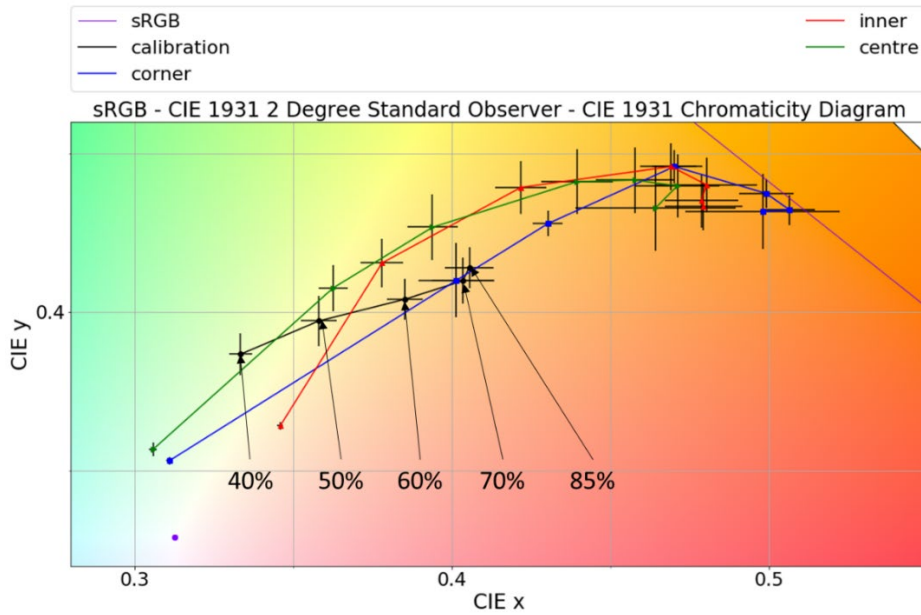


Figure 3-22 Colour change of the different dots for the sample containing PET with Al foil, compared to the calibration curve. the closest point of the calibration curve to the measured coordinates gives the RMC values presented in Figure 3-23.

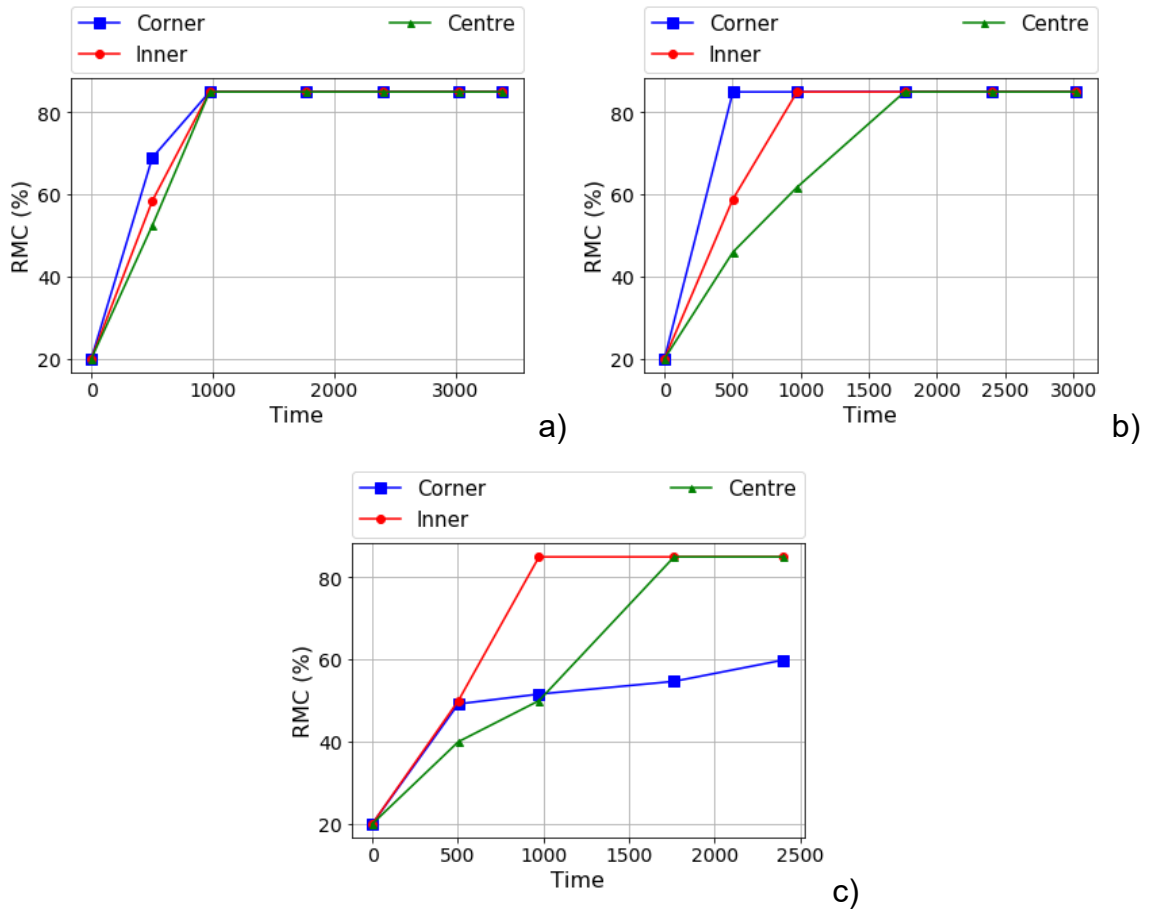


Figure 3-23 RMC evolution of the corner, inner and centre dot for the sample encapsulated with a) PET backsheet with Al foil, b) monolayer transparent PET backsheet and c) no backsheet.

For all samples, the colour coordinates of the dots change according to the moisture to which they are exposed. Firstly, the colour of the corner dots changes, followed by the inner and finally those at the centre of the PV cells. The colour of the corner dots follows a slightly different path, as they may be affected by multiple moisture routes due to their proximity to the edges of the PV module (Figure 3-22). This effect is stronger on the rear-side exposed PV cell, as the corner dots are in almost direct contact with the environment, so their colour is affected by both environmental and polymer moisture (Figure 3-23c). By comparison, of the centre dots of the three samples, after 1763 hrs of exposure (Figure 3-24) the highest moisture content was absorbed by the PET backsheet with Al foil sample, closely followed by that with the transparent PET backsheet. Although the PET backsheet with Al foil should be more robust to moisture according to the literature [128], the type of PET and the corrosion of the Al foil at high levels of temperature and humidity might affect negatively the backsheet (see severe decomposition in section 4.3.3.2). For the rear-side exposed sample, the absorbed moisture content was the least, which agrees with the findings of section 3.5.2, which show that stand-alone EVA absorbs lower moisture content (due to lower solubility), than if it were attached to a backsheet. These results indicate that the amount of moisture absorbed by a PV module is dependent on the interaction between the encapsulant and the backsheet. For this reason, any conclusions about when the samples become saturated may be misleading, as the calibration was performed on samples that did not contain backsheet, meaning exclusion of the effect of the backsheet on the moisture content absorbed by the EVA.

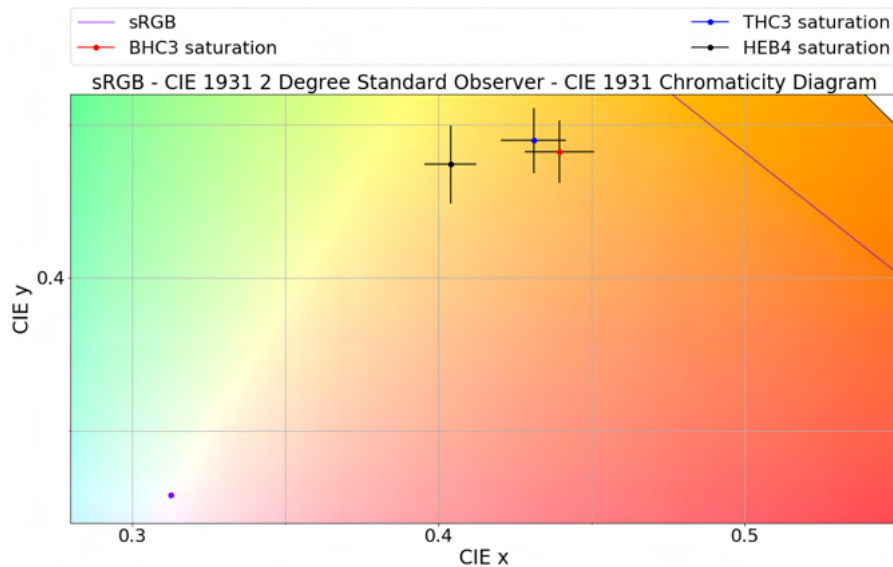


Figure 3-24 Colour coordinates of the centre dots of the sample laminated with PET with Al foil (BHC3), transparent PET (THC3) and the half-encapsulated PV cell (HEB4), after 1763 hrs of exposure.

However, the colour of all dots continues to change, even if the calibration indicates saturation. The dots are calibrated only with EVA encapsulation, which excludes interactions of the encapsulant with the different backsheets. Another possibility is that when the samples are saturated, the remaining cobaltous chloride dissolves within the wet polymer, migrates from the cards and their colour changes due to the decreasing concentration of the compound. Yet another possibility is that yellowing of the EVA interferes with the colour of the cards. The fourth possibility is that cobalt (II) remaining after saturation reacts with acetic acid produced by hydrolysis of the EVA, generating a complex of  $\text{CoCl}_2$  and acetic acid. The colour of this compound is red, and the dots do indeed become darker after 2402 hrs of DH exposure [129].

The migration of  $\text{CoCl}_2$  and/or the existence of the complex of  $\text{CoCl}_2$  and acetic acid within the 2402 hrs aged samples, is indicated in EL images (Figure 3-25). The dark areas around the cards may be caused by front metallisation degradation due to the mentioned compounds. These findings agree with other publications that show acetic acid on the front side of the PV cells within a PV module after 2000 hrs of aging under DH conditions [130]. The acetic acid generation shortly after moisture saturation of a sample is analysed in section 3.7. Another observation resulting from the EL images is that the cards may crack the cells. A solution to this problem was

found and is described in section 3.6.4. Further disruption of the moisture ingress might be introduced by the new moisture paths formed between the cards and the PV cell.

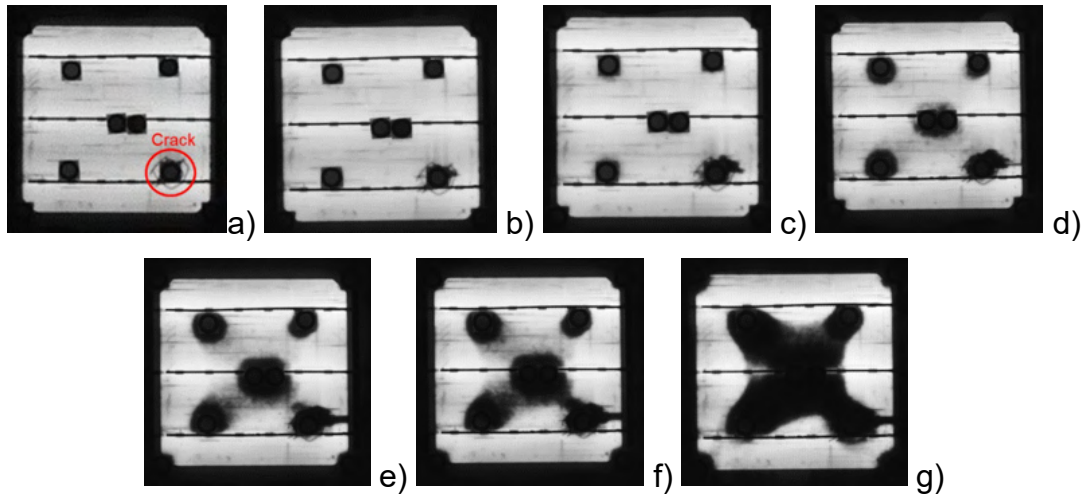


Figure 3-25 EL images of samples, containing PET with Al foil after a) 503 hrs, b) 974 hrs, c) 1763 hrs, d) 2402 hrs, e) 3023 hrs, f) 3383 hrs and g) 5350 hrs.

### 3.6.4. Structure of samples to prevent the formation of cracks

In some of the experiments shown in the previous section a crack was observed in the solar cell (Figure 3-25) that was caused during lamination by the additional thickness of the humidity indicator card. To avoid this, a second round of experiments was undertaken with samples prepared using a modified lamination procedure. In this case, an extra layer of EVA was inserted at the PV cell – humidity indicator cards interface (see Figure 3-20) into which holes were made to accommodate the thickness of the cards and still allow them to make direct contact with the cells (Figure 3-26). The samples were tested as before in the Sanyo Gallenkamp HCC065.PF4 chamber and the results were similar to those obtained in the previous experimental round (section 3.6.3).

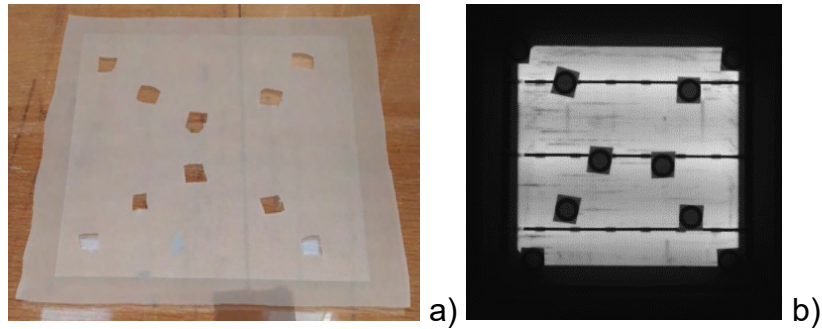


Figure 3-26 a) EVA layer placed on the PV cell. -. The holes accommodate the humidity indicator cards and allow their direct contact with the cell. b) EL image of the PV module with the additional EVA layer.

### **3.7. Acetic acid generation shortly after moisture saturation of polymer laminates**

To test the hypothesis discussed in section 3.6.3 that acetic acid is generated shortly after a sample is saturated due to moisture ingress, two specimens with the structure glass – EVA – backsheets were aged under DH 85°C / 85% RH conditions (Figure 3-28), and removed at different time intervals, for reflectance spectra measurements. The goal of the experiment was to monitor any yellowing occurring on the EVA, which is an indication of degradation that may interfere with the colour of the humidity indicator cards. More specifically, high moisture and temperature levels cause degradation of the EVA, which produces discolouring chromophores (e.g. polyenes) and acetic acid, according to the reaction demonstrated in Figure 3-27 [131], [46], [132]. Moreover, additional additives may degrade under the same conditions.



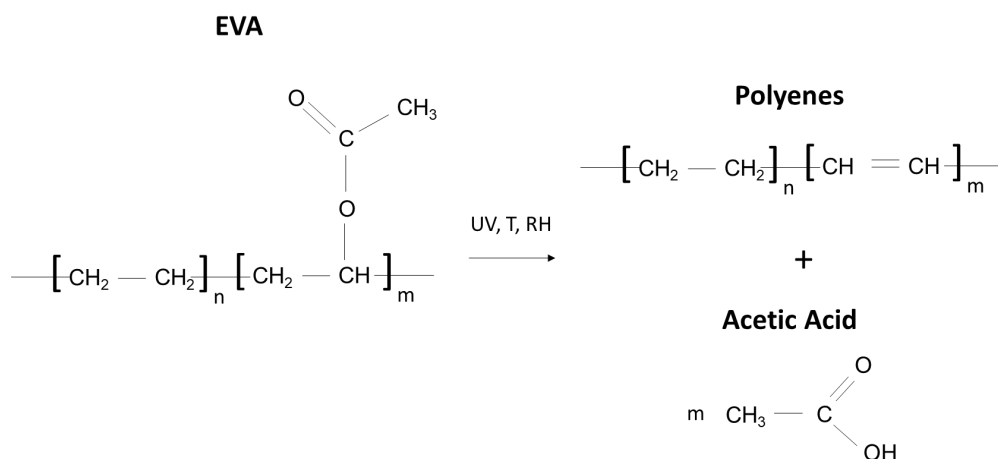


Figure 3-27 The interaction of EVA with UV, T and RH, resulting in polyenes and acetic acid production. The reaction may occur in the absence of UV or RH, but their addition accelerates the process [131], [46], [132].

The reflectance spectra were measured through the glass with a UV-Vis-near infrared Cary 5000i spectrophotometer. According to the measurement set up, a light beam which includes UV, visual and near infrared spectra, is incident to the sample, with a detector receiving the reflectance spectra and a spectrophotometer analysing them. The measurements were acquired at two different points, at the centre and at a point slightly lower than the centre, to avoid biased results, due to any local peculiarity of the optical behaviour of the EVA. A transparent PET backsheet was used for less interference of the colour of the backsheet with the EVA colour due to aging, as the polymer of interest is the EVA and optical changes of the backsheet should not be detected. During the measurements, a white sheet (PET) was placed behind the sample, for the achievement of the reflectance measurements. The long-term repeatability of the instrument, which could be affected due to potential aging of the light-source used for the measurements, was checked with a baseline measurement of the instrument light source before each round of measurements (Figure 3-29). The average spectra of all the measurements<sup>9</sup> are plotted for each time interval in Figure 3-30. It is observed that, already after 424 hrs of exposure, the reflectance within 400 - 800 nm, and

<sup>9</sup> For the estimation of the average spectra, the values of reflectance measured at specific wavelengths were averaged for both measurements acquired for the total of the samples.



especially between 400 and 500 nm, increases, which indicates yellowing due to the hydrolysis of the EVA and degradation of additives.

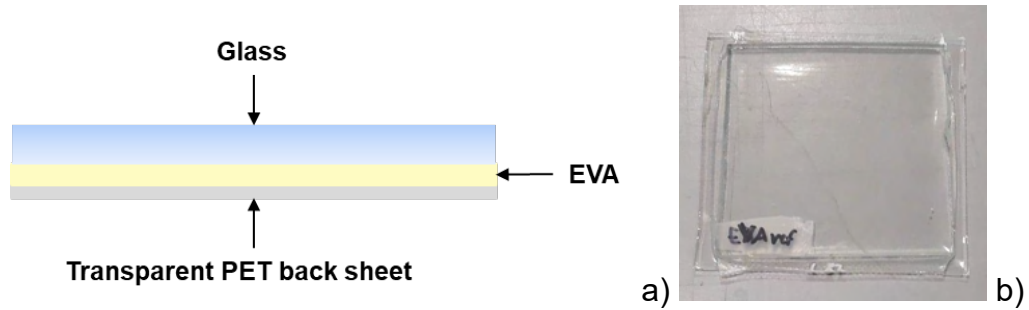


Figure 3-28 a) The cross-section and b) image of the glass – EVA – backsheet sample.

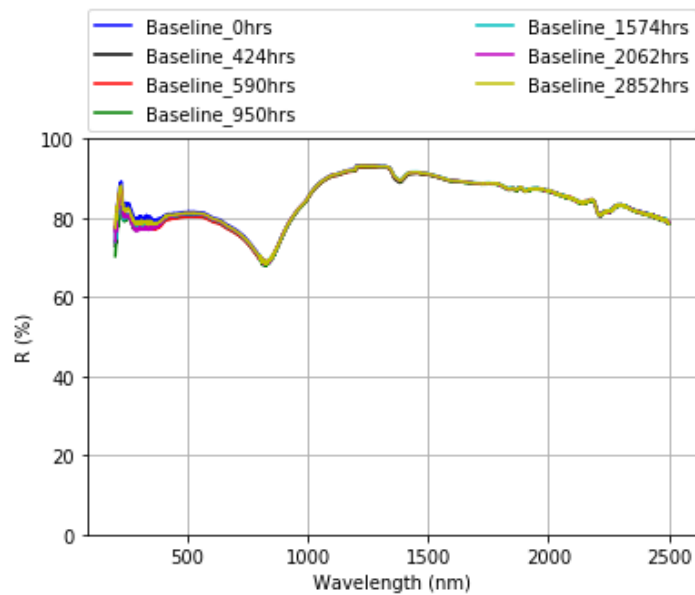


Figure 3-29 Baseline repeatability for each time interval.

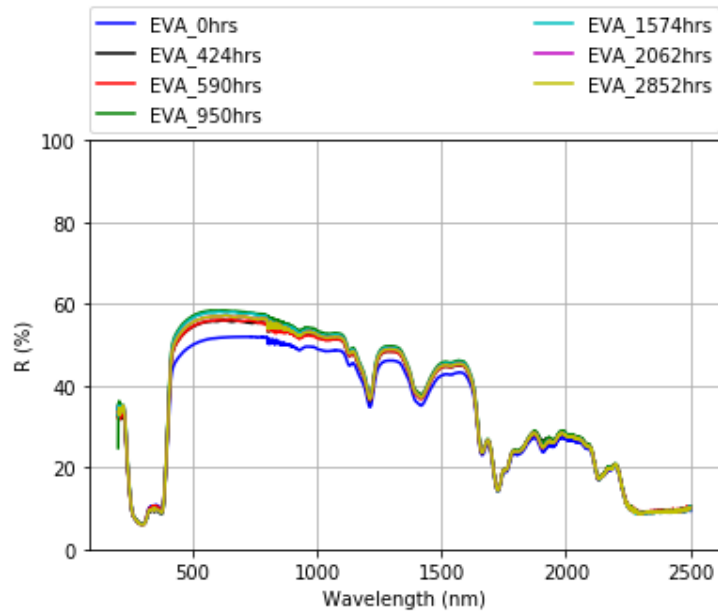


Figure 3-30 Reflectance spectra of the samples for each interval of DH 85°C / 85% RH exposure.

For the observation of the colour change of the humidity indicator cards, samples of the structure described in section 3.6.1.2 were exposed to DH 85°C / 85% RH conditions. Measurements of the 50% humidity dot show that colour change continues long after the saturation point, which indicates both continuous evolution of the encapsulant discolouration and acetic acid generation (Figure 3-31).

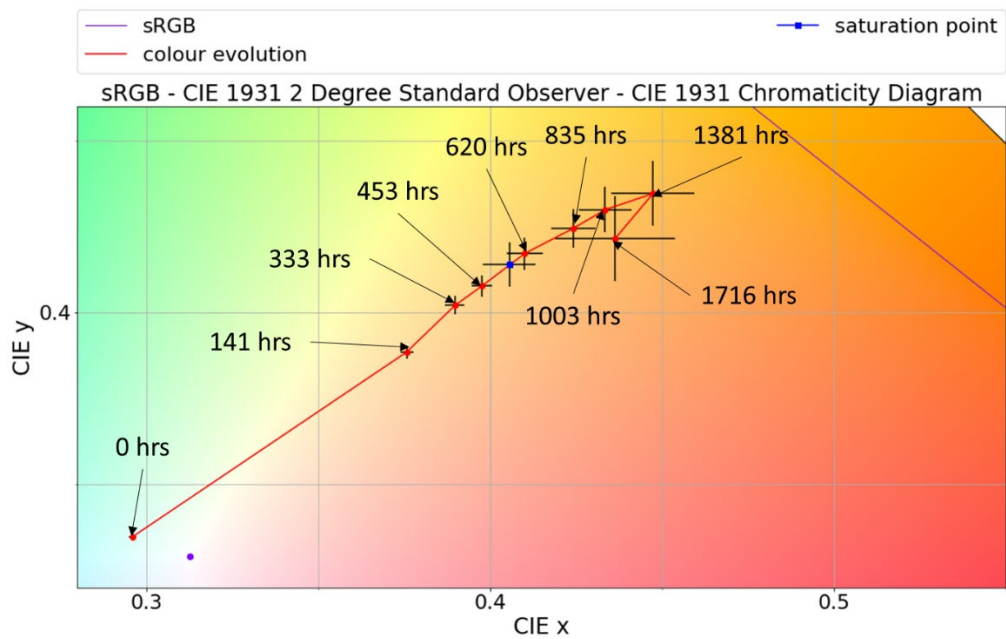


Figure 3-31 Colour evolution of the 50% dot embedded within a glass – EVA – EVA specimen exposed to DH 85°C / 85% RH conditions.

### **3.8. Comparison of measured and simulated moisture profiles within a PV module**

In addition to the optical visualisation of moisture ingress within a mini-module presented in section 3.6.3, the moisture profile at the front side of the PV cell (front layer EVA between the PV cell and the glass) was investigated by theoretical simulation. The simulation was carried out in COMSOL Multiphysics, applying the same methodology as in section 3.4.3, without the fitting part. The difference is that for the solution of 3D Fick's law (eq. (3-5)), the 3D space dimension is required.

For the simulation of PV modules that include a backsheet, the structure of the single-cell mini-module was represented by a 20 x 20 cm polymer stack, with an unequal-octagonal (square-like) impermeable thin layer (4 long sides 12.6 cm each and 4 short sides 2.12 cm each) placed between the layers of EVA, acting as the c-Si PV cell (Figure 3-32). The thickness of each of the two layers of EVA was set to 0.517 mm while the thickness of the backsheet was set to 0.37 mm for PET containing Al foil [133] and 0.302 mm for the transparent PET [134] (Figure 3-33a). For the moisture ingress into a half-encapsulated PV cell, a similar structure as described above was used, but instead of the layers representing the rear-side EVA and backsheet, another layer was simulated, which acted as a thin layer of atmosphere (Figure 3-33b). This atmosphere layer was added for the convenience of the structure composition, as, according to COMSOL Multiphysics, two layers are required for the introduction of the thin impermeable layer within them, representing the PV cell.

The model parameters used are listed in Table 3-7. Two simulations were performed for different diffusion coefficients of the backsheet, one for a PET backsheet with Al foil (using values measured while on secondment to FhG CSP) and one for a transparent PET backsheet (using a value from the literature [91]). An additional simulation was performed for the half-encapsulated PV cell, with the diffusion coefficient of the moisture within the atmosphere layer set as mentioned in the literature [135]. The diffusion coefficient of the EVA was taken as the average of the values measured while on secondment to FhG CSP and a value taken from literature [91]. The initial and boundary conditions of moisture content (initial

moisture content of EVA and moisture content applied on the boundaries of the backsheet and PV module edges, respectively) were taken from the results presented in section 3.5.2, and converted to mol/m<sup>3</sup> according to the procedure described in section 3.4.2 (eq. (3-7)). For the simulation of the PV modules, the absorbed moisture content taken was that of EVA when it is attached to a PET backsheet with Al foil. Similar backsheet - EVA interactions were taken into consideration for both types of samples, as analysis of the interaction between the transparent PET backsheet and the EVA was not available (this assumption may lead to a slight overestimation of the moisture ingress according to the results presented in section 3.6.3.). For the simulation of the half-encapsulated PV cell, the absorbed moisture content assumed was the one for the stand-alone EVA.

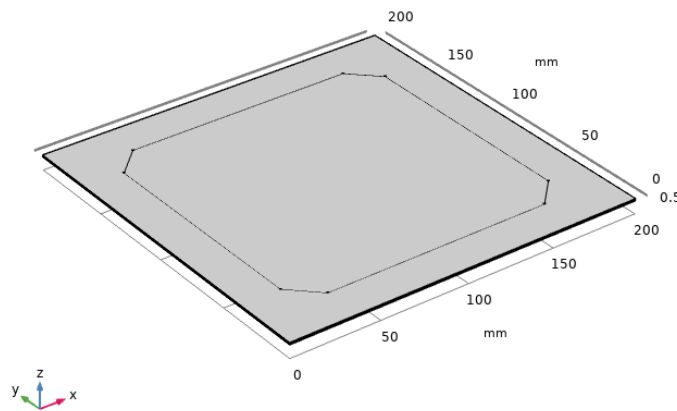


Figure 3-32 Top view of the geometry used for the simulation of moisture ingress into a single-cell mini-module or a half-encapsulated PV cell.

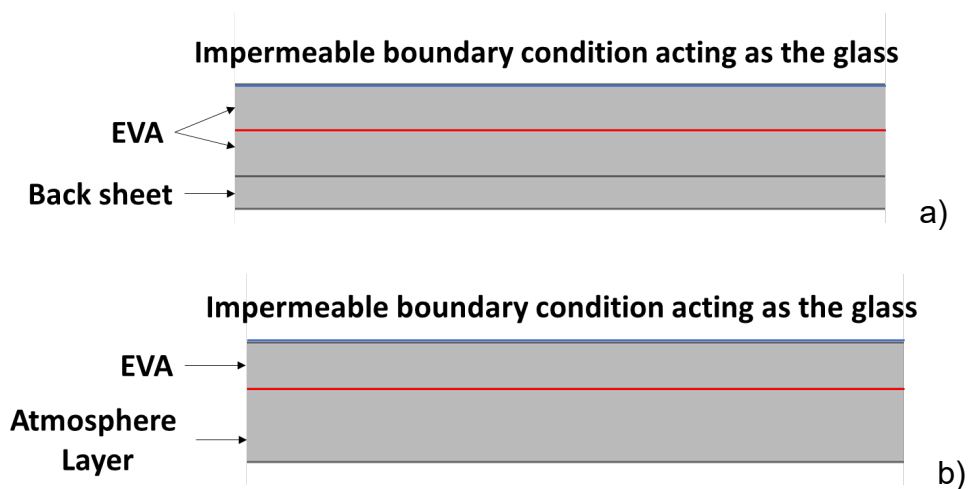


Figure 3-33 Cross-section of the geometry of a) a mini-module and b) a half-encapsulated PV cell. The red line indicates the interface where the impermeable layer (PV cell) is introduced.

Table 3-5 Model parameters for the simulation of moisture ingress into mini-modules manufactured with PET backsheet with Al foil, or PET transparent backsheet, and half-encapsulated PV cells.

Name	Value PET+Al	Value Transparent PET	Value Half- encapsulated	Description
<b>T<sub>amb</sub></b>	358.15 K	358.15 K	358.15 K	ambient temperature
<b>C<sub>ini</sub></b>	13.06 mol/m <sup>3</sup> @ 20% RH	13.06 mol/m <sup>3</sup> @ 20% RH	8.24 mol/m <sup>3</sup> @ 20% RH	initial moisture concentration
<b>C<sub>0</sub></b>	88.37 mol/m <sup>3</sup> @ 85% RH	88.37 mol/m <sup>3</sup> @ 85% RH	56.79 mol/m <sup>3</sup> @ 85% RH	boundary moisture concentration
<b>D<sub>eva</sub></b>	5.2e-10 m <sup>2</sup> /s	5.2e-10 m <sup>2</sup> /s	5.2e-10 m <sup>2</sup> /s	EVA diffusion coefficient
<b>D<sub>b</sub></b>	1.41e-11 m <sup>2</sup> /s	2.1e-11 m <sup>2</sup> /s	3.8e-5 m <sup>2</sup> /s	Backsheet / atmosphere diffusion coefficient

Figure 3-34, Figure 3-35 and Figure 3-36 demonstrate the comparison between the measured RMC profiles from the humidity indicator cards and the moisture content profiles resulting from the simulations, for the mini-module laminated with PET backsheet containing Al foil, the mini-module manufactured with transparent PET backsheet and the half encapsulated PV cell, with the rear side exposed to the environment, respectively. The RMC profiles were generated by considering the measurement of the five 50% relative humidity indicator cards embedded on the upper surface of the PV cells. The resulting moisture profile was mirrored for the lower part of the mini-modules as the 60% humidity indicator cards embedded there could not be measured accurately due to the extended degradation for long humidity exposure (after 980 hrs). The results show that, although the effect of the interactions between the EVA and backsheet on the moisture content absorbed by the EVA, are not considered for the calibration, and acetic acid degrades the cards, they are still a good indicator of the moisture profile. More specifically, for the PV

module containing the transparent PET backsheet and the half-encapsulated PV cell, the RMC profile estimated by the humidity indicator cards is very similar to the one calculated from the simulation, with saturation occurring between 1760 hrs and 2400 hrs of exposure. The cards appeared to be already saturated after 1760 hrs of DH aging, while the simulations show a moisture profile close to saturation, with this difference (~10% for both samples) probably attributed to the sensitivity of the measurement method.

Although the calibration curve used for the translation of colour to RMC, provided results comparable to the simulation, for the PV module containing transparent PET backsheet and the half-encapsulated PV cell, this was not the case for the sample laminated with PET backsheet including Al foil. While the simulation indicated saturation after 1760 hrs of exposure (similar to the other two samples), the measured moisture concentration reached saturation after only 980 hrs. This observation means that the scale introduced by the calibration curve is smaller than the concentrations measured in the PV module containing Al foil, which absorbs higher amount of moisture.

Finally, comparing the simulations of the three samples, it is observed that all of them need almost the same time to saturate (2400 hrs), regardless the type of backsheet or even the absence of rear-side encapsulation. Thus, it is concluded that the diffusion coefficient of the backsheet does not play significant role on how fast the PV module reaches saturation, as the time demanded for the moisture to reach the rear side of a PV cell is much less (~60hrs [89]) than the diffusion duration from the edges of the PV cell towards the centre. However, further research is required to claim that these conclusions are valid for a full-size PV module, including edge sealant and frame.

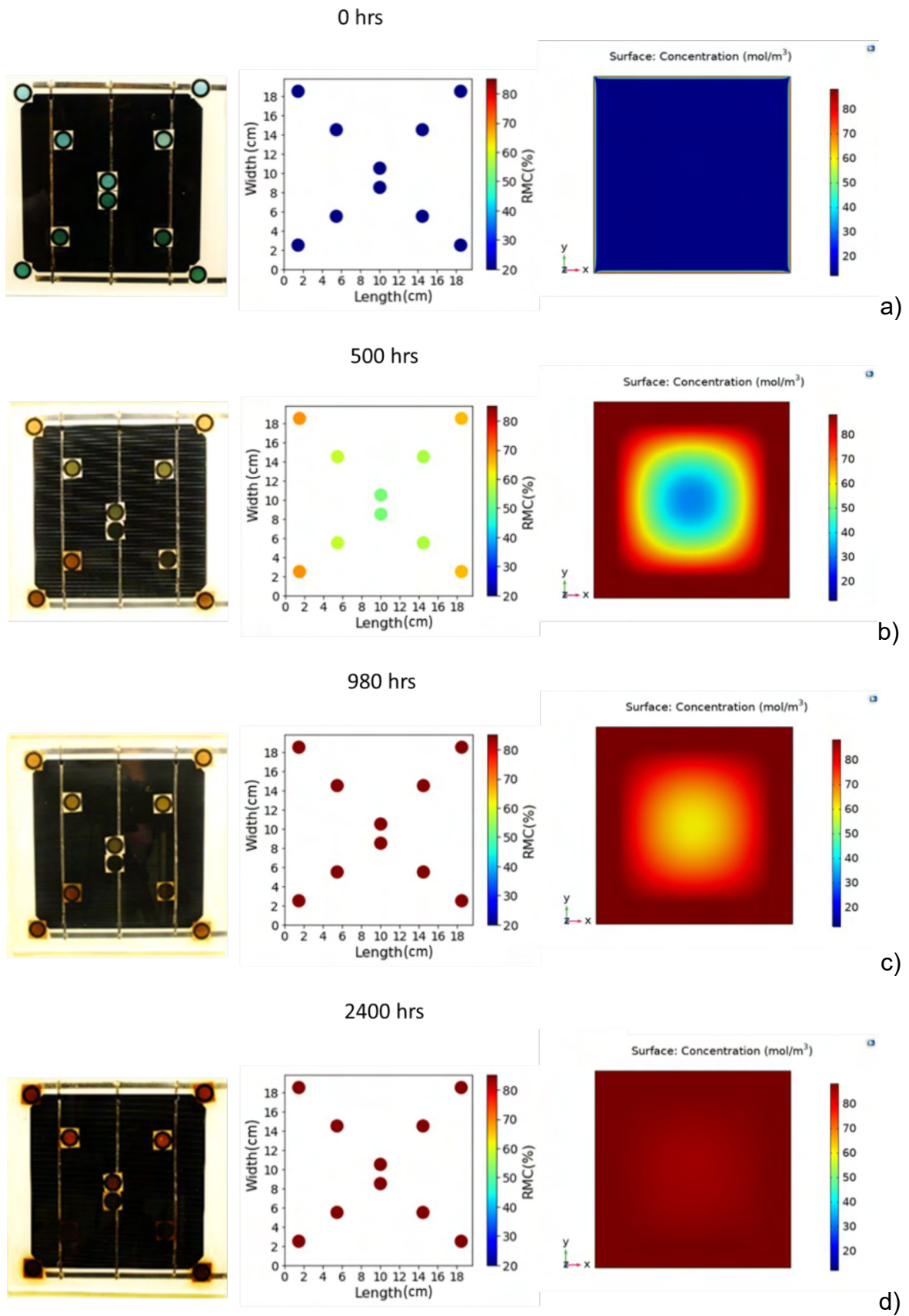


Figure 3-34 Comparison between the results observed with the humidity indicator cards and the moisture profiles obtained from the Comsol Multiphysics simulations, for a mini-module laminated with PET backsheet containing Al foil

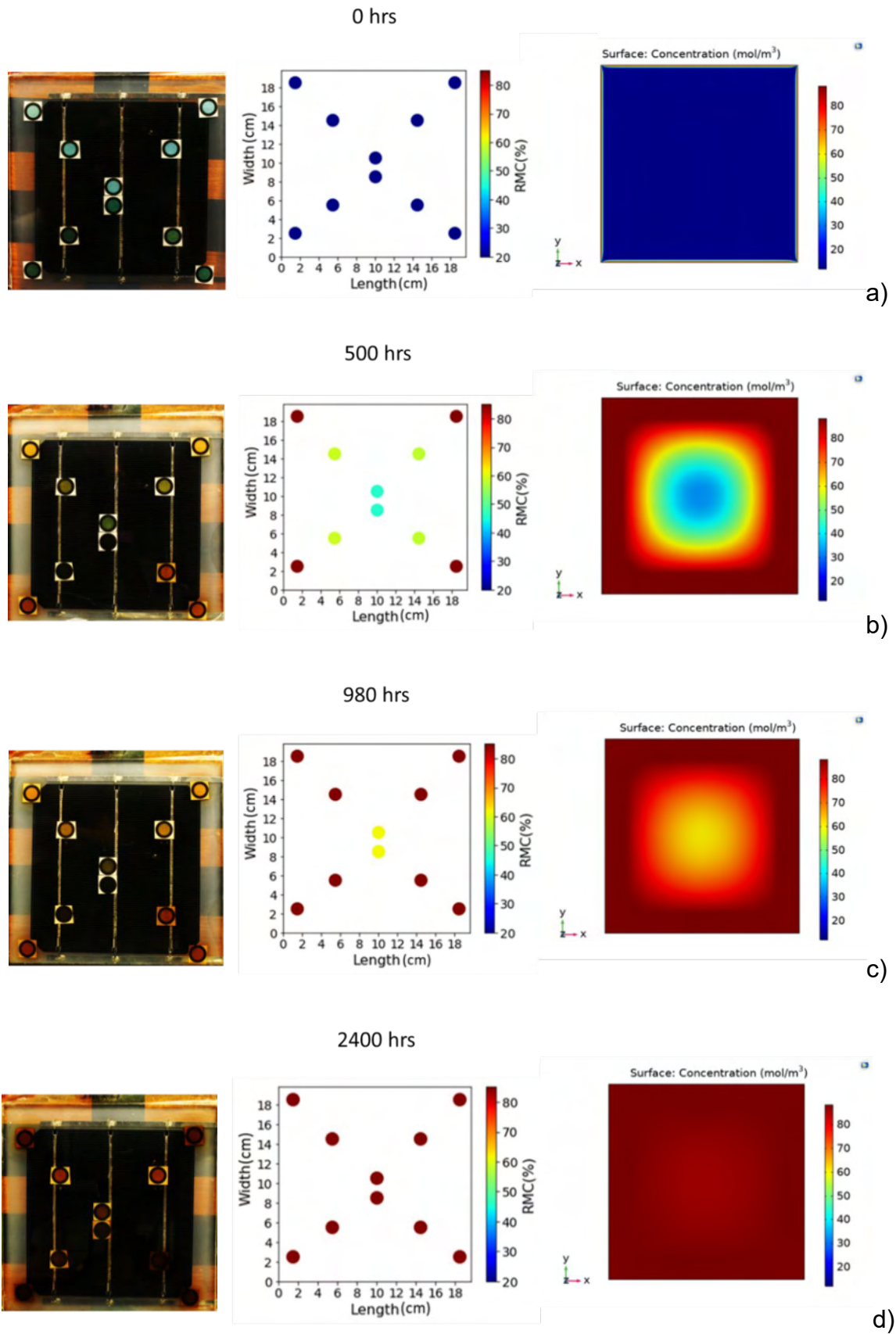


Figure 3-35 Comparison between the results observed with the humidity indicator cards and the moisture profiles obtained from the Comsol Multiphysics simulations, for a mini-module laminated with PET transparent backsheets.



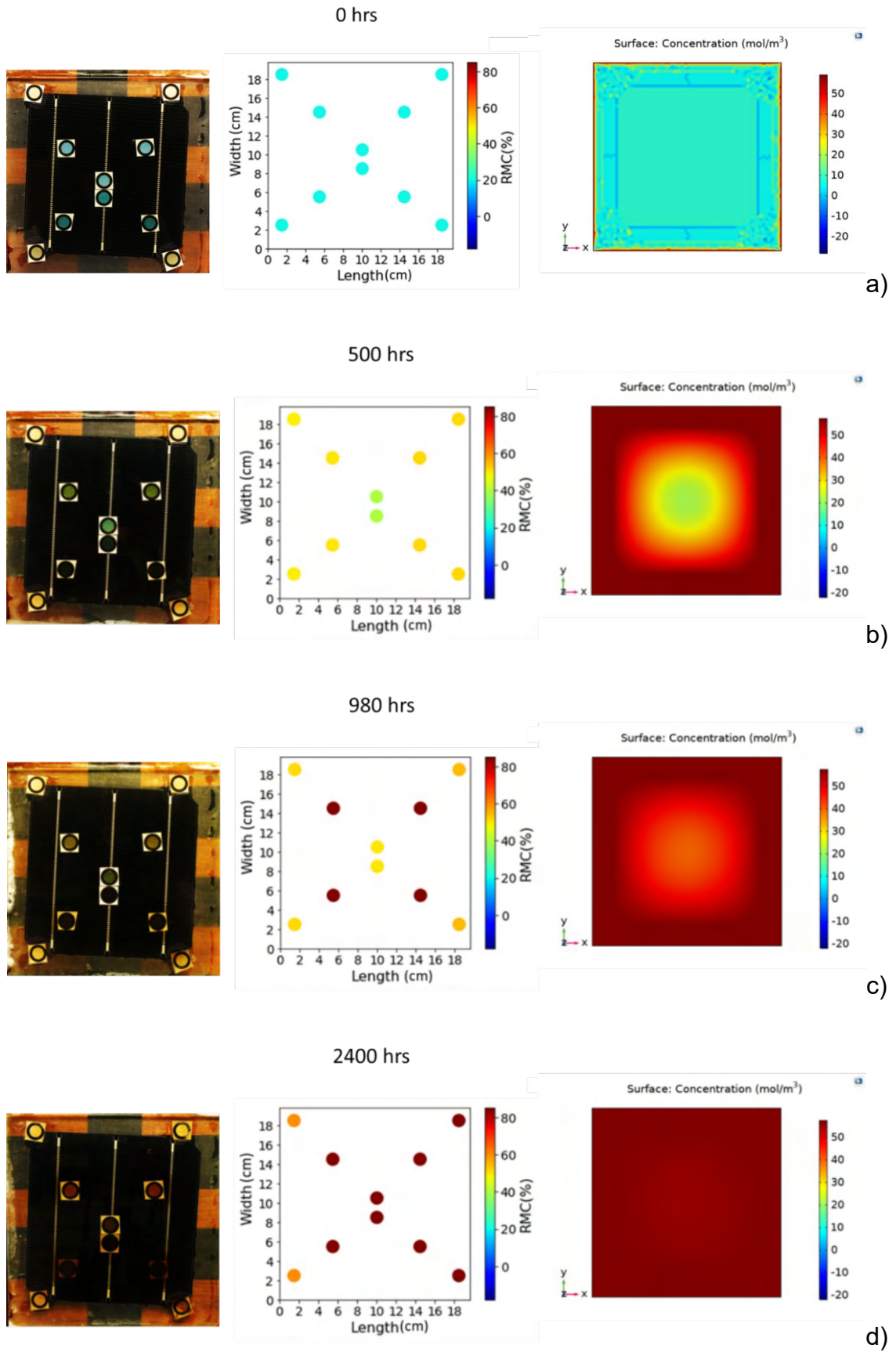


Figure 3-36 Comparison between the results observed with the humidity indicator cards and the moisture profiles obtained with the Comsol Multiphysics simulations, for a half-encapsulated cell.

### 3.9. Conclusions

The work presented in this chapter analysed the theoretical and experimental quantification of moisture absorbed by a PV module. To achieve this, different models and experimental methods were used.

To test the suitability of Fick's law for the representation of moisture ingress and egress into a glass-polymer structure similar to PV encapsulation, the model was fitted to relative moisture content data, measured by embedded digital humidity sensors. The results show that while the model describes the moisture diffusion to some extent, there are some deviations which indicate that either a modification of the model or a recalibration of the sensors according to the material they measure is needed.

For the identification of the absorption isotherm that the polymers follow, two theoretical models, Henry's law and Perrin and Favre model, were fitted against the moisture contents absorbed by different types of polymers at various combinations of environmental relative humidity and temperature. According to these results, the Perrin and Favre model provides the better description of the absorption isotherm of the materials commonly used in PV laminates. Moreover, the moisture content that the EVA absorbs has been shown to be affected by the addition of the backsheets, indicating that the solubility of water in the EVA and the interaction with the backsheets (moisture interaction or crosslinking degree of EVA impacted by the backsheets) should be considered carefully when selecting materials to use for PV encapsulation.

For quantification of the moisture accumulated between the front side of the PV cells and the EVA, an alternative method was developed involving encapsulation of humidity indicator cards. According to the experimental observations and the comparison to simulations, the method is potentially useful for measurement of the moisture content of the PV modules, considering that the calibration includes the interactions between the EVA and the backsheets. Moreover, the method may be more accurate when the encapsulant used is not EVA, which produces acetic acid and degrades the cards. Finally, as observed from both experiment and simulations, the value of the diffusion coefficient of the EVA is very important, as the time

demanded for saturation is mostly affected by it, and not the diffusion coefficient of the backsheet. This finding is valid for the studied types of samples, however, further research is required to extend the conclusion to a full-size PV module.

The knowledge gained in this chapter, regarding the insights of the moisture ingress within a PV module, will be used for the corrosion study included in Chapter 4.

# Chapter 4 Corrosion behaviour of different components in a PV module

## 4.1. Introduction

As shown in earlier chapters, visible corrosion and discolouration are the degradation mechanisms most observed for Ethylene Vinyl Acetate (EVA) encapsulated PV modules under real field operating conditions [35]. In addition, it is proposed that the reduction of power output from PV modules observed after DH aging is caused by corrosion [136]. Much work has been conducted towards understanding the link between the changes observed in the output during DH testing to the degradation observed in PV modules exposed to real aging conditions [137], [138], [139], [140], [141]. However, although some corrosion mechanisms are well understood, not all reactions and their impact on the power output are well established yet.

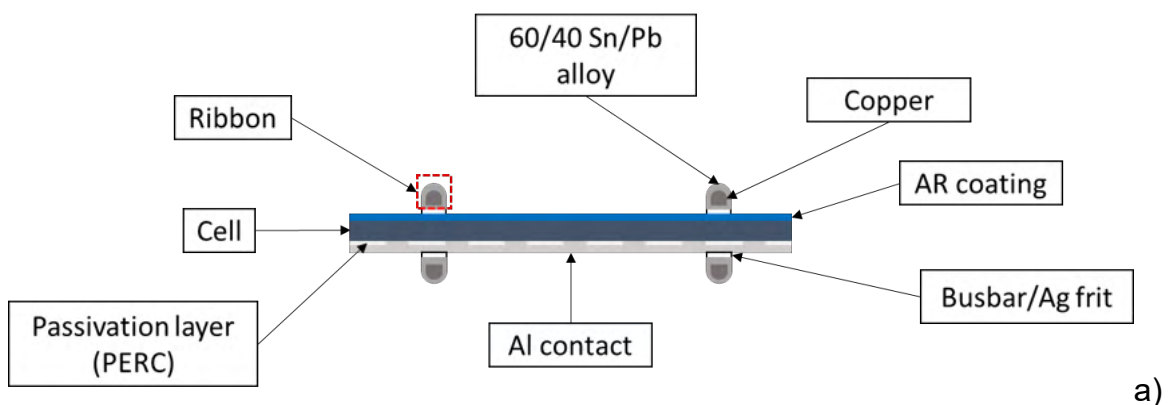
For modules that are encapsulated with EVA, acetic acid is generated as a product of the hydrolysis reaction when moisture is absorbed. The acetic acid which accumulates in the module may react with lead oxide that is contained in the glass frit of the silver front contact. This interaction can cause loss of adhesion at the interface between the contact metallisation and the cell surface [23]. Moreover, acetic acid and moisture may react with the lead and tin coating of the ribbon material used to connect cells to each other, causing their detachment from the front contact busbars [37]. Acetic acid and moisture may also attack the aluminium of the back contact, leading to embrittlement [21]. Although the mechanisms of metallisation and ribbon corrosion are already well understood (experiments conducted by acetic acid liquid and vapour exposure, or DH aging) [23], [37], [39], [142], there is less detail available about the reactions occurring in the case of aluminium back contact corrosion and the impact on the PV cell electrical

performance (previous tests have included acetic acid or moisture vapour exposure or DH aging) [21], [24], [143].

The work reported in this chapter contributes to the further understanding of these degradation mechanisms and their impacts on power output. The chapter begins with a review of the literature on the acetic acid corrosion mechanisms and then presents the results of a series of experiments designed to investigate in particular the effects of acetic acid corrosion on the PV cells.

## 4.2. Background review of corrosion reactions

This section presents the most frequent reactions that are described in the literature between acetic acid (produced during hydrolysis of EVA as described in Chapter 3) and the front contact metallisation, ribbons and aluminium back contact of c-Si or mc-Si PV cells (Figure 4-1).



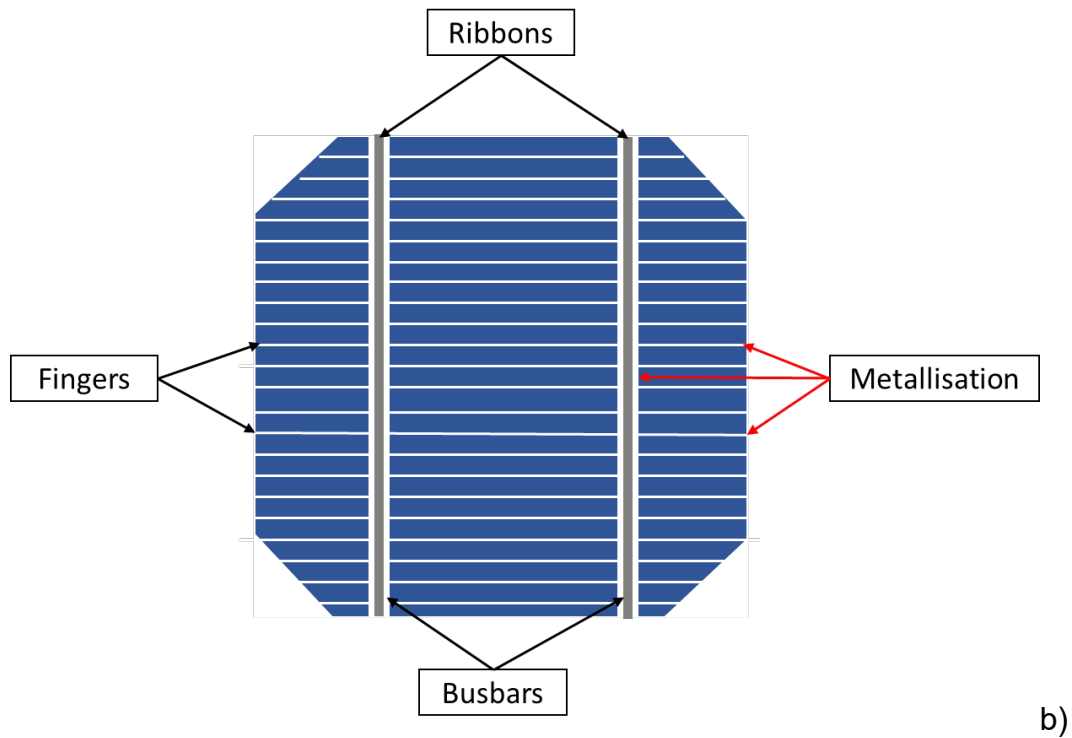


Figure 4-1 a) Cross-section and b) front side of a c-Si PV cell including metallisation (fingers and ribbons that make up the front contact).

#### 4.2.1. Silver front contact metallisation corrosion

The silver paste that is applied to form the busbars and fingers of the front contact includes silver (Ag) particles, glass frits, organic solvents, cellulose resin, inorganic additives and surfactants. The main compound of the glass frit is lead oxide (PbO), but an alternative material that can be used instead of lead is bismuth. According to Kraft et al. [23] the lead oxide reacts with locally produced acetic acid following the reaction below to produce lead acetate:



Lead acetate has a high solubility in water (221g/100g at 50°C [144]) and higher concentrations of acetic acid will dissolve greater quantities of lead oxide. This reaction is accelerated when an electric field is applied, as the lead ions are redeposited on the cell, reducing the concentration in solution and enabling more lead to be dissolved [23]. Because of the dissolution of the glass frit, voids are

formed at the interface of the metallisation and PV cell. This leads to an increase in the series resistance ( $R_s$ ) and a decrease in the short circuit current ( $I_{sc}$ ) [39].

#### 4.2.2. Cell interconnect ribbon corrosion

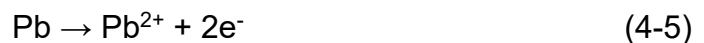
The core of the cell interconnect ribbons is copper (Cu), with a solder coating of an alloy of tin and lead, usually 60/40 Sn/Pb by weight although other compositions are used also. When the cell is in contact with acetic acid, Cu, Sn, Pb and Ag (from the contact) form six galvanic couples. Sn and Pb have the lowest values of oxidation potential, so will act as sacrificial metals as they react first according to the following reactions [24]:



Because of the dissolution of Sn and Pb, the whole surface of the solder corrodes, with the interface between the silver contact and the ribbon being separated [24]. The separation starts from the edges of the joint, as these are the areas first exposed to the acetic acid, and then extends towards the centre.

A similar degradation route is followed for corrosion of the cells in water, but the reaction rate is much slower. The reactions that occur for in this case are [24]:

Anode (60/40 Sn/Pb alloy):



Cathode:



### 4.2.3. Aluminium back contact corrosion

For water or acetic acid immersion, Ag, Cu, Sn, Pb and aluminium (Al) form ten galvanic couples. Al has the lowest value of oxidation potential and, as a result, it corrodes first. The reactions of Al with water are presented below [24]:

Anode (Al):



Cathode:



The corresponding reaction between Al and acetic acid is [24]:



The reaction of Al with water (when Al acts as a sacrificial metal) is more serious than with acetic acid, since in that reaction aluminium acetate is produced which inhibits further reaction [145]. When the aluminium back contact is exposed to liquid water, amorphous aluminium oxide is produced first, then it dissolves in the water and, finally, aluminium hydroxide precipitates [146]. Corrosion of the Al back contact can reduce electrical conductivity and increase series resistance of the PV cell [24].

### 4.2.4. Anti-reflection (AR) coating / passivation layer corrosion

To minimise surface recombination of carriers at the front side of c-Si or mc-Si PV cells, a passivation layer is applied (Figure 4-1). One of the most commonly used materials is SiO<sub>2</sub>. By elimination of the front side recombination, the open circuit voltage of the solar cells is increased [147]. However, the interface between SiO<sub>2</sub> and Si may degrade due to exposure to high levels of relative humidity and temperature, according to the following process [75]:

H<sub>2</sub>O is absorbed by SiO<sub>2</sub>

- i) H<sub>2</sub>O diffuses through the larger rings of Si-O-Si bridges



ii) OH and H passivate bonds with free radicals at the SiO<sub>2</sub>/Si interface

To avoid such a reaction, a SiN<sub>x</sub> protective coating, which acts also as an anti-reflective coating, may be applied, as it is an effective moisture barrier, in contrast with titanium dioxide which does not provide any moisture protection [11], [148]. SiN<sub>x</sub> can corrode in highly acidic environments, as reported in section 4.3, but is not a very likely process at the PV module level in normal operation.

### **4.3. Experimental Investigation of Corrosion in PV modules**

As described above, the presence of acetic acid can lead to a number of potential corrosion mechanisms. These were investigated through controlled experiments by immersion of PV cells and modules into water and acetic acid solutions of different concentrations. For the separation of the degradation caused by front and rear side corrosion and identification of the weakest interface, half encapsulated c-Si and mc-Si PV cells (with either front or rear side exposed) were prepared. The connection between material degradation and change in power output characteristics was examined and compared to material changes observed by optical and electron microscopy. For better understanding of the relevance of the degradation patterns observed with acetic acid immersion to those observed under DH exposure and for the investigation of the severity of the acetic acid impact on the PV module degradation, another set of fully and half encapsulated PV cells was aged under DH conditions. In addition, two different types of backsheet were used to examine the influence of varied moisture ingress on the PV module corrosion. The range of samples that were DH tested included PERC c-Si PV cells, which were the dominant cell types produced during 2019 [149]. Moreover, mini-modules from other projects, previously aged under the same DH conditions, were also characterised for comparison and additional evidence.

### **4.3.1. Acetic acid immersion trials**

#### **4.3.1.1. Materials and immersion configuration**

The experimental work was separated into two phases. For the first phase, half encapsulated cells were immersed in acetic acid solutions with concentrations of 50%, 30% and 10% v/v, with the front side of the cells exposed in the solutions (Figure 4-2). The cells used were commercially available c-Si cells with two busbars. A bare soldered PV cell was also tested as a trial sample. For the second phase, the cells were immersed in acetic acid solutions of concentration 30%, 10% and 0.3% v/v, and were constructed so that either the front side or the rear side was exposed to the acetic acid (Figure 4-3a and b). The cells were commercially available mc-Si cells with four busbars. Standard 2-mm-wide and 0.15-mm-thick Pb-Sn-Cu ribbons were soldered manually to the solar cells with a commercial standard flux. The higher acetic acid concentrations (50%, 30% and 10% v/v) were used initially for the more rapid investigation of the reactions and their dependence on concentration. In the second phase, testing in 0.3% v/v concentration acetic acid was used as close to observed levels in literature for PV modules tested in DH conditions [150]. The solutions were prepared using glacial acetic acid [151] that was mixed with deionised water (the experiment considering rear side immersion was repeated also with carbon filtered water, to ensure the repeatability of the results), with 300 ml volume of the solution, so that the cells were immersed 1 cm below the liquid surface when placed flat in the container. To maintain a constant pH and temperature of the solution, frequent measurements were carried out with a pH meter. The values of the pH of the solutions were  $1.7 \pm 0.2$ ,  $1.9 \pm 0.2$ ,  $2.3 \pm 0.2$  and  $3.4 \pm 0.2$  for concentrations of 50%, 30%, 10% and 0.3% respectively and the temperature of them all was  $19 \pm 1^\circ\text{C}$ . The samples were stored on a lab bench with a lid on each box. The exposure of the samples to light during storage was not controlled, but was at minimal levels (lab interior lighting). 18 samples were tested, two of each category.

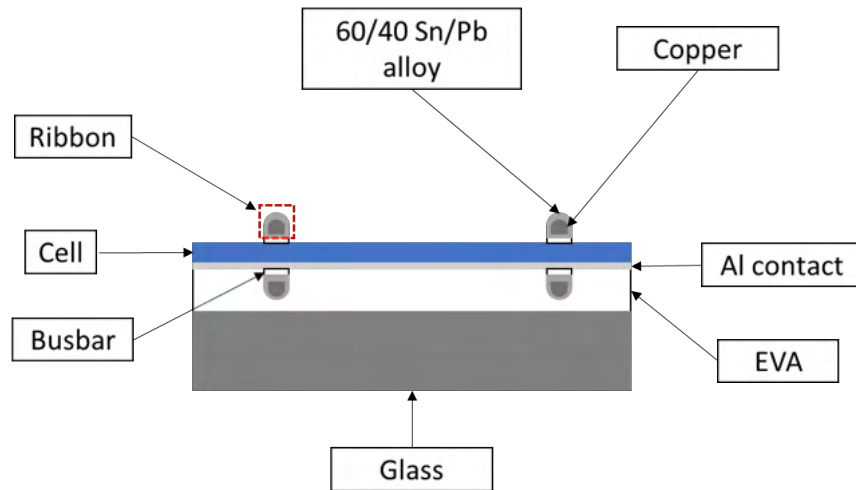


Figure 4-2 Half-encapsulated PV cells with two busbars used in the first phase of the experiments.

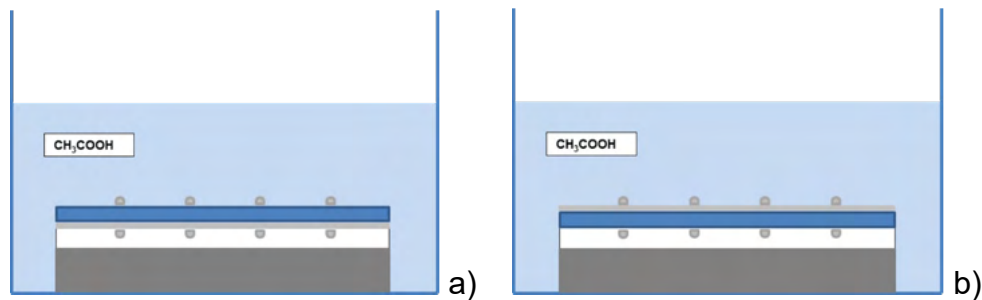


Figure 4-3 Half-encapsulated PV cells with four busbars used in the second phase of the experiments for a) front side exposure and b) back side exposure.

#### 4.3.1.2. Characterisation methods

The procedure followed for both phases of the experiments is described in Figure 4-4. All samples were measured every 1-3 days of immersion initially, with the later frequency of measurement varying depending on the degradation observed. After removal from the acetic acid and before characterisation, the samples were dried by covering with absorbent paper, which was changed when wet, until no moisture could be seen on the surface. All measurements were acquired sequentially, within the same day. The experiment stopped when the samples could no longer be measured, due to detachment of the ribbons, high series resistance because of Al contact degradation, or interconnection breakage.

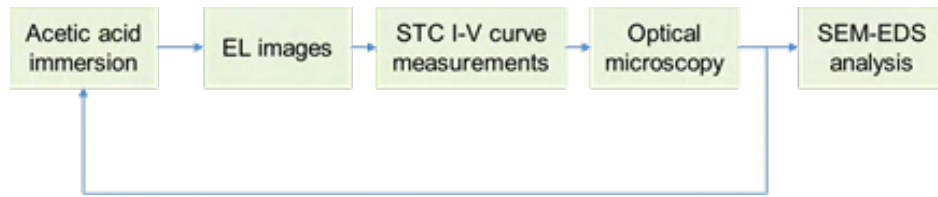


Figure 4-4 Flowchart demonstrating the procedure followed for both phases of the experiments.

To acquire an electroluminescence (EL) image, a forward bias is applied to the PV cell, at such a level that the external net-current is equal to the  $I_{sc}$  (in this case the  $I_{sc}$  current value was used, however, EL imaging can be conducted for different current levels). A CCD camera captures the radiative recombination of the minority carriers (infrared emission) in a dark room [152], [153]. This method is used for the detection of  $R_s$  increase (dark regions due to contact disruption) and shunting (localised dark regions due to non-radiative recombination at material defects and grain boundaries) [154], [155], [156]. If increased non-radiative recombination is extended to a larger surface of the cell, the recombination current increases, resulting in a decrease in  $V_{oc}$  (see the impact of the increased recombination of the carriers on the  $V_{oc}$  of an I-V curve in Chapter 2). Thus, EL imaging is appropriate for the detection of the voltage distribution over a PV cell. The relationship between the luminescence intensity and the local voltage is exponential according to the following equation:

$$\Phi(x) = C(x) \cdot \exp\left(\frac{V(x)}{V_T}\right), \quad \text{for } V(x) \gg V_T, \quad (4-10)$$

where  $C(x)$  is the local calibration factor, depending on the material and optical features of the module and camera used, and  $V_T$  is the thermal voltage [157].

The illuminated I-V curves of the PV cells were measured using a Pasan IIIb solar (flash) simulator under Standard Test Conditions (STC)<sup>10</sup>. This model simulator is class AAA as per IEC 60904-9 and operates by applying a voltage ramp to sweep the I-V curve while the PV cell is illuminated by the four Xenon flash tubes. The

<sup>10</sup> Temperature 25 °C, irradiance 1000 W/m<sup>2</sup> and air mass 1.5 (AM1.5).

irradiance is monitored with a calibrated PV cell, while the temperature is maintained by local lab air conditioning.

Optical microscopy images were collected using an Olympus CX41 microscope, with Infinity 2 camera, and the objective lens set to 10x in order to inspect any differences in the material surface as a result of the acetic acid immersion.

SEM-EDS (Scanning Electron Microscopy – Energy Dispersive Spectroscopy) analysis was undertaken in a Zeiss 1530VP system and used only on completion of the immersion trials for a particular sample for the final detection of material reactions and identification of compounds produced during acetic acid exposure. For the preparation of the SEM-EDS samples, the area of interest was cut (including the EVA and glass) with a diamond glass cutter from the full PV cell and attached to an aluminium pin stub, using an adhesive carbon tab. The acceleration voltage of the electron beam was 20 kV (as high as possible for the detection of elements so that the energy transition enables the emission of X-rays) in combination with high beam current (to achieve a higher number of electrons reaching the sample surface, thereby increasing the signal intensity).

#### **4.3.1.3. Results**

In Figure 4-5, an unencapsulated, soldered solar cell from the first phase of the experiments is shown that had been immersed in 50% acetic acid concentration for 37 hours. The significance of this sample is that the delamination at both interfaces of solar cell/silver contact and silver contact/ribbon, is evident, which confirms experimentally the expectations of corrosion-driven delamination of the front contact elements (see sections 4.2.1 and 4.2.2 for the respective theory). However, as the bare cell shows unrealistically extreme degradation, due to additional stress introduced by handling, the rest samples of phase 1 and 2 are further analysed.

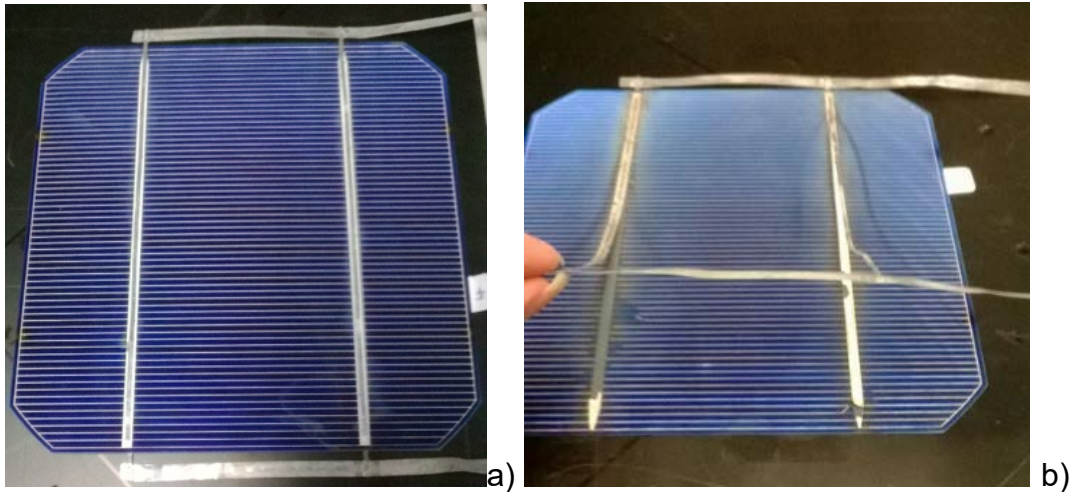
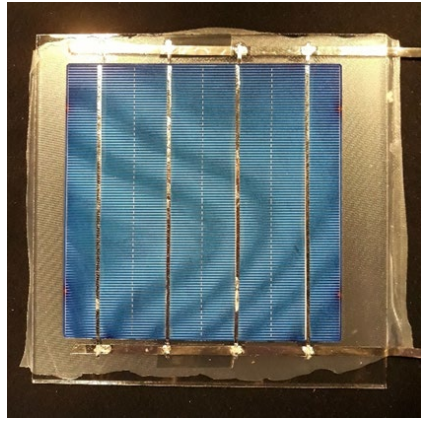
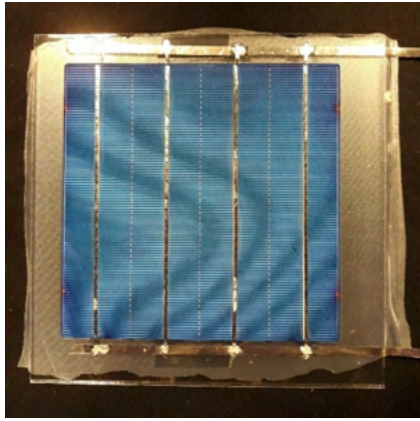


Figure 4-5 a) Unaged unencapsulated PV cell and b) delamination of ribbon/silver contact and silver contact/cell interfaces from an unencapsulated PV cell after acetic acid (50% HAc) immersion, for 37 hrs.

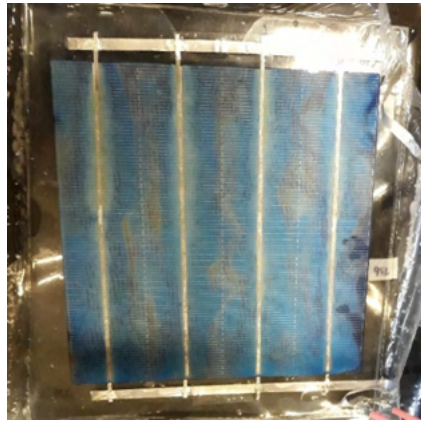
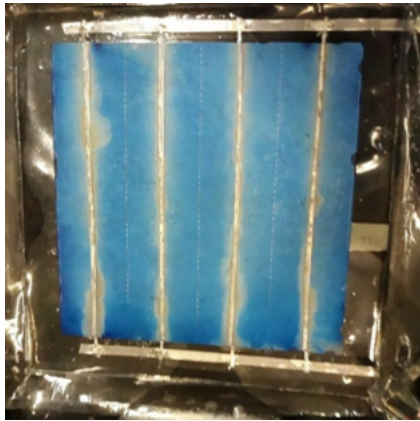
In the rest of the first and second phase experiments, samples with the front side exposed showed two types of pattern around the ribbons for higher and lower concentration acetic acid (HAc) immersion. A brown pattern appeared for the 50% and 30% concentrations, and when the cells were immersed in 10% concentration HAc, a white pattern was observed close to the ribbons (Figure 4-6). The origin of these patterns is further analysed by SEM-EDS analysis, presented later in this section.

When the aluminium (Al) contact (rear side) was exposed to HAc, the aluminium was observed to peel off for all concentrations of acetic acid (Figure 4-7), which confirms the theory on Al contact corrosion (section 4.2.3). Finally, when the cells were immersed in 0.3% concentration of HAc solution, after 2000 hrs of front-side exposure, breakage of the interconnections was noticed (Figure 4-8, the region indicated in the red ellipse).

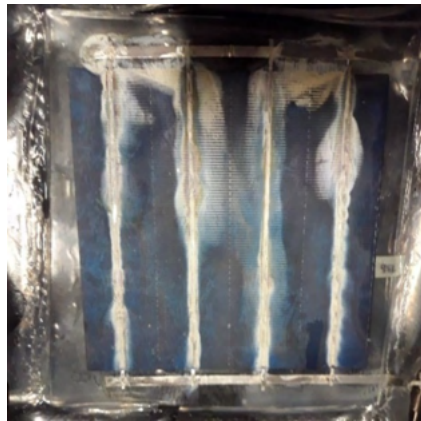
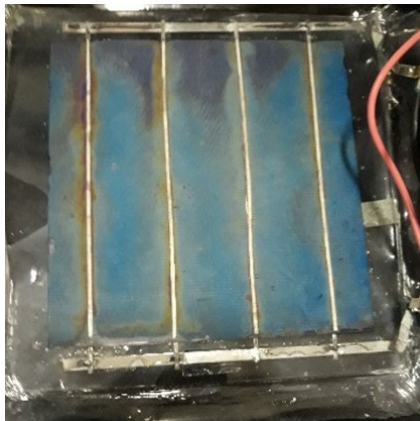




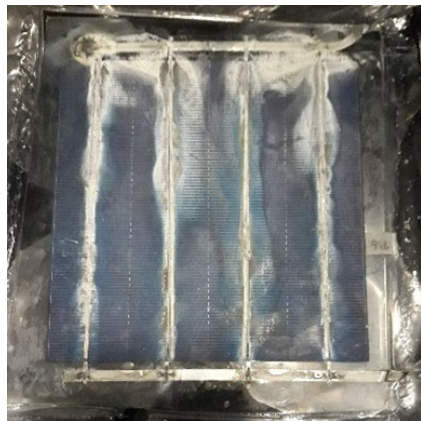
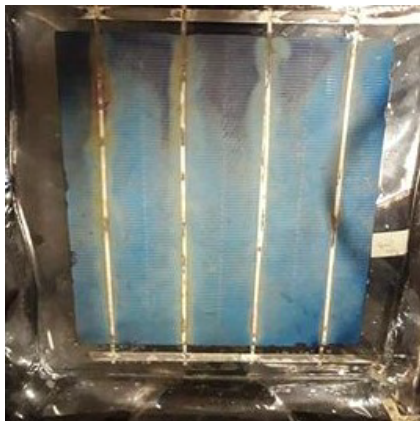
0 hrs



42 hrs



131 hrs



197 hrs

Figure 4-6 Cells immersed in 30% HAc solution (left) and 10% (right), for 0, 42, 131 and 197 hrs.

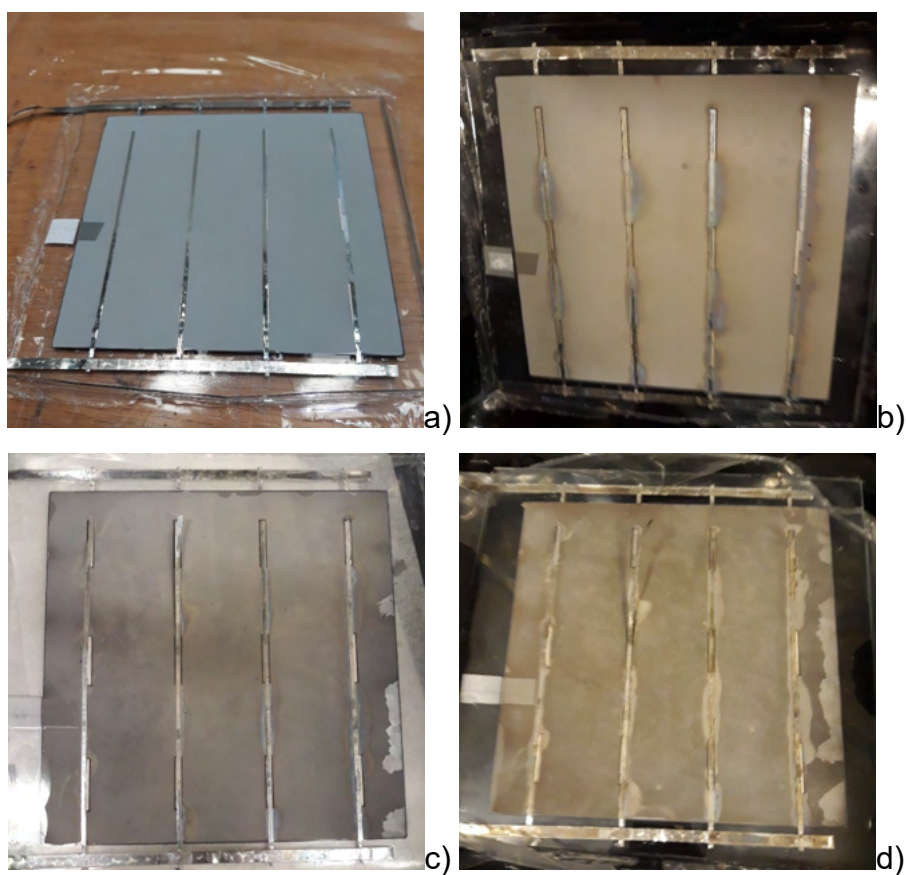


Figure 4-7 The Al back contact of a PV cell immersed in HAc solution of 0.3% concentration for a) 0 hrs, b) 46 hrs, c) 234 hrs and d) 378 hrs.



Figure 4-8 Breakage of the interconnection of a PV cell immersed into acetic acid solution of 0.3% concentration for 2000 hrs.



For the first phase of experiments, the illuminated I-V curves (Figure 4-9a) were obtained for the cells with front side exposure to 50%, 30% and 10% HAc. The open circuit voltage ( $V_{oc}$ ) did not vary for any of the cells within the 175 hours storage time. However, the maximum power ( $P_{max}$ ) degradation for the mentioned duration was about 6-7.5% for the PV cells immersed in 50% and 30% HAc. The main reason is Fill Factor (FF) and  $I_{sc}$  reduction. For the samples immersed in 10% concentration the FF did not change and  $P_{max}$  degraded by 4% which was  $I_{sc}$  driven. The reason responsible for this observation is analysed later in this section. For the second phase of experiments, the I-V curves of the mc-Si cells with the front side immersed in 30%, 10% and 0.3% HAc, are presented in Figure 4-9b. For the front side immersion, similar results to phase 1 were obtained for the reduction of  $P_{max}$ , FF and  $I_{sc}$ . The  $P_{max}$  degradation was observed to be around 8% for the cells immersed in 30% HAc, and 2% for the cells immersed in 10% HAc. The cells immersed in 0.3% HAc did not show any degradation for the first 2000 hrs of immersion, but sudden interconnect breakage was observed after 2000 hrs (Figure 4-9b).

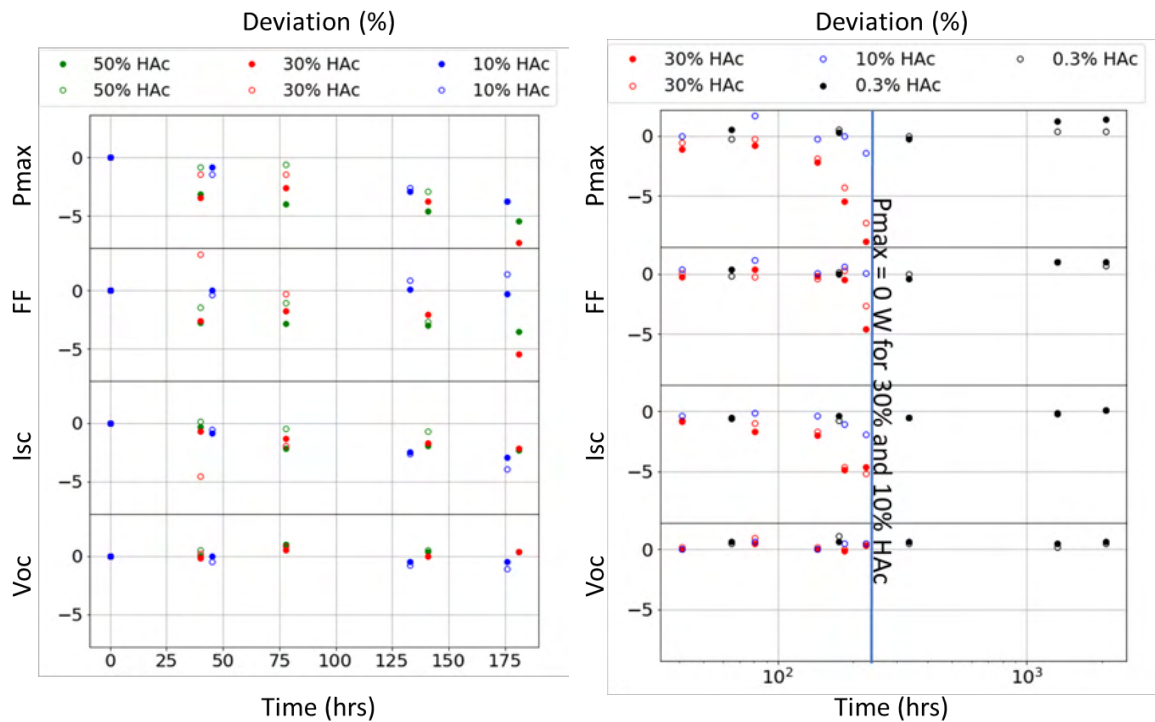


Figure 4-9 Percentage deviation of the I-V curve key parameters of the first (left) and second (right) phase PV cells for the exposed front side immersion.

For the rear side immersion (Figure 4-10), a faster degradation was observed for the cells in 0.3% HAc than the cells immersed in 30% and 10% HAc. The FF degradation was the main reason for  $P_{max}$  reduction, and the  $I_{sc}$  and  $V_{oc}$  did not change. All the cells showed a  $P_{max}$  degradation of around 25%, but the cells immersed in higher concentrations of HAc (30% and 10%) reached this value much later (900 hrs) than the cells immersed in 0.3% HAc (200 hrs). This occurs because of the protective layer of aluminium acetate that is formed when Al reacts with higher concentrations of acetic acid. These results demonstrate that the Al-back contact corrosion should have a bigger impact on the power output of the cells (-25%) than the front side corrosion (-8% at the worst case) if this occurs in the field.

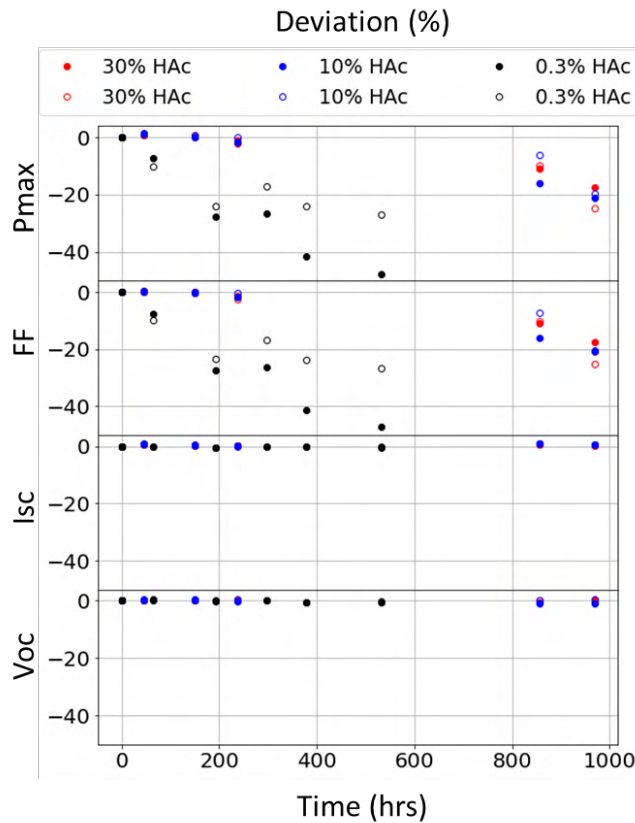


Figure 4-10 Percentage deviation of the diode model parameters of the mc-Si PV cells for the rear side immersion.

Both types of cell after immersion in HAc showed a similar behaviour in the EL images (Figure 4-11). Due to ribbon delamination (similar to this observed in Figure 4-5b), part of the current flow is concentrated at the points that remain attached to the cell (the rest of the current is not collected, as there is no contact for the current

to reach the metallisation and, eventually, the PV cell) and causes bright areas close to the busbars. In the EL images of mc-Si PV cells that had been immersed with the Al-back contact exposed to the acetic acid solution (Figure 4-12a and b) the low (0.3%) concentration caused darkening of the overall EL image of the PV cell, that is an indication of  $R_s$  increase. On the contrary, for the cells immersed in the higher concentration (30%) the specific darkening was not evident.

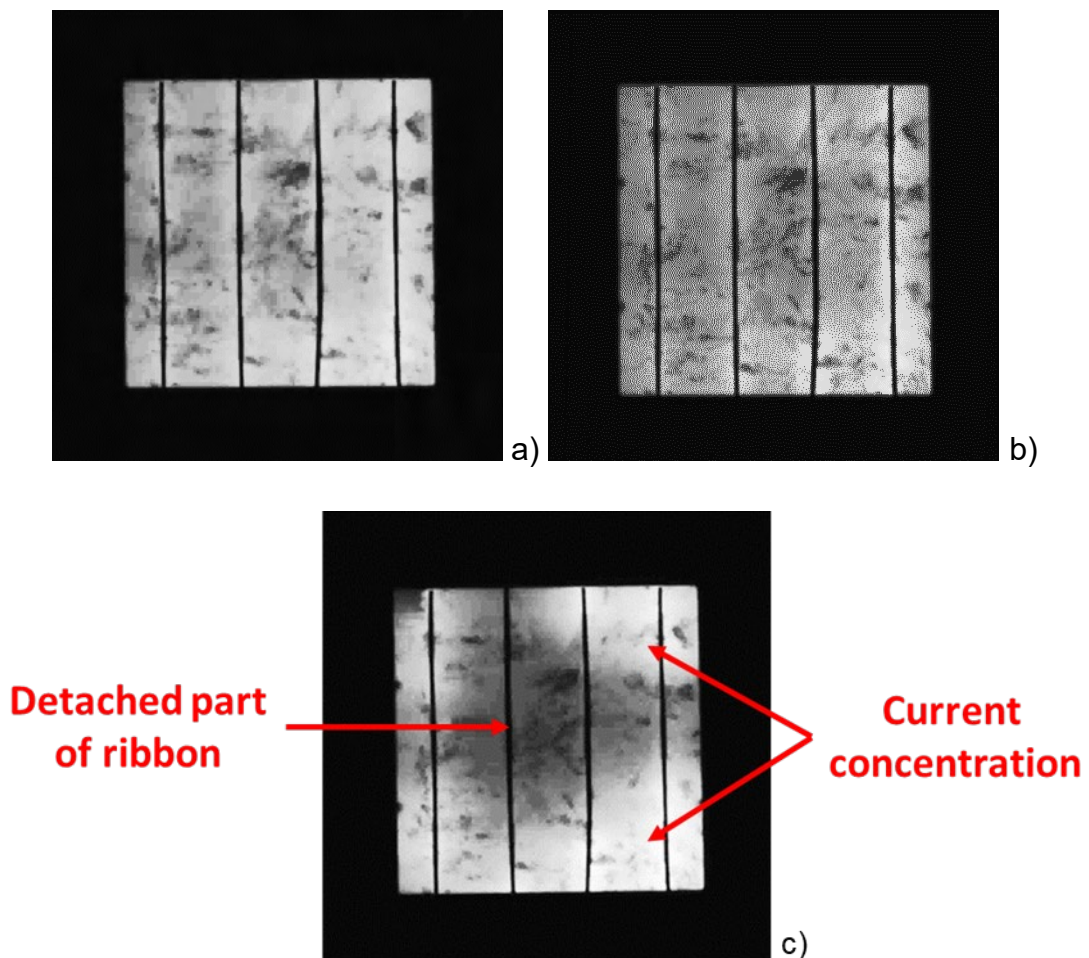


Figure 4-11 EL images of a front-side exposed mc-Si PV cell to 10% HAc for a) 0 hrs, 226 hrs and c) 290 hrs.

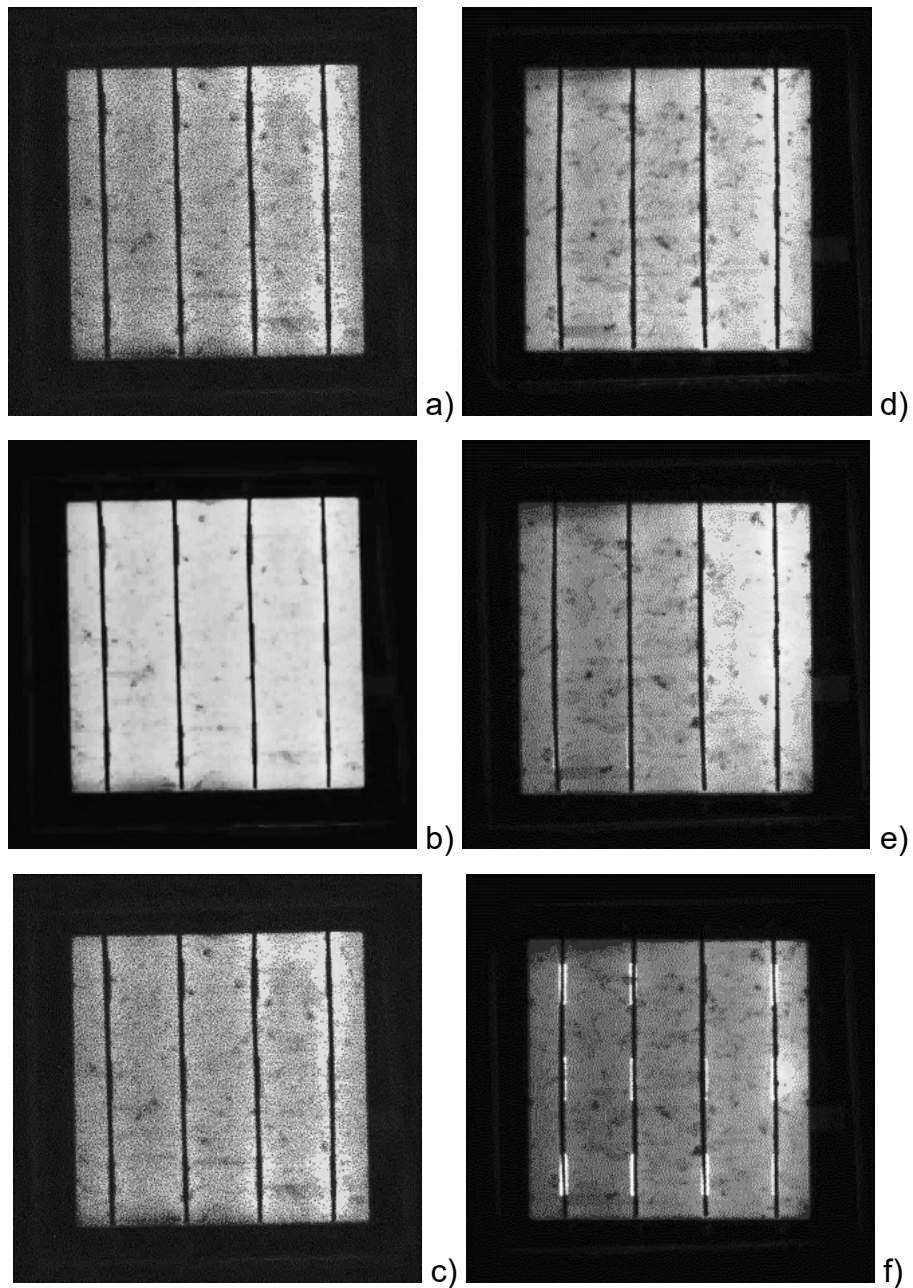


Figure 4-12 EL images of PV cells with the Al-back contact immersed in 30% HAc for a) 0 hrs, b) 86 hrs and c) 150 hrs (left) and immersed in 0.3% HAc for d) 0 hrs, e) 65 hrs and f) 150 hrs (right).

Figure 4-13 shows an optical microscopy image of a PV mc-Si cell front-side immersed in acetic acid solution of 30% concentration, for 226 hrs. The image shows brown patterns on the ribbon both around and on the metallization. The surface of the aged cell appears to have a brighter colour than the surface of the unaged cell, indicating that the antireflective coating is degraded. This is one of the main reasons for the  $I_{sc}$  decrease observed in the I-V curves presented previously in this section.



Figure 4-14 shows the same for a cell front-side immersed in 10% concentration of acetic acid for 290 hrs. In these images, white patterns are observed on the surface of the PV cell and fewer brown patterns are visible (see the SEM-EDS analysis later in this section for the origin of the identified patterns).

Figure 4-15 shows optical microscopy images of the aging of the Al-back contact of a PV cell, rear-side exposed to 10% HAc for 969 hrs. The aluminium seems to be significantly dissolved and some white and brown patterns are visible close to the ribbons, as a result of the secondary reaction of acetic acid with the ribbons.

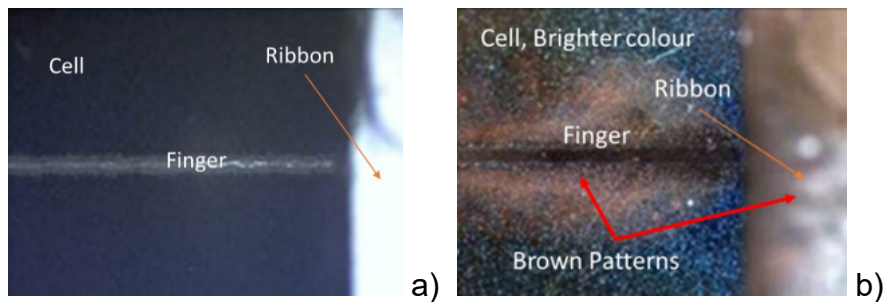


Figure 4-13 Optical microscopy of the metallization and the ribbon of a) an unaged and b) an aged cell in 30% HAc, for 226 hrs. After aging, the surface of the cell appears brighter and brown patterns are visible on the ribbon and finger.

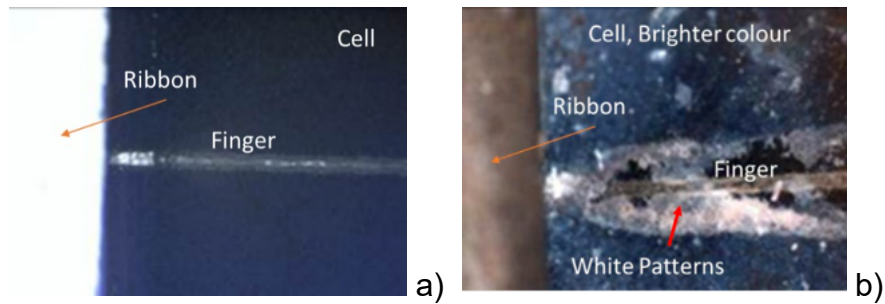


Figure 4-14 Optical microscopy of the metallization and the ribbon of a) an unaged and b) an aged cell in 10% HAc, for 290 hrs. Also in this case, after aging, the cell appears brighter and mostly white patterns appear around the finger.

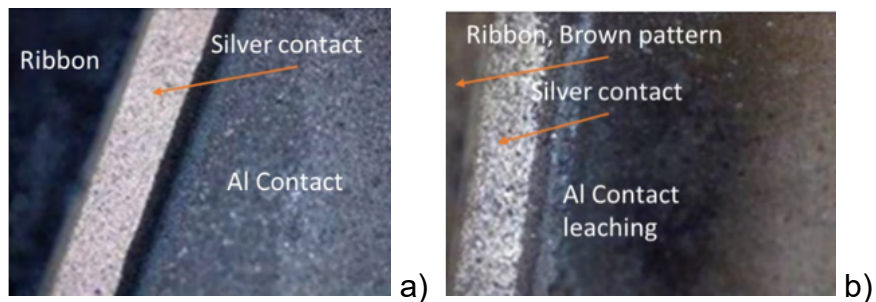


Figure 4-15 Optical microscopy of a) an unaged and b) an aged Al-back contact of a PV cell, rear-side exposed to 10% HAc for 969 hrs. After aging, the Al contact is visible and brown patterns appear on the ribbon.

Figure 4-16 shows the EDS (Energy Dispersive Spectroscopy) analysis of a silver contact of an unaged and unsoldered mc-Si cell, where the Ag and Pb from the glass frit are visible. In addition, the EDS analysis of a silver contact of an mc-Si cell that had been immersed in 30% HAc for 226 hours and of a mc-Si PV cell after aging in 10% HAc for 290 hours are illustrated. The transfer of the elements Pb and Sn, presumably as dissolved salts that precipitate out of solution, from the ribbons towards the silver contact and the cell surface can be observed when compared to the unaged cell, where Sn and Cu are not detected and the only Pb visible is this of the glass frit. The transfer of Cu is also noticed, as, after Pb and Sn dissolution, Cu is also exposed to the acetic acid. The regions in which Cu is detected are those of the brown patterns of the optical microscopy image in Figure 4-13. The white patterns observed in the optical microscopy image of the mc-Si PV cell after aging in 10% concentration of acetic acid for 290 hours are identified by EDS analysis of the same sample as areas of high Pb and Sn concentration. For lower concentration (10%) of HAc, Sn and Pb are the main elements visible, as they are etched first and there is not enough acetic acid to cause the severe dissolution of Cu that is observed for reaction with higher concentration of HAc.

The ribbons of the cells immersed in 30% and 10% HAc were found to detach after almost the same immersion duration, but the I-V curves of the cell immersed in 30% of acetic acid showed greater loss of performance due to more severe degradation of the core material (Cu) of the ribbons. The interface suffering the most severe corrosion is identified to be that between the solder and the busbar and secondarily between the busbar and the cell, as indicated in the EDS analysis (Figure 4-17) of the detached side of the ribbon that belongs to the sample shown in the right side of Figure 4-16. Only some Ag particles are observed, indicating minor silver paste detachment. Moreover, a part of the  $I_{sc}$  reduction that these cells show, is possibly caused due to the Pb and Sn salt precipitation on the cell surface.

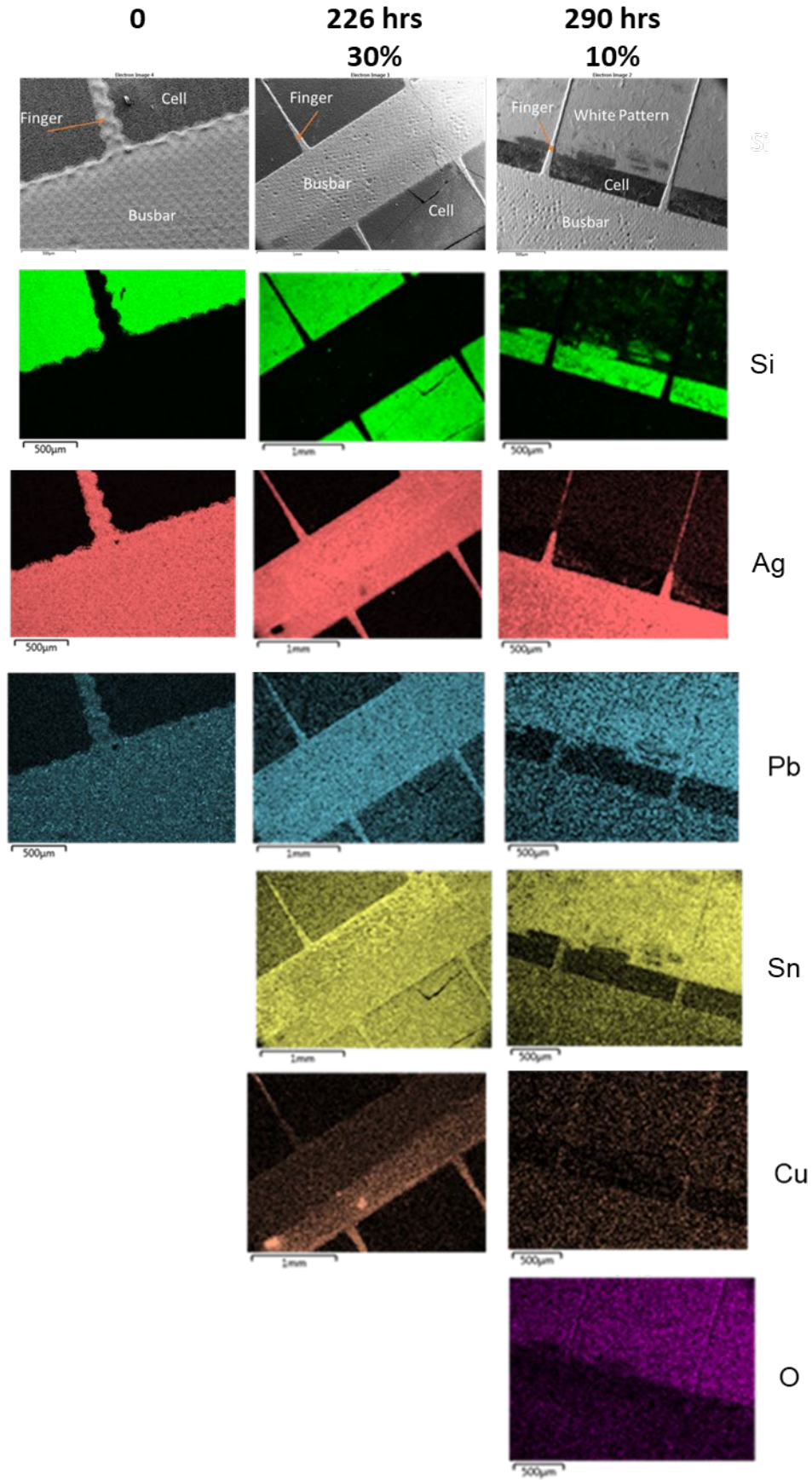


Figure 4-16 EDS analysis of the silver contact of an unaged and unsoldered PV cell (left), a mc-Si cell aged in 30% HAc for 226 hours (centre) and a mc-Si cell aged in 10% HAc for 290 hrs.

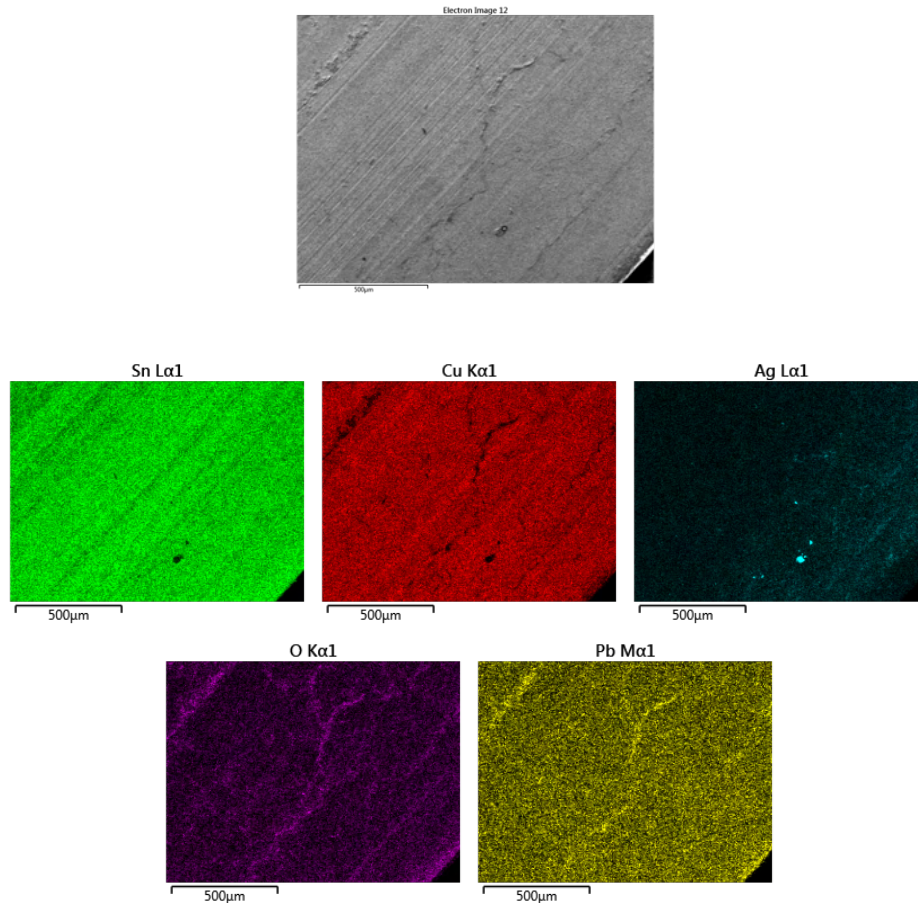


Figure 4-17 The detached side of the ribbon previously attached to the sample of Figure 4-20.

Figure 4-18 presents the EDS analysis of an unaged and an aged mc-Si cell with the Al-back contact exposed to 0.3% HAc solution for 531 hrs. By comparing the EDS analysis of the unaged cell to the aged one, and considering the optical microscopy image of the same cell (Figure 4-15), the dissolution and the oxidation of the Al-back contact is visible. The brown patterns observed in the optical microscopy image are correlated with the areas associated with Cu, while the white patterns are associated with Pb and Sn. Pb and Sn are detected due to secondary reaction of the remaining acetic acid with the ribbons.



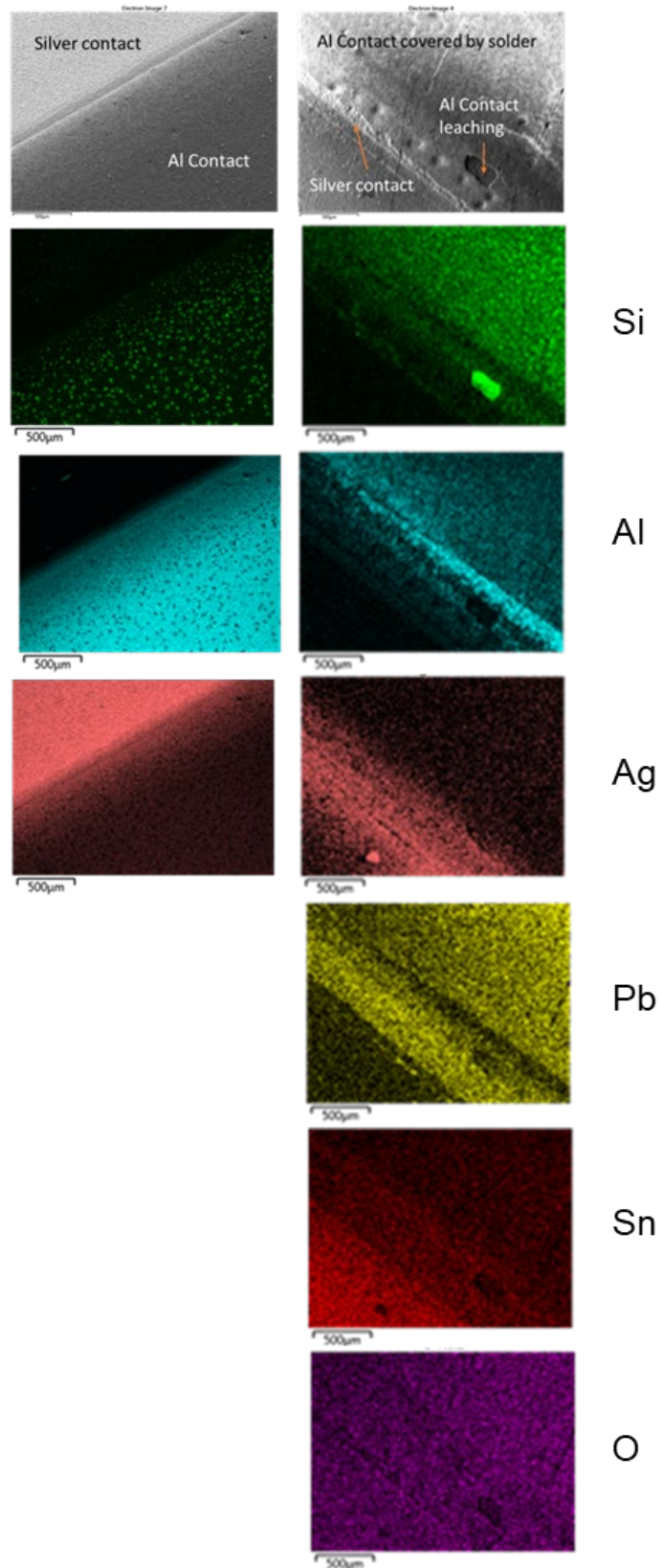


Figure 4-18 EDS analysis of the Al-back contact of an unaged mc-Si cell (left) and a mc-Si cell immersed in 0.3% HAc, with the rear side exposed, for 531 hrs (right).

### 4.3.2. Water immersion

The identification of the reactions occurring in the absence of HAc is very important for the evaluation of the impact of the acidic environment on the degradation of the PV cells. For the water immersion experiments, half encapsulated c-Si PV cells with two busbars were immersed in 300 ml of deionised water, 1 cm below the water surface with the front side exposed. The structure of the samples was the same as that presented in section 4.3.1.1, and their temperature was maintained at  $19\pm 1^\circ\text{C}$  during immersion.

Figure 4-19a shows an aged PV cell after 4973 hrs of front-side immersion in water. The white patterns that are noticeable on the surface of the cell are an indication of the dissolution of Pb and Sn and their redeposition as salts. Brown patterns that would be expected if Cu dissolution had taken place are not observed, so the ribbons are therefore not thought to be severely corroded.

In Figure 4-19b the variation of the diode model parameters of a PV cell immersed in water is presented. A degradation of the  $I_{sc}$ , which recovers after 2426 hrs, is observed, caused probably by redeposition of Pb and Sn dissolved in the solution. Water is seen to cause much less degradation as the samples survived more than 4973 hrs of immersion (verifying the theory of section 4.2.2), in contrast to the samples immersed in 0.3% HAc, that survived for only 2000 hrs.

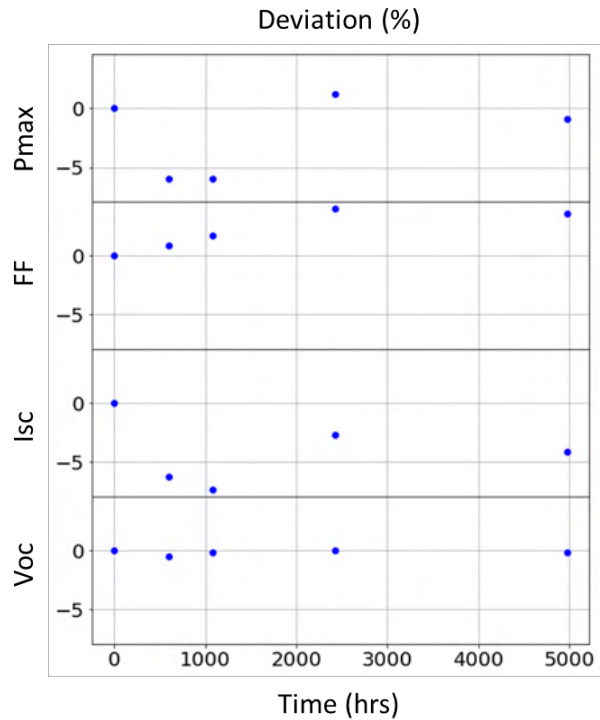
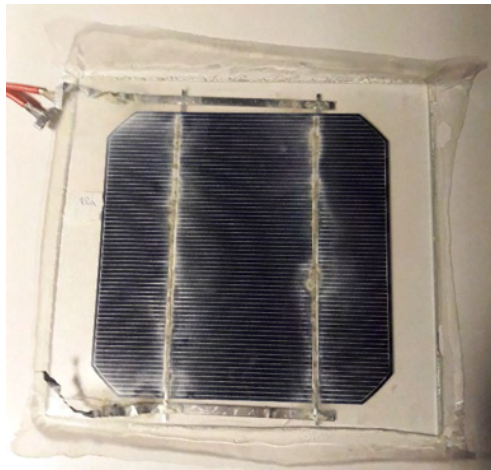


Figure 4-19 a) Aged PV cell after 4973 hrs of immersion in water. b) Variation of the performance parameters of a PV cell immersed in water.

### 4.3.3. DH test of single cell mini modules

#### 4.3.3.1. Sample preparation, DH aging methods and characterisation

For comparison of the reactions identified above for the acetic acid and water immersion to those observed on fully encapsulated PV modules aged under high levels of temperature and relative humidity, a damp heat test was conducted. Four types of samples were exposed in a humidity chamber. The first two types had structure: glass – EVA – cell – EVA – PET backsheet (Figure 4-20). The PET+Al samples contained a white PET backsheet of multiple layers with aluminium foil (Figure 4-21a), while the PET\_Tr samples were laminated with a single transparent PET layer (Figure 4-21b). The other two types of samples were half encapsulated PV cells, with the front (HEFront) or the rear side (HERear) exposed, as previously described in section 4.3.1.1. The two different types of backsheet were chosen in order to study the impact of different moisture diffusion on the corrosion of the

different components. The exposure of the half – encapsulated PV cells was used for the investigation of the relevance of the rear contact corrosion and the examination of the acetic acid influence on the front side corrosion. The humidity indicator cards described in Chapter 3 were also embedded within some additional samples (see 3.6.3) for quantification of the moisture accumulated on the front side of the PV modules during the trials.

The modules contained c-Si PERC PV cells with three busbars. Standard 2-mm-wide and 0.15-mm-thick Pb-Sn-Cu ribbons were soldered manually on the PV cells with a commercial standard flux. The conditions of the chamber for exposure were 85% relative humidity (RH) and 85°C. Two rounds of experiments were conducted to check repeatability of the results. The samples of the first round were aged in a Thermatron SM-32 chamber up to 974 hours of exposure and then moved to a Sanyo Gallenkamp HCC065.PF4 chamber for the rest of the experiment duration. The second round took place exclusively in the Sanyo Gallenkamp HCC065.PF4 chamber. The samples examined in this section and the rounds of experiments are summarised in Table 4-1.

Table 4-1 The type of samples and the respective testing rounds of DH exposure.

Name	Round	Chamber(s)
PET+Al_ref	Reference*	-
PET_Tr_ref	Reference**	-
HEFront_ref	Reference***	-
PET+Al_1	1	Thermatron / Sanyo
PET+Al_3	1	Thermatron / Sanyo
PET_Tr_1	1	Thermatron / Sanyo
PET_Tr_2	1	Thermatron / Sanyo
HERear_1	1	Thermatron / Sanyo
HERear_3	1	Thermatron / Sanyo
PET+Al_4	2	Sanyo
PET+Al_5	2	Sanyo
PET_Tr_4	2	Sanyo
PET_Tr_5	2	Sanyo
HEFront_4	2	Sanyo
HEFront_5	2	Sanyo

\*Bref was a single cell mini-module containing PET backsheet with Al foil.

\*\*Tref was a single cell mini-module containing transparent PET backsheet.

\*\*\*The HEFref sample was used only as a reference sample for the SR characterisation.

The samples were removed from the chamber regularly for characterisation using I-V curve measurements for the electrical performance and EL images to detect locations within the modules with increased series resistance. Furthermore, spectral response (SR) measurements were acquired for some of the samples, in order to cross-check the findings of the other two characterisation methods.

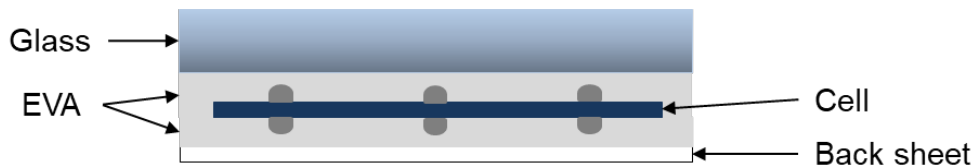


Figure 4-20 The structure of the fully encapsulated PV modules (Type 1 and 2) aged under DH conditions.

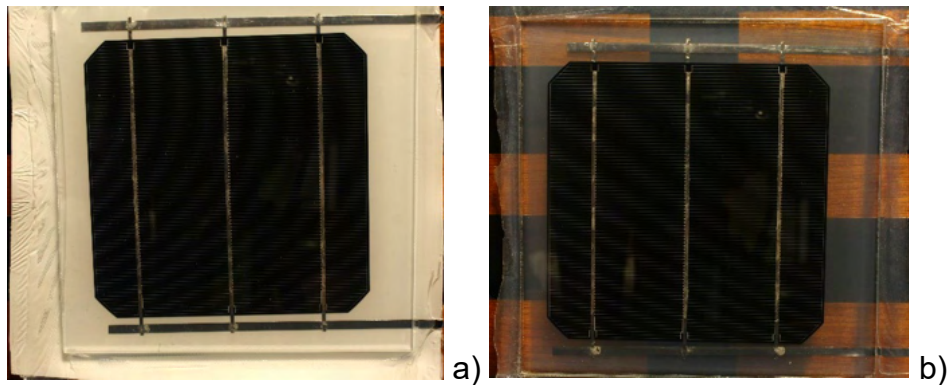


Figure 4-21 Fully encapsulated PV modules with a) white PET backsheet of multiple layers with aluminium foil (Type 1) and b) single transparent PET layer backsheet (Type 2).

Spectral Response (SR) of a PV cell is defined as the ratio of the current produced by the cell to the incident radiation, as a function of wavelength [158], [159]. Changes in carrier recombination or diffusion length within a PV cell affect the SR accordingly. More specifically, variances corresponding to short wavelengths (blue) are affected by front side recombination, while changes observed for the long wavelengths (red – near infrared) reveal the impact of the rear surface recombination. Overall decrease of the signal indicates a low diffusion length and reduced photon collection [160], [161].

For the identification of potential changes in the surface (front or rear) recombination of the PV cells, unaged and fully aged samples were subjected to SR measurements. The samples were placed into a dark chamber at a temperature of  $25 \pm 0.03$  °C. A mask was used, made of black anodised aluminium foil, for the measurement of a defined specific area, equal to  $400 \text{ mm}^2$ , at the centre of the PV cells (Figure 4-22a). To prevent disruption of the measurements due to light reflection from the glass of the fully encapsulated cells, the edges of the mini-modules were covered with fabric (Figure 4-22b). The samples were constantly illuminated by LEDs at an intensity of 1 sun and simultaneously illuminated by chopper-modulated monochromatic light generated by a two-lamp and filter cassette system, to probe over different wavelengths. The lamps used were Xenon (higher intensity at “blue” wavelengths), for the measurements up to 725 nm, and halogen for the longer wavelengths (higher intensity at “red-infrared” wavelengths). The bias dependence of the module was kept to 0 by a Keithley Instruments source-measure unit. The current produced by the modulated monochromatic light was measured by lock-in amplifiers, which separate the current generated due to the constant LED illumination from that produced by the monochromatic light. The irradiance for each wavelength was calculated from a calibration step, which included measurement of a cell with a known spectral response. Three measurements were recorded for each wavelength to reduce uncertainty.

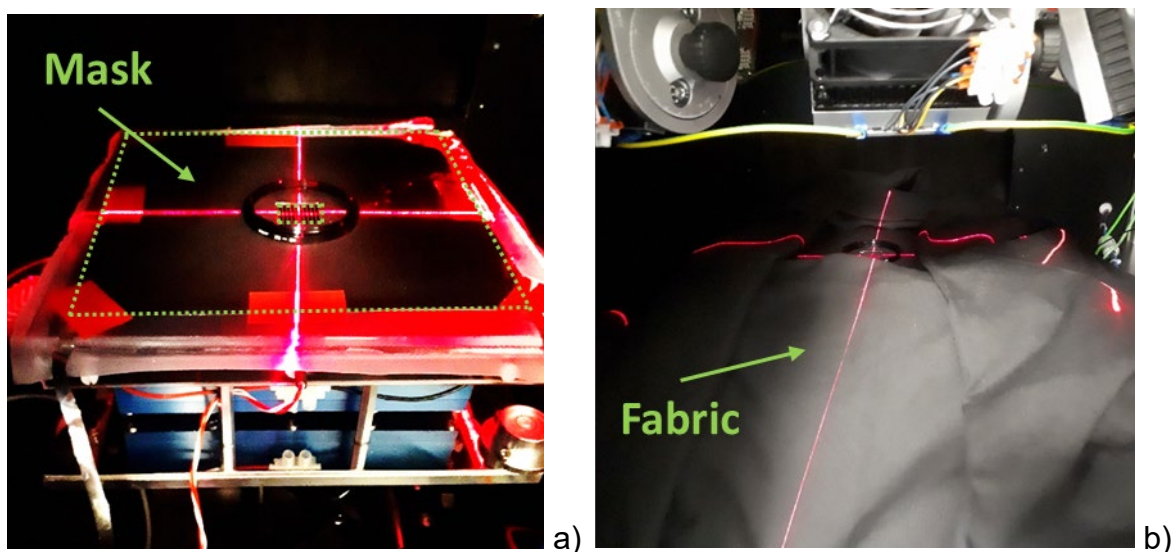


Figure 4-22 SR measurement configuration with the addition of a) mask and b) fabric.

To quantify the impact of corrosion on the electrical performance, estimation of the  $R_s$  evolution is very important. In this chapter, the estimation method proposed by Bowden and Rohatgi [162] is used. According to this method, I-V curves of the mini-modules must be recorded at two different intensities of irradiance, 1000 W/m<sup>2</sup> and 100 W/m<sup>2</sup>. The  $R_s$  is then calculated by the following relationship:

$$R_s = \frac{V_{OC,low\ irr.} - V_A}{I_{SC,high\ irr.} - I_{SC,low\ irr.}} \quad (4-11)$$

where,  $V_{OC,low\ irr.}$  is the open circuit voltage of the I-V curve received at an irradiance of 100 W/m<sup>2</sup>,  $I_{SC,high\ irr.}$  is the short circuit current of the I-V curve of irradiance at 1000 W/m<sup>2</sup> and  $I_{SC,low\ irr.}$  is the respective short circuit current at 100 W/m<sup>2</sup>.  $V_A$  is the voltage that corresponds to the current value equal to  $I_{SC,high\ irr.} - I_{SC,low\ irr.}$ , which is estimated by linear interpolation (see Appendix 3) of the points of the I-V curve measured at 1000 W/m<sup>2</sup> (Figure 4-23). By assuming that at 100 W/m<sup>2</sup> the I-V curve received is almost equivalent to the dark I-V curve, which does not include the  $R_s$ , the described methodology estimates the  $R_s$  by calculating the slope of the light I-V curve relative to the slope of the dark I-V curve, on the side of the  $V_{OC}$ . This method is preferred because the  $R_s$  is extracted accurately without fitting of the I-V curve, where more parameters are extracted at the same time. For each  $R_s$  calculation, three I-V curves for each irradiance were recorded and three values of  $R_s$  were estimated, the average of which yields the final  $R_s$  value. The error of the calculated values is insignificant, due to the high accuracy of the I-V curve measurements.



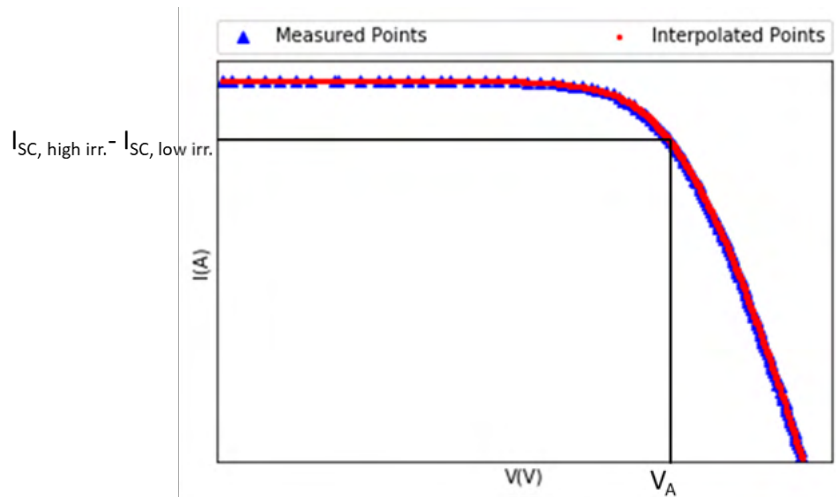


Figure 4-23 Interpolation of the I-V curve points and estimation of  $V_A$ .

#### 4.3.3.2. Results

In Figure 4-24a the evolution of the electrical parameters of the half – encapsulated PV cells, with the rear side exposed to DH conditions, is visible. The  $P_{max}$  was degraded by 9.3% after 3023 hrs of exposure. The  $I_{sc}$  seems to not contribute to the maximum power output degradation, with  $V_{oc}$  and FF being the main reason for the degradation. The  $V_{oc}$  dropped by 2.1%, with the more severe degradation starting after ~2000 hrs of exposure. The FF was reduced by 6.7%, with  $R_s$  increase playing a significant role, as it rises initially by 25.2% and then remains constant until reaching 4000 hrs of exposure, where it then slightly decreases. The reason for this is the instant oxidation of aluminium (Figure 4-25a), caused by the moisture that accumulates within crevices or cavities of the Aluminium contact, which was previously observed on the half-encapsulated rear side exposed PV cells to HAC immersion in section 4.3.1.3. The degradation due to  $R_s$  increase and  $V_{oc}$  decrease is also visible in the EL images, as sharp dark spots initially and general darkening of the cell, respectively (Figure 4-26).

Figure 4-24b shows degradation of the electrical parameters of half encapsulated PV cells, with their front side exposed. The  $P_{max}$  was observed to drop by 6.7% and 2.6% for HEF4 and HEF5 samples respectively, after 2948 hrs of aging, driven by  $V_{oc}$  and FF degradation. The degradation observed is lower than this obtained for



the half-encapsulated rear side exposed PV cells. For sample HEF4 that showed more significant degradation, the  $V_{OC}$  decreased by 2.3% and the FF was reduced by 3.6%. The  $R_s$  seems to contribute to the FF reduction, as it is increased by 7%, a lower rise than this observed for the half-encapsulated rear side exposed PV cells. The region causing the  $R_s$  increase is visible on the bottom of the EL image (Figure 4-27), which is associated, by visual inspection, to cell whitening of areas and scattered spots, due to finger corrosion (Figure 4-25b).

In Figure 4-24c the degradation of the electrical parameters observed for mini-modules containing PET backsheet with Al foil is demonstrated. The average maximum power output degradation was 5.6% for the first round of experiments after 3023 hrs of aging, while for the second round, a drop of 5.9% of maximum power was seen after 2948 hrs of exposure. The short circuit current, open circuit voltage and FF seemed to affect the maximum power output degradation similarly for the respective amounts of time. The short circuit current is measured to be reduced by 2.7% and 2.2% for the first and second round, respectively, due to the gradual loss of the light reflection gain from the inner side of the backsheet, because of backsheet and encapsulant yellowing (Figure 4-24e). The open circuit voltage calculations show a drop of 1% for round 1 and 2.1% for round 2. The FF factor showed a degradation between 1.1% and 3.8% for the same exposure times, with the highest value observed for a PV module that developed a crack under the busbar (sample PET+Al\_3). The FF factor degradation is not affected by series resistance increase, as series resistance did not show any variance, except for the value obtained for the PV module with the crack.

Figure 4-24d represents the evolution of the electrical parameters of PV modules encapsulated with the transparent PET backsheet. The maximum power degradation is estimated to be 3.2% for the specimens of the first round of experiments and 3.7% for those of the second round, after 3023 hrs and 1967 hrs respectively. The samples of the first round need ~1000 hrs more to reach similar degradation level compared to the samples of the second round. The degradation of these samples is mainly affected by the  $V_{OC}$  and FF reduction, while  $I_{sc}$  variance plays a minor role. The samples of the first round show a  $V_{OC}$  drop of 1.6% while, for those of the second round, the reduction is equal to 1% for the mentioned amounts of time. Differences on the  $V_{OC}$  degradation between the two different

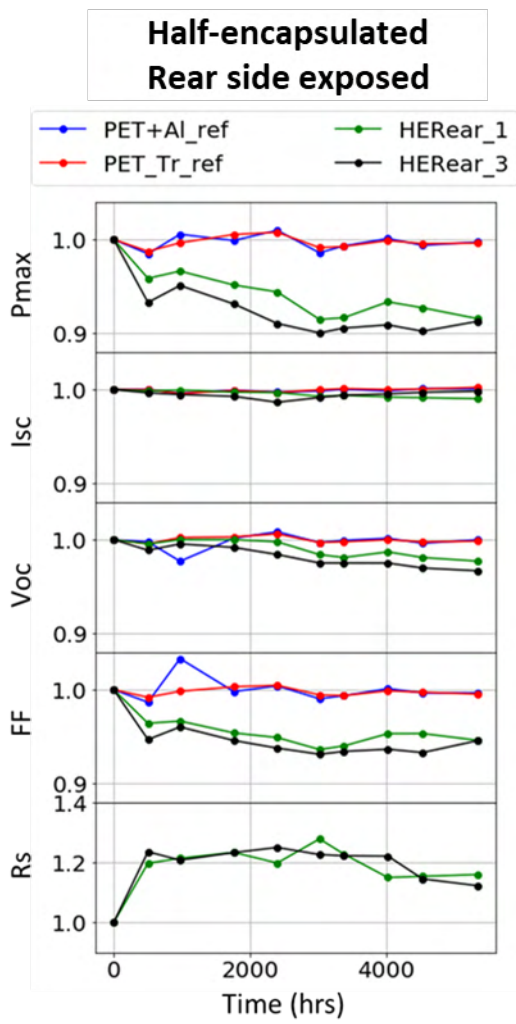
rounds may be caused by variances between the two chambers (although the conditions set were the same, differences between the actual values might occur), while  $V_{OC}$  differences between the two different types of mini-modules may be attributed to varied thermal properties of the backsheet. For the mentioned exposure times, the FF decrease was measured as 1.4% for the samples of the first round and 1.8% for those of the second round.  $R_s$ , also in this case, seems not to contribute significantly to the FF reduction, except sample PET+Al\_4 which shows a 4.7%  $R_s$  increase after 2000 hrs, for unspecified reasons.

By comparison of the degradation behaviour of the different types of samples, it is observed that the rear-side exposed PV cells experience completely different degradation mechanisms than the rest of the specimens. For this reason, rear side corrosion is not considered as a relevant degradation mode for fully encapsulated PV modules, as moisture needs to condense on the Al surface and liquify within any existing cavities or crevices. This does not happen for a fully encapsulated PV module, as the polymer is attached to the cell and prevents liquification. The moisture, only in the form of vapour, is not corrosive to the Al paste, as it already contains aluminium oxide, and without the presence of liquid water the aluminium oxide may not dissolve<sup>11</sup> [146]. Moreover, as it is concluded from section 4.3, acetic acid is not corrosive for the aluminium contact, as the aluminium acetate generated from the reaction between the acetic acid and the aluminium does not dissolve in the solution and protects the contact.

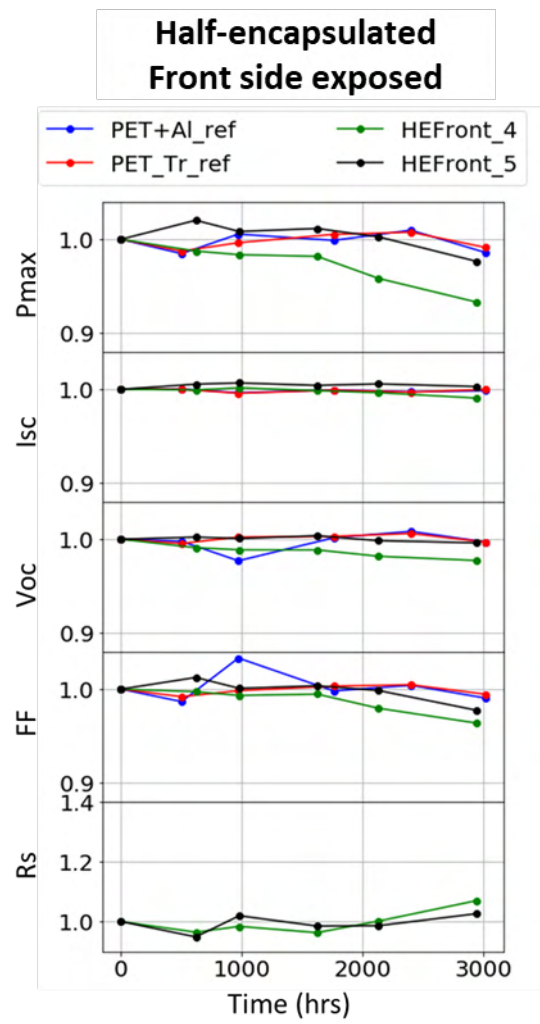
The  $V_{OC}$  degradation observed for all the aged specimens is accompanied by visible dark regions in the EL images of the cells (Figures 4-26 to 4-29), indicating increased recombination losses (see section 4.3.1.2 for the correlation between the  $V_{OC}$ , recombination current and EL intensity). More extensive examination of the cause of this effect will be presented later in this section.

---

<sup>11</sup> Water is corrosive for the Al when combined with Pb and Sn, because it acts as a sacrificial metal.



a)



b)

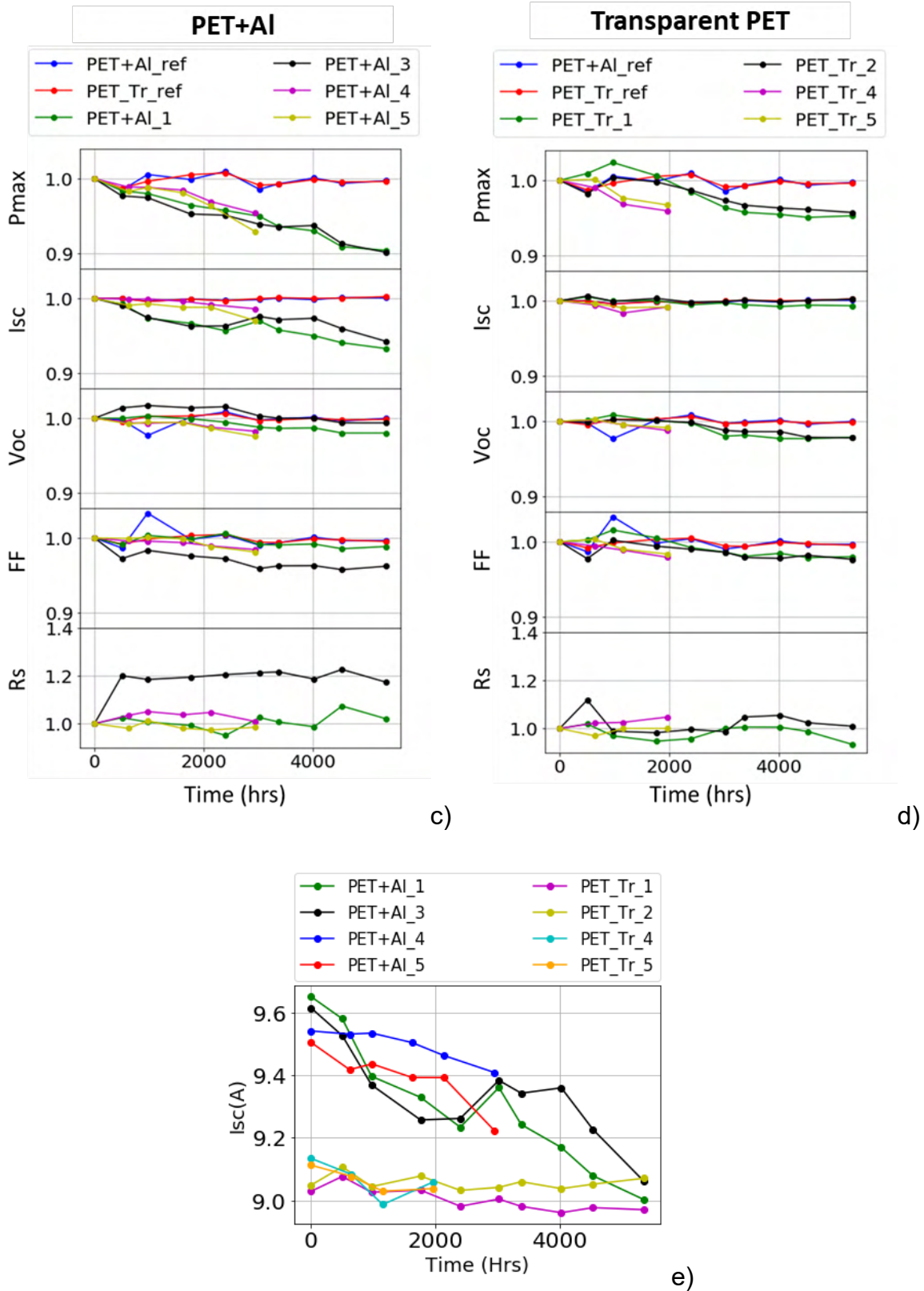
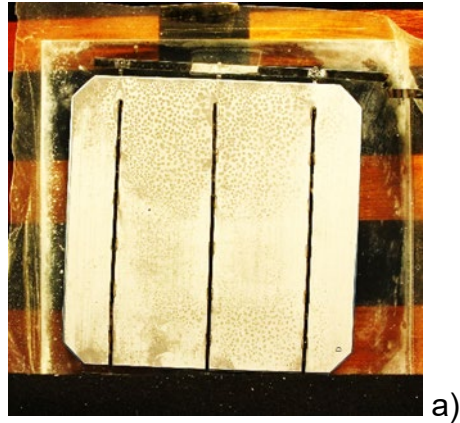
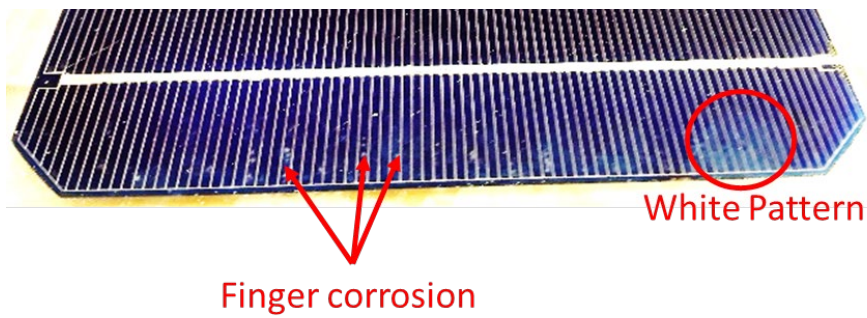


Figure 4-24 Effect of 85°C/85%RH exposure on the performance parameters of a) half – encapsulated PV cells, rear side exposed, b) half – encapsulated PV cells, front side exposed, c) PV modules encapsulated with a PET backsheet that includes Al foil and d) PV modules encapsulated with transparent PET backsheet. e) Comparison of the  $I_{sc}$  evolution of the mini-modules laminated with backsheet including Al foil to that of the samples containing a transparent backsheet.



a)



b)

Figure 4-25 a) Oxidation observed on the rear side of a half – encapsulated PV cell, rear side exposed (sample HERear\_1), aged under DH conditions and b) Regions with cell whitening and finger corrosion on the surface of a half – encapsulated PV cell, front side exposed (sample HEFront\_4).

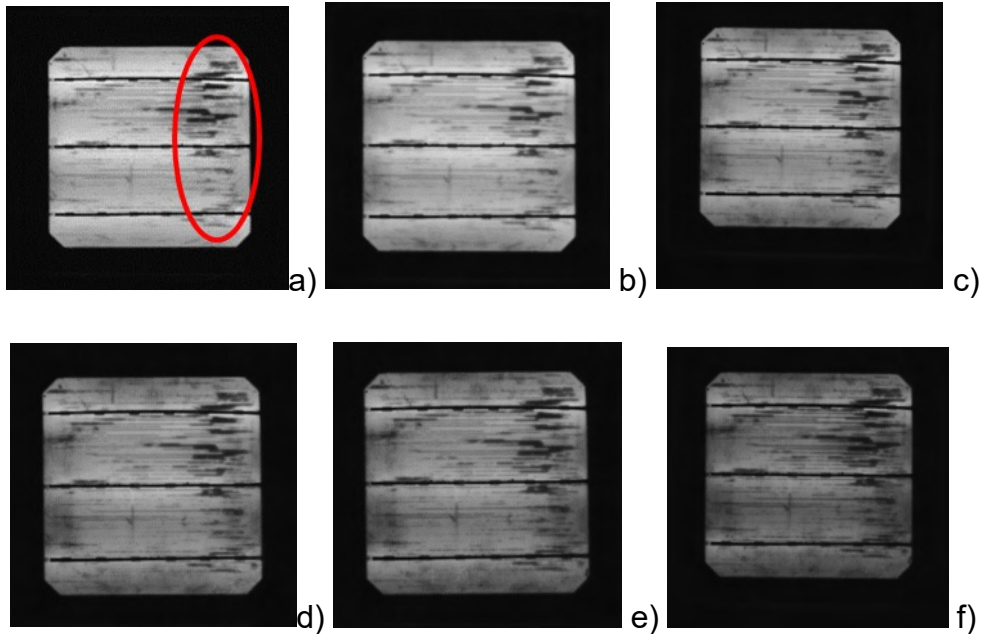


Figure 4-26 EL images of a half – encapsulated PV cell, rear side exposed (sample HERear\_1) after a) 503 hrs, b) 1763 hrs, c) 2402 hrs, d) 3023 hrs, e) 4028 hrs and f) 5350 hrs of aging. The red ellipse indicates the regions with increased series resistance due to Al oxidation, as identified by visual inspection.

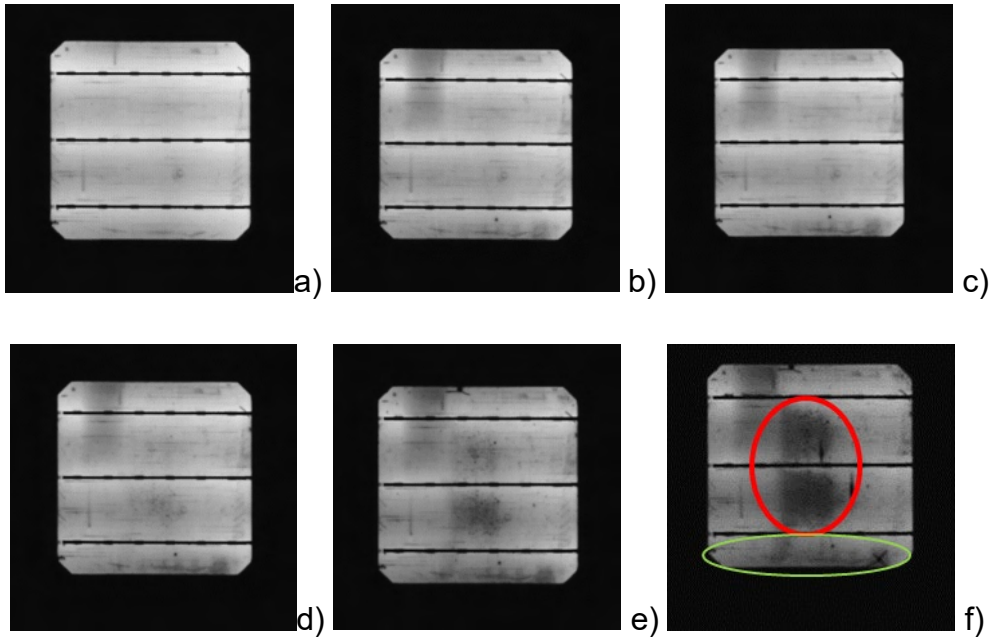


Figure 4-27 EL images of a half – encapsulated PV cell, front side exposed (sample HEFront\_4) after a) 0 hrs, b) 621 hrs, c) 981 hrs, d) 1626 hrs, e) 2135 hrs and f) 2948 hrs of aging. The red ellipse indicates the dark patterns caused by non-radiative recombination of the carriers. The green ellipse includes the region with finger corrosion, observed by visual inspection.

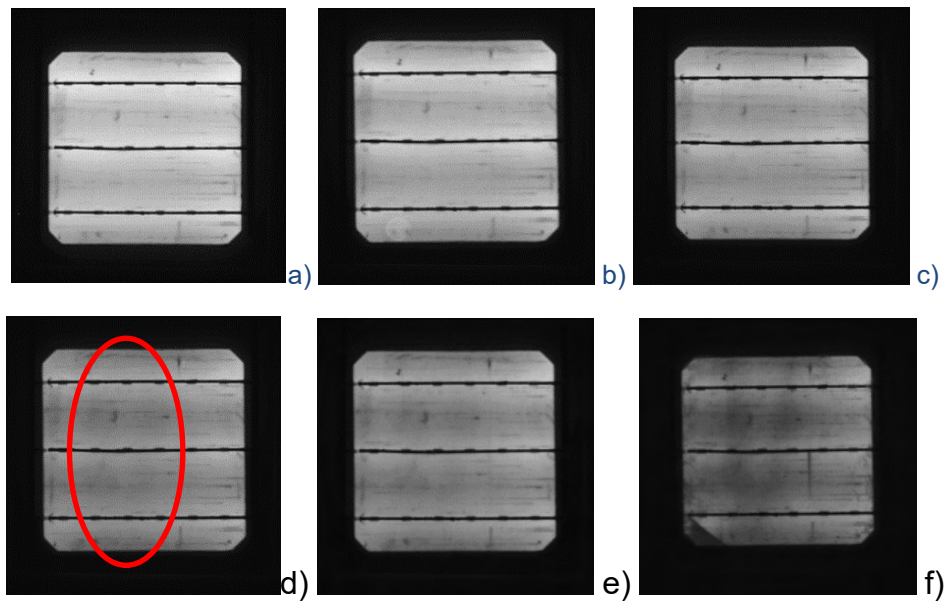


Figure 4-28 EL images of PV modules encapsulated with PET backsheet that includes Al foil (sample PET+Al\_1) after a) 0 hrs, b) 1763 hrs, c) 2402 hrs, d) 3023 hrs, e) 4028 hrs and f) 5350 hrs of DH aging. The red ellipse indicates the dark patterns (their origin will be discussed later in this section) that start to appear.



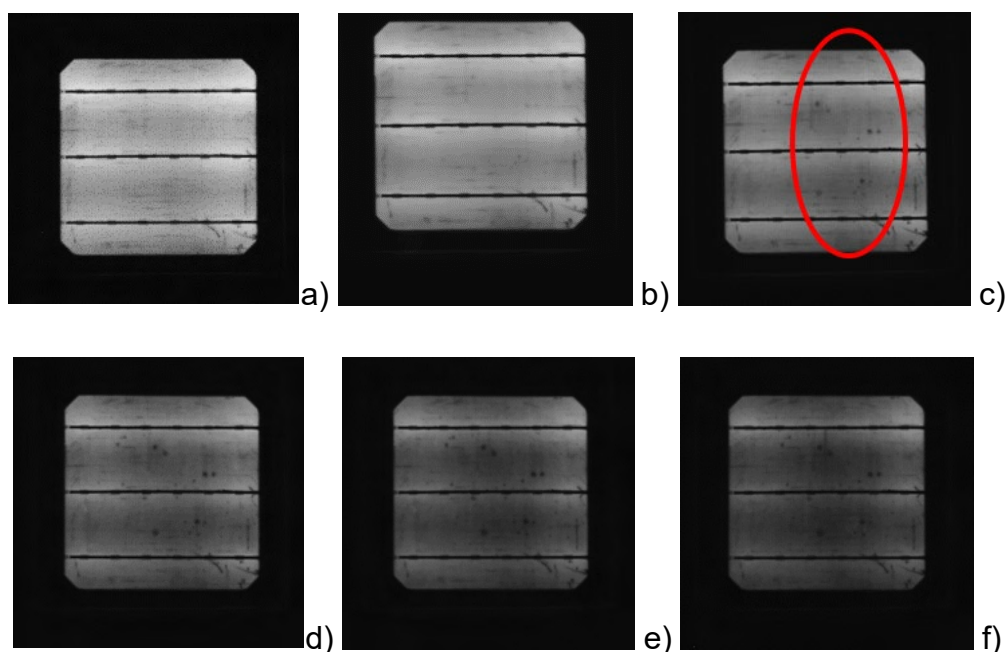


Figure 4-29 EL images of PV modules encapsulated with transparent PET backsheet (sample PET\_Tr\_1) after a) 0 hrs, b) 1763 hrs, c) 2402 hrs, d) 3023 hrs, e) 4028 hrs and f) 5350 hrs of aging. The red ellipse indicates the dark patterns (their origin will be discussed later in this section) that start to appear.

Moreover, all the fully encapsulated samples show backsheet embrittlement (Figure 4-30a and b), and gradual yellowing. Furthermore, the samples of the first round developed severe edge delamination (Figure 4-30c) which was not observed for the samples of the second round. These findings are significant for the investigation of the samples' degradation if general, but they are not further analysed here as they deviate from the specific study of corrosion in this chapter. Finally, the two different types of mini-modules did not show varied degradation related to moisture ingress, which can be explained by the findings of Chapter 3, as the moisture ingress was not significantly different for the two types of samples.

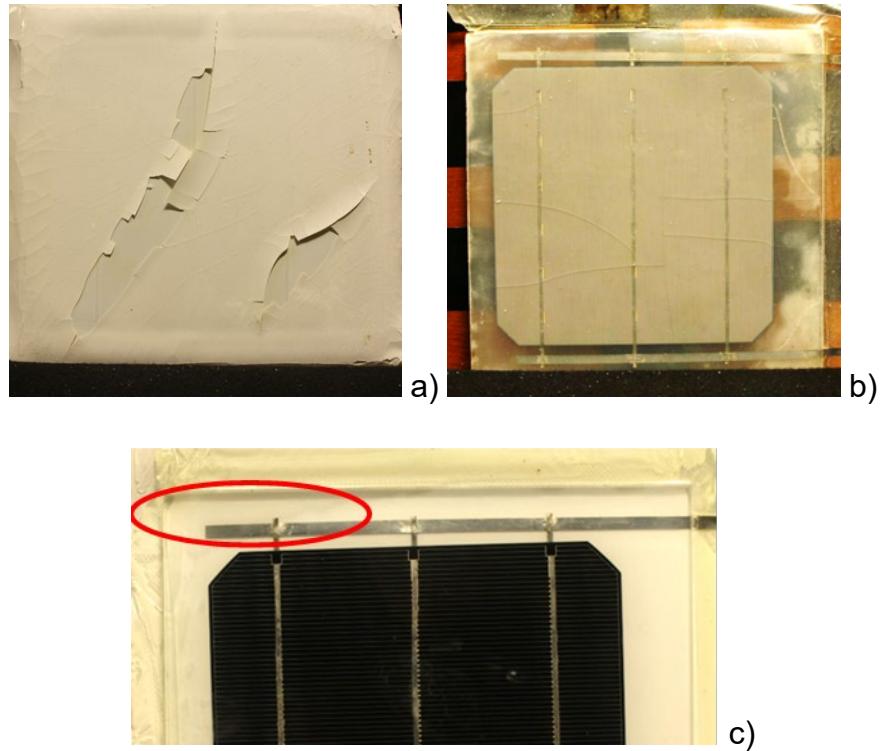


Figure 4-30 Backsheet embrittlement observed on PV modules encapsulated with a) PET backsheet that includes Al foil (sample PET+Al\_1) and b) transparent PET backsheet (sample PET\_Tr\_1) after 5350 hrs of DH exposure. c) Severe edge delamination observed for sample PET+Al\_1 after 974 hours of DH exposure.

According to the results presented before in this section, the  $V_{oc}$  of all the samples decreased. It is postulated this is due to increase of the recombination current, however, the combination of I-V curves and EL imaging (which showed regions with increased recombination current) was not sufficient for the identification of the reason responsible. However, Spectral Response is an adequate method, as it can better demonstrate the light absorption of a PV cell and, subsequently, the regions of increased recombination current, across its thickness. Although, as indicated in the literature [138], [139], [140] the  $V_{oc}$  of c-Si or mc-Si PV cells does not degrade when exposed to DH conditions, PERC cells do not seem to comply with this behaviour [163]. Although detailed research is conducted regarding the understanding of LeTID (see Chapter 2), insufficient information is available regarding the DH exposure. The work presented in this chapter agrees with the findings of Herguth et al. [81] and indicates that the mechanism responsible for LeTID occurs also in the absence of light, but a longer duration is required. The specific mechanism suggests that hydrogen incorporated during the deposition of



the rear-side passivation layer (combination of  $\text{AlO}_x\text{:H}$ ,  $\text{SiO}_x\text{:H}$  and/or  $\text{SiN}_x\text{:H}$ ) diffuses towards the bulk of the cell, causing defects on the rear-side of the silicon [81]. These defects are the reason for the increased recombination current and, subsequently, the decreased  $V_{oc}$ .

The effect of the described mechanism is visible in the comparison between the SR of an unaged and an aged sample seen here, with the SR decreasing within the red-near infrared region ( $>800\text{ nm}$ ), indicating reduced collection or increased rear-surface recombination. The examined regions showed also EL darkening, which additionally confirmed the increased recombination current. The effect is stronger on the half – encapsulated, front side exposed sample (comparison between HEFront\_ref and HEFront\_4, which was aged for 3644 hrs, presented in Figure 4-31a) than the sample encapsulated with PET backsheet that includes Al foil (comparison between PET+Al\_ref and PET+Al\_4, which was aged for 3644 hrs, shown in Figure 4-31b), as expected according to the  $V_{oc}$  and EL intensities of the samples.

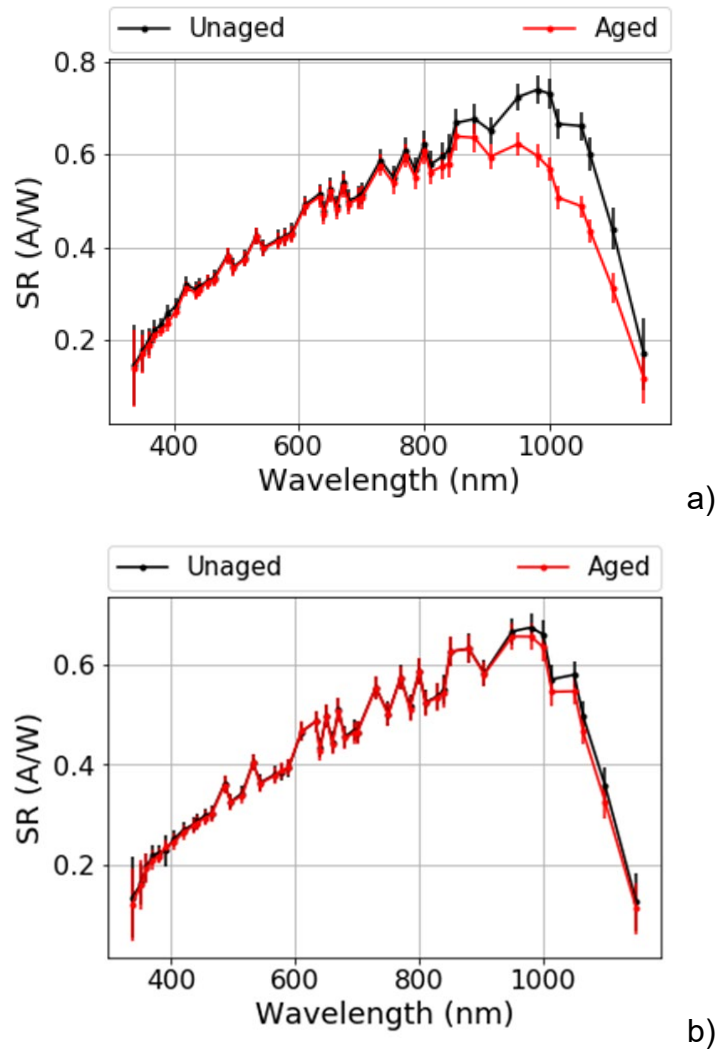


Figure 4-31 The SR comparison between an unaged and an aged sample for a) half – encapsulated, front side exposed PV cell and b) PV module encapsulated with PET backsheet including Al foil.

Regarding the front side corrosion, the degradation of the different interfaces, cell-busbar and busbar-ribbon, due to acetic acid immersion, was examined in section 4.3. According to the results, the interface more susceptible to corrosion was the one between the busbar and the ribbon, due to solder dissolution. The relevance of this observed failure during the DH aging was confirmed by comparison between material analysis of ribbons from a PV cell aged by exposure to acetic acid and ribbons obtained from part of a mini-module, from another study, exposed to DH. Figure 4-32 compares the EDS analysis of the upper surface of a ribbon of a PV cell aged by exposure in acetic acid environment (30% HAc for 290 hrs) and a ribbon of a PV cell, part of a mini-module exposed to DH (85°C/85% RH extended),

respectively. For both experiments Pb and Sn have been dissolved and the core Cu of the ribbons is clearly detected, while for an unaged ribbon (Figure 4-32 top) the Cu signal is not detected or it is very weak. The EDS analysis of the rear side of the ribbon from the PV module aged under DH conditions (Figure 4-33) shows evidence that the busbar / cell interface is weaker for the DH exposure comparing to acetic acid immersion, as the signal of Ag on the ribbon is stronger. Material analysis conducted on PV modules aged under DH conditions, or exposed to real field environment, presents the same findings [164], [165].

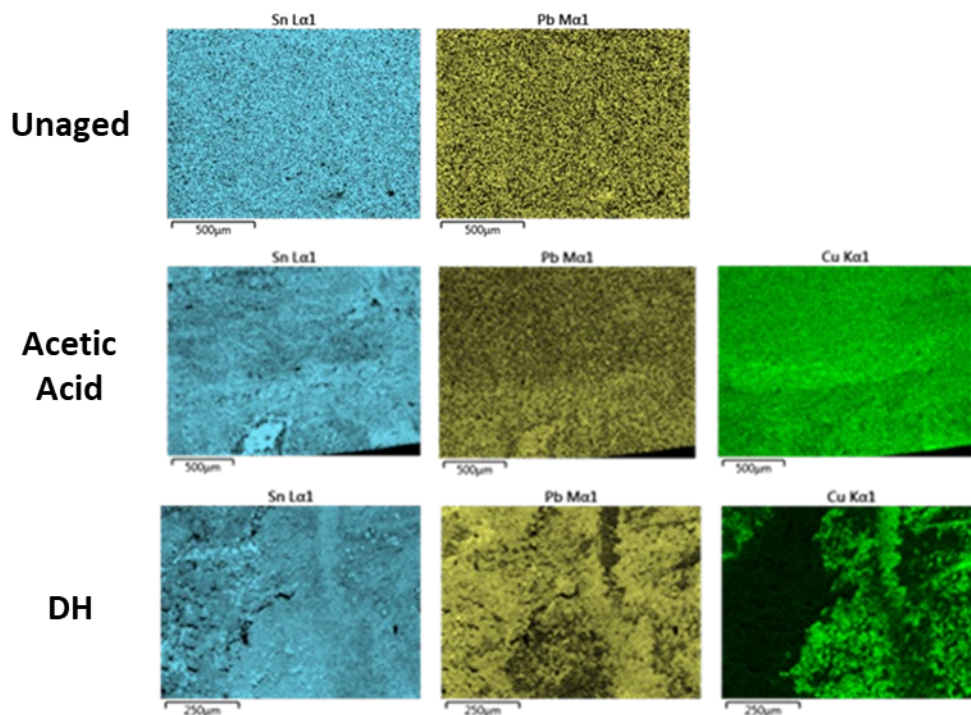


Figure 4-32 EDS analysis of an unaged ribbon (top), a ribbon of a PV cell aged by exposure in acetic acid environment (middle) and the front side of a ribbon of a PV cell aged under DH exposure (bottom).

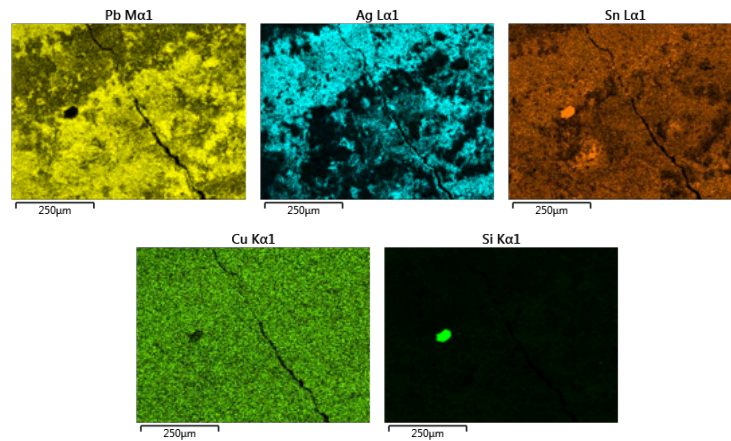


Figure 4-33 EDS analysis of the rear side of a ribbon of a PV cell aged under DH exposure.

These findings indicate that the corrosion of metallisation and ribbons is a relevant degradation mode, although, in contrast, it was not observed on the fully encapsulated samples including PERC PV cells. One possible reason responsible for this, is that the mini-modules containing PERC PV cells were single-cell and not sealed, something that may allow the acetic acid to diffuse and escape through the edges. Considering that acetic acid escaped, the moisture vapour alone is not enough to corrode the fingers and the busbars, unless the surface is in direct contact or the fingers are pre-damaged due to cracking. Another possibility is that the decrease of  $V_{OC}$  interferes with the variance of the  $R_s$  (slope close to  $V_{OC}$ ), so  $R_s$  increase may not be detected.

#### 4.4. Conclusions

The research presented in this chapter focuses on the study and the separation of the different corrosion mechanisms and their impact on the electrical performance of c-Si, mc-Si and PERC c-Si PV cells. The initially identified corrosion mechanisms were the following:

- Corrosion and detachment of the ribbons due to solder dissolution (Pb and Sn), as a result of the reaction with water or acetic acid. Severe corrosion of the solder leads to additional corrosion, as the core Cu is exposed.
- Detachment of the busbars and the fingers from the cell, due to the reaction of water, or acetic acid, with the lead oxide contained in the silver paste/frit.
- Corrosion of the Al back contact, with the Al acting as the sacrificial metal when combined with Pb and Sn, while exposed to water or acetic acid.

For the separation between the different mechanisms, half-encapsulated c-Si and mc-Si PV cells, front or rear side exposed were immersed in water and different concentrations of HAc. Moreover, for the examination of the realistic occurrence of these mechanisms, the results were compared with those obtained by DH exposure of half and fully encapsulated PERC c-Si PV cells. Previously aged samples were also considered for a better justification of the results.

By consideration of all the findings, it is concluded that corrosion of the ribbons and metallisation located on the front side of the cell is a relevant failure to DH aged PV modules, although not observed on the fully encapsulated PERC c-Si PV modules, but visible on the PV module previously aged in CREST. The comparison between the ribbon – busbar and busbar – cell interfaces showed that they are both likely to fail, depending on the concentration of acetic acid and temperature level. Furthermore, when moisture is absorbed by the polymer and not free in the form of liquid or vapour, it is not observed to cause as much corrosion. Acetic acid exposure is observed to be the main reason causing corrosion.

Regarding the Al-contact corrosion, although it is observed on the cells aged by immersion in acetic acid solutions of different concentration, it is not a relevant failure to DH aged PV modules. For the observation of corrosion, the moisture needs to liquify on the surface of the Al contact (e.g. within crevices), so the

aluminium oxide may dissolve, which is not the case when a PV cell is encapsulated. Moreover, acetic acid does not cause any harm to the Al contact, due to the formation of aluminium acetate, as a product of the reaction.

Except corrosion, which was the main topic of this chapter, another significant failure was observed on the DH aged PERC c-Si cells, related to high temperature conditions. The degradation mechanism is likely to be the same as that responsible for LeTID, with the difference that the studied PV modules were not exposed to light. The electrical parameters affected are the  $V_{OC}$  and FF, probably due to increased carrier recombination, close to the rear side passivation layer. These observations indicate that hydrogen incorporated during the deposition of the rear-side passivation layer diffuses towards the bulk of the cell, causing defects on the rear-side of the silicon. However, although the results are supported by similar observations in literature, further research is required for the confirmation of these findings. The selection of different type of backsheets showed slightly varied results. Further work is required, regarding the examination of different manufacturing processes, for the elimination of the issue.

Finally, the variation of backsheets, did not show any difference regarding moisture induced degradation mechanisms.

# Chapter 5 The impact of corrosion on PV modules aged in the field

In this chapter, the series resistance evolution of a number of different types of PV modules installed in an outdoor test facility at Loughborough University, UK, for 7 years is analysed. The values of the series resistance are extracted by fitting the single diode model to the I-V curves measured for the PV modules. Visual inspection is applied to investigate signs of metallic corrosion. Potential additional failure modes are identified and their impact on the rest performance parameters is estimated.

## 5.1. Previous studies and models of corrosion in the field

Metallic corrosion is one of the most frequently detected failure mechanisms for PV modules operating in the field. Jordan et al. [20] conducted statistical research on failures occurring in PV modules exposed to three different types of climate and showed that metallic corrosion was the second most significant failure observed in PV systems installed within the last 10 years, in terms of frequency and severity. The authors of the study, and Omazic et al. in [49] concluded that although metallic corrosion affects more severely PV modules installed in tropical climate conditions, it is also relevant to other types of climate.

A lot of research has been conducted on PV modules exposed to tropical climate conditions in terms of identifying failure modes and underlying mechanisms. According to the findings of Han et al. [22] severe corrosion and power output degradation of 24%, mainly due to FF degradation, were observed for PV modules operating for 18 years under tropical climate conditions in China (Shenzhen, subtropical monsoon), possibly caused by an increase in  $R_s$  and not in other diode model parameters, as identified from their EL images. Wohlgemuth and Kempe

[166] detected severe metallic corrosion on PV modules installed in Florida for 23 years. Li et al. [167] estimated the degradation rate of a variety of PV modules (both c-Si and mc-Si) exposed to hot and humid environmental conditions and found that 44% of them showed a power output degradation rate higher than 1%/yr, meaning that these modules will not maintain the manufacturer's standards throughout 25 years of operation. On some of the modules, corrosion of the ribbons was observed even after just 3 years of exposure.

Climatic conditions other than tropical may cause metallic corrosion, but with a lower probability and severity. Czanderna and Pern [46] reported detection of metallic corrosion products within PV modules installed in Carissa Plains, CA, which has a semi-arid climate. Moreover, Rajput et al. [168] reported that metallic corrosion was the most commonly observed failure in solar modules exposed for 22 years to the climate conditions of India (Gurgaon, hot semi-arid climate). In addition, according to Bandou et al. [169], solar modules exposed to Saharan environmental conditions for 28 years suffered from metallic corrosion, although this was a secondary failure mechanism, since the main failure observed was encapsulant discolouration. Regarding temperate and warm climates, Smith et al. [170] identified FF degradation, due to series resistance increase, in PV modules installed in Golden, CO for 17 years. Annigoni et al. [41] observed 27% FF degradation, due to metallic corrosion, for PV modules aged for 35 years at Lugano in Switzerland (humid temperate climate). Furthermore, according to Liu et al. [171] PV modules located at Sacramento Municipal Utility District (SMUD), CA, USA, operating for 30 years, show reductions of power output of 20% and 13% due to cell metallisation and interconnection corrosion, respectively. Finally, even PV systems exposed to humid continental and subarctic climates showed evidence of corrosion, as, according to Bradley et al. [172], 10% of the solar panels installed for 20 years at a site in Quebec, Canada, were affected by metallic corrosion.

Series resistance is the main diode model parameter that is affected when PV module performance suffers due to metallic corrosion. However, there are not many published studies regarding the evolution of the series resistance of a PV module exposed to outdoor conditions over a significant number of years. Hrelja et al. [173] fitted the single diode model to the measured I-V curves for PV modules which had been operating for 8 years at an EDF monitoring test site. They showed an increase



in series resistance over the 8 years, but without presenting a specific pattern for the evolution with time. In another study, Liu et al. [174], [175] calculated the series resistance of PV modules exposed for 8 years to different climatic conditions, but used the inverse of the slope of the I-V curve close to  $V_{oc}$ , which is not an exact measure of the series resistance, although it is approximately proportional to it. Moreover, no research is available which separates the series resistance increase due to corrosion from the series resistance evolution due to interconnection deterioration occurring as a result of thermomechanical fatigue.

As metallic corrosion is a very significant cause of failure, its prediction is crucial. Various Arrhenius based models, that include parameters which are calculated by fitting of the models to performance results, obtained for PV modules aged under DH conditions, are available. The reaction rate, responsible for corrosion, is given by the following relationship:

$$R_D = \frac{dC}{dt}, \quad (5-1)$$

where C is the reactant concentration (e.g. the concentration of the metals reacted and caused corrosion). The most well-known models for the estimation of the reaction rate are Peck's [176] and Eyring's [177], with Peck's model showing the smallest deviation, when fitted to the results from artificial aging experiments [178]. According to these models, the  $R_D$  value is dependent on the temperature and humidity to which a PV module is exposed, as well as the activation energy of the mechanisms, with the correlations being different for each model.

The calculated  $R_D$  value derived from the above models is used for the fitting of Pan's [179] or Braisaz's [180] model for the estimation of the degradation of  $P_{max}$  or  $R_s$ . Although both of these approaches show very good agreement with the data from accelerated (indoor) testing, large differences are observed between them when applied to outdoor conditions for the prediction of the metallic corrosion degradation of naturally aged PV modules [178]. The reason for this is that both models are empirical, which makes them sensitive to the parameters estimated by fitting to the indoor data. For example, when these models are applied to outdoors weather data, if different initial values are chosen for the parameters, completely

different final values are estimated, and therefore the degradation prediction is unreliable.

For a more accurate prediction of corrosion under actual operating conditions, the pattern of the series resistance increase should be observed on a sufficient number of PV modules installed in the field, that show indications of corrosion. A combination of visual inspection and EL measurements may reveal such symptoms.

## **5.2. Site information and data collection method**

The CREST Outdoor Monitoring System is a continuously-populated test facility, in operation since the late 20<sup>th</sup> century. The modules analysed in this work were originally installed on industrially-funded projects in the early stages of the UK's PV feed-in tariff scheme, by former and some still current members of the Applied PV Research Group (special thanks to Brian Goss, Ian Cole, Alex Smith and Charles Greenwood). The installation that the studied PV modules belong to is located on the roof of the Sir David Davies Building at Loughborough University (52.76°N 1.24°W). The climate is temperate oceanic (Cfb) according to the Köppen–Geiger climate classification system. Fourteen PV modules are mounted facing south at a 34 degree tilt to the horizontal (Figure 5-1). The types, technologies and electrical characteristics of the PV modules are listed in Table 5-1. The modules are connected to fourteen Photovoltaic Measurement System (PVMS250) units for the measurement of the I-V curves. These units maintain the PV modules at maximum power point (MPP) operating conditions between the I-V trace measurements [181]. The correspondence between the measurement units (channel numbers) and modules are also presented in Table 5-1. The I-V curves and module temperatures are recorded every minute, while the in-plane irradiance is monitored every second by a pyranometer. All the results are imported into a database and downloaded via PostgreSQL manager. The modules measured by channels 1 and 5 are not studied in this chapter, as the I-V curve measurements were interrupted during 2015, as their temperature sensors were damaged.



Figure 5-1 Installation of the PV modules on the roof.

Table 5-1 The types, technologies and electrical characteristics\* of the PV modules studied.

Model	No. of Modules	Technology	I <sub>sc</sub> (A)	V <sub>oc</sub> (V)	P <sub>max</sub> (W)	Channel No.
<b>Solarworld_SW245_mono</b>	2	c-Si	8.25	37.7	245	1,2
<b>Solarworld_SW245_poly</b>	2	mc-Si	8.49	37.5	245	3,4
<b>Trina_TSM-235PC05</b>	2	mc-Si	8.55	37.2	235	5,6
<b>Trina_TSM-180DC01A</b>	2	c-Si	5.35	44.2	180	7,8
<b>Trina_TSM-195DC80.08</b>	2	c-Si	5.70	45.4	195	9,10
<b>Sanyo-HIT_HIT-N240SE11</b>	2	HIT	5.85	52.4	240	11,12
<b>Kyocera_KD240GH-2PB</b>	2	mc-Si	8.59	36.9	240	13,14

\* The electrical characteristics are at STC conditions as listed in the datasheets.

### 5.3. I-V curve fitting

Increase in series resistance is typically the principal indicator of module performance degradation due to corrosion. For the extraction of the series resistance values (and the other electrical parameters secondarily) from the I-V curve measurements, the single diode model was fitted to the I-V curve data (the initial model was developed by Elena Koumpli [182] and modified for the application to data received outdoors in this thesis. The accuracy of the model is further confirmed in this thesis by sensitivity analysis). The fitting method used was trust-region optimisation, which is the most robust and suitable method for non-linear problems, when compared to dogleg (not recommended for problems with rank-deficient Jacobian) and Levenberg-Marquardt algorithms (not applicable with bounds and sparse Jacobians) [183]. According to this method, the following procedure is followed [182], [184], [185], and was implemented in the code using the Python function *scipy.optimize.curve\_fit()* [186]:

- Initial ( $I_{ph} = I_{SC,meas}$ ,  $I_0 = 1 \cdot 10^{-8}$  A,  $R_s = 0.01 \Omega$ ,  $R_{sh} = 200 \Omega$ ,  $n = 1$ ) values are assigned to the five parameters of the diode model (realistic values selected according to Monte Carlo Sensitivity Analysis, which is presented later in this section);
- The fitting algorithm search space for each of these parameters is given a lower boundary ( $I_{ph} = 0$  A,  $I_0 = 0$  A,  $R_s = 0 \Omega$ ,  $R_{sh} = 0 \Omega$ ,  $n = 0$ ) and upper boundary ( $I_{ph} = 10$  A,  $I_0 = 1 \cdot 10^{-2}$  A,  $R_s = 1 \cdot 10^4 \Omega$ ,  $R_{sh} = 1 \cdot 10^4 \Omega$ ,  $n = 35$ ), so the range of the allowed parameters is large enough (see Monte Carlo Sensitivity Analysis below);
- The equation of the single diode model (see Eq. 2-7 from Chapter 2) is solved for the initial values (using the Newton-Raphson method, as described in Appendix 4) and the quality of fit is assessed using the Least Squares function,  $F(x) = 0.5 \cdot \sum_{i=0}^{m-1} f_i(x)^2$ , where  $f_i(x)$  is the difference between the measured and estimated I-V curves at point  $x$ ;
- A region of potential solutions is defined (by the radius in Euclidean norm) around the current solution and a step is set within that region, depending on the radius of the region and the gradient of the current point [184], [185];

- In the second iteration, the single diode model receives the values according to the step set. If the new  $F(x)$  is smaller than the previous one, the new diode parameters are set to the model, else the region of trust changes, and a new step is set, with a size and direction that depends on the change of value of the previous  $F(x)$ . The iteration procedure that the algorithm follows is described in Figure 5-2. An example of the values that  $F(x)$  receives at each iteration until reaching the minimum, for a specific I-V curve fitting is presented in Figure 5-3.
- The iterations stop when the gradient of the  $F(x)$ ,  $\nabla F(x)$ , at the point is equal to or smaller than  $1 \cdot 10^{-8}$  [183].

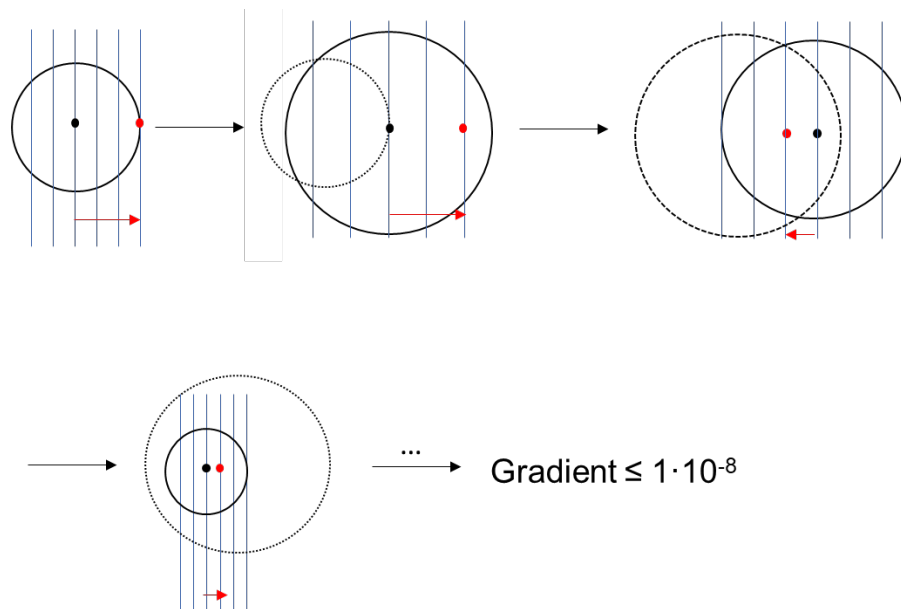


Figure 5-2 The procedure that the algorithm follows, explained graphically. The black circle represents the current trust-region, the dashed circle is the previous trust-region, the blue lines are the step, the red arrow indicates the step direction, while the black and red dots represent the previous and the current minima, respectively. First, the minimum of  $F(x)$  is found on the border of the trust region, which means that the algorithm needs to continue searching for the minimum towards the same direction with different step. Then, a minimum is found, meaning that the algorithm is required to change searching direction, with a different step to find a new minimum. When the new minimum is found, the algorithm searches between the two minima with smaller step, to identify the overall minimum, when the gradient is equal to or smaller than  $1 \cdot 10^{-8}$ .

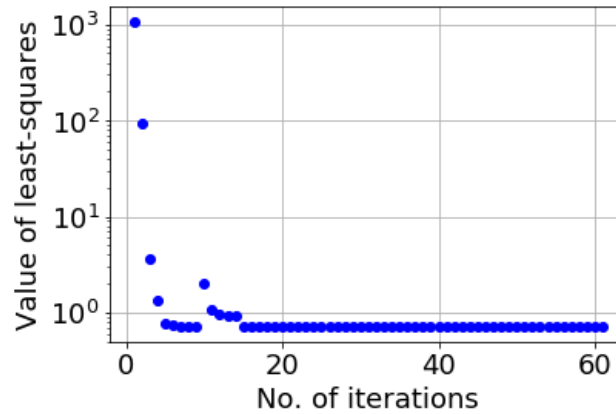


Figure 5-3 Values that the least-squares receive during fitting of an I-V curve, plotted over the number of iterations.

For the selection of the initial and boundary conditions and to investigate how the fitting is affected by them, a Monte Carlo sensitivity analysis was performed [187]. To achieve this, the model was fitted to two I-V curves with known diode model parameters ( $I_{ph} = 8.3 \text{ A}$ ,  $I_0 = 1 \cdot 10^{-8} \text{ A}$ ,  $R_s = 0.01 \text{ } \Omega$ ,  $R_{sh} = 200 \text{ } \Omega$ ,  $n = 1$  for low series resistance, and  $I_{ph} = 8.3 \text{ A}$ ,  $I_0 = 1 \cdot 10^{-8} \text{ A}$ ,  $R_s = 0.8 \text{ } \Omega$ ,  $R_{sh} = 200 \text{ } \Omega$ ,  $n = 1$ , for relatively high series resistance) and with additional noise on the current values. The study was performed for 10,000 different random initial values and two different upper boundary conditions ( $I_{ph} = 10 \text{ A}$ ,  $I_0 = 1 \cdot 10^{-2} \text{ A}$ ,  $R_s = 1 \cdot 10^4 \text{ } \Omega$ ,  $R_{sh} = 1 \cdot 10^4 \text{ } \Omega$ ,  $n = 35$  and  $I_{ph} = 20 \text{ A}$ ,  $I_0 = 1 \cdot 10^{-2} \text{ A}$ ,  $R_s = 1 \cdot 10^4 \text{ } \Omega$ ,  $R_{sh} = 1 \cdot 10^6 \text{ } \Omega$ ,  $n = 200$ ).

The sensitivity analysis (Figure 5-4) showed that the change of the upper boundary did not have a significant impact on the fitting. For series resistance  $0.01 \text{ } \Omega$  (very low value), the mean fitted  $R_s$  value was equal to  $0.063 \pm 0.29 \text{ } \Omega$ , when the lower upper boundary was used, and  $0.045 \pm 0.24 \text{ } \Omega$  for the higher upper boundary. These findings reveal that the model is sensitive for such levels of series resistance, something expected, as the I-V curves do not vary significantly for different low series resistance values. However, this is not the case for  $R_s = 0.8 \text{ } \Omega$  (relatively high but still realistic level, as  $R_s = 1.2 \text{ } \Omega$  occurs for a PV module aged under DH conditions according to Zhu et al. [26]), as the fitted mean value is equal to  $0.77 \pm 0.15 \text{ } \Omega$  for lower upper boundary conditions and  $0.74 \pm 0.13 \text{ } \Omega$  for higher upper boundary conditions. According to these results, the model can accurately calculate the real series resistance value of an I-V curve with relatively high  $R_s$ , regardless

the choice of initial conditions. This is very important to this study, as the purpose is the detection of high series resistance due to corrosion. Furthermore, the series resistance of an unaged PV module is between 0.2 and 0.5  $\Omega$ , which means that the proposed fitting method is suitable for this range of series resistance values.

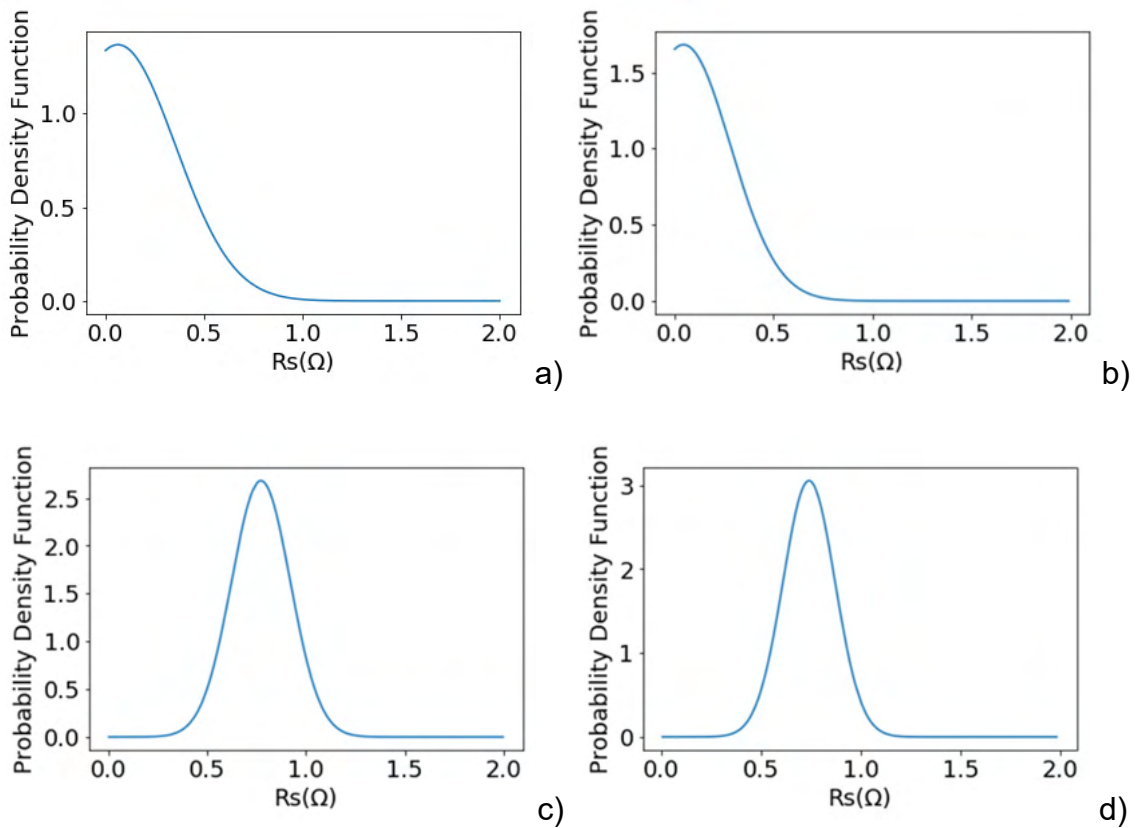


Figure 5-4 Probability density function of the Monte Carlo sensitivity analysis for a)  $R_s = 0.01 \Omega$  and lower upper boundary conditions, b)  $R_s = 0.01 \Omega$  and higher upper boundary conditions, c)  $R_s = 0.8 \Omega$  and lower upper boundary conditions and d)  $R_s = 0.8 \Omega$  and higher upper boundary conditions.

### 5.3.1. Data filtering

For each of the twelve modules studied, there are many sets of I-V data available, however a significant proportion of these are affected by noise, shading, etc, and only the data likely to provide the most reliable estimates of series resistance were used after applying a strict filtering procedure before fitting of the single diode model. The procedure applied to the data is described below:

- Only I-V curves at irradiance levels higher than  $200 \text{ W/m}^2$  were selected for fitting, to avoid low irradiance data with higher measurement uncertainty [188].
- I-V curves affected by partial shading were excluded. The procedure followed for this part of the filtering is presented in section 5.3.2.
- Spurious spikes were removed from the remaining I-V curves, in case of low numbers of extreme outliers within individual I-V curves, artefacts of the measurement loads. The method applied is described in section 5.3.3.

After fitting the single diode model to the measured I-V curves according to the procedure described in paragraph 5.3, the data were further filtered by their Root Mean Square Error values for more reliable results. The filter applied is presented in section 5.3.4.

### **5.3.2. Exclusion of I-V curves affected by shading or measurement noise**

To exclude I-V curves affected by shading (Figure 5-5) each curve is analysed in turn: Their first derivative (gradient) is calculated. Then values of the gradient between  $1/6 \cdot V_{OC}$  and  $5/6 \cdot V_{OC}$  (empirically chosen by application to the data) are used for the calculation of the second derivative. The values outside this range are neglected because of multiple measurements of the same I-V curve point at both the beginning and the end of the trace that are often present (an artefact of the operation of the I-V load sweep). The maximum value of the second derivative is calculated and the number of peaks with Signal-to-Noise Ratio (SNR) greater than 1 are counted [189]. Only those curves whose second derivative maximum is below a specific threshold value (chosen empirically after fitting of a small sample of I-V curves to the single-diode model and then comparing the Root Mean Square Errors), which is documented for each module in Table 5-2, and where the number of positive inflection points is no more than 1, are selected. So, the example in Figure 5-5 (left) would be rejected with respect to both criteria. For a more detailed description of the methods used (e.g. gradient, SNR calculation), see Appendix 5.



Table 5-2 Threshold permitted maximum values of the second derivative for acceptance\* of the I-V curves for each measured PV module corresponding to the specific channels.

Channel No.	Threshold value of second derivative (A/V <sup>2</sup> )
1	-
2	0.009
3	0.003
4	0.009
5	-
6	0.01
7	0.005
8	0.01
9	0.003
10	0.007
11	0.007
12	0.007
13	0.01
14	0.008

\*The values are different for each channel, as they are calculated from individual evaluation, after fitting of a small sample of I-V curves to the single-diode model and comparing the RMSE. The value is depended mostly on the measurement of the channel.

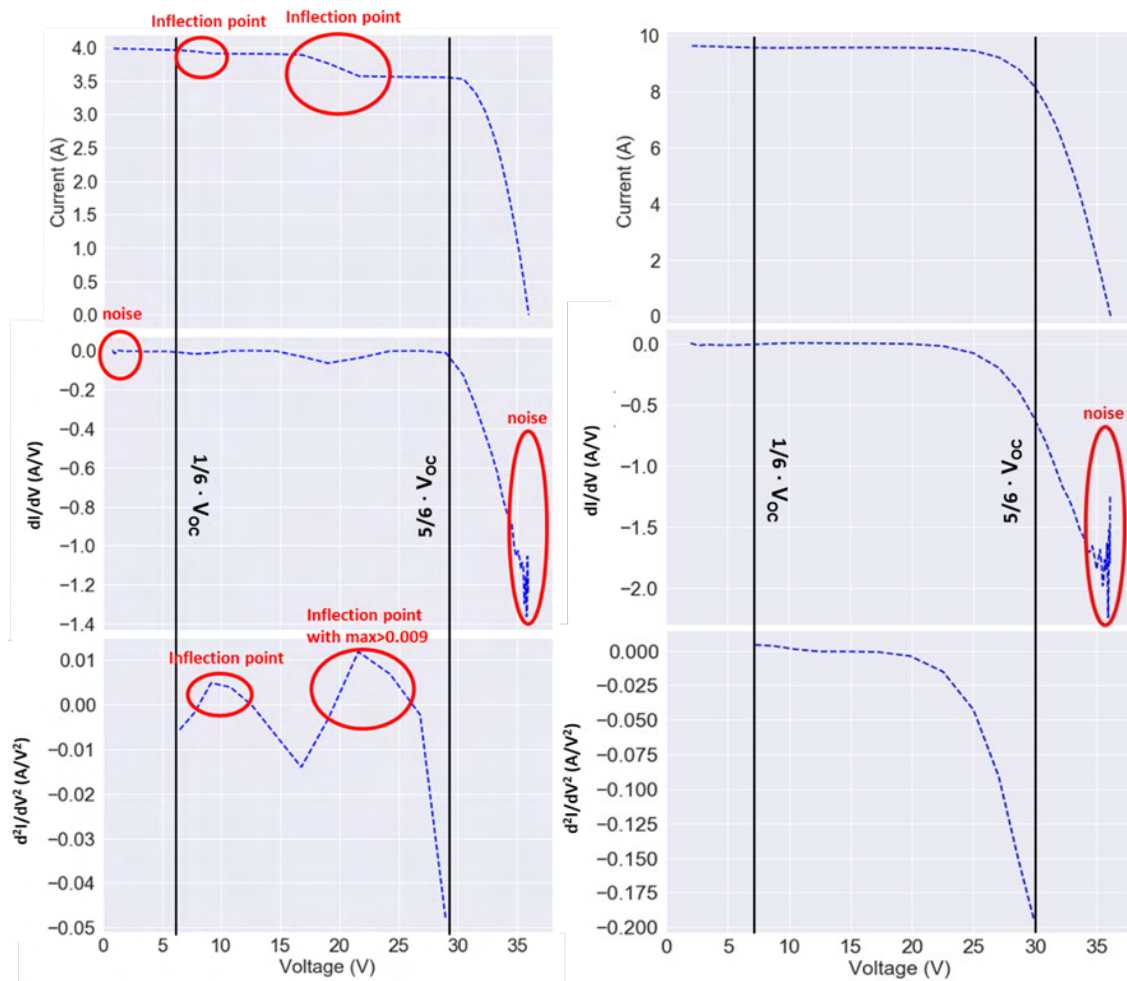


Figure 5-5 Examples of I-V curves and their derivatives for channel 4: with inflection points due to shading (left), and without inflection points (right).

### 5.3.3. De-spiking of the I-V curves

In the case of a noisy I-V curve that contains spikes (spurious single points that do not follow the curve, caused by defective signal of the measurement unit), de-spiking is required. This method is specific to the measurement system and not a generally-applicable method, as other measurement systems may have different idiosyncrasies and need specific data quality control procedures. To achieve this, the absolute z-score (the number of standard deviations difference between the point and the mean current, see Appendix 6 for further details) of the current, for voltages between 0 and  $0.55 \cdot V_{oc}$  (the largely constant-current part of the I-V curve) is calculated, as potential spikes are only observed within this part of the I-V curves.

If only a single current point is found with an absolute z-score value higher than 3, then the current-value point is replaced with that of the previous point of the I-V curve (the voltage step and curve gradient are both small). The steps of this procedure are shown in Figure 5-6. If more than one point has a high z-value, the I-V curve is regarded to contain some noise (small enough to not be detected by the procedure described in section 5.3.2) and then undergoes the rest of the filtering criteria.

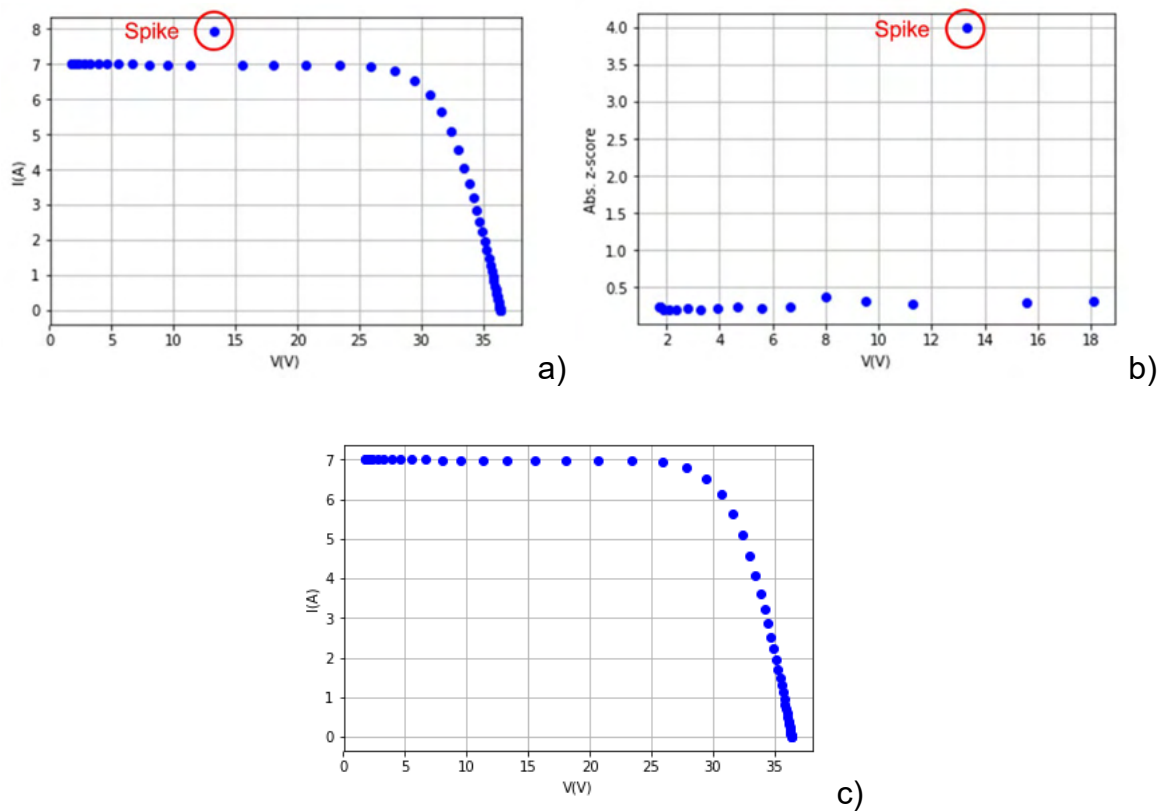


Figure 5-6 The de-spiking procedure: (a) I-V curve before de-spiking, (b) the absolute z-scores and c) the I-V curve after de-spiking.

#### 5.3.4. Filtering of fitted I-V curves according to the fitting RMSE value

For the selection of the I-V curves which show the best fitting, to obtain a more accurate  $R_s$  extraction, the fitted I-V curves are filtered according to their Root Mean Square Error (RMSE) to the corresponding measured curve. Assuming that, due to the Trust Region optimisation, the diode model parameters selected correspond to

the minimum RMSE, I-V curves with high RMSE should be excluded, as the high RMSE values indicate that the calculated diode model parameters are far from these of the measured I-V curve. The acceptable threshold for RMSE between the simulated and measured I-V curve, is set to be 0.02. To give examples of how variation in the fit RMSE appears, the fitting of three I-V curves, of RMSE 0.012, 0.0199 and 0.046 are presented in Figure 5-7. Areas of divergence between the data and fitted curve are highlighted in red.

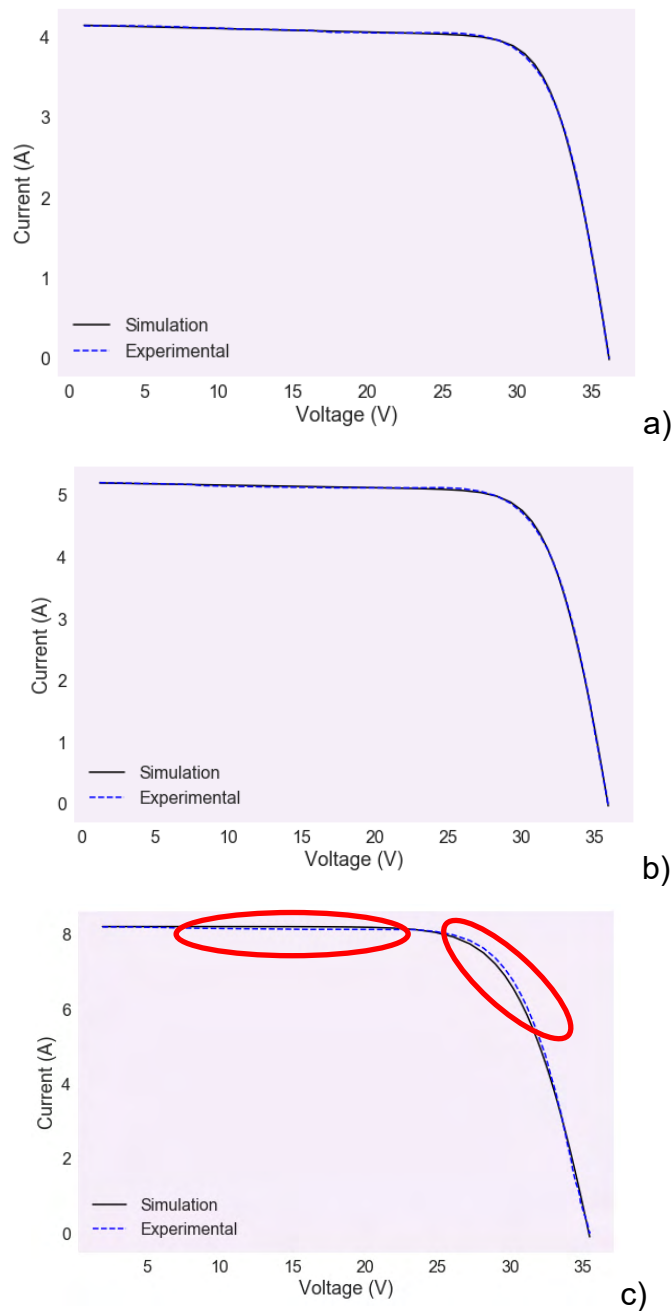


Figure 5-7 The fitting of three I-V curves with a) RMSE = 0.012, b) RMSE = 0.0199 and c) RMSE = 0.046.

## 5.4. Results

This section will analyse the  $R_s$  evolution and the impact on FF and power output for the investigated PV modules over the studied years. For the verification of the observed evolution pattern, the average  $R_s$  values are calculated for bins of measurements by different months and at various temperature and irradiance range combinations. If the power output of a PV module shows a degradation pattern, which  $R_s$  values cannot explain, further investigation is conducted into the  $I_{SC}$  and  $V_{OC}$  evolution.

### 5.4.1. Availability of data

After selecting the data corresponding to the specific bins described and analysed in section 5.4.4, but before the further filtering and fitting of the model for extraction of  $R_s$  and the other electrical parameters, the number of data sets for each month were counted to check the data availability (Figure 5-8). For all the PV modules, there is no data around 2014-15, as a lightning strike hit the roof and the measurements stopped until repairs could be completed. Shortly after the repairs, the measurements were interrupted for a second time, due to some module rearrangements.

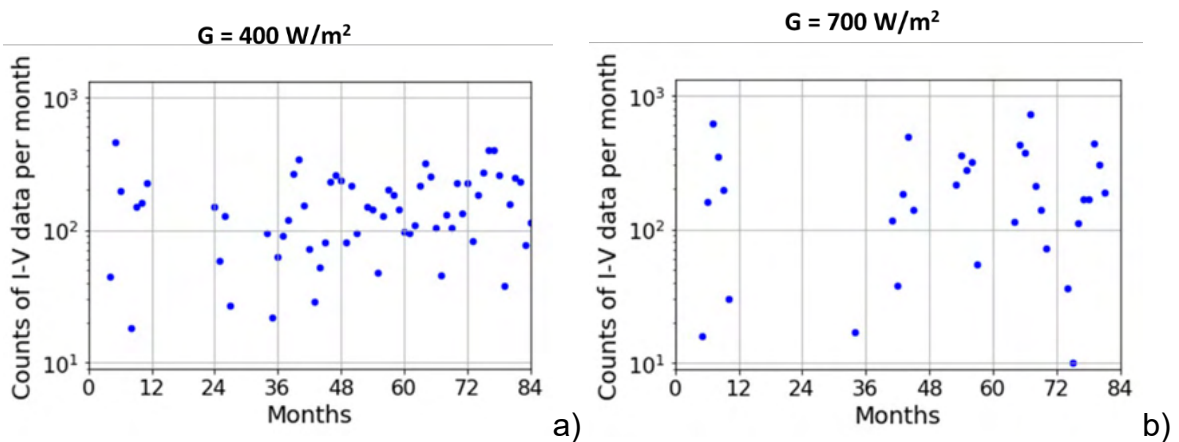


Figure 5-8 Counts of the I-V curve data per month for all the years and the PV module measured by channel 2 for the bin of a)  $G = 400 \text{ W/m}^2$  and b)  $G = 700 \text{ W/m}^2$ .

#### 5.4.2. Data usability after fitting

Table 5-3 demonstrates the percentage of I-V curves that met the filtering criteria (according to section 5.3.1) used for the extraction of the electrical parameters per year, for all of the PV modules studied. The PV module with the best quality data seems to be the one connected to channel 7 (23% - 94.6% usability), while the PV module that shows the worst quality data is that measured by channel 3 (2.8% - 15.1% usability). Useful I-V curves could not be obtained for the modules connected to channels 11 and 12 for the last years of operation, as, although the signal was measured, it was not representing an I-V curve due to disconnection. Bad quality data may correspond to a larger number of I-V curves affected by shading, or more noisy data due to the signal that the channel receives. Channel 2 seems to be mainly affected by shading (due to some structures on the roof that partially block the illumination during the early morning hours), while for the other channels, no clear pattern is observed. This leads to the conclusion that the quality of the data obtained is dependent on the communication systems of the channels. This can be also confirmed for the PV modules connected to channels 7, 9, 11, 12, 13 and 14, as they show completely different data quality when they are reconnected at the end of the year 2015.

Table 5-3 Percentage of I-V curves suitable\* for the extraction of the electrical parameters per year for all the studied PV modules.

Year	CH002 (%)	CH003 (%)	CH004 (%)	CH006 (%)	CH007 (%)	CH008 (%)
2013	11.0	15.1	75.6	9.7	23.0	12.1
2014	19.4	3.3	44.8	9.4	41.0	11.4
2015	9.0	4.5	50.9	14.2	49.7	12.5
2016	4.6	2.8	68.7	17.9	94.6	12.2
2017	6.6	3.1	66.6	20.8	93.9	10.5
2018	5.5	3.8	64.3	18.2	94.4	8.5
2019	5.4	3.7	59.3	20.7	94.4	7.9
<b>Average</b>	8.8	5.2	61.5	15.8	70.2	10.7

Year	CH009 (%)	CH010 (%)	CH011 (%)	CH012 (%)	CH013 (%)	CH014 (%)
2013	6.8	11.9	6.6	9.0	20.2	29.0
2014	6.9	11.4	7.0	5.8	25.0	39.4
2015	7.4	11.8	8.5	9.5	29.6	41.5
2016	38.0	11.0	26.7	40.8	88.5	85.0
2017	37.8	10.2	24.7	46.9	90.5	87.4
2018	40.2	11.3	30.9	-	91.7	85.0
2019	43.5	11.2	-	-	83.4	90.6
<b>Average</b>	25.8	11.3	17.4	22.4	61.3	65.4

\*The data obtained for the year 2014 were not used for the evolution analysis as they only correspond to the I-V curves measured during half a month.

### 5.4.3. Accuracy of the fitting model examined by the comparison between the simulated and measured $P_{max}$

To verify the accuracy of the fitted one-diode model to the I-V curve measurements, the average  $P_{max}$  values, obtained by measurement for each year for the module measured by channel 2, were compared to the corresponding values extracted from the fitted diode model. The conditions chosen were  $250 < G < 350 \text{ W/m}^2$  ( $300 \pm 50 \text{ W/m}^2$ , a larger filter than the  $\pm 20 \text{ W/m}^2$  applied in literature [190], as some of the I-V curves are filtered out and more data are needed) and  $290 < T < 294 \text{ K}$  ( $292 \pm 2 \text{ K}$  according to the standard IEC 60904-1 [191]). Figure 5-9 represents the good correlation of the model to the measured values, as the highest deviation between them is only 0.34%.

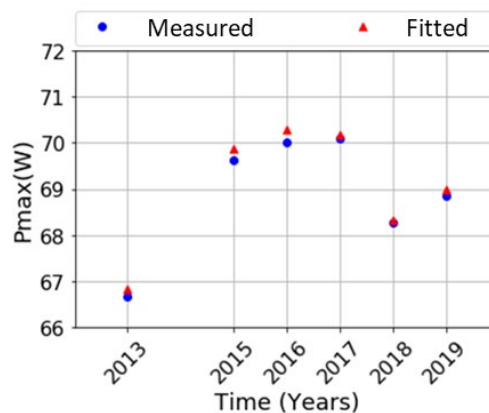


Figure 5-9 Yearly average values of  $P_{max}$  measured and fitted points.

#### 5.4.4. Performance evolution for all the PV modules at specific temperature and irradiance conditions

The maximum power output of the PV module is the most significant performance indicator for a PV module. For the observation of the  $P_{\max}$  evolution, the simulated  $P_{\max}$  values, extracted from I-V curves measured within specific irradiance and temperature conditions, were averaged for two selected months. For this analysis, the conditions chosen were  $400 \pm 50 \text{ W/m}^2$  and  $292 \pm 2 \text{ K}$  (combination of low temperature and irradiance) for month October and  $700 \pm 50 \text{ W/m}^2$  and  $315 \pm 5 \text{ K}$ <sup>12</sup> (combination of high temperature and irradiance) for month July. The specific months were chosen due to the seasonality of the data. For modules with no data available at these specific months, May was chosen instead of October (Channels 8, 11 and 12) and June alternatively to July (Channel 12), according to the availability of the data. The same procedure was repeated for the calculation of the evolution of the rest parameters.

From Figure 5-10, it is observed that five out of twelve PV modules did not show any change. For three PV modules, those connected to channels 6, 8 and 12, a degradation in  $P_{\max}$  was observed of 10.7%, 10.2% and 5.5% respectively, with all the reduction percentages being within the relative standard deviation values. The more significant decrease occurs between 2016 and 2017, depending on the PV module. Furthermore, for the PV modules monitored by channels 4 and 9, one month did not experience any degradation, and for the other month, the  $P_{\max}$  decreased by 7.3% and 6.2% respectively, but still within the respective relative standard deviation values. The modules measured by channels 3 and 10 showed similar behaviour as channels 4 and 9, but the reduction was higher (17% and 16.4% respectively) than the relative standard deviation values. According to the  $I_{sc}$  evolution of the PV modules presented in Figure 5-10, the power output degradation is observed to occur due to  $I_{sc}$  reduction, as the degradation pattern is the same and the decrease is by 16.3% and 17.4% for the modules connected to channel 3

---

<sup>12</sup> The range of the filter is larger, as less data are available for high temperatures and irradiances, for this specific type of climate.

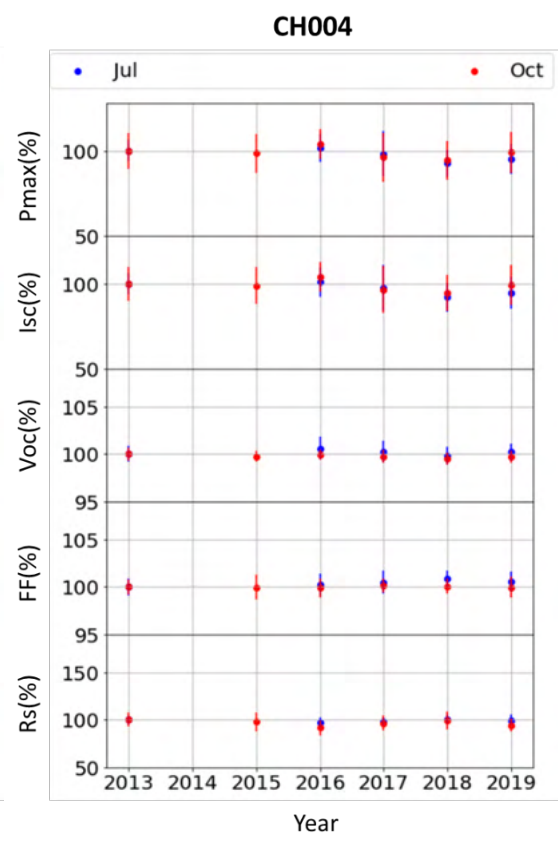
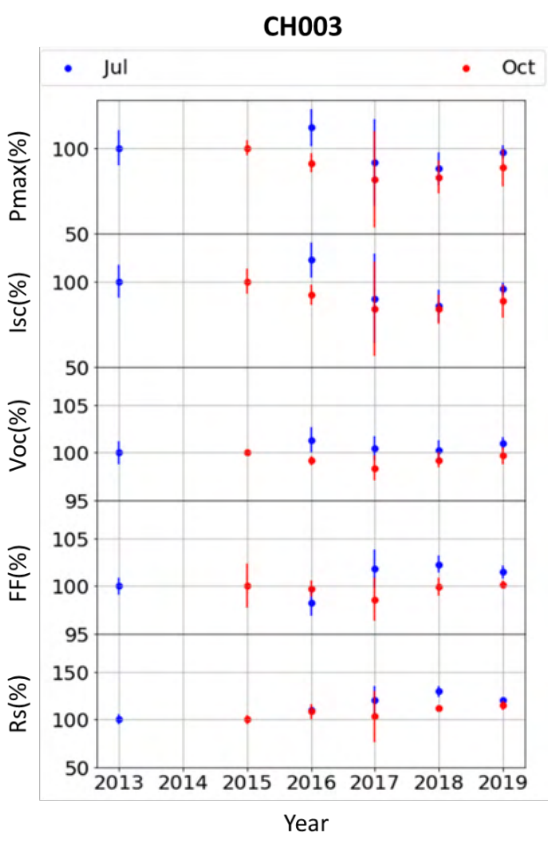
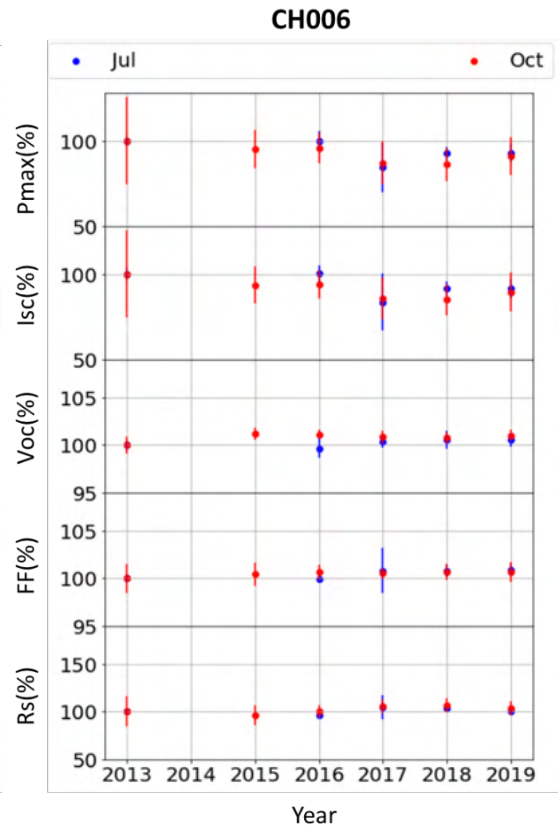
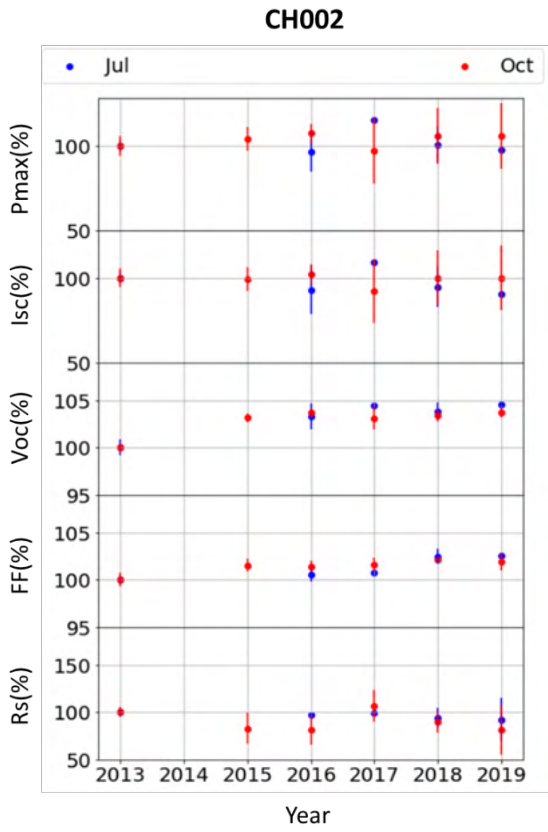


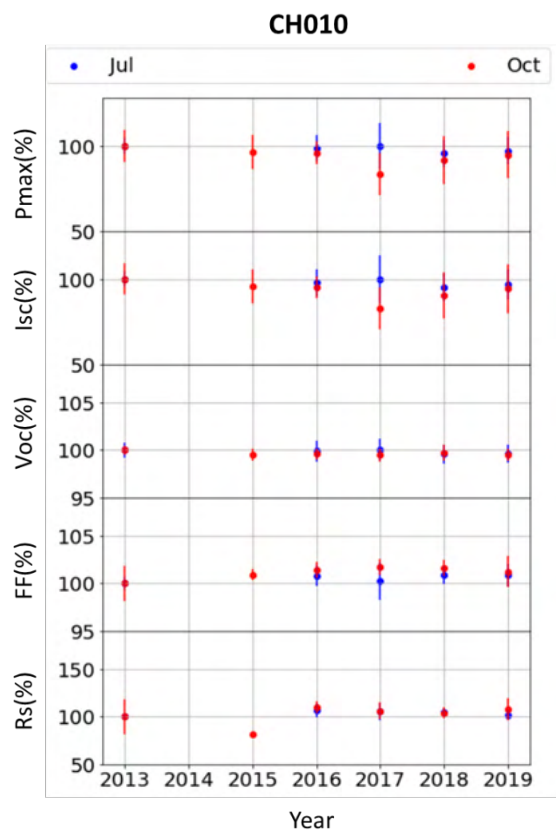
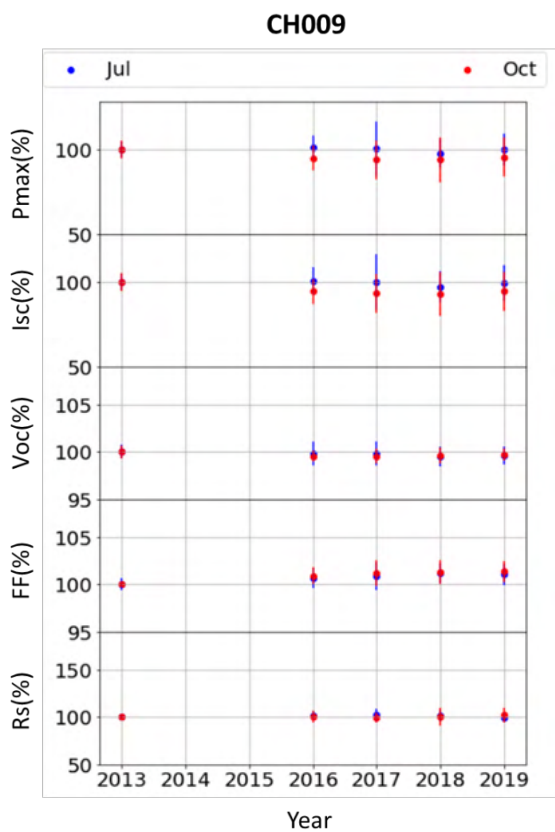
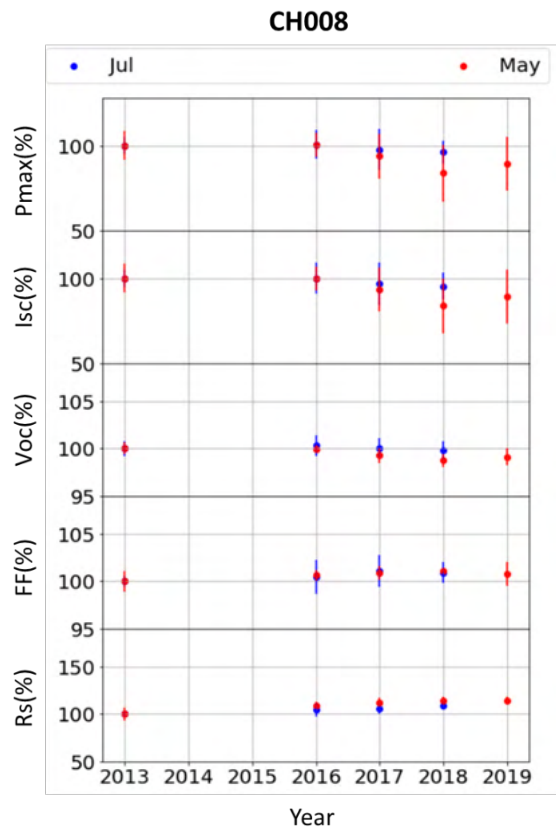
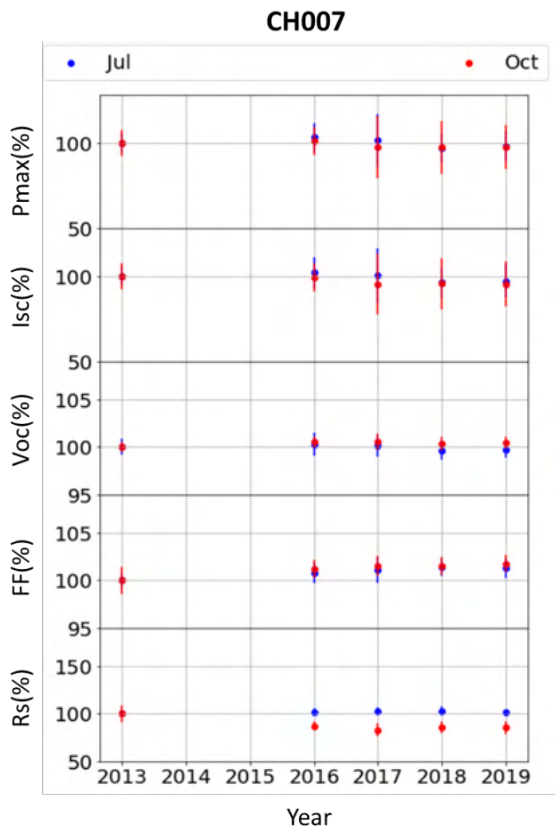
and 10, respectively. The  $I_{SC}$  evolution of the rest of the PV modules was either stable or within the relative standard deviation values.

Regarding the behaviour of the  $V_{OC}$ , the module measured by channel 2 increases by 4.2%, which is higher than the relative standard deviation values. Furthermore, for the PV modules measured by channel 11 and 12, reduction by 3.2% and 2% is identified, respectively, higher than the relative standard deviation values. However, the  $V_{OC}$  change is not strong enough to impact the  $P_{max}$  degradation, with  $I_{SC}$  being the main factor that affects the  $P_{max}$  evolution.

As the purpose of this chapter is to identify power output degradation of PV modules aged outdoors due to corrosion, the behaviour of the FF of the modules should be investigated as well. Significant change is not observed in the FF evolution for all the PV modules, or when obtained, the variation is within, or very close to the relative standard deviation of the values. This observation indicates that if any increase of the  $R_s$  is detected, does not have any impact on the FF of the PV modules.

Last, but not least, the evolution of the  $R_s$  through the years is analysed, as the main diode model parameter affected by corrosion. It was found that for five out of twelve PV modules (Channels 2, 4, 6, 9, 10) the change in  $R_s$  did not follow any trend. For the modules measured as channels 3, 8, 11 and 12 the average increase was 22%, 11.5%, 49% and 40.2% respectively, which is significant when compared to the relative standard deviation values, but does not lead to significant changes in power because the absolute values of  $R_s$  are still very small (m $\Omega$ ). The rise for the mentioned PV modules occurs after year 2016. The PV modules connected to channels 13 and 14 showed an average  $R_s$  decrease by 9.2% and 11.7% respectively, which is slightly higher than relative standard deviation values observed. Finally, for the PV module monitored by channel 7, no significant difference was observed for month July, but a significant decrease for unspecified reasons (14.9%) was obtained for the month of October, compared to the average relative standard deviation value. However, this decrease does not have any impact on the power output for the reasons described in the analysis of channels 3, 8, 11 and 12.





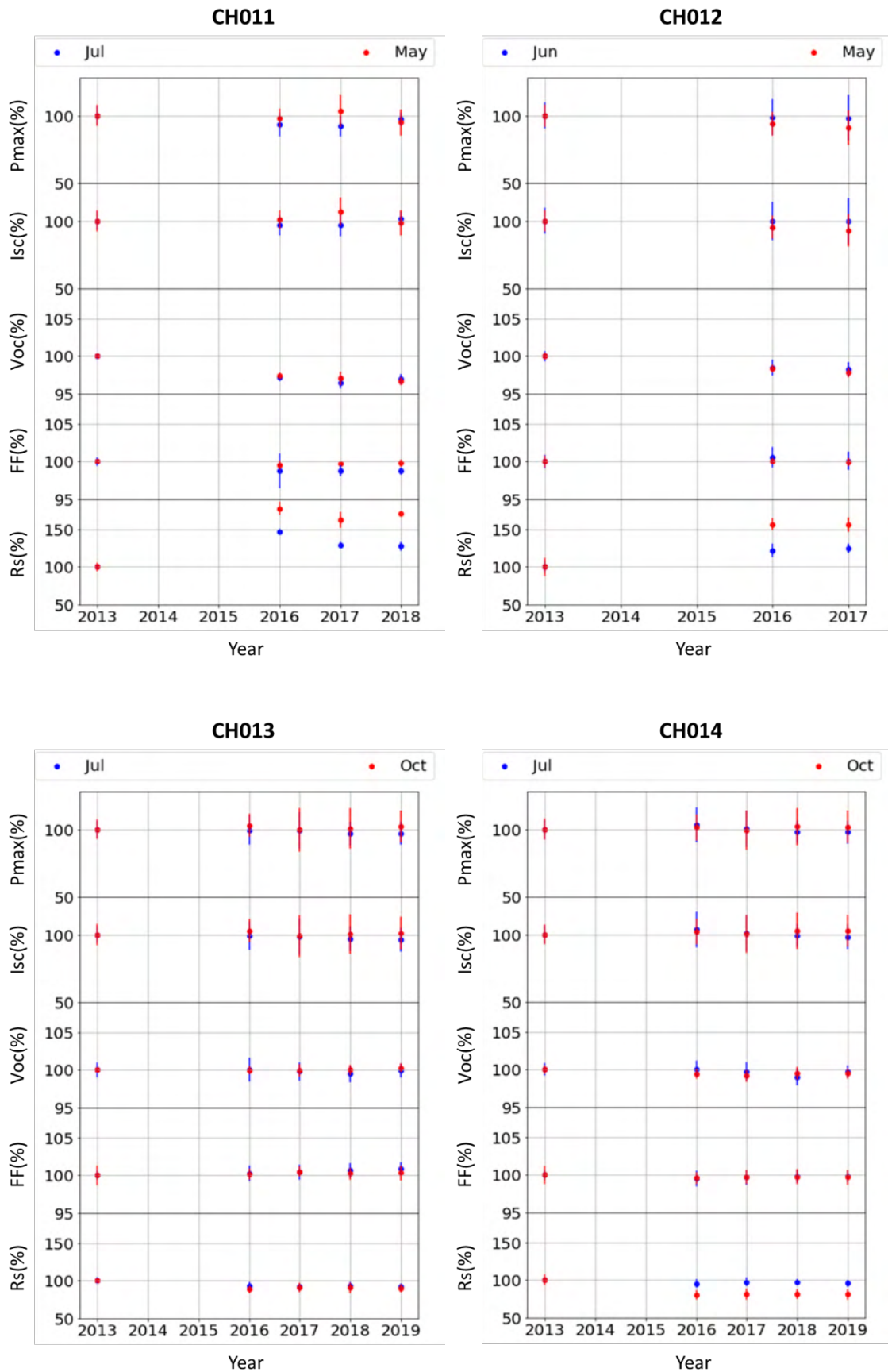
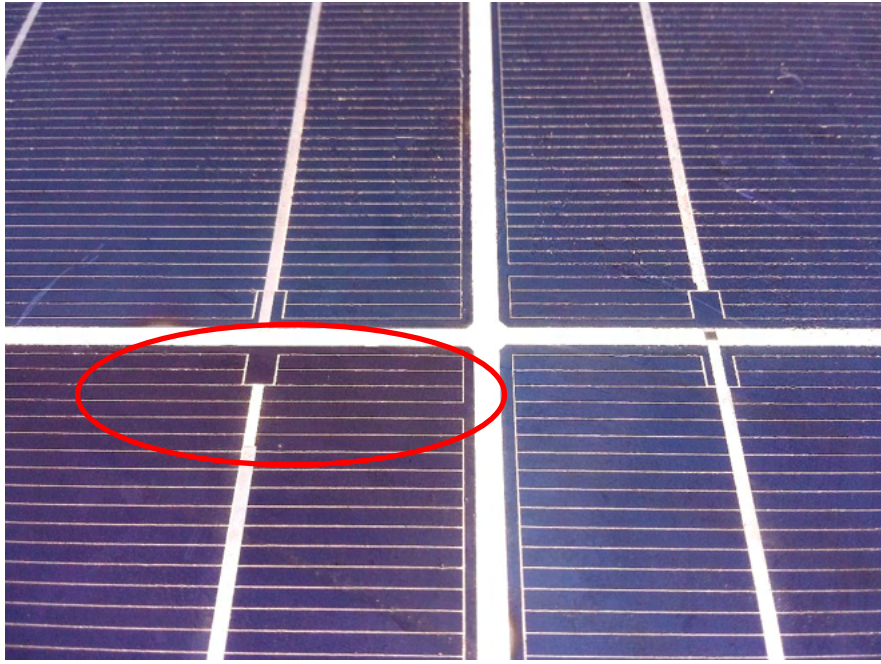


Figure 5-10 Evolution of the performance parameters for all the studied PV modules and the different bins analysed.

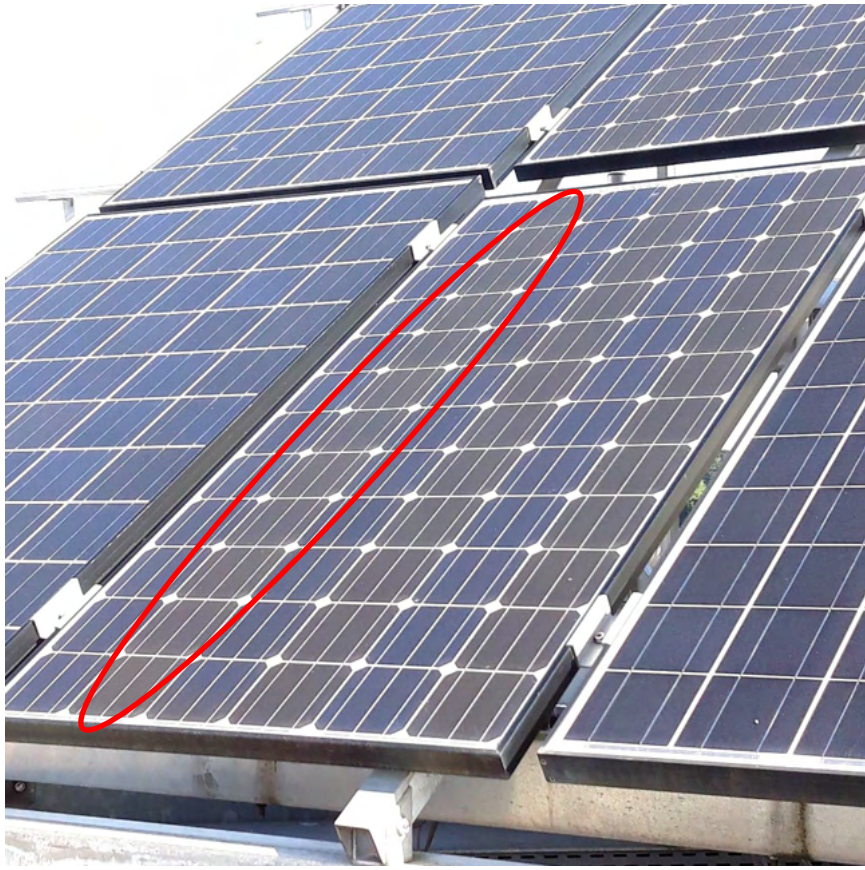
#### 5.4.5. Identification of failure modes by visual inspection

To identify the failure modes responsible for the changes in electrical parameters seen in the previous sections, the studied PV modules were inspected visually. Eight of the twelve PV modules did not show any defects. The modules connected to channels 3 and 4 developed heterogenous encapsulant discolouration on the edges of the cells, close to the initiation of the ribbons' soldering (Figure 5-11a). The reason responsible is possibly faulty soldering during the manufacturing process, which caused local increase of temperature due to a high resistance and, subsequently, encapsulant discolouration. A thermographic image could possibly confirm this scenario. The observed degradation mechanism explains the  $R_s$  increase on the PV module measured by channel 3 (faulty soldering), and the  $P_{max}$  and  $I_{sc}$  decrease on the PV modules monitored by channels 3 and 4 (encapsulant discolouration), with channel 4 impacted less (within the uncertainty) than channel 3. Furthermore, for the modules connected to channels 11 and 12 (heterojunction, HIT technology) discolouration, possibly due to the transparent conductive oxide, was observed on some cells (Figure 5-11b), which may be triggered by exposure to UV irradiation and humidity [192]. Although no  $P_{max}$  degradation was observed, the degradation mechanism affected the  $R_s$  and  $V_{OC}$  of the PV modules, but not significantly. Regarding the PV module monitored by channel 10, although  $P_{max}$  and  $I_{sc}$  reduction was observed, no defect was identified by visual inspection. Finally, corrosion was not observed on any PV module.





a)



b)

Figure 5-11 Visual inspection of the PV modules measured by channels a) 4 and b) 12. The red ellipses indicate the encapsulant and transparent conductive oxide discolouration, respectively.

## 5.5. Conclusions

The purpose of the work in this chapter was to investigate the contribution of corrosion on the power output degradation of PV modules exposed to a non-tropical environment, and more specifically temperate oceanic (Cfb), according to the Köppen–Geiger climate classification system. To achieve this goal, the I-V curves of twelve PV modules, installed in for 7 years, were fitted to the single diode model mainly for the extraction of the  $R_s$  values and secondary for the evaluation of the other performance parameters. Filtering was applied to remove I-V curves affected by shading or signal noise and de-spiking was used for the removal of any spikes. Furthermore, only the data that showed good fitting to the model were used, for the final estimation.

The average values of the parameters at two specific environmental conditions (low and high temperature-irradiance) were used for the identification of the evolution pattern over the years. The results show that the  $R_s$  change identified for some of the modules did not affect the FF and, subsequently, the  $P_{max}$  evolution, due to the initially very low value of  $R_s$ . Most of the studied PV modules did not show any  $P_{max}$  degradation, except two, where the  $P_{max}$  decrease coincides with  $I_{sc}$  reduction and is significant. The reason responsible for this degradation, for one PV module, is identified by visual inspection, as heterogenous encapsulant discolouration due to faulty soldering during the manufacturing process, which caused locally increased temperature. No obvious defects were detected for the other PV module. Furthermore, although the  $P_{max}$  of the HIT PV modules did not degrade, discolouration possibly due to transparent conductive oxide degradation was visible, which resulted to  $R_s$  increase and  $V_{oc}$  decrease, and was probably provoked, according to literature, by UV light and humidity exposure, something that needs further investigation for a most robust conclusion. Although no corrosion was observed, we cannot conclude that this type of climate does not provoke such reactions, as the studied performance data regard only a relatively short exposure period and not the lifetime of the PV modules.

The described methodology can be applied to I-V curve data of PV modules exposed to different climates, for the investigation of corrosion and other types of

degradation mechanisms. Moreover, when accompanied by EL imaging different degradation mechanisms with similar electrical signature can be distinguished.



# Chapter 6 Thesis Conclusions

## 6.1. Conclusions arising from this work

The purpose of the work described in this thesis was to investigate the degradation mechanisms that cause corrosion of different components of PV cells and determine the impact on the electrical output of PV modules. More specifically, the research topics analysed were:

- Theoretical and experimental quantification of the moisture content and determination of the moisture distribution within a PV module exposed to specific environmental conditions.
- Investigation of the chemical reactions occurring and identification of the separate impact of the component corrosion on the PV performance of a PV module.
- Quantification of the corrosion impact on the electrical performance of PV modules exposed to outdoor conditions, for a temperate oceanic (Cfb) climate.

### 6.1.1. Moisture ingress into PV modules

The research presented in Chapter 3 investigated the quantification of the moisture content absorbed by a PV module and the moisture profiles over time, due to accumulation at the front side of the PV cells, when exposed to a given environment. Different theoretical models for simulation of the diffusion and prediction of the absorbed content were applied and validated with multiple experimental methods. For correct interpretation of the moisture diffusion, Fick's law was validated against Relative Moisture Content (RMC) measurements within laminates, obtained with embedded digital humidity sensors for both moisture ingress and egress over time. According to the results, the model describes the moisture diffusion with some small

deviations (+10%, -14% maximum) which indicate that either a modification of the model or a recalibration of the sensors, according to the material they measure, is needed.

For the accurate quantification of moisture content absorbed by a PV module, two different models, Henry's law and the Perrin and Favre model, were fitted to measurements obtained by Karl-Fisher Titration taken on different combinations of materials exposed to different environmental conditions. The Perrin and Favre model is better for the representation of the absorption isotherm of the materials ( $R^2 \sim 1$  with random residual pattern), when compared to Henry's law ( $R^2 \sim 0.95$  with specific residual pattern, which shows that the uncertainty that the model introduces to the fitting is not random, meaning that the fitting method is biased). In addition, the moisture content absorbed by the EVA varies when the backsheet is added, which is an indication that the interactions between the two materials should be considered for the correct estimation of the moisture content absorbed by a multi-layer laminate PV module. Moreover, the crosslinking of the EVA may vary when laminated with other polymers.

Regarding the mapping of moisture distribution within the EVA layer between the front side of the PV cell and the glass, a novel measurement method is introduced, involving embedding humidity indicator cards, which change colour according to the moisture level to which they are exposed. The results show that the method is appropriate for moisture quantification, with the provision that it is adequately calibrated according to the exact polymer structure on which the measurement is acquired. Furthermore, the method is more compatible with polymers that do not require crosslinking and/or produce acetic acid due to hydrolysis.

Finally, from the simulation of the moisture ingress (application of Fick's law) in single-cell mini-modules with different types of back-sheet, or with the rear side exposed, and the identification of the moisture profile by the embedded humidity indicator cards, it is concluded that the time demanded for the moisture saturation is mainly affected by the diffusion coefficient of the EVA and not that of the backsheet, especially for this specific structure of samples.

### 6.1.2. Corrosion behaviour of the different components in a PV module

The analysis presented in Chapter 4 regarded the development of a method for identification and separation of the different corrosion mechanisms and their impact on the PV electrical output. Half encapsulated PV cells were immersed in acetic acid solutions and water, with their front or rear side exposed, or aged under DH conditions. The mechanisms identified are related to those occurring for fully encapsulated PV modules exposed to the same DH conditions. The combination of electrical (I-V curves, EL imaging and SR measurements) and material (optical microscopy and SEM-EDS analysis) characterisation is used for the investigation of the different mechanisms. PERC c-Si cells were also considered, as the currently most used technology.

As concluded from the results, front side corrosion may occur in fully encapsulated PV modules. According to the comparison between the acetic acid immersion and DH exposure, for higher concentrations of acetic acid at room temperature the weakest interface is that between the ribbon and the busbar, due to solder etching, while for higher temperatures (DH exposure) both ribbon-busbar and busbar-cell interfaces are susceptible. Moreover, acetic acid is the main factor responsible for the front side corrosion, as water is not so reactive when absorbed by the encapsulant, as observed for the DH aged PERC mini-modules.

Although front side corrosion may occur in a PV module, this is not the case for the Al-contact corrosion, something that contradicts the research presented in the literature, which supports that Al-contact corrosion is relevant to fully encapsulated PV modules and increases with highly acidic environment. According to the results, the moisture is not so reactive when the PV cell is fully encapsulated, as it does not condense on the surface of the Al contact. Furthermore, the reaction with acetic acid is not severe, as it is terminated immediately when a protective oxide is produced.

Regarding DH degradation of PERC c-Si cells, decreased  $V_{oc}$  and FF were observed, which is not usually the case for typical c-Si cells. The reason was most likely a failure related to increased defects caused on the rear surface of the silicon,

due to temperature related degradation of the passivation layer. However, this finding requires further investigation for a more valid conclusion.

Finally, the difference in backsheet for this experiment did not affect the performance of the mini-modules regarding degradation modes related to moisture ingress.

### **6.1.3. The impact of corrosion on PV modules aged in the field**

The work analysed in Chapter 5 achieved a method to partially understand the effect of corrosion (and detect additional degradation modes) on the electrical performance of PV modules exposed to a non-tropical (temperate oceanic) environment, despite the difficulty to differentiate between the electrical signatures of various degradation modes occurring simultaneously. The procedure involves the estimation of the series resistance evolution in the first place, and secondarily the remaining performance parameters, of PV modules operating at Loughborough university for 7 years. The methodology includes filtering of partially-shaded or noisy I-V data, de-spiking of curves having single-point outliers and fitting to the one-diode model. Visual inspection is used for identification of the degradation modes causing the observed electrical signatures.

According to the results obtained, the  $R_s$  increase observed for four out of twelve PV modules did not influence the FF and  $P_{max}$  evolution. Only two PV modules developed significant  $P_{max}$  degradation, which evolved after the year 2017 (year 5 of exposure), correlated to  $I_{sc}$  reduction. Visual inspection reveals that the specific electrical signature is linked to heterogenous encapsulant discolouration for one of them, while no specific degradation mode was identified for the other. Moreover, the HIT PV modules developed  $R_s$  increase and  $V_{oc}$  reduction, which did not affect the  $P_{max}$ , as the change of  $V_{oc}$  was small and increase in  $R_s$ , when the initial value is low, does not have a significant impact in the I-V curves. The mentioned degradation was likely caused by transparent conductive oxide discolouration, as the visual inspection showed, but further characterisation is required to confirm this finding. Accurate conclusions regarding the correlation between corrosion and the

specific climate cannot be drawn, as the duration of the analysis is very short compared to the lifetime of a PV module in such an operating environment (non-tropical).

## **6.2. Future avenues for research identified in this work**

For prediction of the degradation mechanisms triggered by moisture that might occur at different climate conditions, the absorption isotherms for more polymers, combinations and environmental conditions need to be identified, following the methodology that this thesis presents. Furthermore, for the improvement of sensor measurements (from digital sensors or indicator cards) the proposed method is that the sensors are calibrated first at different combinations of temperature and RH, while encapsulated at the exact laminate structure (excluding the PV cell) that they will be used afterwards for measurement, as the addition of backsheet to the encapsulant causes variations on the absorbed concentration. At the same time, the moisture uptake of the combination of the polymers should be quantified by Karl-Fischer Titration, to match the sensor value to the exact moisture content. After the described procedure, the law that the moisture diffusion follows could be accurately verified. If the measurement method used is the humidity indicator cards, their compatibility with different encapsulants and UV exposure (in case of combinatory aging tests, or outdoor exposure) should be confirmed.

Regarding the rear side corrosion which was not observed on PV modules laminated with backsheet, further research is required on double-glass modules, as the moisture in this case is trapped within the EVA layer between the rear side of the PV cell and the glass and is more likely to accumulate on the Al-rear contact. In addition, different combinations of encapsulants (e.g. TPO or POE) and backsheets (e.g. PVF or PVDF) and various wiring configurations should be studied (e.g. multiple wires or IBC), following the methodology presented in this thesis, for the research on the different corrosion mechanisms.

Furthermore, as corrosion does not affect equally the PV modules exposed to different climates and DH 85°C / 85% RH does not represent the corrosion occurring even after 25 years of exposure in some of them, different corrosion tests

should be designed for the needs of each climate (one test may not be representative for all the climates, as in some of them corrosion occurs much faster than the rest), taking into consideration the respective acceleration factors. The impact of the current flow and UV light should be incorporated additionally, as they further accelerate the procedure, but a way to isolate only their impact on corrosion must be identified (e.g. by separating the impact of the various failure modes occurring on the different electrical parameters).

Regarding the observation of corrosion on PV modules aged outdoors, future work recommends the application of the methodology presented in Chapter 5 to various PV module types (different PV polymers or cell and contact technologies) exposed to different climates for several years (life-time if possible), to identify possible patterns of  $R_s$  increase. Similar studies may have been done in the past, but not with this methodology and not so extensively. The  $R_s$  then can be linked to corrosion cases when accompanied by visual inspection and high resolution EL imaging. The  $R_s$  obtained for the PV modules with degradation identified due to corrosion, can be used as a threshold (as  $R_s$  degradation could be caused also by solder fracturing under thermal cycling) for the estimation of the respective acceleration factors, when the specific values are compared to those obtained by accelerated aging. Furthermore, the method is suitable for the analysis of different failure modes (including visual inspection and EL imaging), as all the electrical parameters can be extracted, and their evolution can be estimated.

The durability of PV modules is very important due to the impact on their lifetime performance. The stable behaviour of the PV modules aged outdoors, presented in this thesis, shows that PV technology is already durable. However, further improvement may be achieved. The research presented in this thesis contributes towards a better understanding of corrosion and other degradation mechanisms, which have a significant impact on both PV durability and project financing. Moreover, the methodologies proposed may be applied in future research, for the determination of the different material interactions and the link to outdoor performance. As a result, the materials used for PV manufacturing may be optimised, to achieve further increase of PV module life-time.

# Nomenclature

Ag: Silver

Al: Aluminium

AlO<sub>x</sub>: Aluminium Oxide

AR: Antireflective

C<sub>0</sub>: Boundary concentration (mol/m<sup>3</sup>)

Ca: Calcium

C<sub>ini</sub>: Initial concentration (mol/m<sup>3</sup>)

C<sub>s</sub>: Saturation concentration (kg/m<sup>3</sup>)

c-Si: monocrystalline silicon

Cu: Copper

D: Diffusion coefficient (m<sup>2</sup>/s)

D<sub>B</sub>: Diffusion coefficient of back sheet (m<sup>2</sup>/s)

D<sub>eva</sub>: Diffusion coefficient of EVA (m<sup>2</sup>/s)

DH: Damp-Heat

d<sub>w</sub>: fraction of the moisture mass per volume

EL: Electroluminescence

EVA: Ethylene Vinyl Acetate

FEA: Finite Element Analysis

FF: Fill Factor

FTIR: Fourier Transform Infrared

G: Irradiance (W/m<sup>2</sup>)

HAc: Acetic acid

I: Current (A)

I<sub>0</sub>: Recombination current (A)

I<sub>mpp</sub>: Current at maximum power point (A)

I<sub>ph</sub>: Photocurrent (A)

I<sub>sc</sub>: Short circuit current (A)

$K_H$ : Henry's coefficient  
LCOE: Levelized Cost of Electricity  
LeTID: Light and elevated Temperature Induced Degradation  
LID: Light Induced Degradation  
mc-Si: multicrystalline silicon  
 $m_w$ : Mass of water (kg)  
n: Ideality factor  
O&M: Operation and Maintenance  
PA: Polyamide  
Pb: Lead  
PbO: Lead oxide  
PERC: Passivated Emitter and Rear Contact  
PET: Polyethylene Terephthalate  
 $p_{H_2O}$  : Partial pressure of water (Pa)  
PID: Potential Induced Degradation  
PID-p: PID related to passivation  
PID-s: PID related to shunting  
 $P_{max}$ : Maximum power (W)  
PV: Photovoltaic  
PVB: Polyvinyl Butyral  
 $R_D$ : Degradation rate  
RH: Relative Humidity  
RMC: Relative Moisture Content in relation to the saturation content  
RMSE: Root Mean Square Error  
 $R_s$ : Series resistance ( $\Omega$ )  
 $R_{sh}$ : Shunt resistance ( $\Omega$ )  
S: Solubility ( $m^3/(m^3 \cdot Pa)$ )  
SiN<sub>x</sub>: Silicon Nitride  
SiO<sub>x</sub>: Silicon Oxide  
Sn: Tin



SNR: Signal-to-Noise Ratio

SR: Spectral Response

STC: Standard Test Conditions

T: Temperature ( $^{\circ}\text{C}$ , or K)

$T_{\text{amb}}$ : Ambient temperature

$\text{TiO}_2$ : Titanium Oxide

UV: Ultraviolet

V: Voltage (V)

$V_{\text{mpp}}$ : Voltage at maximum power point (V)

$V_{\text{oc}}$ : Open circuit voltage (V)

$V_{\text{p}}$ : Volume of polymer ( $\text{m}^3$ )

$V_{\text{w}}$ : Volume of water ( $\text{m}^3$ )

$\alpha$ : Activity

$\varphi$ : Moisture concentration (v/v)

# Appendices

## Appendix 1. Transformation of RGB colour coordinates to CIE xy 2D projections

### 1.1. Transformation of RGB to CIE XYZ colour coordinates

For the transformation of the RGB to CIE XYZ colour coordinates the procedure described in the following relationship is applied [193]:

$$\begin{bmatrix} X \\ Y \\ Z \end{bmatrix} = \frac{1}{b_{21}} \begin{bmatrix} b_{11} & b_{12} & b_{13} \\ b_{21} & b_{22} & b_{23} \\ b_{31} & b_{32} & b_{33} \end{bmatrix} \begin{bmatrix} R \\ G \\ B \end{bmatrix} = \frac{1}{0.17697} \begin{bmatrix} 0.49000 & 0.31000 & 0.20000 \\ 0.17697 & 0.81240 & 0.01063 \\ 0.00000 & 0.01000 & 0.99000 \end{bmatrix} \begin{bmatrix} R \\ G \\ B \end{bmatrix}, \quad (1)$$

The values of the matrix are specified by the CIE1931 RGB colour space standards [194].

### 1.2. Conversion of the CIE XYZ colour coordinates to xy 2D projections

After the transformation of the RGB colour coordinates to CIE XYZ colour coordinates, the second step is for them to then be converted to the CIE xy 2D projections. The equations applied for this purpose are [195]:

$$x = \frac{X}{X+Y+Z}, \quad (2)$$

$$y = \frac{Y}{X+Y+Z}, \quad (3)$$

## Appendix 2. Example of a full 2D colour plot on a CIE chromaticity diagram

The colour measurements obtained from the reference cards, respective to the humidity indicator cards measurements, for the PV module containing a backsheet with Al foil (after the first round of testing), are represented on a CIE chromaticity diagram in Figure 1.

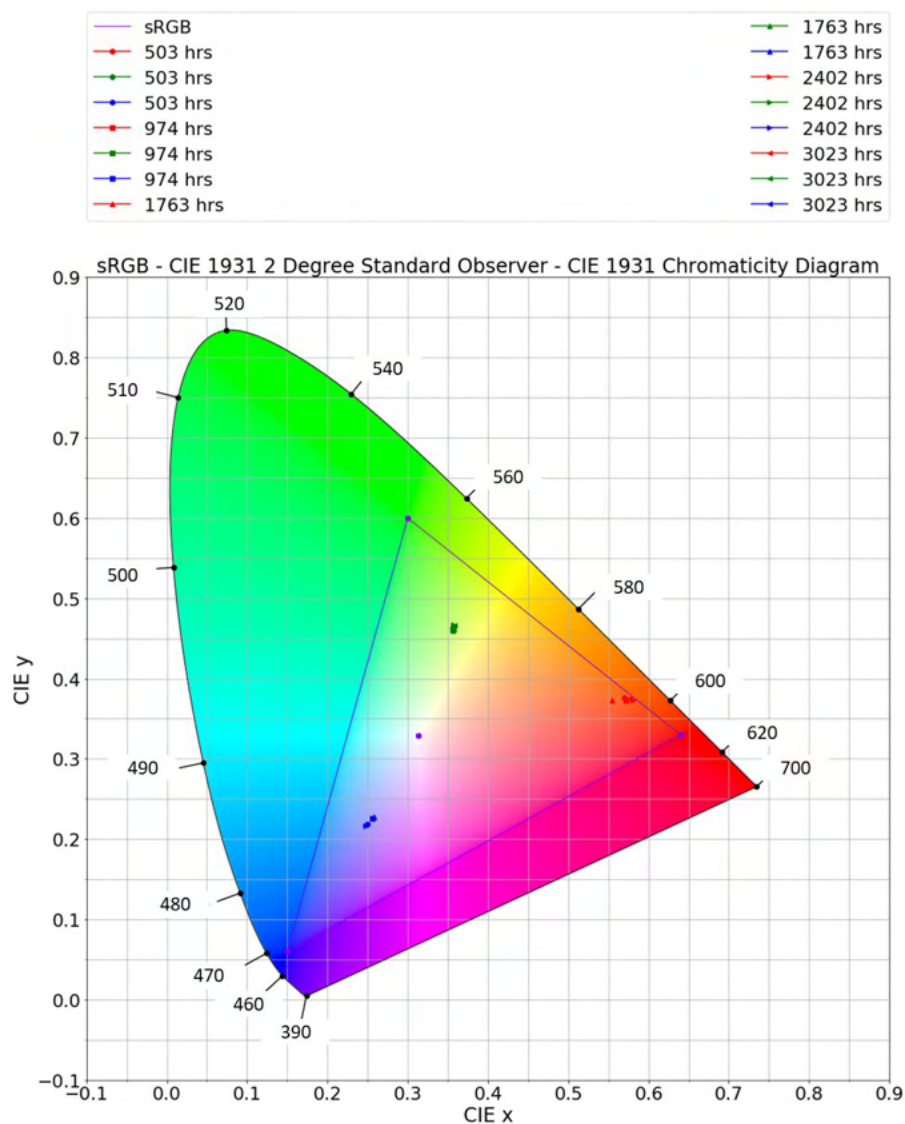


Figure 12 Colour measurements for the reference cards, respective to the humidity indicator cards measurements, for the PV module containing backsheet with Al foil (first round).

### Appendix 3. Linear interpolation of the I-V curves

Although the I-V curve measurements are taken with small I/V steps ( $\sim 0.017$  V), for the estimation of a specific pair of non-measured values that belong to a specific I-V curve, a linear interpolation function is required. To achieve that, initially, the V axis is split into very small intervals using the Python NumPy function `np.linspace()` to give a total of 6000 values [196]. After that, for each  $V_i$  of the new V axis, the equation below is applied [197] for the estimation of the respective  $I_i$  (Figure 2), by using the Python SciPy function `interpolate.interp1d()` [198].

$$I_i = \frac{I_2 - I_1}{V_2 - V_1} (V_i - V_1) + I_1, \quad (4)$$

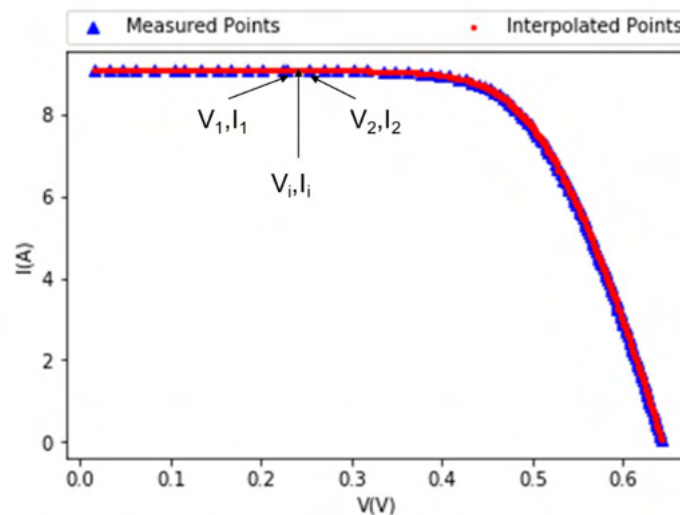


Figure 13 Graphical representation of the linear interpolation applied to an I-V curve.

## Appendix 4. Newton-Raphson method for the solution of the single diode model

For the solution of the single diode model the Newton-Raphson method was used. According to this method, an initial estimation of a voltage (or current value) is assumed and then iteratively improved, according to the algorithm:

$$V_{D,(k+1)} = V_{D,k} - \frac{f(V_D)}{\left[\frac{df(V_D)}{dV_D}\right]} \Big|_{V_D=V_{D,k}}, \quad (5)$$

Where  $V_{D,k}$  is the  $k^{\text{th}}$  estimation,  $V_{D,(k+1)}$  the  $(k+1)$  estimation and  $\frac{df(V_D)}{dV_D} \Big|_{V_D=V_{D,k}}$  the derivative of  $f(V_D)$  at  $V_{D,k}$  [199]. In the case of the single diode model the  $f(V_D)$  for a current  $I$  is given by the following equation:

$$f(V_D) = I_{\text{ph}} - I_0 \left[ \exp\left(\frac{q(V+IR_s)}{nk_B T}\right) - 1 \right] - \frac{V+IR_s}{R_{\text{sh}}} - I, \quad (6)$$

where  $I_{\text{ph}}$ ,  $I_0$ ,  $q$ ,  $R_s$ ,  $n$ ,  $k_B$  and  $R_{\text{sh}}$  are described in section 2.2.

The iterations stop when the voltage value, that satisfies sufficiently the relationship below, is found.

$$f(V_D) = 0, \quad (7)$$

The procedure starts for  $I = 0$  A and  $V_D = V_{\text{OC}}$  and continues for the remaining measured values  $I$  for each I-V curve.

## Appendix 5. Derivative calculation and counting of peaks

### 5.1. Derivative calculation

For the estimation of the current derivative, i.e. the rate of change of current,  $I$ , with  $V$ , the current is regarded as an  $I(V)$  function and the following relationship is applied [200]:

$$\hat{I}_i^{(1)} = \frac{h_s^2 I(V_i + h_d) + (h_d^2 - h_s^2) I(V_i) - h_d^2 I(V_i + h_s)}{h_s h_d (h_d + h_s)} + O\left(\frac{h_d h_s^2 + h_s h_d^2}{h_d + h_s}\right), \quad (8)$$

where,  $h_s$  is the difference between  $V_i$  and  $V_{i-1}$  and  $h_d$  the difference between  $V_i$  and  $V_{i+1}$ . For the calculation of the second derivative of the gradient, the same function is then applied to the first derivative (gradient) results.

### 5.2. Counting of peaks

In order to count the number of positive peaks in the second derivative of the current ( $d^2I/dV^2$ ), the following procedure is followed, by applying the `sp.signal.find_peaks_cwt()` Python function. First, the Continuous Wavelet Transform (CWT) matrix [201] of the second derivative of current is estimated. The rows of the matrix are the Ricker function [202] applied to the second current gradient for a range of widths, as defined by the  $V$  values i.e:

$$f_{\text{ricker}} = A \cdot \left(1 - \frac{X_i^2}{V^2}\right) \cdot \exp\left(\frac{-X_i^2}{2 \cdot V^2}\right), \quad (9)$$

Where the  $X_i$  are the second current gradient values,  $V$  the widths and  $A = \frac{2}{\pi^4 \cdot \sqrt{3 \cdot V}}$ .

After the CWT matrix estimation, the ridge lines are identified [189]. To achieve this, the relative maxima of the matrix are calculated. At each row, a ridge line is only connected if the relative max at row[n] is within a specific maximum distance (one quarter of the width of the specific row) from the relative maximum at row[n+1]. If a

relative maximum value is not found, then a gap is identified. If the number of gaps is bigger than 1, then the ridge line is discontinued. For counting of the peaks, the ridge lines must be filtered [189]. The lines selected are only those where their length is bigger than 1/4 of the total count of the widths. Moreover, the ratio between the CWT matrix, at the point of the line with the shortest length scale, and the 10<sup>th</sup> percentile<sup>13</sup> of the CWT matrices of the rest of the points contained within a specific window (1/20 of number of points of the second current gradient), must be bigger than 1 (i.e. the SNR is greater than 1) [189].

## Appendix 6. Z-score

A z-score gives the difference between an individual point and the mean value of all of the other points, within a set of values, in terms of the number of standard deviations. The z-score is calculated according to the relationship below [203], [204]:

$$z_i = \frac{x_i - \bar{x}}{s}, \quad (2)$$

where  $x_i$  is the value of the point,  $\bar{x}$  is the mean value of the set of points and  $s$  is the standard deviation of the set of points.

---

<sup>13</sup> The 10<sup>th</sup> percentile is a specific number within a dataset, with 10% of the data being at a lower value than this number [206].

# Publications

## Conference publications

[1] N. Kyranaki, J. Zhu, T. R. Betts, and R. Gottschalg, "The Impact of Acetic Acid Corrosion on the Front-side Contacts and the Finger Electrodes of c-Si PV Cells," in *14th Photovoltaic Science, Applications and Technology Conference (PVSAT-14)*, 2018, pp. 1–4. Oral presentation.

[2] N. Kyranaki, J. Zhu, R. Gottschalg, and T. R. Betts, "Investigating the Degradation of Front and Rear Sides of c-Si cells Exposed to Acetic Acid," in *35th European Photovoltaic Solar Energy Conference and Exhibition*, 2018, pp. 1372–1375. Visual presentation.

[3] N. Kyranaki, M. Jankovec, M. Topic, R. Gottschalg, and T. R. Betts, "Investigation of Moisture Ingress and Egress in Polymer – Glass Laminates for PV Encapsulation," in *15th Photovoltaic Science, Applications and Technology Conference (PVSAT-15)*, 2019, pp. 1–4. Oral presentation.

[4] N. Kyranaki, D. Whalley, D. Hutt, R. Gottschalg, and T. R. Betts, "Direct measurement of moisture ingress in PV laminates," in *36th European Photovoltaic Solar Energy Conference and Exhibition*, 2019, pp. 1045–1049. Visual presentation.

## Future journal publications

[1] N. Kyranaki, F. Herbst, M. Wendt, J. Nagel, D. A. Hutt, D. C. Whalley, S. Meyer, R. Gottschalg, T. R. Betts "Determination of the Absorption Isotherm of the Polymers Contained Within a PV Laminate".

[2] N. Kyranaki, A. Smith, D. A. Hutt, D. C. Whalley, R. Gottschalg, T. R. Betts "Damp-heat induced degradation in photovoltaic modules manufactured with Passivated Emitter and Rear Contact solar cells".

## Prizes

"The Impact of Acetic Acid Corrosion on the Front-side Contacts and the Finger Electrodes of c-Si PV Cells", 1<sup>st</sup> prize for best oral presentation and paper, Wolfson School Conference, Loughborough University, 2018.



## References

- [1] M. Schmela, G. Masson, and N. N. T. Mai, "Global Market Outlook for Solar Power 2016–2020," Brussels, Belgium, 2016.
- [2] E. Bellini, "Global cumulative PV capacity tops 480 GW, IRENA says," *PV Magazine*, Apr-2019.
- [3] A. L. Koefoed and M. Rinaldo, "DNV GL Energy transition Outlook 2019," Høvik, Norway, 2019.
- [4] Martin Schachinger, "Module Price Index, May 2019: Fridays forever," *PV Magazine*, May-2019.
- [5] M. A. B. Ala' K. Abu-Rumman, Iyad Muslih, "Life Cycle Costing of PV Generation System," *J. Appl. Res. Ind. Eng.*, vol. 4, no. 4, pp. 252–258, 2017.
- [6] A. Limmanee, S. Songtraï, and N. Udomdachanut, "Degradation analysis of photovoltaic modules under tropical climatic conditions and its impacts on LCOE," *Renew. Energy*, vol. 102, pp. 199–204, 2017.
- [7] C. P. Cameron and A. C. Goodrich, "The levelized cost of energy for distributed PV: A parametric study," in *Conference Record of the IEEE Photovoltaic Specialists Conference*, 2010, pp. 529–534.
- [8] A. Jäger-Waldau, "PV Status Report 2019," 2019.
- [9] S. Philipps and W. Warmuth, "Photovoltaics Report," Freiburg, Germany, 2020.
- [10] M. A. Munoz, M. C. Alonso-García, N. Vela, and F. Chenlo, "Early degradation of silicon PV modules and guaranty conditions," *Sol. Energy*, vol. 85, no. 9, pp. 2264–2274, 2011.
- [11] X. Dai and K. R. McIntosh, "Protection of Si-SiO<sub>2</sub> interfaces from damp heat by overlying SiN<sub>x</sub> and Si<sub>3</sub>N<sub>4</sub> coatings," in *Conference Record of the IEEE Photovoltaic Specialists Conference*, 2010, pp. 3205–3209.
- [12] A. G. Aberle, "Surface passivation of crystalline silicon solar cells: a review," *Prog. Photovoltaics Res. Appl.*, vol. 8, no. 5, pp. 473–487, 2000.
- [13] H. Seigneur *et al.*, "Manufacturing metrology for c-Si photovoltaic module reliability and durability, Part I: Feedstock, crystallization and wafering," *Renew. Sustain. Energy Rev.*, vol. 59, pp. 84–106, 2016.
- [14] D. Sperber, A. Graf, D. Skorcka, A. Herguth, and G. Hahn, "Degradation of Surface Passivation on Crystalline Silicon and Its Impact on Light-Induced Degradation Experiments," *IEEE J. Photovoltaics*, vol. 7, no. 6, pp. 1627–1634, 2017.
- [15] M. Lu, S. Bowden, U. Das, and R. Birkmire, "Interdigitated back contact

- silicon heterojunction solar cell and the effect of front surface passivation,” *Appl. Phys. Lett.*, vol. 91, no. 063507, pp. 1–3, 2007.
- [16] K. Lin *et al.*, “Detection of soldering induced damages on crystalline silicon solar modules fabricated by hot-air soldering method,” *Renew. Energy*, vol. 83, pp. 749–758, 2015.
- [17] M. Kempe, “Overview of scientific issues involved in selection of polymers for PV applications,” in *Conference Record of the 37th IEEE Photovoltaic Specialists Conference*, 2011, pp. 000085–000090.
- [18] G. Jorgensen, K. Terwilliger, S. Glick, J. Pern, and T. McMahon, “Materials testing for PV module encapsulation,” in *National Center for Photovoltaics and Solar Program Review Meeting*, 2003.
- [19] M. Köntges *et al.*, “Review of Failures of Photovoltaic Modules,” 2014.
- [20] D. C. Jordan, T. J. Silverman, J. H. Wohlgemuth, S. R. Kurtz, and K. T. VanSant, “Photovoltaic failure and degradation modes,” *Prog. Photovolt Res. Appl.*, vol. 25, pp. 318–326, 2017.
- [21] A. Masuda, N. Uchiyama, and Y. Hara, “Degradation by acetic acid for crystalline Si photovoltaic modules,” *Jpn. J. Appl. Phys.*, vol. 54, no. 4, 2015.
- [22] H. Han *et al.*, “Analysis of the Degradation of Monocrystalline Silicon Photovoltaic Modules after Long-Term Exposure for 18 Years in a Hot-Humid Climate in China,” *IEEE J. Photovoltaics*, vol. 8, no. 3, pp. 806–812, 2018.
- [23] A. Kraft *et al.*, “Investigation of Acetic Acid Corrosion Impact on Printed Solar Cell Contacts,” *IEEE J. Photovoltaics*, vol. 5, no. 3, pp. 736–743, 2015.
- [24] H. Xiong *et al.*, “Corrosion behavior of crystalline silicon solar cells,” *Microelectron. Reliab.*, vol. 70, pp. 49–58, 2017.
- [25] M. Koehl, M. Heck, and S. Wiesmeier, “Modelling of conditions for accelerated lifetime testing of Humidity impact on PV-modules based on monitoring of climatic data,” *Sol. Energy Mater. Sol. Cells*, vol. 99, pp. 282–291, 2012.
- [26] J. Zhu *et al.*, “Changes of solar cell parameters during damp-heat exposure,” *Prog. Photovolt Res. Appl.*, vol. 24, no. 10, pp. 1346–1358, 2016.
- [27] V. Sharma and S. S. Chandel, “Performance and degradation analysis for long term reliability of solar photovoltaic systems: A review,” *Renew. Sustain. Energy Rev.*, vol. 27, pp. 753–767, 2013.
- [28] M. Zeman, “Solar Cells,” *TU Delft OpenCourseWare*, 2016. [Online]. Available: <https://ocw.tudelft.nl/courses/solar-cells/>. [Accessed: 19-Nov-2019].
- [29] T. Markvart and L. Castañer, “Chapter I-1-A - Principles of Solar Cell

- Operation,” in *Practical Handbook of Photovoltaics*, 2nd Ed., Elsevier Ltd, 2012, pp. 7–31.
- [30] J. L. Gray, “Chapter 3: The Physics of the Solar Cell,” in *Handbook of Photovoltaic Science and Engineering*, 1st Ed., John Wiley & Sons, Ltd, 2011.
- [31] H. Tian, F. Mancilla-David, K. Ellis, E. Muljadi, and P. Jenkins, “A cell-to-module-to-array detailed model for photovoltaic panels,” *Sol. Energy*, vol. 86, no. 9, pp. 2695–2706, 2012.
- [32] S. Speaks, “Reliability and MTBF Overview,” 2002.
- [33] T. Cooper, C. Coggins, A. Davies, J. Davis, J. Hanna, and A. Moore, “Beyond The longer life option The longer life option,” *New Econ. Found.*, no. November, pp. 1–22, 1994.
- [34] A. Ndiaye, A. Charki, A. Kobi, C. M. F. Kébé, P. A. Ndiaye, and V. Sambou, “Degradations of silicon photovoltaic modules: A literature review,” *Sol. Energy*, vol. 96, pp. 140–151, 2013.
- [35] M. Köntges *et al.*, “Report IEA-PVPS T13-09:2017:Assessment of Photovoltaic Module Failures in the Field,” 2017.
- [36] R. Laronde, A. Charki, and D. Bigaud, “Lifetime Estimation of a Photovoltaic Module Subjected to Corrosion Due to Damp Heat Testing,” *J. Sol. Energy Eng.*, vol. 135, no. 2, pp. 1–8, 2013.
- [37] J.-H. Kim, J. Park, D. Kim, and N. Park, “Study on mitigation of solder corrosion for crystalline photovoltaic modules,” *Int. J. Photoenergy*, vol. 2014, pp. 1–9, 2014.
- [38] R. Khatri, S. Agarwal, I. Saha, S. K. Singh, and B. Kumar, “Study on long term reliability of photo-voltaic modules and analysis of power degradation using accelerated aging tests and electroluminescence technique,” *Energy Procedia*, vol. 8, pp. 396–401, 2011.
- [39] T. Tanahashi, N. Sakamoto, H. Shibata, and A. Masuda, “Electrical Detection of Gap Formation underneath Finger Electrodes on c-Si PV Cells Exposed to Acetic Acid Vapor under Hygrothermal Conditions,” in *43rd IEEE Photovoltaic Specialists Conference*, 2016, pp. 1075–1079.
- [40] M. D. Kempe, G. J. Jorgensen, K. M. Terwilliger, T. J. McMahon, C. E. Kennedy, and T. T. Borek, “Acetic acid production and glass transition concerns with ethylene-vinyl acetate used in photovoltaic devices,” *Sol. Energy Mater. Sol. Cells*, vol. 91, pp. 315–329, 2007.
- [41] E. Annigoni, A. Virtuani, M. Caccivio, G. Friesen, D. Chianese, and C. Ballif, “35 years of photovoltaics: Analysis of the TISO-10-kW solar plant, lessons learnt in safety and performance—Part 2,” *Prog. Photovoltaics Res. Appl.*, vol. 27, no. 9, pp. 760–778, 2019.

- [42] M. A. Cluintana, D. L. King, T. J. McMahon, and C. R. Osterwald, "Commonly observed degradation in field-aged photovoltaic modules," in *Conference Record of the Twenty-Ninth IEEE Photovoltaic Specialists Conference*, 2002, pp. 1436–1439.
- [43] M. Owen-bellini, "Thermomechanical Degradation Mechanisms of Silicon Photovoltaic Modules," Loughborough University, 2017.
- [44] N. C. Park, J. S. Jeong, B. J. Kang, and D. H. Kim, "The effect of encapsulant discoloration and delamination on the electrical characteristics of photovoltaic module," *Microelectron. Reliab.*, vol. 53, pp. 1818–1822, 2013.
- [45] G. Oreski and G. M. Wallner, "Delamination behaviour of multi-layer films for PV encapsulation," *Sol. Energy Mater. Sol. Cells*, vol. 89, pp. 139–151, 2005.
- [46] A. W. Czanderna and F. J. Pern, "Encapsulation of PV modules using ethylene vinyl acetate copolymer as a pottant : A critical review," *Sol. Energy Mater. Sol. Cells*, vol. 43, pp. 101–181, 1996.
- [47] A. Skoczek, T. Sample, E. D. Dunlop, and H. A. Ossenbrink, "Electrical performance results from physical stress testing of commercial PV modules to the IEC 61215 test sequence," *Sol. Energy Mater. Sol. Cells*, vol. 92, no. 12, pp. 1593–1604, 2008.
- [48] G. Oreski *et al.*, "Properties and degradation behaviour of polyolefin encapsulants for photovoltaic modules," *Prog. Photovoltaics Res. Appl.*, vol. 28, no. 12, pp. 1277–1288, 2020.
- [49] A. Omazic *et al.*, "Relation between degradation of polymeric components in crystalline silicon PV module and climatic conditions: A literature review," *Sol. Energy Mater. Sol. Cells*, vol. 192, pp. 123–133, 2019.
- [50] F. J. Pern and A. W. Czanderna, "EVA degradation mechanisms simulating those in PV modules," in *AIP Conference Proceedings*, 2008, vol. 268, no. 1, pp. 445–452.
- [51] D. C. Jordan, J. H. Wohlgemuth, and S. R. Kurtz, "Technology and climate trends in pv module degradation," in *27th European Photovoltaic Solar Energy Conference and Exhibition*, 2012, pp. 3118–3124.
- [52] C. Peike, C. Peike, I. Hädrich, K. Weiß, I. Dürr, and F. Ise, "Overview of PV module encapsulation materials," *Photovoltaics Int.*, vol. 19, no. November, pp. 85–92, 2013.
- [53] S. Kaplanis and E. Kaplani, "Energy performance and degradation over 20 years performance of BP c-Si PV modules," *Simul. Model. Pract. Theory*, vol. 19, no. 4, pp. 1201–1211, 2011.
- [54] A. Omazic *et al.*, "Increased reliability of modified polyolefin backsheets over commonly used polyester backsheets for crystalline PV modules," *J. Appl.*

*Polym. Sci.*, vol. 137, pp. 1–8, 2020.

- [55] G. C. Eder *et al.*, “Error analysis of aged modules with cracked polyamide backsheets,” *Sol. Energy Mater. Sol. Cells*, vol. 203, pp. 1–14, 2019.
- [56] C.-C. Lin, Y. Lyu, L.-C. Yu, and X. Gu, “Correlation between mechanical and chemical degradation after outdoor and accelerated laboratory aging for multilayer photovoltaic backsheets,” in *Reliability of Photovoltaic Cells, Modules, Components, and Systems IX, SPIE Optics + Photonics for Sustainable Energy*, 2016, vol. 9938, pp. 1–11.
- [57] M. Köntges, I. Kunze, and S. Kajari-Schröder, “Quantifying the risk of power loss in pv modules due to micro ceacks,” in *Photovoltaic, European Energy, Solar Conference, World Conversion, Photovoltaic Energy*, 2010, pp. 6–10.
- [58] M. Kontges, S. Kajari-Schroder, and I. Kunze, “Crack statistic for wafer-based silicon solar cell modules in the field measured by UV fluorescence,” *IEEE J. Photovoltaics*, vol. 3, no. 1, pp. 95–101, 2013.
- [59] S. Kajari-Schröder, I. Kunze, U. Eitner, and M. Köntges, “Spatial and orientational distribution of cracks in crystalline photovoltaic modules generated by mechanical load tests,” *Sol. Energy Mater. Sol. Cells*, vol. 95, no. 11, pp. 3054–3059, 2011.
- [60] J. B. M. Sander, S. Dietrich, M. Pander, and M. Ebert, S. Schweizer, “Investigations on crack development and crack growth in embedded solar cells,” in *Proc. Reliability of Photovoltaic Cells, Modules, Components, and Systems IV, SPIE Solar Energy + Technology*, 2011.
- [61] I. Duerr, J. Bierbaum, J. Metzger, J. Richter, and D. Philipp, “Silver Grid Finger Corrosion on Snail Track affected PV Modules - Investigation on Degradation Products and Mechanisms,” *Energy Procedia*, vol. 98, pp. 74–85, 2016.
- [62] S. Meyer *et al.*, “Silver nanoparticles cause snail trails in photovoltaic modules,” *Sol. Energy Mater. Sol. Cells*, vol. 121, pp. 171–175, 2014.
- [63] S. Richter, M. Werner, S. Swatek, and C. Hagendorf, “Understanding the snail trail effect in silicon solar modules on microstructural scale,” in *27th European Photovoltaic Solar Energy Conference and Exhibition*, 2012, pp. 3439–3441.
- [64] J. Berghold, S. Wendlandt, and P. B. Ag, “Electrochemical Corrosion within Solar Panels,” in *Proceedings of the 27th European Photovoltaic Congress and Exhibition*, 2012, pp. 3511–3517.
- [65] P. Hacke *et al.*, “Characterization of Multicrystalline Silicon Modules with System Bias Voltage Applied in Damp Heat,” in *25th European Photovoltaic Solar Energy Conference and Exhibition*, 2010, pp. 3760–3765.
- [66] W. Luo *et al.*, “Investigation of the Impact of Illumination on the Polarization-Type Potential-Induced Degradation of Crystalline Silicon Photovoltaic

- Modules,” *IEEE J. Photovoltaics*, vol. 8, no. 5, pp. 1168–1173, 2018.
- [67] W. Luo *et al.*, “Potential-induced degradation in photovoltaic modules: A critical review,” *Energy Environ. Sci.*, vol. 10, no. 1, pp. 43–68, 2017.
- [68] D. Lausch *et al.*, “Sodium outdiffusion from stacking faults as root cause for the recovery process of potential-induced degradation (PID),” *Energy Procedia*, vol. 55, pp. 486–493, 2014.
- [69] V. Naumann *et al.*, “Potential-induced degradation at interdigitated back contact solar cells,” *Energy Procedia*, vol. 55, pp. 498–503, 2014.
- [70] P. Hacke *et al.*, “Test-to-failure of Crystalline Silicon Modules,” in *35th IEEE Photovoltaic Specialists Conference*, 2010, pp. 244–250.
- [71] E. L. Meyer and E. E. Van Dyk, “Assessing the reliability and degradation of photovoltaic module performance parameters,” *IEEE Trans. Reliab.*, vol. 53, no. 1, pp. 83–92, 2004.
- [72] S. Jonai, K. Nakamura, and A. Masuda, “Universal explanation for degradation by charge accumulation in crystalline Si photovoltaic modules with application of high voltage,” *Appl. Phys. Express*, vol. 12, no. 101003, pp. 1–4, 2019.
- [73] K. Morita and K. Ohnaka, “Novel Selective Etching Method for Silicon Nitride Films on Silicon Substrates by Means of Subcritical Water,” *Ind. Eng. Chem. Res.*, vol. 39, no. 12, pp. 4684–4688, 2000.
- [74] E. L. Meyer and E. E. van Dyk, “Monitoring Isc , Voc and performance parameters of photovoltaic modules,” in *Proceedings of the 17th European Photovoltaic Solar Energy Conference*, 2001, pp. 524–527.
- [75] K. R. McIntosh and X. Dai, “Damp-heat degradation and repair of oxide-passivated silicon,” *Phys. Status Solidi Appl. Mater. Sci.*, vol. 208, no. 8, pp. 1931–1936, 2011.
- [76] F. Kersten *et al.*, “A new mc-Si degradation effect called LeTID,” in *2015 IEEE 42nd Photovoltaic Specialist Conference*, 2015.
- [77] Dr Radovan Kopecek, “Is LeTID degradation in PERC cells another degradation crisis even worse than PID?,” *PVtech*, p. 1, Nov-2018.
- [78] A. Graf, A. Herguth, and G. Hahn, “Determination of BO-LID and LeTID related activation energies in Cz-Si and FZ-Si using constant injection conditions,” in *AIP Conference Proceedings*, 2019, pp. 140003-1-140003–5.
- [79] J. Arumughan *et al.*, “Light Induced Degradation in PERC Solar Cells and Comparison with Oxymap,” in *32nd European Photovoltaic Solar Energy Conference and Exhibition*, 2016, pp. 545–549.
- [80] A. Herguth, C. Derricks, and D. Sperber, “A Detailed Study on Light-Induced Degradation of Cz-Si PERC-Type Solar Cells: Evidence of Rear Surface-Related Degradation,” *IEEE J. Photovoltaics*, vol. 8, no. 5, pp. 1190–1201,

2018.

- [81] D. Sperber, A. Herguth, and G. Hahn, "Instability of Dielectric Surface Passivation Quality at Elevated Temperature and Illumination," *Energy Procedia*, vol. 92, pp. 211–217, 2016.
- [82] M. Fuhs, "Challenges and solutions for anti-LID treatment," *PV Magazine*, Sep-2018.
- [83] W. Herrmann, W. Wiesner, and W. Vaassen, "Hot spot investigations on PV modules-new concepts for a test standard and consequences for module design with respect to bypass diodes," in *Conference Record of the Twenty-Sixth IEEE Photovoltaic Specialists Conference.*, 1997, pp. 1129–1132.
- [84] K. Kato, "'PVResQ!' PV Module Failures Observed in the Field," in *PVPS Workshop*, 2012, pp. 1–24.
- [85] M. Köntges *et al.*, "Assessment of PV Module Failures in the Field Assessment of PV Module Failures in the Field," in *Report IEA-PVPS T13-09:2017*, 2017, pp. 1–118.
- [86] P. Hülsmann and K. A. Weiss, "Simulation of water ingress into PV-modules: IEC-testing versus outdoor exposure," *Sol. Energy*, vol. 115, pp. 347–353, 2015.
- [87] G. J. Å. Jorgensen *et al.*, "Moisture transport , adhesion , and corrosion protection of PV module packaging materials," vol. 90, pp. 2739–2775, 2006.
- [88] A. Fick, "V. On liquid diffusion," *Phil. Mag.*, vol. 10, no. 63, pp. 30–39, 1855.
- [89] M. Jankovec *et al.*, "In-Situ Monitoring of Moisture Ingress in PV Modules Using Digital Humidity Sensors," *IEEE J. Photovoltaics*, vol. 6, no. 5, pp. 1152–1159, 2016.
- [90] J. Crank, *The Mathematics of Diffusion*, Second. London W.I: Oxford University Press, Ely House, 1975.
- [91] M. Jankovec *et al.*, "In-Situ Monitoring of Moisture Ingress in PV Modules with Different Encapsulants," in *32nd European Photovoltaic Solar Energy Conference and Exhibition*, 2016, pp. 2265–2269.
- [92] S. Mitterhofer, C. Barretta, L. F. Castillon, G. Oreski, M. Topič, and M. Jankovec, "A Dual-Transport Model of Moisture Diffusion in PV Encapsulants for Finite-Element Simulations," *IEEE J. Photovoltaics*, vol. 10, no. 1, pp. 94–102, 2020.
- [93] M. D. Kempe, "Modeling of rates of moisture ingress into photovoltaic modules," *Sol. Energy Mater. Sol. Cells*, vol. 90, no. 16, pp. 2720–2738, 2006.
- [94] J. Slapsak, S. Mitterhofer, M. Topic, and M. Jankovec, "Wireless System for In Situ Monitoring of Moisture Ingress in PV Modules," *IEEE J.*

- Photovoltaics*, vol. 9, no. 5, pp. 1316–1323, 2019.
- [95] A. Virtuani, E. Annigoni, and C. Ballif, “One-type-fits-all-systems: Strategies for preventing potential-induced degradation in crystalline silicon solar photovoltaic modules,” *Prog. Photovoltaics Res. Appl.*, vol. 27, no. 1, pp. 13–21, 2019.
- [96] W. Henry, “Experiments on the quantity of gases absorbed by water, at different temperatures, and under different pressures,” *Phil. Trans. R. Soc. Lond.*, vol. 93, pp. 29–42, 1803.
- [97] R. Meitzner and S. H. Schulze, “Method for determination of parameters for moisture simulations in photovoltaic modules and laminated glass,” *Sol. Energy Mater. Sol. Cells*, vol. 144, pp. 23–28, 2016.
- [98] T. Carlsson, J. Halme, P. Lund, and P. Konttinen, “Moisture sensor at glass/polymer interface for monitoring of photovoltaic module encapsulants,” *Sensors Actuators, A Phys.*, vol. 125, no. 2, pp. 281–287, 2006.
- [99] M. O. Reese, “Measuring and understanding moisture ingress for photovoltaics,” *DuraMAT Webinar*, Apr-2020.
- [100] M. D. Kempe and J. H. Wohlgemuth, “Evaluation of temperature and humidity on PV module component degradation,” *Conf. Rec. IEEE Photovolt. Spec. Conf.*, vol. 3, pp. 120–125, 2013.
- [101] J. Kapur, K. Proost, and C. A. Smith, “Determination of moisture ingress through various encapsulants in glass/glass laminates,” *Conf. Rec. IEEE Photovolt. Spec. Conf.*, pp. 001210–001214, 2009.
- [102] R. E. Kumar, G. von Gastrow, J. Leslie, R. Meier, M. I. Bertoni, and D. P. Fenning, “Quantitative Determination of Moisture Content in Solar Modules by Short-Wave Infrared Reflectometry,” *IEEE J. Photovoltaics*, vol. 9, no. 6, pp. 1–6, 2019.
- [103] “EVA SOLARCAP ® FC100014E / A-STT Datasheet,” *EVASA*. [Online]. Available: [https://www.ensolar.com/pv/eva-datasheet/255?utm\\_source=ENF&utm\\_medium=material\\_profile&utm\\_campaign=enquiry\\_company\\_directory&utm\\_content=13810](https://www.ensolar.com/pv/eva-datasheet/255?utm_source=ENF&utm_medium=material_profile&utm_campaign=enquiry_company_directory&utm_content=13810). [Accessed: 12-May-2020].
- [104] “Back sheet dyMat PYE3000®,” *Coveme*, 2012. [Online]. Available: <https://www.ensolar.com/pv/backsheet-datasheet/305>. [Accessed: 12-May-2020].
- [105] E. H. Wong, K. C. Chan, T. B. Lim, and T. F. Lam, “Non-Fickian moisture properties characterisation and diffusion modeling for electronic packages,” *1999 Proceedings. 49th Electron. Components Technol. Conf.*, pp. 302–306, 1999.
- [106] T. Glaskova-Kuzmina, A. Aniskevich, J. Sevchenko, A. Borriello, and M. Zarrelli, “Cyclic Moisture Sorption and its Effects on the Thermomechanical



- Properties of Epoxy and Epoxy/MWCNT Nanocomposite,” *Polymers (Basel)*., vol. 11, no. 9, pp. 1–14, 2019.
- [107] K. Y. Foo and B. H. Hameed, “Insights into the modeling of adsorption isotherm systems,” *Chem. Eng. J.*, vol. 156, no. 1, pp. 2–10, 2010.
- [108] Z. Xia, D. W. Cunningham, and J. H. Wohlgemuth, “A non-solvent extraction method for measuring gel content of ethylene vinyl acetate,” in *Conference Record of the IEEE Photovoltaic Specialists Conference*, 2009, pp. 000124–000126.
- [109] S. Marais, Q. T. Nguyen, D. Langevin, and M. Métayer, “Transport of water and gases through EVA copolymer films, EVA 70/PVC, and EVA70/PVC/gluten blends,” *Macromol. Symp.*, vol. 175, pp. 329–347, 2001.
- [110] R. M. Hodge, T. J. Bastow, G. H. Edward, G. P. Simon, and A. J. Hill, “Free volume and the mechanism of plasticization in water-swollen poly(vinyl alcohol),” *Macromolecules*, vol. 29, no. 25, pp. 8137–8143, 1996.
- [111] K. Gotoh, A. Yasukawa, and Y. Kobayashi, “Wettability characteristics of poly(ethylene terephthalate) films treated by atmospheric pressure plasma and ultraviolet excimer light,” *Polym. J.*, vol. 43, no. 6, pp. 545–551, 2011.
- [112] B. Xiong, S. Zhu, Y. Fan, H. Li, M. Shi, and Y. Cao, “Hydrophobic modification of poly(Ethylene Terephthalate) with epoxy-modified polysiloxane by reactive extrusion,” *J. Macromol. Sci. Part B Phys.*, vol. 51, no. 4, pp. 630–641, 2012.
- [113] T. Aizawa, “Fabrication of porosity-controlled polyethylene terephthalate porous materials using a CO<sub>2</sub>-Assisted polymer compression method,” *RSC Adv.*, vol. 8, no. 6, pp. 3061–3068, 2018.
- [114] S. Brunauer, P. H. Emmett, and E. Teller, “Adsorption of Gases in Multimolecular Layers,” *J. Am. Chem. Soc.*, vol. 60, no. 2, pp. 309–319, 1938.
- [115] G. K. Van Der Wel and O. C. G. Adan, “Moisture in organic coatings - a review,” *Prog. Org. Coatings*, vol. 37, no. 1, pp. 1–14, 1999.
- [116] E. Favre, R. Clement, Q. T. Nguyen, P. Schaezel, and J. Neel, “Sorption of Organic Solvents into Dense Silicone Membranes Part 2.-Development of a New Approach based on a Clustering Hypothesis for Associated Solvents,” *J. Chem. Soc. Faraday Trans.*, vol. 89, no. 24, pp. 4339–4346, 1993.
- [117] P. J. Flory, “Thermodynamics of high polymer solutions,” *J. Chem. Phys.*, vol. 10, no. 51, pp. 51–61, 1942.
- [118] M. L. Huggins, “Solutions of long chain compounds,” *J. Chem. Phys.*, vol. 9, no. 5, p. 440, 1941.
- [119] R. H. Byrd, P. Lu, J. Nocedal, and C. Zhu, “A Limited Memory Algorithm for Bound Constrained Optimization,” *SIAM J. Sci. Comput.*, vol. 16, no. 5, pp.

1190–1208, 1995.

- [120] “minimize(method='L-BFGS-B'),” *SciPy.org*, 2020. [Online]. Available: <https://docs.scipy.org/doc/scipy/reference/optimize.minimize-lbfgsb.html#optimize-minimize-lbfgsb>. [Accessed: 16-Aug-2020].
- [121] G.Mon, L.Wen, and R.Ross, “Water-module interaction studies.pdf,” in *Conference Record of the Twentieth IEEE Photovoltaic Specialists Conference*, 1988, pp. 1098–1102.
- [122] M. Miyashita, S. Kawai, and A. Masuda, “Measuring method of moisture ingress into photovoltaic modules,” *Jpn. J. Appl. Phys.*, vol. 51, no. 10 PART 2, 2012.
- [123] “3M™ Humidity Indicator Cards (HICs) datasheet.” [Online]. Available: <https://docs-emea.rs-online.com/webdocs/1446/0900766b81446f54.pdf>. [Accessed: 15-Aug-2019].
- [124] M. Jankovec *et al.*, “Long term stability of humidity sensors , laminated in EVA encapsulant,” in *M I D E M 2 0 1 5 - International Conference on Microelectronics, Devices and Materials with the Workshop on Terahertz and Microwave Systems*, 2015, pp. 1–6.
- [125] “Python colour library tutorial.” [Online]. Available: <https://colour.readthedocs.io/en/develop/tutorial.html>. [Accessed: 04-Sep-2019].
- [126] K. Thaworn, P. Buahom, and S. Areerat, “Effects of Organic Peroxides on the Curing Behavior of EVA Encapsulant Resin,” *Open J. Polym. Chem.*, vol. 02, no. 02, pp. 77–85, 2012.
- [127] M. Rahman and K. Lyle, “Sharing chemistry with the community: A colorful catalyst,” *Chem13 News Magazine*, 2014. [Online]. Available: <https://uwaterloo.ca/chem13-news-magazine/march-2014/activities/sharing-chemistry-community-colorful-catalyst>. [Accessed: 25-Nov-2019].
- [128] Y. Voronko, G. C. Eder, M. Knausz, G. Oreski, K. A. Berger, and T. Koch, “Correlation of the loss in photovoltaic module performance with the ageing behaviour of the backsheets used,” *Prog. Photovolt Res. Appl.*, vol. 23, pp. 1501–1515, 2015.
- [129] P. J. Proll and L. H. Sutcliffe, “Species of cobalt(II) in acetic acid. Part II. Cobalt(II) in the presence of lithium bromide, lithium chloride and ammonium thiocyanate,” *J. Phys. Chem.*, vol. 65, no. 11, pp. 1993–2000, 1961.
- [130] T. Shioda, “Acetic acid production rate in EVA encapsulant and its influence on performance of PV modules,” in *2nd Atlas/NIST PV Materials Durability Workshop*, 2013.
- [131] D. Wu, “Investigation of the reliability of the encapsulation system of photovoltaic modules,” Loughborough University, 2015.

- [132] G. Oreski, "Degradation of materials in PV modules," in *EU Cost Action PEARL PV Seminar*, 2019.
- [133] "Back sheet dyMat APYE®," *Coveme*, 2012. [Online]. Available: <https://www.enfsolar.com/pv/backsheet-datasheet/297>. [Accessed: 22-May-2020].
- [134] "Back sheet dyMat ClrPYE®," *Coveme*, 2012. [Online]. Available: <https://www.enfsolar.com/pv/backsheet-datasheet/301>. [Accessed: 22-May-2020].
- [135] "Air - Diffusion Coefficients of Gases in Excess of Air," *Engineering ToolBox*, 2018. [Online]. Available: [https://www.engineeringtoolbox.com/air-diffusion-coefficient-gas-mixture-temperature-d\\_2010.html](https://www.engineeringtoolbox.com/air-diffusion-coefficient-gas-mixture-temperature-d_2010.html). [Accessed: 02-Jun-2020].
- [136] C. Peike *et al.*, "Origin of damp-heat induced cell degradation," *Sol. Energy Mater. Sol. Cells*, vol. 116, pp. 49–54, 2013.
- [137] N. C. Park, W. W. Oh, and D. H. Kim, "Effect of temperature and humidity on the degradation rate of multicrystalline silicon photovoltaic module," *Int. J. Photoenergy*, vol. 2013, pp. 1–9, 2013.
- [138] K. Whitfield, A. Salomon, S. Yang, and I. Suez, "Damp Heat versus Field Reliability for Crystalline Silicon," in *38th IEEE Photovoltaic Specialists Conference*, 2011, pp. 1864–1870.
- [139] M. Koehl, S. Hoffmann, and S. Wiesmeier, "Evaluation of damp-heat testing of photovoltaic modules," *Prog. Photovoltaics Res. Appl.*, vol. 25, no. 2, pp. 175–183, 2017.
- [140] W. Herrmann and N. Bogdanski, "Outdoor weathering of PV modules - Effects of various climates and comparison with accelerated laboratory testing," in *Conference Record of the IEEE Photovoltaic Specialists Conference*, 2011, pp. 002305–002311.
- [141] J. H. Wohlgemuth;, D. W. Cunningham;, A. M. Nguyen;, and J. Miller, "Long term reliability of PV modules," in *Proceedings of the 20th European PV Solar Energy Conference*, 2005, pp. 1942–1948.
- [142] T. H. Kim, N. C. Park, and D. H. Kim, "The effect of moisture on the degradation mechanism of multi-crystalline silicon photovoltaic module," *Microelectron. Reliab.*, vol. 53, no. 9–11, pp. 1823–1827, 2013.
- [143] T. Tanahashi, N. Sakamoto, H. Shibata, and A. Masuda, "Corrosion under Front Electrodes of Crystalline Silicon Photovoltaic Cells Predominantly Contributes to Their Performance Degradation," in *IEEE 46th Photovoltaic Specialists Conference (PVSC)*, 2019, pp. 2013–2016.
- [144] P. Patnaik, *Handbook of Inorganic Chemicals*. Burlington, VT, USA: McGraw-Hill, 2002.
- [145] A. I. Onuchukwu and F. K. Oppong-Boachie, "The corrosion behaviour of

- aluminum alloy AA1060 in p-quinone and acetic acid media," *Corros. Sci.*, vol. 26, no. 11, pp. 919–926, 1986.
- [146] W. Vedder, Latham, and D. A. Vermilyea, "Corrosion Inhibiting Environment for Aluminum," 3,672,822, 1972.
- [147] S. W. Glunz and F. Feldmann, "SiO<sub>2</sub> surface passivation layers – a key technology for silicon solar cells," *Sol. Energy Mater. Sol. Cells*, vol. 185, pp. 260–269, 2018.
- [148] M. C. Talló and K. R. McIntosh, "Permeability of TiO<sub>2</sub> antireflection coatings to damp heat," *Proc. 24th EU PVSEC*, pp. 2037–2040, 2009.
- [149] Finlay Colville, "PV CellTech 2020 to explain why n-PERT emerging as differentiated play for Chinese leaders," *PVtech*, p. 1, Dec-2019.
- [150] B. Ketola and A. Norris, "Degradation Mechanism Investigation of Extended Damp Heat Aged PV Modules," in *proceedings of 26th EU PVSEC*, 2011.
- [151] "Acetic Acid, Glacial (Certified ACS), Fisher Chemical," *Fisher Scientific*. [Online]. Available: [https://www.fishersci.com/shop/products/acetic-acid-glacial-certified-acs-fisher-chemical-9/A38P20?gclid=Cj0KCQjwrlf3BRD1ARIsAMuugNvOFvakKCbcEvBoFArDJhT8TXgnfF4CYw8vmU5kDBD7thDNRKa1icQaAshiEALw\\_wcB&ef\\_id=Cj0KCQjwrlf3BRD1ARIsAMuugNvOFvakKCbcEvBoFArDJhT8TXg](https://www.fishersci.com/shop/products/acetic-acid-glacial-certified-acs-fisher-chemical-9/A38P20?gclid=Cj0KCQjwrlf3BRD1ARIsAMuugNvOFvakKCbcEvBoFArDJhT8TXgnfF4CYw8vmU5kDBD7thDNRKa1icQaAshiEALw_wcB&ef_id=Cj0KCQjwrlf3BRD1ARIsAMuugNvOFvakKCbcEvBoFArDJhT8TXg). [Accessed: 11-Jun-2020].
- [152] Karl Georg Bedrich, "Quantitative electroluminescence measurements of PV devices," Loughborough University, 2019.
- [153] M. Köntges, M. Siebert, and D. Hinken, "Quantitative analysis of PV-modules by electroluminescence images for quality control," in *Proceedings of the 24th European Photovoltaic Solar Energy Conference*, 2009, pp. 3226–3231.
- [154] V. Gazuz and C. Buerhop, "Detection of power losses in busbar solder contacts by electroluminescence imaging of solar cells," *Meas. Sci. Technol.*, vol. 22, no. 11, 2011.
- [155] O. Breitenstein, J. Bauer, T. Trupke, and R. A. Bardos, "On The Detection of Shunts in Silicon Solar Cells by Photo- and Electroluminescence Imaging," *Prog. Photovolt Res. Appl.*, vol. 16, pp. 325–330, 2008.
- [156] K. Bothe, P. Pohl, and J. Schmidt, "Electroluminescence imaging as an in-line characterisation tool for solar cell production," in *21st European Photovoltaic Solar Energy Conference*, 2006, pp. 597–600.
- [157] T. Potthoff, K. Bothe, U. Eitner, D. Hinken, and M. Königes, "Detection of the voltage distribution in photovoltaic modules by electroluminescence imaging," *Prog. Photovoltaics Res. Appl.*, vol. 18, no. 2, pp. 100–106, 2010.
- [158] "Spectral Response," *pveducation.org*, 2019. [Online]. Available:

- <https://www.pveducation.org/pvcdrom/solar-cell-operation/spectral-response>. [Accessed: 16-Jul-2020].
- [159] J. S. Hartman and M. A. Lind, "Spectral response measurements for solar cells," *Sol. Cells*, vol. 7, no. 1–2, pp. 147–157, 1982.
- [160] "Quantum Efficiency," *pveducation.org*, 2019. [Online]. Available: <https://www.pveducation.org/pvcdrom/solar-cell-operation/quantum-efficiency>. [Accessed: 17-Apr-2020].
- [161] N. H. Reich *et al.*, "Weak Light Performance and Spectral Response of Different Solar Cell Types," in *Proc 20th European Photovoltaic Solar Energy Conference and Exhibition*, 2005, pp. 4–7.
- [162] S. Bowden and A. Rohatgi, "Rapid And Accurate Determination of Series Resistance and Fill Factor Losses in Industrial Silicon Solar Cells," in *17th European Photovoltaic Solar Energy Conference and Exhibition*, 2001.
- [163] F. Kersten *et al.*, "Stability investigations of CZ-PERC modules during damp heat testing and transport: The impact of the boron-oxygen defect," *AIP Conf. Proc.*, vol. 2147, no. 090001, pp. 1–6, 2019.
- [164] S. Kumar, R. Meena, and R. Gupta, "Imaging and micro-structural characterization of moisture induced degradation in crystalline silicon photovoltaic modules," *Sol. Energy*, vol. 194, pp. 903–912, 2019.
- [165] W. Oh *et al.*, "Migration of Sn and Pb from Solder Ribbon onto Ag Fingers in Field-Aged Silicon Photovoltaic Modules," *Int. J. Photoenergy*, vol. 2015, pp. 1–7, 2015.
- [166] J. H. Wohlgemuth and M. D. Kempe, "Equating Damp Heat Testing with Field Failures," in *IEEE 39th Photovoltaic Specialists Conference (PVSC)*, 2013, pp. 126–131.
- [167] H. Li, F. Lv, H. Diao, X. Chen, and W. Wang, "Evaluation of temperature and humidity on PV module degradation- in field degradation analysis of crystalline silicon module," in *2019 IEEE 46th Photovoltaic Specialists Conference (PVSC)*, 2019, pp. 1986–1990.
- [168] P. Rajput, G. N. Tiwari, O. S. Sastry, B. Bora, and V. Sharma, "Degradation of mono-crystalline photovoltaic modules after 22 years of outdoor exposure in the composite climate of India," *Sol. Energy*, vol. 135, pp. 786–795, 2016.
- [169] F. Bandou, A. Hadj Arab, M. S. Belkaid, P. O. Logerais, O. Riou, and A. Charki, "Evaluation performance of photovoltaic modules after a long time operation in Saharan environment," *Int. J. Hydrogen Energy*, vol. 40, no. 39, 2015.
- [170] R. M. Smith, D. C. Jordan, and S. R. Kurtz, "Outdoor PV module degradation of current-voltage parameters," in *World Renewable Energy Forum, WREF*, 2012, pp. 2547–2554.

- [171] Z. Liu *et al.*, “Quantitative analysis of degradation mechanisms in 30-year-old PV modules,” *Sol. Energy Mater. Sol. Cells*, vol. 200, no. April, pp. 1–8, 2019.
- [172] A. Bradley, T. Dhir, and Y. Poissant, “Initial analysis of a 22-year old PV system in Quebec , Canada,” in *PV Module Reliability Workshop (PVMRW)*, 2015.
- [173] N. Hrelja *et al.*, “Single Diode Model Applied to PV Module Aging,” in *35th European Photovoltaic Solar Energy Conference and Exhibition*, 2018, pp. 1290–1293.
- [174] M. Wang *et al.*, “Evaluation of Photovoltaic Module Performance Using Novel Data-driven I-V Feature Extraction and Suns-V OC Determined from Outdoor Time-Series I-V Curves,” in *2018 IEEE 7th World Conference on Photovoltaic Energy Conversion, WCPEC 2018 - A Joint Conference of 45th IEEE PVSC, 28th PVSEC and 34th EU PVSEC*, 2018, pp. 778–783.
- [175] J. Liu, J. L. Braid, and R. H. French, “Real-world PV Module Degradation across Climate Zones Determined from Suns - V oc , Loss Factors and I - V Steps Analysis of Eight Years of I-V , Pmp Time-series Datastreams,” *46th IEEE Photovolt. Spec. Conf.*, pp. 680–686, 2019.
- [176] D. S. Peck, “Comprehensive Model for Humidity Testing Correlation,” in *24th Annual Reliability Physics Symposium*, 1986, pp. 44–50.
- [177] S. Glasstone, K. J. Laidler, and H. Eyring, *The theory of rate processes: the kinetics of chemical reactions, viscosity, diffusion and electrochemical phenomena*, 1st ed. New York, United States: McGraw-Hill, 1941.
- [178] S. Lindig, I. Kaaya, K. A. Weis, D. Moser, and M. Topic, “Review of statistical and analytical degradation models for photovoltaic modules and systems as well as related improvements,” *IEEE J. Photovoltaics*, vol. 8, no. 6, pp. 1773–1786, 2018.
- [179] R. Pan, “Degradation Analysis of Solar Photovoltaic Modules : Influence of Environmental Factor,” in *Proceedings - Annual Reliability and Maintainability Symposium*, 2011.
- [180] B. Braisaz, C. Duchayne, M. Van Iseghem, and K. Radouane, “PV Aging Model Applied to Several Meteorological Conditions,” in *29th European Photovoltaic Solar Energy Conference and Exhibition*, 2014, pp. 2303–2309.
- [181] “Photovoltaic Measurement System, PVMS-250/80/12, User Manual,” *egni TEC*, 2012. .
- [182] E. Koumpli, “Impact of Data Quality on Photovoltaic (PV) Performance Assessment,” Loughborough University, 2017.
- [183] “scipy.optimize.least\_squares,” *SciPy.org*, 2019. [Online]. Available: [https://docs.scipy.org/doc/scipy/reference/generated/scipy.optimize.least\\_squares.html#scipy.optimize.least\\_squares](https://docs.scipy.org/doc/scipy/reference/generated/scipy.optimize.least_squares.html#scipy.optimize.least_squares). [Accessed: 29-Nov-2019].

- [184] M. A. Branch, T. F. Coleman, and Y. Li, "A Subspace, Interior, and Conjugate Gradient Method for Large-Scale Bound-Constrained Minimization Problems," *SIAM J. Sci. Comput.*, vol. 21, no. 1, pp. 1–23, 1999.
- [185] N. Mayorov, S. Troisi, P. van Mulbregt, M. Gwózdź, A. Nelson, and A. Gautam, "implementation note of the trf library," *GitHub*, 2020. [Online]. Available: [https://github.com/scipy/scipy/blob/master/scipy/optimize/\\_lsq/trf.py](https://github.com/scipy/scipy/blob/master/scipy/optimize/_lsq/trf.py). [Accessed: 08-Jun-2020].
- [186] "scipy.optimize.curve\_fit," *SciPy.org*, 2019. [Online]. Available: [https://docs.scipy.org/doc/scipy/reference/generated/scipy.optimize.curve\\_fit.html](https://docs.scipy.org/doc/scipy/reference/generated/scipy.optimize.curve_fit.html). [Accessed: 08-Jun-2020].
- [187] R. Y. Rubinstein, *Simulation and the Monte Carlo Method*, 1st ed. USA: John Wiley & Sons, Inc., 1981.
- [188] D. C. Jordan *et al.*, "Reducing Interanalyst Variability in Photovoltaic Degradation Rate Assessments," *IEEE J. Photovoltaics*, vol. 10, no. 1, pp. 1–7, 2019.
- [189] "scipy.signal.find\_peaks\_cwt," *SciPy.org*, 2014. [Online]. Available: [https://docs.scipy.org/doc/scipy-0.14.0/reference/generated/scipy.signal.find\\_peaks\\_cwt.html](https://docs.scipy.org/doc/scipy-0.14.0/reference/generated/scipy.signal.find_peaks_cwt.html). [Accessed: 04-Dec-2019].
- [190] A. M. Gracia, N. Taylor, and R. Kenny, "Preparation and Validation of PV Module Outdoor Performance Datasets," Ispra, Italy, 2014.
- [191] IEC, "IEC 60904-1 Photovoltaic Devices Part 1: Measurement of Photovoltaic Current-Voltage Characteristics," 2006.
- [192] H. M. Mirlitz, K. A. Peterson, I. T. Martin, and R. H. French, "Degradation of transparent conductive oxides: Interfacial engineering and mechanistic insights," *Sol. Energy Mater. Sol. Cells*, vol. 143, pp. 529–538, 2015.
- [193] H. S. Fairman, M. H. Brill, and H. Hemmendinger, "How the CIE 1931 color-matching functions were derived from Wright-Guild data," *Color Res. Appl.*, vol. 22, no. 1, pp. 11–23, 1997.
- [194] CIE, "Commission internationale de l'Eclairage proceedings, 1931." Cambridge University Press, Cambridge, 1932.
- [195] "CIE 1931 Color Space," *Colblindor*, 2007. [Online]. Available: <https://www.color-blindness.com/2007/01/18/cie-1931-color-space/>. [Accessed: 19-Dec-2019].
- [196] "numpy.linspace," *SciPy.org*, 2019. [Online]. Available: <https://docs.scipy.org/doc/numpy/reference/generated/numpy.linspace.html>. [Accessed: 19-Dec-2019].

- [197] M. Hazewinkel, "Linear interpolation," *Encyclopedia of Mathematics*, 2001. [Online]. Available: [https://www.encyclopediaofmath.org/index.php/Linear\\_interpolation](https://www.encyclopediaofmath.org/index.php/Linear_interpolation). [Accessed: 19-Dec-2019].
- [198] "scipy.interpolate.interp1d," *SciPy.org*, 2019. [Online]. Available: <https://docs.scipy.org/doc/scipy/reference/generated/scipy.interpolate.interp1d.html>. [Accessed: 19-Dec-2019].
- [199] S.P. Venkateshan and P. Swaminathan, "Chapter 4 - Solution of Algebraic Equations," in *Computational Methods in Engineering*, 1st ed., 2014, pp. 155–201.
- [200] "numpy.gradient," *NumPy*, 2020. [Online]. Available: <https://numpy.org/doc/stable/reference/generated/numpy.gradient.html>. [Accessed: 03-Jul-2020].
- [201] "scipy.signal.cwt," *SciPy.org*, 2014. [Online]. Available: <https://docs.scipy.org/doc/scipy-0.14.0/reference/generated/scipy.signal.cwt.html#scipy.signal.cwt>. [Accessed: 21-Jan-2020].
- [202] "scipy.signal.ricker," *SciPy.org*, 2014. [Online]. Available: <https://docs.scipy.org/doc/scipy-0.14.0/reference/generated/scipy.signal.ricker.html#scipy.signal.ricker>. [Accessed: 21-Jan-2020].
- [203] "scipy.stats.zscore," *SciPy.org*, 2019. [Online]. Available: <https://docs.scipy.org/doc/scipy/reference/generated/scipy.stats.zscore.html>. [Accessed: 24-Jan-2020].
- [204] "Z-Score: Definition, Formula and Calculation," *Statistics How To*, 2020. [Online]. Available: <https://www.statisticshowto.datasciencecentral.com/probability-and-statistics/z-score/>. [Accessed: 24-Jan-2020].
- [205] M. Xiajie, "The complexity of LID, LeTID and HID," *PVtech*, Jan-2019.
- [206] D. J. Rumsey, *Statistics For Dummies*, 2nd Ed. New York, United States: John Wiley & Sons Inc, 2016.